Universität Rostock

HELMHOLTZ MUNICH

JOINT MASS SPECTROMETRY CENTRE

Comprehensive physical and elemental characterization of traffic derived metalliferous non-exhaust emissions: A study of automotive brake and railway wear particles

Cumulative Dissertation

submitted to
the Faculty of Mathematics and Natural Sciences of the University of Rostock
in fulfillment of the requirements for the academic degree
doctor rerum naturalium (Dr. rer. nat.)

by

Jean Carsten Alexander Neukirchen

born May 28th, 1993 in Cologne

Rostock, November 2024

https://doi.org/10.18453/rosdok_id00005074

Gutachter:

1. Prof. Dr. Ralf Zimmermann,
   Institut für Chemie, Universität Rostock

2. Prof. Dr. Jorma Jokiniemi
   University of Eastern Finland, Kuopio, Finnland

Datum der Einreichung: 15. November 2024
Datum der Verteidigung: 28. Januar 2025

Doktorandinnen/Doktoranden-Erklärung gemäß § 4 Absatz 1 Buchstaben g und h der Promotionsordnung der Mathematisch-Naturwissenschaftlichen Fakultät der Universität Rostock

Jean Carsten Alexander Neukirchen
Dahlienstraße 67
85599 Vaterstetten

Ich habe eine Dissertation mit dem Titel:

„ Comprehensive physical and elemental characterization of traffic derived metalliferous non-exhaust emissions: A study of automotive brake and railway wear particles"

an der Mathematisch-Naturwissenschaftlichen Fakultät der Universität Rostock angefertigt. Dabei wurde ich von Herrn **Professor Doktor Ralf Zimmermann** betreut.

Ich gebe folgende Erklärung ab:

1. Die Gelegenheit zum vorliegenden Promotionsvorhaben ist mir nicht kommerziell vermittelt worden. Insbesondere habe ich keine Organisation eingeschaltet, die gegen Entgelt Betreuerinnen/Betreuer für die Anfertigung von Dissertationen sucht oder die mir obliegenden Pflichten hinsichtlich der Prüfungsleistungen für mich ganz oder teilweise erledigt.
2. Ich versichere hiermit an Eides statt, dass ich die vorliegende Arbeit selbstständig angefertigt und ohne fremde Hilfe verfasst habe. Dazu habe ich keine außer den von mir angegebenen Hilfsmitteln und Quellen verwendet und die den benutzten Werken inhaltlich und wörtlich entnommenen Stellen habe ich als solche kenntlich gemacht.

Rostock, _____ _____

Jean Carsten Alexander Neukirchen

I want to express my heartfelt gratitude to the remarkable persons, who guided me and helped me master the challenges of my doctoral thesis. Without the following persons, I would not have been able to successfully complete my work.

First, I would like to thank ***Prof. Dr. Ralf Zimmermann*** *for his support and most importantly for allowing me to conduct my doctoral research under his supervision. His scientific input and advice were always welcome and extremely helpful for an early stage scientist like me.*

Furthermore, I would like to thank ***Prof. Dr. Thomas Adam,*** *for his supervision and for welcoming me to his team at UniBw. He allowed me to grow both personally and professionally, by encouraging me to pursue my research ideas and to travel both across the country and abroad. With his guidance and support he helped me master the challenges that I was presented with along the way.*

A special thanks belongs to my coworkers at UniBw, especially ***Sara****,* ***Ajit****,* ***Seongho****,* ***Mo****,* ***Jan****,* ***Marius****,* ***Barbara****,* ***Günter*** *&* ***Wolfi****, which I regard not only as colleagues, but as friends. I am grateful for all the fantastic memories and stories we experienced throughout the last years, and I would not want to miss the special moments I shared with each one of you. All of you influenced me for the better with your loyal and welcoming nature and your invaluable support.*

I also want to thank my colleagues at the Joint Mass Spectrometry Center (JMSC) both in Rostock and in Munich, especially ***Thomas Gröger****,* ***Johannes Becker*** *and* ***Lukas Schwalb****, which helped and participated in my research,*

Furthermore, I would also like to thank the project partners ***AiP Automotive*** *and* ***HDC Blueprints*** *for a good partnership and a productive cooperation in developing the brake and tire dynamometer. I thoroughly enjoyed participating in the development stages of the brake dynamometer, from mere ideas during conceptualizations to its final form. I specifically want to thank* ***Michael Mäder*** *&* ***Philipp Czasch*** *for their support and help during the brake wear measurements.*

I am grateful for my ***parents,*** *my* ***sister*** *and my* ***friends*** *for their support and encouragement, which I could count on not only during the three and a half years of my PhD studies, but throughout my whole studies. Even though it might have not always been easy with me, you had my back regardless and believed in me. For this I am very thankful!*

Last but not least, I would like to thank ***Caro*** *and* ***Ellie****. They were always by my side and cheered me up and supported me during tough times. Without your backup, I would not have been able to master this important step stone in my life and I will be always grateful for your unconditional love and support!*

Table of Contents

LM	Low metallic
LOQ	Limit of quantification
m/z	Mass-to-charge (ratio)
NEE	Non-exhaust emissions
EDX	Energy-dispersive X-ray spectroscopy
SEM	Scanning electron microscopy
ICP-MS/MS	Inductively coupled plasma tandem mass spectrometry
NAO	Non-asbestos organic
SDD	Silicon drift detector
FET	Field effect transistor
RF coils	Radiofrequency coils
SE	Secondary electrons
BSE	Backscattered electrons
EHT	Electron high tension
PC filters	Polycarbonate membrane filters
OPS	Optical particle sizer
PMP	Particle measurement programme
UNECE	United Nations Economic Commission for Europe
GTR24	United Nations Global Technical Regulation No. 24
WLTP	Worldwide Harmonized Light Vehicle Test Procedure
6-PPD	N-(1,3-dimethylbutyl)-N'-phenyl-p-phenylenediamine
CPC	Condensation particle counter
TPC	Total particle counter
TPN	Total particle number
SPC	Solid particle counter
SPN	Solid particle number
GMD	Geometric mean diameter
PM	Particulate matter
PN	Particle number
ROS	Reactive oxygen species
EF	Emission factor
ILS II	Global interlaboratory study
GMD	Geometric mean diameter
D_A	Equivalent aerodynamic diameters

Zusammenfassung

Während verbrennungsbedingte Emissionen aus dem Verkehrsbereich durch gesetzliche Vorgaben in den letzten Jahrzehnten stark gesunken sind, stellen nicht-Verbrennungs-Emissionen (NEE; engl.: Non-exhaust emissions) weiterhin eine große Herausforderung dar. NEE entstehen primär durch den Abrieb von mechanisch beanspruchten Teilen, wie Bremsen und Reifen, sowie Schienen und Rädern aus dem Schienenverkehr. Während Reifenabrieb signifikant zur Mikroplastikproblematik beiträgt, steuern andere NEE Quellen einen großen Anteil an anthropogenen Schwermetalleinträgen in die Umwelt bei und gelten als toxikologisch bedenklich sowie umweltgefährdend.

Ziel dieser Arbeit ist die physikalische und morphologische Charakterisierung, sowie die Bestimmung der elementaren Zusammensetzungen verschiedener metallhaltiger NEE Quellen aus dem Straßen- und Schienenverkehr. Zu diesem Zweck wurde ein an die EURO 7 Norm angelehnter Prüfstand zur Erfassung von Bremsenabrieb entwickelt, mit welchem repräsentative Proben von zwei verschiedenen Bremsbelägen generiert und untersucht wurden. Der Fokus der Analysen lag auf der chemischen Untersuchung mittels Tandem-Massenspektrometrie mit induktiv gekoppeltem Plasma (ICP-MS/MS; engl.: inductively coupled plasma tandem mass spectrometry) zur sensitiven Bestimmung von Schwermetallen und anderen Elementen in Filterproben, sowie der Einzelpartikelanalyse mittels Rasterelektronenmikroskopie (SEM; engl.: scanning electron microscopy), gekoppelt mit energiedispersiver Röntgenspektroskopie (EDX; engl.: energy dispersive x-ray spectroscopy). Hierzu mussten zunächst geeignete Probenvorbereitungsroutinen erarbeitet und auf ihre Tauglichkeit geprüft werden. Weiterhin wurde ein automatisierter SEM/EDX Klassifizierungsalgorithmus entwickelt, welcher in Kombination mit einem mobilen Messsystem eingesetzt wurde, um das Münchener U-Bahn System zu untersuchen und so besonders stark belastete Zonen zu identifizieren. Filterproben wurden mithilfe des Algorithmus automatisiert vermessen und basierend auf zuvor aufgestellten Klassifizierungsregeln einer Emissionsquelle zugeordnet.

Der automatisierte SEM/EDX Algorithmus war in der Lage bis zu 99 % der über 200 000 analysierten Partikel einer Klasse zuzuordnen, während die Emissionswerte des Bremsenprüfstand gut vergleichbar mit Ergebnissen des globalen Ringversuchs waren. Die ermittelten Emissionsfaktoren der beiden untersuchten Bremsbeläge überschritten den zukünftigen Grenzwert mehr als zweifach, während Emissionen in der Münchener U-Bahn, im Vergleich zu Messungen außerhalb des Tunnelsystems, teils um einen Faktor von bis zu 47 erhöht waren. Der Aufbau und die Größe der Haltestellen hatte hierbei große Auswirkung auf die gemessenen Partikelkonzentrationen.

Obwohl Abriebsquellen oft größere Partikel zugeschrieben werden, lagen die aerodynamischen Durchmesser im Schnitt bei 123 nm & 143 nm für die beiden Bremsbeläge und zwischen 200 – 300 nm für Emissionen aus dem Schienenverkehr. Morphologische Untersuchungen ergaben, dass Partikel aus beiden Quellen raue, stark zerklüftete Oberflächen aufwiesen und bevorzugt in bestimmten Formen auftraten. Beide NEE Quellen bestanden zu einem Großteil aus stark eisenhaltigen Partikeln, mit durchschnittlichen Konzentrationen von 54 % und 57 % in der $PM_{2.5}$ Fraktion (Partikel < 2.5 µm) für die beiden Bremsbeläge, sowie ein Maximum von 69 % der $PM_{2.5}$ Fraktion in U-Bahn Proben. Bis zu 97 % der U-Bahn Partikel ≥1 µm und 63 % der Partikel ≤1 µm wurden zudem als stark eisenhaltig klassifiziert. Weitere Schwermetalle wie Cu, Zn, Sn und Cr wurden in teils erhöhten Mengen in beiden Quellen gefunden, was die toxikologische Bewertung der Emissionsquellen zusätzlich erschwert.

Abstract

While exhaust derived traffic emissions have steeply decreased due to regulatory limits in the last decades, non-exhaust emissions (NEE) still remain a large challenge. NEE are primarily formed by abrasion of mechanically stressed components, such as tires and brakes, as well as rails and wheels from railway traffic. While tire abrasion contributes heavily to the microplastic problem, other NEE sources make up a large margin of anthropogenic heavy metal emissions to the environment and are considered as toxic and harmful to the environment.

The aim of this thesis is the physical and morphological characterization as well as the determination of elemental compositions of different NEE sources from metalliferous automotive and railway sources. Therefore, a EURO 7 derived brake dynamometer was developed, with which representative samples from two different brake pads were drawn for detailed analysis. The focus of the chemical analysis was on inductively coupled plasma tandem mass spectrometry (ICP-MS/MS) for sensitive quantification of heavy metals and other elements in filter samples, as well as on single particle analysis via scanning electron microscopy (SEM) coupled with energy dispersive x-ray spectroscopy (EDX). For this purpose, sample preparation routines needed to be developed and tested regarding their suitability. Furthermore, an automated SEM/EDX classification algorithm was developed, which in combination with a mobile measurements setup was used to analyze the Munich subway system, to identify hot spots. Filter samples were automatically analyzed by the algorithm and emission sources were assigned based on pre-defined rulesets.

The automated SEM/EDX algorithm was capable of classifying up to 99 % of the over 200,000 analyzed particles, while emissions obtained from the brake dynamometer were well comparable with results from the global interlaboratory study. Obtained emission factors for the two analyzed brake pads were more than twice as high as the future maximum permitted value, while emissions in the subway showed elevated concentrations up to 47 times higher than values from ambient measurements outside the tunnel system. Size and design of the platforms had a large influence on measured PM values.

Even though abrasion sources are normally linked to the generation of larger particles, the average aerodynamical diameters of particles from the two brake pads were found at 123 nm & 143 nm and the average diameter of the railway emissions was found between 200 – 300 nm. Morphological analysis revealed rough-edged, jagged surfaces for both emission sources, with particles frequently occurring in certain shapes. Both NEE sources consisted predominantly of iron containing particles, with average Fe concentrations of 54 % and 57 % in the $PM_{2.5}$ fraction (particles < 2.5 µm) for the two brake pads and a maximum of 69 % for the $PM_{2.5}$ fraction in subway samples. Furthermore, up to 97 % of the analyzed subway particles ≥1 µm and 63 % of particles ≤1 µm were classified as iron rich. Other heavy metals, like Cu, Zn, Sn and Cr were also found for both brake and railway wear, with occasionally elevated concentrations, further complicating the toxicological assessment of the emission sources.

1 Motivation

Due to the ongoing decrease of exhaust traffic emission over the last decades, non-exhaust emissions (NEE) primarily caused from abrasive wear, have recently gained increasing attention. Due to the regulation driven decline of exhaust particles, automotive NEE, such as brake and tire abrasion, have surpassed engine exhaust emissions as largest traffic derived contributors to urban PM_{10} pollution [1]. NEE from metallic sources, e.g. brake and railway wear, are a major contributor to anthropogenic heavy metal emissions, such as Fe and Cu [2–4], while tire abrasion has been identified as largest single-source contributor to the microplastic problem [5].

Most NEE accumulate at roadsides and are transferred to nearby rivers by stormwater runoffs [6], where they can cause significant harm to the aquatic environment [7]. For example, Tian et al. identified the oxidized state of the common tire antiozonant N-(1,3-dimethylbutyl)-N'-phenyl-p-phenylenediamine (6-PPD), called 6-PPD-Quinone, as main contributor to reoccurring acute mortality events in coho salmon [8], showcasing the need to study the environmental implications of NEE. Subway emissions, in contrast, are confined within a poorly ventilated area and accumulate in tunnel systems over years, leading to constantly increasing amounts of particles that are resuspended by passing trains [9].

While iron rich particulate mass (PM) is often regarded as innocuous, many studies have shown the adverse health effects following inhalation of both iron and iron oxides [10–12]. The assessment of potential health risks, originating from NEE exposure is further complicated by the presence of other heavy metals, such as Cu, Zn, Cr and Sn [13–16], which are common constituents of brake and railway wear particles.

Even though many studies on NEE generation have been conducted in the past, they have concluded a variety of often contradictory statements, originating from the vast variety of employed modes of particle generation and sampling [1]. Therefore, many particle properties, such as size distributions and chemical compositions remain to be studied under universally accepted, standardized testing procedures, to obtain a better understanding of the complex nature of NEE and their impact on human health and the environment.

The aim of this thesis was the comprehensive physical and elemental characterization of automotive brake dust and railway emissions, studying the homogeneity of particles elemental compositions, as well as morphological features across the different size ranges emitted under real-world applicable conditions. To achieve this goal a custom-built brake dynamometer, as well as an automated SEM/EDX imaging approach for the analysis of subway emissions were developed. Subway emissions were chosen for analysis of railway contributions to NEE, since the tunnel systems enable a suitable way of sampling wear particles from rails and wheels in the real-world.

A strong emphasis was put on the application of realistic testing conditions for brake wear particles, which cannot be readily sampled in the real-world and need to be transferred to a dynamometer. The second challenge was the development of a measurement approach, capable of filtering out and characterizing subway particles, even though they occur in an environment, which is mixed with other anthropogenic and natural emission sources.

2 Introduction

2.1 Importance of NEE

NEE are of rapidly growing interest for researchers worldwide, due to their potential as environmental pollutants and hazardous substances. Nowadays NEE pose a significant share of total traffic related emissions, due to the ongoing decline of exhaust emission in the last decades, generating the need to develop realistic measurement procedures capable of addressing their environmental implications as well as potential health risks associated to prolonged exposures.

NEE are estimated to make up 73 to 87 % of traffic derived PM10 emissions [17, 18], with their share constantly increasing throughout the last years [1]. NEE originate primarily from abrasion processes and are formed from frictional wear of roads, tires, brake pads and discs, rail wheels, or other sources [1, 17, 19–22]. Additionally, particles might be generated from sparking of electric components, like rail catenaries and pantographs [23, 24]. Common sources of traffic derived NEE are illustrated in Figure 2-1.

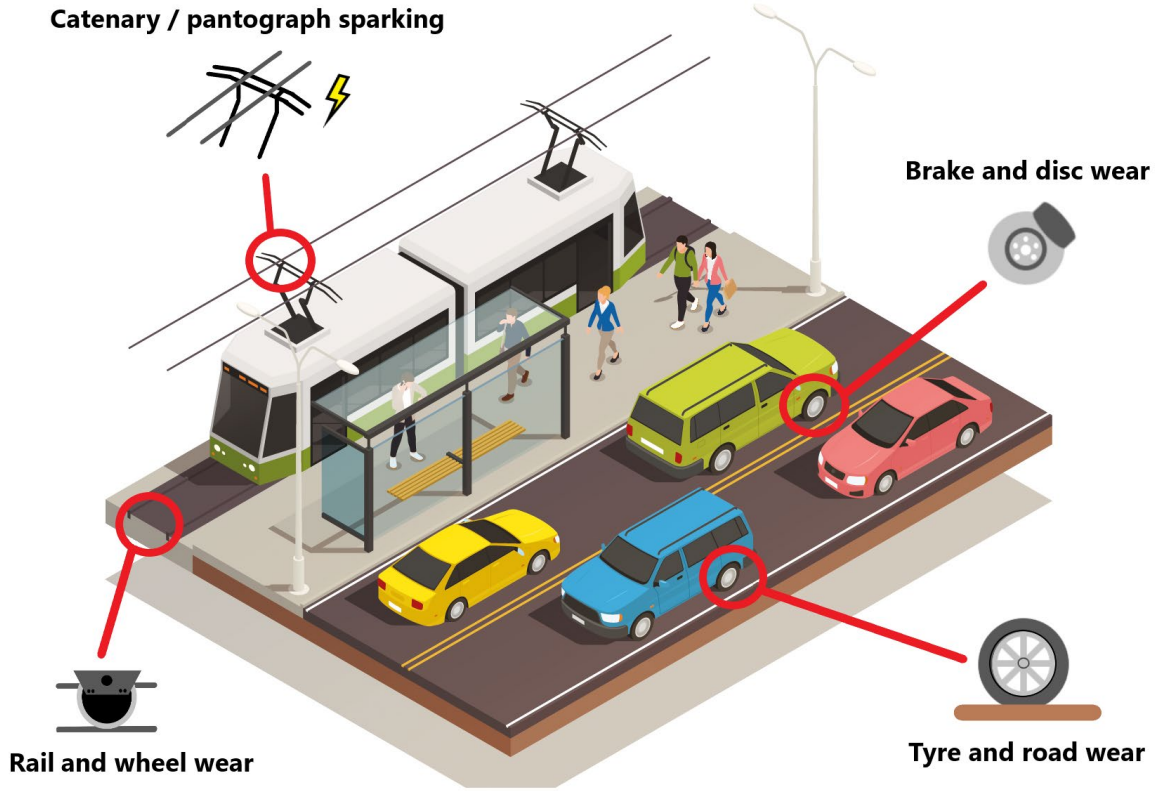

Figure 2-1: Sources of traffic derived NEE. Figure created with permission from assets designed by macrovector / Freepik [25]

While obtaining representative filter samples of particles from exhaust sources is relatively easy, due to the possibility to directly sample from the exhaust air stream, NEE sources do not offer such an option and sampling methodology is therefore more complicated. Furthermore, emission characteristics of NEE are primarily depending on the applied test conditions and chosen parameters, such as the temperature, can significantly alter particle sizes and chemical compositions. Most NEE exhibit a critical temperature, above which the primary mode of particle generation switches from abrasion to evaporation [26],

resulting in a steep increase in particle number (PN) levels and a shift in particle size from the µm scale to ultrafine particles [27, 28]. To address these challenges a need for universally agreed testing conditions arises, which is partially covered by the upcoming EURO 7 legislation, which will include maximum emission factors and standardized testing procedures for automotive brake and tire wear for the first time [29]. Other NEE sources, like railway emissions however, remain unregulated.

Most NEE sources, apart from tire and road wear particles, consist mainly of a variety of heavy metals, such as Fe and Cu and can form reactive oxygen species (ROS) through the Fenton reaction [30]. The generation of ROS in the respiratory tract by heavy metal bearing particles is known to induce chronic respiratory diseases and pro inflammatory responses [31]. Especially small particles carrying large amounts of heavy metals are of concern, since particles smaller than 0.1 µm can deposit in the alveoli, from where they eventually reach the bloodstream via the blood-air barrier [32]. Furthermore, metal containing nanoparticles were found to penetrate to the central nervous system via uptake and transport in the olfactory nerve via the nasal route [33, 34]. While Cu particles are widely regarded as one of the most toxic types of heavy metal bearing particles in mammals [16], inhalation of Fe rich particles is often disregarded as innocuous, due to comparably high concentrations of Fe in the human body, caused by its central role in oxygen transport reactions [30]. While the human body has numerous pathways of preventing generation of ROS from orally ingested Fe, such as chelation of unbound iron in the digestive tract [30, 35, 36], the human lung does not possess pathways of dealing with large amounts of unliganded iron species [37]. In fact, several studies showed severe health effects following inhalation of iron rich particles [10–12, 38–40], such as pro inflammatory and damage to tight junction, possibly decreasing lung epithelial barrier functions in the process [41].

2.1.1 Brake emissions as part of the EURO 7 regulation

Brake wear emissions are a major contributor to automotive NEE's, being estimated to contribute around 16 to 55 % depending on the braking frequency of vehicles at the studied location [22]. To reduce air pollution caused by brake wear particles, the upcoming EURO 7 legislation defines maximum PM_{10} emission factors (EF) for wear from brake discs and pads for the first time. From 2026 onwards, maximum permitted EF of 3 mg/km for pure electric vehicles, 7 mg/km for internal combustion engines and hybrid cars, as well as 11 mg/km for internal combustion engine vans are defined, which will be changed to 3 mg/km for all light-duty vehicles in 2035 [42]. These values pose a challenging task for brake developers, since modern automotive brakes can emit more than twice the amount of 7 mg/km, permitted from 2026 onwards [43].

Many studies in the past have concluded a wide range of often contradictory results on PM and PN EFs, as well as emitted particle sizes [17]. While this can be partially attributed to different measurement instrumentation, the more likely reason is the usage of a variety of test setups, including pin-on-disc tribometers, brake dynamometers with various designs, environmental and real-drive sampling [1, 44, 45]. Besides this, the application of a variety of testing parameters, like temperatures, axle loads and test cycles, which range from repetition of the same braking event to complex testing cycles such as the Los Angeles City Traffic Test, result in poor comparability of studies. For this reason, the EURO 7 legislation specifies the usage of brake dynamometers that comply with the United Nations Global Technical Regulation No. 24 (GTR24) of the particle measurement programme (PMP) of the United Nations Economic Commission for Europe (UNECE). Furthermore, emission tests have to apply the Worldwide Harmonized Light Vehicle Test Procedure (WLTP) brake cycle, as well as a strict

measurement procedure with defined maximum allowed deviations for speed, temperature and a range of other relevant parameters, to ensure comparability of emission measurements worldwide. While first studies on emissions from GTR24 compliant brake dynamometers are emerging, these focus primarily on PM and PN levels, neglecting size distributions as well as chemical composition of brake wear particles [43, 46].

While most brake discs consist of gray cast iron [1], brake pads consist of a variety of materials, such as fibers, fillers, frictional additives and abrasives [26, 47, 48], which show an inhomogeneous distribution among the binding matrix of the pad. The proportions of these classes of additives vary with different types of brake lining materials that are employed, which can be summarized as non-asbestos organic (NAO) types, low metallic (LM) and semi-metallic brake pads. Semi-metallic brake pads, which are often used for heavy vehicles and extreme braking conditions, contain the most iron of all types, with metal concentrations reaching up to 65 % of their mass [1]. LM pad formulations on the other hand contain around 10 – 30 % of mass in the form of metals and are predominantly found on European cars [49]. NAO types are typically found on cars in the U.S. and Asia [49] and feature low metal contents, typically less than 10 % [50]. While higher metal contents in brake pad formulations generally result in better braking performance, emission rates are typically also increased, due to higher wear rates of rotors [1, 43, 46]. In addition to pad types, brake pad compositions are also influenced by local regulations , most prominently the EPA's Memorandum of Understanding on Copper Mitigation in Watershed and Waterways [51], limiting the amounts of asbestiform fibers, chromium(VI)-salts, mercury and lead to 0.1 %, cadmium compounds to 0.01 % and copper to 5 % of weight from 2021, with a further reduction of the maximum amount of copper to 0.5 % starting in 2025. The EPA's memorandum was established as response to environmental studies, which estimated EFs for the nine sub-watersheds in the San Francisco Bay Area of 53.8 tons of Cu/year as airborne emissions, plus an additional 50.4 tons of Cu/year released to roadways [2]. Further studies suggest that 2.4 kilotons of Cu are deposited to surface waters annually and that up to 75% of the atmospheric copper input in the North Sea might originate from brake wear [4]. SEM/EDX elemental maps of LM and NAO brake pads showing the inhomogeneous distribution of additives are shown in Figure 2-2.

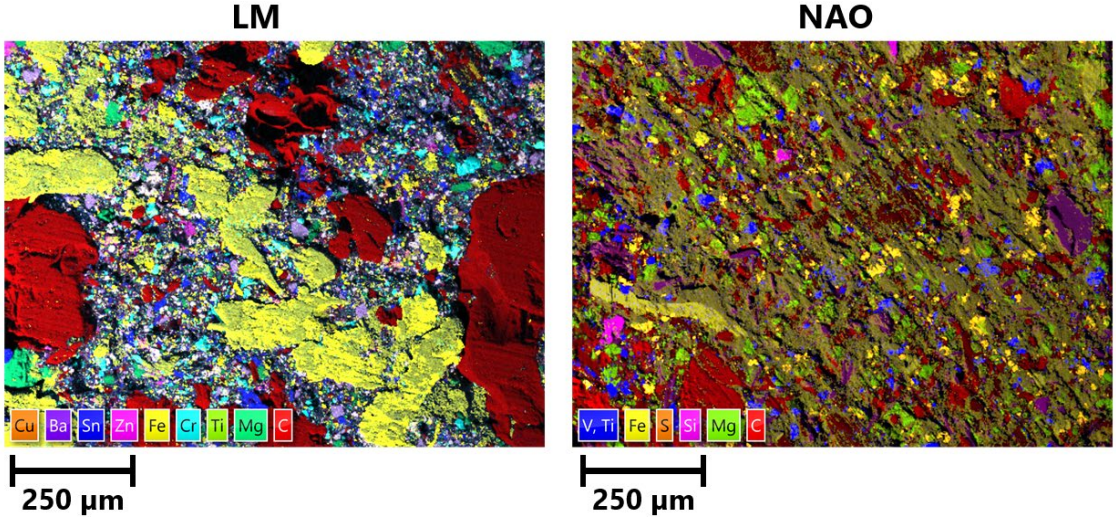

Figure 2-2: Chemical mapping of brake pad linings at 100 x magnification measured via SEM/EDX. Reprinted with permission from Neukirchen et al. [52]

2.1.2 NEE from railways and trains

While the importance of automotive NEE, such as brake and tire wear, is publicly recognized, railway wear particles remain an often-underestimated topic. Nonetheless, particles derived from wear of train wheels and rails are of concern, especially in urban subways, due to the confined, poor ventilated design of most subway tunnels and platforms. PM_{10} and $PM_{2.5}$ concentrations in subways have been found to exceed WHO ambient air quality guidelines [53, 54] and negative health effects of subway PM have been reported in various studies [55–58]. Apart from brake wear of trains, subway PM is dominated by Fe containing particles [59], originating from abrasion of steel wheels and rails [60, 61] and are often accompanied by Cu containing particles from sparking at the current collectors of the trains [23].

Due to the enclosed nature of subway micro-environments, particles can accumulate over long periods and are periodically resuspended by passing trains due to the piston-effect [62], leading to short-term spikes in PM10 and PM2.5 concentrations [63, 64].

While brake dust can be studied as single emission source on a dynamometer, the sampling of subway emissions is more complicated, due to the less controllable environment. The construction of a dynamometer for railway emission measurements that features all contributing sources, such as abrasion from rails and wheels, as well as sparking of current collectors is not possible. Therefore, subway emissions need to be sampled in the real-world, where they are commonly mixed with other emission sources, such as mineralogical dusts brought in by commuters, fibers from clothing, as well as anthropogenic emissions from the interaction with the outside world [65].

Various studies have investigated personal exposures of commuters and stationary air quality in metro systems all over the world [60, 66–69], however, few studies on the spatio-temporal distribution of subway PM and PN is presented in the literature [70].

2.2 Analytical techniques

2.2.1 Scanning electron microscopy (SEM)

Scanning electron microscopy is a powerful technique, commonly used to obtain high-resolution images for environmental studies and material analysis. Electron microscopy was invented, when traditional light microscopes started being limited by their maximum achievable resolution [71]. The resolving power of modern light microscopes, which is characterized by the Rayleigh criterion, is limited due to the quality and number of magnifying lenses, as well as the wavelength of the used light source. Simplifying the Rayleigh equation results in an empirical limit of the resolution of approximately half the incident wavelength of the utilized light [71]. When using white light, which ranges from 400 to 700 nm, the practically achievable resolution of light microscope is therefore limited to around 200 – 350 nm. Electron microscopes in contrast offer far superior resolutions that depend on the quality of their objective and the utilized acceleration voltage of the electron beam and can vary between a few nm and sub nm resolution. Due to the wave particle duality of electrons, as defined by the de Broglie relationship, the wavelength of a primary electron depends on the applied acceleration voltage of the SEM, also called electron high tension (EHT). Typical SEM accelerating voltages can range from 500 eV up to 30 keV [72].

A SEM uses a focussed electron beam, that is shifted via scanning coils, to scan the surface of a specimen, thus creating an image in the process. On impact the electron beam penetrates the sample until a certain depth, that is depending on the applied EHT, before interacting with the sample material, thereby producing a variety of signals [73]. By correlating the signal intensity to the beams position, the image is successively generated during the scanning process.

The two most common types of signals used for generating images in an SEM are secondary electrons (SE) and backscattered electrons (BSE) [74]. SE which primarily originate from inelastic scattering processes, are mainly used for topographical images, since they are generated close to the surface of the sample and therefore carry the most information about the specimen surface. BSE, in contrast, are the result of elastic scattering and are usually used to obtain information on the surface composition, due to the high material contrast of BSE detectors. The positive charge of an atom's nucleus results in electrostatic repulsion of the electron beam, causing a deflection of electrons from the beam, which are eventually reemitted from the specimen surface [72]. Heavier atoms in the sample result in higher BSE signal yields, due to higher amounts of positive charges in the nucleus, causing a correlation of image brightness and atomic number of the studied material. Furthermore, elemental analysis of the surface composition can be achieved by using energy dispersive X-ray spectroscopy (EDX) detectors, utilizing characteristic X-rays, that are generated at high acceleration voltages [75].

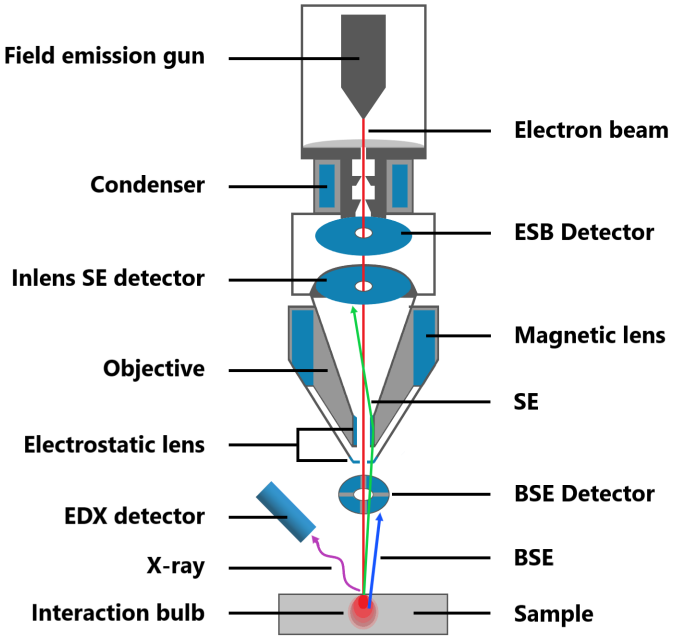

Figure 2-3: Schematic overview of the working principle and components of a SEM

An important criterion to achieve the best resolution with a SEM is to focus the electron beam as narrow as possible. To achieve this, the design of the electron emitter, often referred to as electron gun, is crucial. In general, three types of emitters are used in modern instruments: Tungsten filament; lanthanum, or cerium hexaboride and Schottky type electron gun designs. Schottky field emission guns, which consist of a zirconium oxide coated tungsten tip and work with the principle of field-assisted thermionic emission, produce the most narrow and coherent electron beams, but are more expensive than other emitters, such as hexaboride electron guns [72]. The emitted electrons are focused to a beam by a combination of lenses, that are built into the objective. Electromagnetic lenses are used to bend the path of off-axis electrons towards the optic axis, while electrostatic lenses accelerate the beam along the column and condenser lenses are employed to reduce the beam diameter [58]. A schematic overview of the working principle of a SEM is given in Figure 2-3.

2.2.2 Energy-dispersive X-ray spectroscopy (EDX)

EDX is a technique commonly used in combination with SEM instruments. The EDX detector measures characteristic X-rays generated from the interaction of the focussed electron beam of the SEM with the studied sample. For particle analysis the EDX technique is especially useful, since it provides single-particle elemental spectra, allowing to assess the homogeneity of the chemical composition for individual particles among a variety of sizes and different particle types.

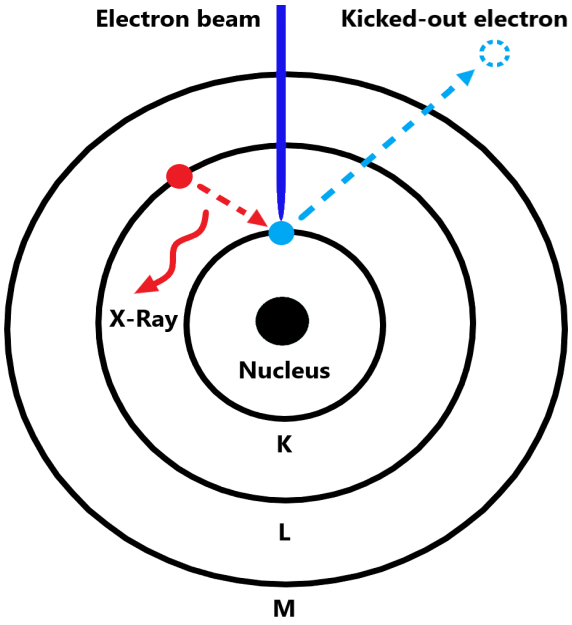

Figure 2-4: Measurement principle of EDX analysis. The electron beam of a SEM knocks an electron from its shell, creating a gap that is filled by an electron from a higher shell.

The electron beam of the SEM knocks-out an electron from a near-core shell of an atom, creating an electron hole in the process. When an electron from a higher shell fills the energetically more favorable position of the removed electron it emits the excess energy as an x-ray that has a characteristic energy for the transition, that can then be quantified. Normally mainly the K-Lines of elements are measured by EDX analysis, however for heavier elements also L-lines are of importance and detectors with sufficient resolution can even distinguish the low energy M-Lines. The process of X-ray generation by interaction with the electron beam to create a Kα line is displayed in Figure 2.6. To quantitatively excite an emission line the EHT of the SEM is normally set to 2–3 times higher than the energy of the emitted x-ray [76]. Choosing the right EHT value is of great importance in EDX analysis, since too low values result in low signal count rates and can lead to insufficient excitation of an emission line with elements missing in the spectrum, while too high values can greatly change the generated spectrum by piercing of the particles and excitation of the underlying sampling medium [76, 77]. Even with comparably high percentages of the beam penetrating a particle an accurate quantification of elemental composition is possible by mathematical exclusion of the substrate peaks in most EDX operating softwares. This, however, is only feasible if the investigated particles do not contain the same elements as the substrate and peaks from the substrate do not interfere with analyte peaks.

The correct excitation energy for a sample can be simulated in a variety of softwares, such as the Monte Carlo simulation software Casino [78]. Electron penetration depths and energy-by-position graphs can be obtained from this software by entering simulation parameters, such as the elemental composition, particle size and EHT. Figure 2-5 shows the simulated electron penetration depth and the measured changes in the EDX spectra of a 200 nm spherical Sn particle on a carbon film when measuring at different acceleration voltages, highlighting the importance of such simulations. As can be seen at 5 kV almost none of the electrons penetrate the particle depicted in red, while at 12 kV and at 20 kV a high proportion of the electrons excite x-ray of the underlying C film. While the Sn emission lines are more abundantly exited with higher acceleration voltages, the effect of the beam piercing still outweighs the elemental spectra measured by the EDX detector, showcasing the severance of a poorly chosen EHT

and highlighting the need for adequate simulation of electron penetration depths not only for varying sample diameters, but also for particles with different elemental compositions.

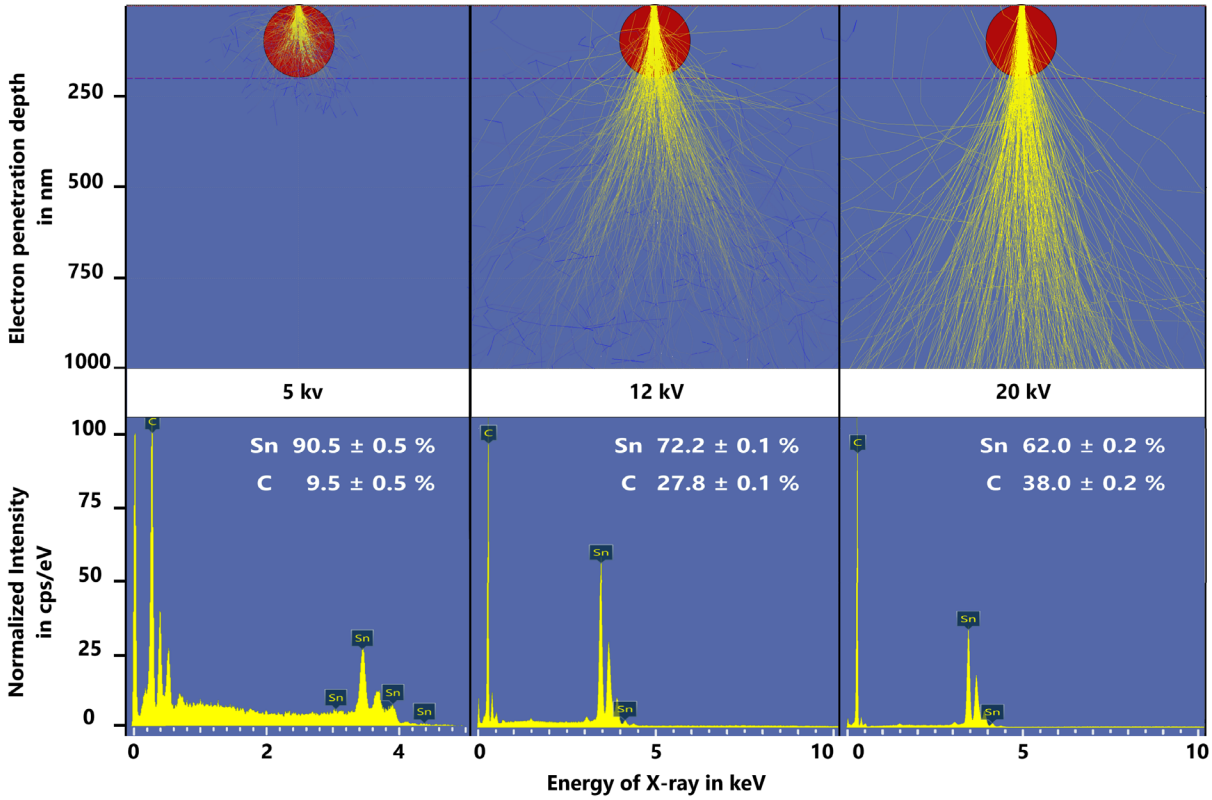

Figure 2-5: Visualization of the piercing of an electron beam through a 200 nm spherical Sn particle on a C film during SEM/EDX analysis at different acceleration voltages. Top: Electron trajectories at different EHT values simulated in the Monte Carlo Casino Software; bottom: Measured EDX spectra and associated elemental compositions at the associated acceleration voltages.

The EDX probe capturing the X-rays is located in the specimen chamber of the SEM and is protected from ambient pressure during sample exchange and analysis in high pressure mode by an entrance window. While Beryllium windows are strong and sturdy, modern EDX probes often utilize thin polymer windows on a supportive grid. These thin polymer windows offer higher transparency to low energy X-rays down to 100 eV, thus enabling the analysis of low-z elements like C, N and O.

Incoming X-rays are detected by a semiconductor-based detector, measuring the charge liberated by ionizing radiation. Two types of detectors are currently in usage, the Si(Li) detector, which consists of a lithium doped silicon single-crystal and the silicon drift detector (SDD). Recently SDDs have largely replaced older Si(Li) type detectors, due their better resolution at high count rates, greatly reducing the analysis time up to 100 times [79]. Furthermore, the high purity of the crystal in the SDD, exhibits a low leakage current, removing the necessity of liquid nitrogen cooling of Si(Li) detectors, by implementation of Peltier elements [80].

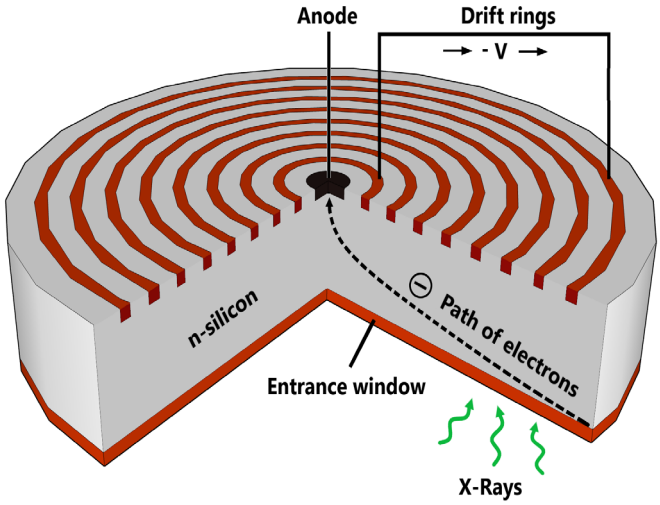

Figure 2-6: Schematic layout of the SDD. Electrons generated from impact of X-rays with silicon crystal travel towards the central collection anode along the transversal field created by the drift rings.

Incoming X-rays ionize the SDDs semiconductor crystal on impact, generating electron-hole pairs in the process. Liberated electrons then drift towards a central collection anode along a transversal field, which is generated by a series of concentric electrodes, also known as drift rings [81].

The charge of the electron cloud liberated by an x-ray is proportional to its characteristic energy and the current of the generated electrons is measured via a low-capacity collection anode in the center of the SDD. Here the current conducted by the detector crystal is first integrated and pre-amplified and then converted to a voltage output via a field effect transistor (FET) [82]. Modern detector designs feature FETs integrated into the detector chip, reducing the capacitance, thus minimizing the noise of the detector.

The voltage output from the FET is then input into a pulse processor in the form of a linearly rising baseline caused by leakage current of the detector, which is superimposed with voltage steps equienergetic to the detected X-rays [83]. To avoid saturation, the circuit is periodically reset, leading to an overall dead time typically around 20- 60 % in which X-rays are processed, to achieve an optimum balance between energy resolution and output count rate [84, 85]. The registered voltage signal is then further processed and transferred to a spectrum in the data system. The operating principle of the SDD is depicted in Figure 2-6.

One of the major drawbacks of SDDs are so-called pulse pile-up peaks, sometimes also referred to as sum peaks, which are generated during the measurement. Pile-up peaks are artifacts attributed to the operating principle of silicon drift detectors, that are created when two electron clouds from different incident x-ray collisions hit the central collection anode in rapid succession. Therefore, their voltage signals cannot be discriminated by the pulse processor and the measured current equals the energy of both X-rays. This can result in falsely detected elements in the spectrum if the measured energy of the two X-rays equals the energy of another elemental emission line [86, 87]. Identifying and mitigating pile-up peaks during measurements is one of the most challenging tasks for operators, to ensure a reliable result without artifacts.

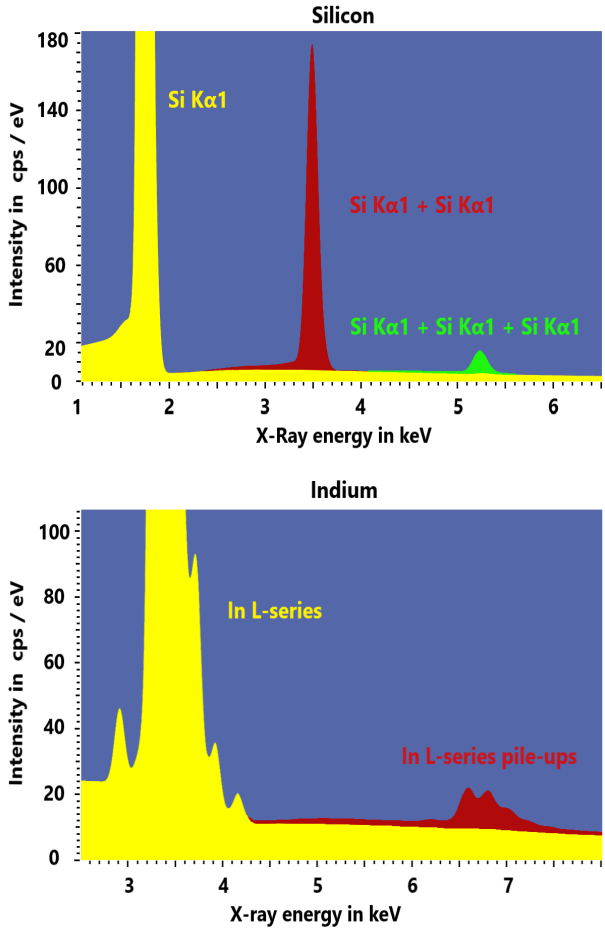

Figure 2-7: Visualization of pile-up peaks obtained by measuring substrate with and without pile-up correction at 20 kV. Yellow color shows the spectrum without pileups, red color indicates double pileups, while green color represents triple pileups. Top: Silicon Kα1 double and triple pileups; Bottom: Indium L-series pile-up continuum

Some softwares feature a pile-up correction mode, which tries to mathematically exclude possible pileups by comparing the ratio of the emission line to other lines of the falsely detected element, that are not present in the case of a pile-up. These correction equations however often over - or underestimate the rate of pile-up effects resulting in visible dents in the baseline and do not yield feasible results if the element attributed to the pileup is also present in the sample.

Pile-up peaks are more abundantly observed when certain elements are present at high concentrations, due to the increased chance of two X-rays with the same energy colliding with the detector surface at the same time. In theory also mixed pileups from two X-rays with different energies are possible, however these are normally not prominent in the spectrum.

Elements with only few prominent lines are more prone to strong pileups. The strong Ka1 line of Si can even generate triple pile-ups at higher acceleration voltages, while other elements with a high number of possible emission lines, like the In L-series produce pileup continuums, due to the large number of possible combinations of different pile-up energies. Si Ka1 double and triple pileups, as well as the In L-series continuum pile-up measured at 20 kV on pure substrates are shown in Figure 2-7, with the pile-ups visualized in red and green.

2.2.3 Inductively coupled plasma tandem mass spectrometry (ICP-MS/MS)

While conventional ICP-MS analysis has long been established as standard for elemental trace analysis of environmental samples, the development and implementation of new components to the traditional instrument setup, like the integration of tandem mass spectrometry, has enabled the technique to measure elements formerly not accessible.

Most ICP-MS systems feature a liquid sample injection system based on a peristaltic pump, which generates the need of solving the sample in advance. An ICP-MS/MS features the same sample introduction system as an ICP-MS, where the liquid sample is first vaporized by spraying it in a nebulizer with an Ar sheath flow. The nebulizer needle is sticking into the spray chamber and the remaining liquid is discarded by a drain, while the sprayed aerosol is transferred to the plasma torch. Once the sample

reaches the plasma torch it is atomized and ionized in an Ar plasma of up to 6500 K, which is maintained inductively by radiofrequency coils (RF coils) [88].

The lens stack of the ion optics marks the entrance to the MS and needs to be of a more rigid design than for other MS applications, since it shields the high vacuum inside from the plasma torch on the outside and residual acid in the sample.

Regardless of the measurement mode, the first quadrupole serves as filter to neglect off-mass ions, that differ from the analyte in their mass-to-charge (*m/z*) ratio. Even though the instrument is often colloquially called an ICP-triple quadrupole device, the second mass filter, which acts as reaction cell, normally consist of an octupole. Octupoles are beneficial for reaction cells, due to their ability to simultaneously transmit ions over the whole *m/z* range, without the need of a band-pass filter, offering more compact designs and a more consistent ion transmission with cell gases, compared to a quadrupole [89]. After the reaction cell ions pass a second quadrupole, which filters the reaction products before transmitting them to the detector. An overview of an ICP-MS/MS device is given in Figure 2-8.

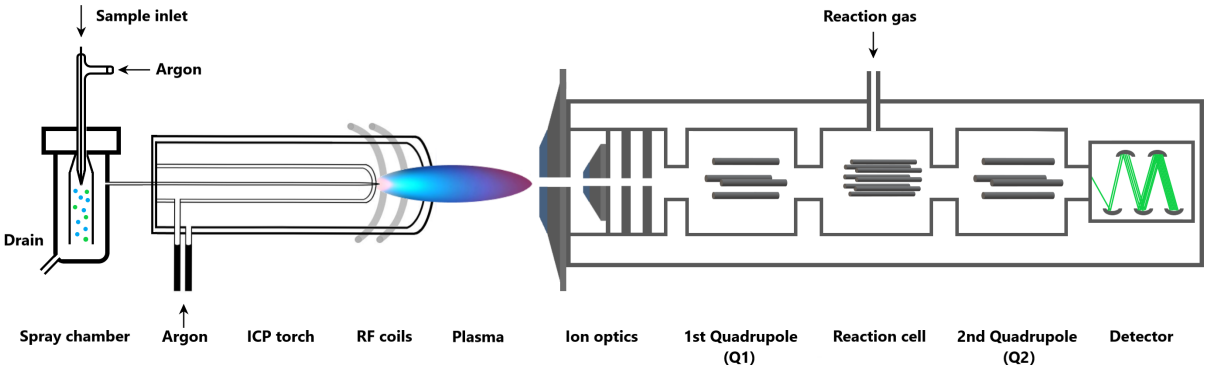

Figure 2-8: Schematic layout of an ICP-MS/MS. The sample is sprayed with an Ar stream in the spray chamber and transferred to the plasma torch. Ionization occurs in the Ar plasma and ions are drawn into the MS via a lens stack, where they are quantified.

Minimizing polyatomic and monoatomic interferences is an important factor in ICP-MS/MS analysis. The easiest way of reducing polyatomic ions is the usage of He as collision gas. This mode of operation is especially important with normal ICP-MS instruments, since it is their only mean of dealing with interferences. In ICP-MS devices an additional octupole collision cell is located before the quadrupole, while in ICP-MS/MS the reaction cell is flooded with He.

Polyatomic ions collide more frequently with the collision gas, due to their larger collision cross-section, compared to a monoatomic ion of the same *m/z* value. Polyatomic ions, therefore, lose more energy in the collision cell and can be rejected from exiting the cell by applying a kinetic energy discrimination bias voltage, while monoisotopic ions retain enough energy to pass the barrier [90]. The He collision mode is capable of reducing most polyatomic interferences but cannot eliminate monoatomic interferences and not sufficiently remove polyatomic ions with high abundances.

Aside from the conventional He collision mode, two modes of operation utilizing reaction gases are possible with an ICP-MS/MS, the on-mass mode, as well as mass-shift measurements. These

measurements utilize reaction gases, such as O_2, H_2 and NH_3 to reduce interferences that cannot be overcome by He collision mode and enable analysis of elements such as ^{40}Ca.

The on-mass mode removes interferences by changing their m/z value due to reactions with the cell gas. A good example for this mode is the measurement of ^{40}Ca, which greatly suffers interference from ^{40}Ar, originating from the Ar plasma [91]. Due to this Ca analysis by ICP-MS has to rely on less abundant Ca isotopes, greatly reducing the limit of quantification (LOQ) of the method. In the on-mass mode of an ICP-MS/MS, however, the ^{40}Ca isotope with an abundance of 96.7 % is accessible using H_2 as reaction gas, which eliminates the Ar interferences, which are then filtered out in the second quadrupole.

The mass shift mode, in contrast, leaves interferences unaltered, while analyte ions are reacted to form analyte product ions of a different *m/z*. This enables for example the measurement of ^{32}S, which is mainly disturbed by $^{16}O_2$, which is highly abundant from the aqueous sample solutions, but also other polyatomic ions like $^{14}N^{16}O^{1}H_2$. By measuring ^{32}S with O_2 as reaction gas it reacts to SO^+, which has the *m/z* 48 and is thus distinguishable from the interfering ions in the second quadrupole. Other ions that would interfere with the *m/z* 48, such as $^{48}Ti^+$, $^{48}Ca^+$, $^{36}Ar^{12}C^+$ and $^{14}N^{16}O^{18}O+$ are removed in the first quadrupole due to precursor mass 32 [92]. The principle of the on-mass and mass-shift modes with reaction gases is illustrated in Figure 2-9.

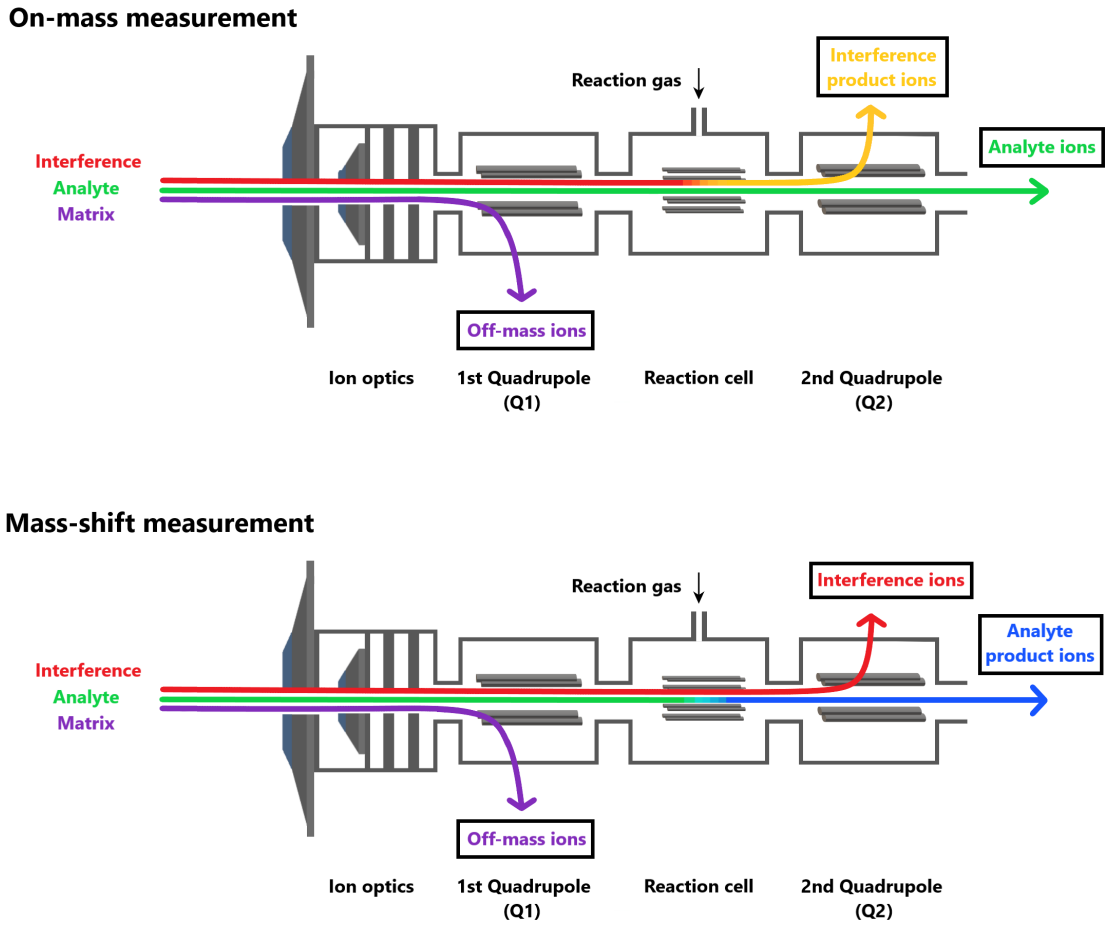

Figure 2-9: Principle of the measurement modes of an ICP-MS/MS. Top: on-mass measurements; Bottom: mass-shift measurements

3 Scope

The comprehensive elemental and physical characterization of metalliferous NEE from brake wear and subway emissions presents a challenging analytical problem. Brake wear is nearly impossible to sample in a quantitative manner in a real-drive scenario, generating the need to transfer testing to a brake dynamometer. Subway emissions, however, can be readily sampled in the tunnel system, but are difficult to analyze due to the mixing with other anthropogenic and natural emission sources. Because of these challenges, this thesis addresses the following tasks, which are listed in their order of importance and will be covered in detail in the next chapters:

I) Chemical, physical and morphological comparison of metalliferous NEE

The main goal of this thesis was the in-depth characterization of metalliferous NEEs originating from automotive brake wear and subway emissions. Particles were evaluated and compared regarding their elemental composition, morphological, as well as physical properties, to give a better understanding of the two emission sources.

II) Development and evaluation of a brake dynamometer, capable of brake wear emission testing as close to the specifications of the GTR24 as possible.

The GTR24 defined standardized testing procedures for brake wear for the first time. However, at the starting time of this thesis no commercially available GTR 24 compliant dynamometers were available, which could have been used for brake wear characterization. For this reason, a custom-built brake dynamometer was developed and compared to the official global interlaboratory study (ILS II), which presents the first publication on GTR24 compliant dynamometer designs.

III) Development of an automated SEM/EDX algorithm for characterization of non-controllable environments with mixed emission sources

Environments with mixed emission sources, like subway systems, require a measurement approach that can preferably give a holistic overview of the whole environment, while also being capable of studying certain types of particles isolated from other emission sources. For this reason, an automated SEM/EDX imaging approach was developed and tested on subway emissions, to study the

IV) Evaluation and enhancement of measurement procedures for the elemental characterization of obtained NEE

Common elemental analysis techniques, like ICP-MS and EDX suffer from the inability to measure certain elements like C, Si and O, that are relevant to the elemental composition of NEE. For this reason, sample preparation procedures for the two techniques were developed and tested regarding their ability to measure relevant elements of interest.

4 Methods & Materials

4.1 Brake dust measurements

A custom-built brake dynamometer was developed to conduct brake emission measurements as close to the PMP specifications as possible. For this an existing test bench architecture, consisting of a closed and isolated test cell with an asynchronous machine as powertrain was converted to house all dynamometer components that are required within the GTR24. Furthermore, the dynamometer was designed with a planned future implementation of a module for the investigation of tire abrasion.

The test cell's temperature and humidity were regulated by an air-conditioning unit, before fresh particle-free air was sucked into the dynamometer through a HEPA filter. The air stream then passed a flow straightening section before entering the enclosure housing the brake. Particles generated during the braking process were transported to the sampling plane via the cooling air flow, which was kept at a constant rate via a constant volume sampler (CVS), located behind the sampling plane to ensure a consistent dilution rate throughout emission measurements. As specified in the GTR24, the sampling probes were located at a distance of six times the air duct diameter, behind the last flow perturbing element, which in this case was a 90° bend of the air duct, and two times the air duct diameter before the next 90° bend to avoid flow disturbances during sampling. Sampling probes were fitted with isokinetic nozzles, to maintain an isokinetic sampling rate between 0.9 and 1.15. The excess air stream passing the sampling plane was exhausted out of the room, to avoid accumulation of particles in the test cell air. A schematic overview of the used brake dynamometer, with images from the initial installation are given in Figure 4-1.

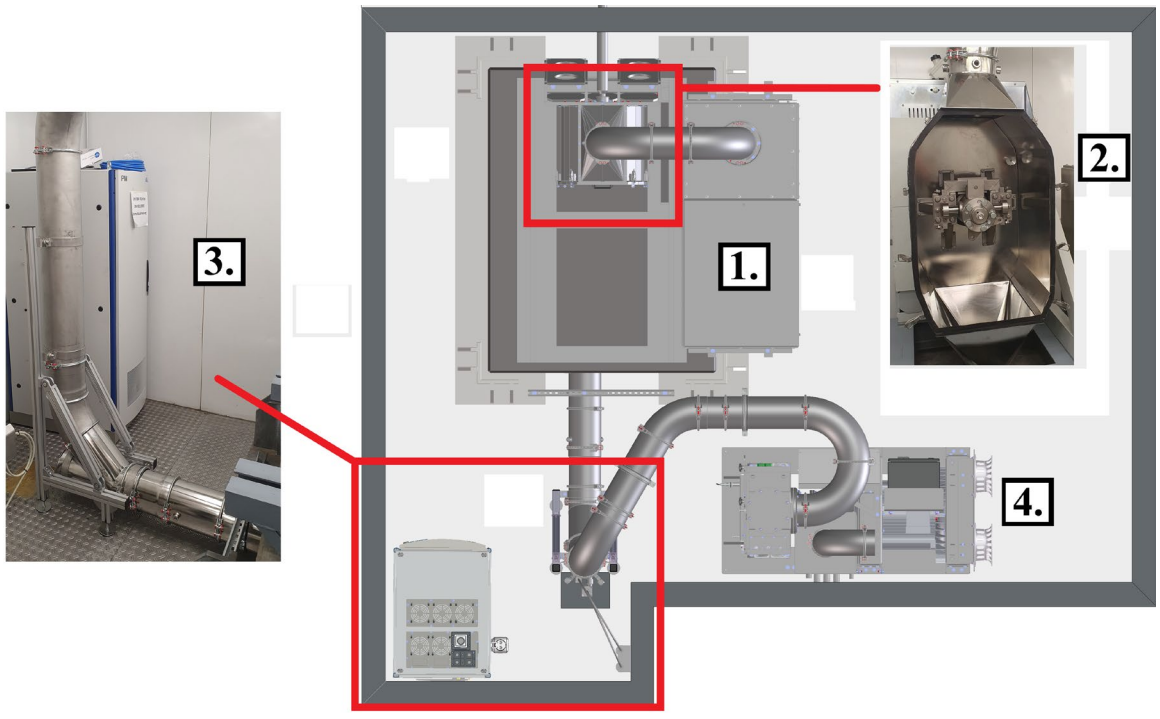

Figure 4-1: Schematic overview of the custom-built brake dynamometer for emission measurements with images from the initial installation. 1. HEPA filter 2. Brake enclosure 3. Sampling point, filter holder location and PN measurement closet 4. CVS system

Brake disc temperatures were measured with a 10 Hz frequency by a type-k thermocouple embedded into the disc and data was wirelessly transferred to a data logger by a telemetry unit fixed to the brake disc via the tire mounting holes. All components consisted of electro-polished stainless steel to minimize flow turbulences and electrostatic attraction of particles to the surface of the air ducts. All GTR 24 requirements for the design of the brake dynamometer, except for the orientation of the brake housing, which is located vertical instead of horizontal, and the symmetry of the housing, which is slightly asymmetrical at the exit point, were met and flow simulations indicated an at least equally efficient transfer of particles.

Original 330 mm by 24 mm brake discs, as well as a brake caliper fitting a 17-inch tire rim were supplied by the original equipment manufacturer of the simulated vehicle and were utilized for all measurements. LM brake pads were directly supplied by the original equipment manufacturer and were tested together with commercially available NAO pads from the aftermarket. Relevant parameters of the simulated vehicle are listed in Table 4-1. EFs at the vehicle level were calculated with a brake force distribution between front and rear axle of 2:1, equaling a share of the braking force applied to the front axle of 66 % of the total braking force and a friction braking share coefficient of 1.0 for vehicles with internal combustion engines. Variation of the brake share coefficient can be employed to simulate electric vehicles on the test bench, which depending on the brake force have either a full, or partial deceleration due to recuperation and therefore rely less on their friction brake.

Table 4-1: Parameters for the vehicle simulation during brake emission testing

Parameter	Vehicle data
Vehicle type	SUV
Vehicle mass (including driver weight)	1895 kg
Wheel load (without driving resistance)	614.4 kg
Wheel load/ Disc mass factor	64.2
Disc/ brake position	Front axle
Brake force distribution front/rear	2:1

Before testing, a minimum of five WLTP brake cycles were conducted for embedding of newly installed brake pads, followed by a cooling air speed adjustment based on Trip #10 of the WLTP brake, as defined by the GTR24. Based on these results the CVS was set to a flow rate of 540 m^3/h for the LM pad and 720 m^3/h for the NAO pad. The results of the cooling air speed adjustment, as well as the GTR24 specifications for the simulated vehicle group, based on the determined wheel load/disc mass group, are listed in Table 4-2.

Table 4-2: Results from cooling air speed adjustment for LM and NAO pads

Dynamometer parameter	LM	NAO	GTR24 specification
Average brake temperature	56.9°C	55.3°C	55°C ≤
Initial brake temperature	57.8°C	57.3°C	75°C ± 25°C
Final brake temperature	86.5°C	88.9°C	115°C ± 35°C
Maximum temperature over WLTP	114.6°C	122.0°C	not specified

A variety of instruments in addition to the instrumentation required by the GTR24, was used for brake wear emission measurements. A condensation particle counter (CPC) (SPC-D-19, AiP automotive) with a catalytic stripper and a 1:100 dilution acted as solid particle counter (SPC) and was located inside the brake dynamometer room next to the sampling probes. The cabinet encasing the SPC also housed mass flow controllers and pumps for two filter holders equipped with PM_{10} and $PM_{2.5}$ cyclones, which were used for gravimetric measurements.

All other equipment was located outside the brake dynamometer room and was connected via two stainless steel sampling tubes with a 12 mm outer diameter. One of the lines was left undiluted and was connected to a Fast Aerosol Sizer (DMS500 Mk II, Cambustion Ltd.), measuring size distributions in the range of 5 nm – 1 µm based on the electric mobility of particles. The second line was diluted by a portable dilution system (Dekati eDiluter Pro, Dekati Ltd.) in a 1:25 ratio to provide suitable concentration ranges to the connected instruments. An optical particle sizer (OPS) (Aerosol Particle Size Spectrometer LAP 322, Topas GmbH), measured particle size-distributions in the range of 0.3 – 2.5 µm with a resolution of 0.5 Hz, while a second CPC (Grimm 5420, Grimm Aerosol Technik GmbH & Co. KG) without catalytic stripper acted as total particle counter (TPC). Additional filter sampling for SEM/EDX analysis was conducted via a gravimetric filter holder (Dekati eFilter, Dekati Ltd.). Polycarbonate membrane filters (PC filters) with a diameter of 47 mm (Whatman, Nucleopore, 2 µm pore-size) with fixated Si wafers (p-type boron dotted 5 x 5 mm, Ted Pella Inc.) and pure Nb substrates (EM-Tec NB12, ø 3 x 0.1 mm, 99.99 % Nb, Micro to Nano) mounted on top, were used for SEM/EDX sampling, while 47 mm PTFE membrane filter discs (Teflo 2 µm, 47 mm, Pall Corporation) were used for gravimetric measurements and ICP-MS analysis.

Gravimetry was conducted by weighing filters before and after each WLTP brake, using a microbalance (Cubis MCA2.7S-2S00-F, Sartorius). Before each weighing filters were pre-conditioned at a relative humidity of 45 % and a temperature of 22 °C for 24 h in a climate-controlled chamber (pureGMC 18-EPA1065), equipped with a corona discharger for filter charge neutralization. Clean air used for dilution of all systems was provided by a zero-air generator (AADCO 737-15, Tisch Environmental Inc.) to avoid contamination.

4.2 Railway emission measurements

The spatio-temporal variability of PN and PM in the subway was studied with a custom-built mobile measurement approach to identify potential hot-spots in the subway system and to investigate inter- and intraday variability of PM and PN levels. For this reason, scouting routes were conducted as a first step, to gain a basic understanding of the Munich subway system and to identify hot spots. Particle concentrations were compared to average concentrations from ambient walks. Afterwards the spatio-temporal distribution of particles in the Munich subway system was studied by repeating the same route three times a day. The approximately 1 h long route was chosen based on results from scouting rides and is described in detail in Bendl, Neukirchen et al. [63]. The route was repeated on several days in the morning, noon and afternoon, to address exposure levels during rush hours (morning and afternoon), with elevated train frequencies and the noon time, with comparably few commuters.

The mobile measurement system consisted of an actively ventilated, waterproof aluminum box, which housed instrumentation for online measurements and filter sampling and omnidirectional inlets located

in the breathing-zone of passengers. PM size distributions were measured via an OPS (OPS 3330, TSI) and size modes were measured with a DISCmini device (Testo). Filter sampling on 47 mm filters for ICP-MS and manual SEM/EDX analysis, as well as gravimetric PM determination, later used for correction of particle density for the OPS, was conducted by a personal sampling device (SG10-2 personal sampler, GSA) with a constant flow of 9 L/min and a $PM_{2.5}$ pre-impactor installed in front.

To further address the inhomogeneous nature of subway emissions, which are mixed with other emission sources and to obtain a more in-depth understanding of the individual components contributing to railway emissions, an automated SEM/EDX imaging algorithm was developed. Automated SEM/EDX imaging is a powerful tool for the characterization and monitoring of particles of interest, that are differentiable from other particles by their elemental composition and are large enough to acquire accurate EDX spectra. Particles are automatically detected by the software, based on their gray values. For this purpose, the BSE detector of a SEM was used, since the high material contrast that it yields is beneficial for automated recognition of features. Once a feature is detected, it is assigned an ID and its morphological data, such as length, area and perimeter are stored. Afterwards an automatic EDX measurement in the geographical center point of the particle is triggered and the spectrum is added to the feature ID. Elemental data, as well as measured and computed morphological parameters e.g. the equivalent circular diameter and aspect ratio, is then compared to pre-defined class rules. If the class boundaries match the obtained data, the fitting class is assigned to the feature, otherwise the next class in the list is checked. Since particles can potentially fit into two or more classes, establishing the right order of class rules to be checked is crucial. With the established ruleset the large datasets can be easily sorted and a variety of tasks can be achieved. Two possible cases, where the technique can be employed, are the analysis of the homogeneity of a single emission source, such as brake dust from a dynamometer, or source apportionment of individual sources in an environment with several emission sources. A third, more specialized application is solving so-called “needle in a haystack” problems, were small quantities of particles of interest (e.g. health relevant particles such as asbestos fibers) are scattered among a large number of other particles. The software Zen core by Zeiss was used for high resolution imaging, to determine morphological descriptors with higher precision, while the software Aztec Features by the company Oxford instruments was used for SEM/EDX based classification of particles. A more detailed description of the purpose of the Zen core and Aztec Features software is given in Neukirchen et al. [65]. A schematic overview of the automated imaging process is given in Figure 4-2.

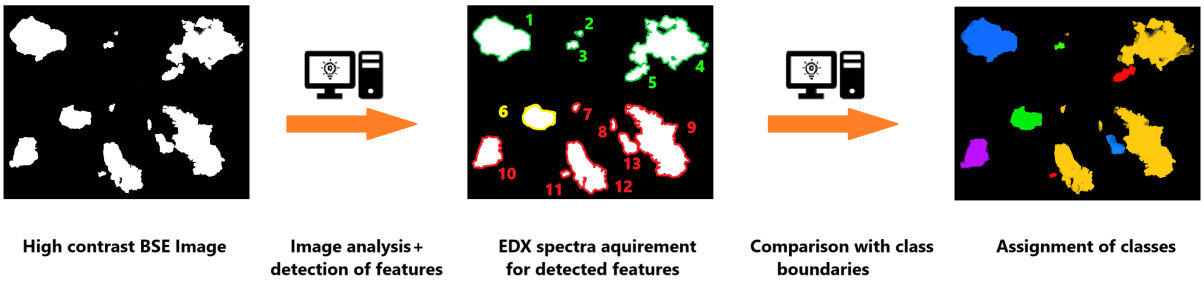

Figure 4-2: Overview of the automated imaging process. Left: High contrast BSE image used for detecting features; middle: Features are being analyzed. Green features have already been processed, the yellow feature is currently being measured, while red features have not been measured yet; right: a

class is assigned to each feature based on the pre-defined boundaries. Modified with permission from Neukirchen et al. [65]

To establish class rules that fit the subway environment, first a thorough literature review was conducted. A list of particle classes that are typical for the environment, such as iron oxides and copper particles, was established based on these results.

Afterwards a list of classes that represent interaction with the outside world, for example mineral dusts and salts, that can be brought in by commuters, was added. The technical cleanliness scheme provided by Oxford Instruments GmbH was used as starting base for building the subway classification scheme. In total, ten main classes were defined, which were further divided into 31 subclasses, to allow for a more accurate distinction of particle sources. The brake wear class, for example, was subdivided into the two classes barium sulfate ($BaSO_4$) and antimony trisulphide (SbS_3), since these are common additives used in the manufacturing of brake pads [44]. Finally, three rejection classes were added to exclude artifacts, such as scratches in the Si wafers due to sample handling and particles originating from conductive silver paint, that was used to mount samples.

Si wafers and 12 mm PC filter punches from the central station platform were used for automated imaging of subway samples. PC filter samples were imaged twice, once with an EHT of 15 kV for particles. The automated particle analysis was carried out at 15 kV for all samples, as well as at 5 kV for the PC filter samples in order to reduce piercing effects and enable automated measurements below the size of 1 µm. Image acquisition parameters were chosen so that 1 µm sized particles were described by at least 5 pixels. EDX Spectra were acquired for 0.3 s per particle, which resulted in approximately 40,000 counts. Image acquisition settings for 5 kV analysis were chosen so that 200 nm sized particles, which is also the smallest particle size that was measured, are described by at least 5 pixels. The EDX spectra were acquired for 2 s per particle, which resulted in approximately 200,000 counts. While larger magnifications for the image acquisition would theoretically enable automated analysis even below the set cut-off of 200 nm, this would result in an exponential increase of measurements time, which was already in the range of 10-12 h per sample. Furthermore, EDX spectra of small particles > 200 nm are less accurate due to piercing effects and need to be checked manually for artifact peaks caused by this effect. For this reason, particles below 200 nm in diameter were manually analyzed at 5 kV. The overlap in particle counts from 770 nm to 1 µm for automated filter measurements at 15 kV and 5 kV was manually deleted from the 15 kV dataset to avoid double counting of particles. The overlapping size region was measured intentionally for normalization between the rates of automated particle recognition, which was later used for compiling size distributions. To account for the different sample types and utilized acceleration voltages during analysis, three different versions of the classification scheme were built, that slightly differed in their ruleset. The most prominent difference is the exclusion of C from PC filters and Si for wafers, since these results might be significantly altered due to piercing effects and might lead to false classification results. A more detailed description of the final classes and their boundaries can be found in Neukirchen et al. [65] and the supplementary information associated to the publication.

Samples for testing of the automated imaging process were collected in the middle of the platform of the Munich central station, called “Hauptbahnhof” (line U4/U5) at different seasons (May, July and August). Samples were collected with a constant flow of 2 L/min by a sampling device (BiVOC2V2

sampler, Holbach) for up to 6 h without the use of a pre-impactor, since the automated imaging algorithm allows for selection of sizes of interest and can discard larger particles automatically. The mobile measurement system was used for sampling and online measurements with all described systems were run to compare results with the automated imaging. The mobile sampling device, as well as the studied area and sampling location for characterization via automated SEM/EDX imaging are displayed in Figure 4-3.

Figure 4-3: 1. Overview of the Munich subway system [93], with the studied area marked in red and the sampling location for automated SEM/EDX imaging encircled 2. Sampling location for testing of the automated imaging algorithm [94] 3. Mobile measurements system for online analysis and offline sampling. Adopted and modified from Neukirchen et al. [65]

While the chosen methodology for this study theoretically enables the quantification of all elements, by combining results from PC filters and Si wafers and yielded feasible results for classifications of subway particles, a general approach that would enable measurements of all elements in single particles would be beneficial. For this purpose, the passive sampling process on substrates was further developed to enable single particle elemental analysis for all elements accessible by EDX analysis (see chapter 4.3.2).

4.3 Sample preparation

4.3.1 Validation of an ICP/MS-MS digestion procedure for metallic wear particles

Assuring the completeness of a digestion method prior to ICP-MS/MS analysis of samples is crucial for accurate and reproducible results. Common digestion procedures feature an oxidative pressure digestion with a mixture of H_2O_2 with various acids, such as HF, HNO_3, or HCl, depending on the analyte matrix. Especially silicate containing samples pose a challenge to the digestion routine, since they do not readily dissolve in digestion mixtures without addition of HF. HF, on the other hand is not only unfavorable due to extensive safety precautions that have to be fulfilled in its handling, but is also unsuitable for most instruments with quartz based nebulizers and spray chambers and without platinum coated sampling and skimmer cones [95].

A digestion routine described in DIN EN 14902:2005-10, consisting of a mixture of suprapure HNO_3 and hydrogen peroxide (8 ml 69 % HNO_3/ 2 ml 30 % H_2O_2) was tested for its suitability. Furthermore, the powders were treated with different ratios of acid to H_2O_2 and the amount of weighed in samples was varied. Since no standard reference material for the elemental analysis of brake dust or railway emissions was purchasable at the time of the studies, the method was tried on ground powders obtained from four different brake pads (NAO, LM, semi-metallic and ceramic). Brake lining bulk powders were generated utilizing a tungsten carbide grinder to avoid metal contamination originating from the tools.

4.3.2 Passive sampling on substrates for quantification of elements of interest via SEM/EDX

An existing SEM/EDX sample preparation routine was evaluated and optimized regarding its suitability for manual and automated SEM/EDX analysis of metallic wear particles. The existing routine utilized 5 x 5 mm Si wafers, which were fixed to the surface PC filters for sampling. The wafers, as well as 12 mm punches from the PC filters were then fixed to 12 mm SEM specimen pin stubs with EDX suitable double-sided adhesive carbon tape. PC filters were also coated with a thin coating of platinum/ palladium (80:20 wt. %) in a plasma sputtering device (Q150T ES Plus, Quorum technologies) to minimize charging effects.

Due to the inaccessibility of Si via ICP-MS/MS in measurements without prior HF digestion and specialized instrument cones and nebulizers, the usage of Si wafers results in a blindness for this element for both orthogonal measurement techniques. Since silicate fillers are a common ingredient in brake pad formulations both for automotive and railway usage, the suitability of various other materials as sampling substrates was studied. The criteria for identification of possible substrate media were the absence of their ingredients in environmental samples, specifically in brake pads and common steel types, their availability on the market, as well as the price of the material.

Based on these considerations, three candidate materials were identified as suitable substrates: Indium foils, which can be easily cut to shape due to the soft and flexible consistency of the metal; titanium plates, which are commercially available as 12 mm round tabs and niobium, which is both available as foils and 12 mm tabs. Due to the hardness of Nb foils, they cannot be easily cut and instead 3 mm punches were taken from the foil, which fitted in specialized TEM grid sample holders in the SEM during analysis, avoiding the delicate and time-consuming transfer and fixation process of the other substrates. Furthermore, PC filters were also investigated as control to avoid possible discrimination during the passive sampling process with substrates. All samples, except the 3 mm Nb punches, were fixed to SEM specimen pin stubs with EDX suitable double-sided adhesive carbon tape.

The main criterion for the evaluation of SEM suitability was the surface homogeneity, which is important for locating and identifying particles of interest, especially in the context of automated imaging. Grooves and scratches, as well as particles that originate from the sampling substrate, can lead to false identification of particles, significantly lengthening the measurement time of automated imaging approaches. Furthermore, the conductivity of the material has to be sufficient to minimize surface charge buildup during prolonged analysis for high resolution images and EDX spot analysis at high acceleration voltages. For EDX analysis the substrates were further analyzed regarding their chemical purity, as well as the ability to cause main and pile-up peaks, which might interfere with elements of interest, by measuring and evaluating generated peaks at an EHT of 20 kV.

5 Results & Discussion

5.1 Sample preparation

5.1.1 Validation of an ICP/MS-MS digestion procedure for metallic wear particles

All digestion methods left behind a white crystalline residue, no matter the concentration of acid and the initial weight of the sample. Prolongation of the pressurized acid digestion up to 4 h did not improve the solubility of the residue, which most likely originated from silicate fillers in the brake pad formulation, which are insoluble in the digestion solution without the addition of hydrofluoric acid. To ensure the viability of the method, the residue was filtered of and a small portion was analyzed for its elemental composition via SEM/EDX, while the rest was digested in fresh acid for a second time. Neither the second digest, where the residue still remained, nor the EDX analysis showed elements of interest and elemental spectra showed the presence of Si together with Mg, Na, K and Ca.

Since the final concentration of acid in the sample has a large influence on the instruments signal response and no benefits were observed with higher acid concentrations, the DIN norm EN 14902:2005-10 was adopted for the digestion of filter samples for both brake and subway studies. Due to the absence of elements of interest in the digestion residue the method was deemed sufficient for analysis of all elements accessible via ICP-MS/MS, except Si and recovery rates equal to those described in the norm can be assumed for the digestion of metallic wear particles.

5.1.2 Passive sampling on substrates for quantification of elements of interest via SEM/EDX

Surface analysis of the studied substrate materials revealed large differences in the topographic features of the samples. Si wafers exhibited an extremely smooth texture, optimal for automated particle detection, which was rarely disrupted by scratches, caused by handling of the wafers with tweezers during sample preparation. Furthermore, large chunks of silica, presumably also caused by handling with tweezers, were found all over the wafers. These particles were readily distinguishable from other particles during manual inspection, however, automatic imaging algorithms are more difficult to train for such artifacts. Falsely detected particles originating from scratches, surface structures and chipped substrates can be automatically excluded by an algorithm, if fitting rejection classes are established, however, they still significantly prolong the measurement time, since the exclusion is normally realized by the EDX spectrum of a feature. The two metallic substrate types exhibited significantly more surface structures, that might interfere with sample analysis. Indium foils showed layered structures on the surface, which are presumably generated during sample transfer to SEM specimen stubs, due to the soft nature of the material. Nb foils and tabs showed shallow grooves in its surface, that were neither a problem during manual, nor automated inspection, while Ti tabs featured significantly deeper grooves, with an almost ravine-like structure, that were frequently interfering with analysis. All sampling substrates possessed sufficient conductivity, that allowed for recording of high-resolution images, which were only partially disturbed by the frequent surface impurities of Ti and Nb substrates.

From the imaging perspective, Si wafers exhibited better characteristics than the other substrate types, while Nb foils were also suitable for automated imaging. Another factor favoring the two materials were the available sampling sizes, since studied samples on 12 mm Nb and Ti tabs showed a

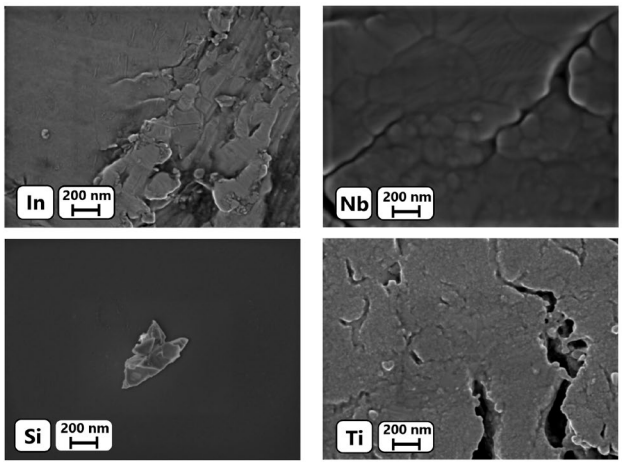

Figure 5-1: SEM overview of substrate surfaces at 50,000 x magnification. Left top: Indium foil with layered plateau structures; Right top: Niobium foil with grooves; Left bottom: Silica wafer with particle from chipping process; Right bottom: Titanium tab with ravine-like structures

significantly decreased particle density compared to smaller substrate diameters. Particles were predominantly located around the perimeter of the samples, indicating that the passive sampling approach worked best for smaller sample diameters. Ti substrates were only available as 12 mm tabs and the material proved to be too hard to effectively process, while In proved to be too soft to maintain its integrity during handling. Only Nb foils of 0.1 mm and 0.05 mm thickness were processable enough to obtain samples with a diameter of 3 mm via specialized punching pliers. These substrates have the added benefit of fitting into TEM grid holders, reducing the possibility of sample loss during the complicated fixation process of the small samples. Prominent surface features of the studied sampling materials are displayed in Figure 5-1, however it should be noted that most materials displayed a significantly smoother surface on average, than depicted in the image.

An investigation of sampling substrate candidates regarding their EDX suitability proved, that all materials were sufficiently pure to allow for analysis. Only the wafers contained elements of interest, namely Si and O, that would interfere during analysis. In foils displayed a variety of peaks from its L-series that can interfere with elements of interest such as Sb, Sn and Co due to the L-series emission lines themselves and the continuum pileup caused by them, which is shown in Figure 2-7 in chapter 2.2.2.. Due to the difficult handling of the material and the bad performance during EDX analysis and high-resolution imaging, In was discarded as potential sampling medium. Ti, while performing comparably well in EDX analysis, where it interfered only with Sb and V, was also deemed unsuitable due to the unavailability of properly dimensioned tabs. The best suited material for EDX analysis was Nb, which caused only minor interference with Ba from a pile-up peak. Interfering main emission lines and pileups of the sampling materials, obtained from analysis at 20 kV, are summarized in Table 5-1, with elements of interest highlighted in bold letters.

Table 5-1: Interfering elements for studied sampling substrate materials measured at 20 kV. Elements critical for the analysis of NEE particles are displayed in bold letters

Substrate material	Interferences due to main peaks	Interferences due to pile-up peaks
Si	W	**Sn**
Nb	Hg, Au, Y, Os	**Ba**, Dy
In	**Ba**, **Ca**, Cd, **K**, **Sb**, **Sn**, I	**Co**
Ti	I, **Sb**, **V**, Cs	Pt

After extensive analysis of the four sampling materials, Nb was identified as good alternative to Si wafers for EDX analysis. Since multiple substrates can be fixed on the surface of a 47 mm PC filter, the final method for SEM/EDX sampling consisted of several Si wafers for the best high-resolution SEM micrographs, that were fixed on the filters together with 3 mm Nb punches for optimum EDX analysis. Substrates were layed out in a suitable pattern leaving a sufficient area uncovered, so that additional punches could be acquired from the filters, to check for discrimination of particles due to the passive sampling approach. This approach was deemed sufficient for elemental characterization of NEEs and goals defined in task IV of the scope were fulfilled.

5.2 Brake dynamometer measurements

A custom-built brake dynamometer was utilized to define EFs for two brake pads following the GTR24 methodology. No deviations from the specified parameters of the GTR24 were observed during repeated testing and measurements indicated a good comparability of the brake disc temperatures between different iterations of the WLTP brake cycle. EFs defined from brake dynamometer tests were compared to the upcoming maximum emitted PM10 value of 7 mg/km, as defined in the EURO 7, as well as data from the recent ILS II [43, 46]. For comparability of the different brake pads, data was compared to the friction couples Br1Fa (LM) and Br1Fb (NAO) of the ILS II, since these pairings featured the only values for LM and NAO pads simulated with the same vehicle. Simulation parameters were similar to the vehicle tested on the custom-built brake dynamometer, however, the weight was slightly lower at 1600 kg [43].

EFs at the vehicle level for the LM brake pad were found at 15.08 ± 0.14 mg/km of PM_{10}, equaling 2.15 times the maximum permitted value of 7 mg/km, while the NAO pad was measured at a 2.32 times higher EF, with PM_{10} emissions of 16.29 ± 0.43 mg/km. Single brake EFs of 5.03 ± 0.05 mg/km for PM_{10} and of 1.81 ± 0.03 mg/km for $PM_{2.5}$ were measured for the LM pad, which is in good agreement with data from the ILS II, which reported average single brake EFs of 5.0 mg/km for PM_{10} and 1.9 mg/km for $PM_{2.5}$ [43]. The NAO pad was measured at 5.43 ± 0.14 mg/km of PM_{10} and 2.41 ± 0.08 mg/km of $PM_{2.5}$, however, the EFs for the NAO pad listed by the ILS II were 2.2 mg/km of PM_{10} and 0.8 mg/km of $PM_{2.5}$ [43], which is only 40.5 % of PM_{10} and 33.2 % of $PM_{2.5}$ found in this study. These differences can be partially explained by the differences in the simulated vehicle weight and wheel load to disc mass ratios, however, the more likely explanation is the chemical composition of the NAO pad, which was found at an unusually high metal concentration of 13.86 ± 1.06 % of its weight. While NAO pads have no strict regulation on their metal contents, they normally contain significantly less metal percentage, which usually ranges between 4 - 7 % [50]. Based on these results, the NAO pad should exhibit emission characteristics similar to a LM pad, which typically range between 10 and 30 % by weight [1] and when comparing the NAO pad to the LM values reported in the ILS II, the results were again in a similar range. These findings underline, that pad type classifications are not always accurate and that chemical characterization of the brake pad material is crucial for comparison of EFs.

Based on the obtained EFs average $PM_{2.5}/PM_{10}$ ratios of 0.36 for the LM pad and 0.44 for the NAO pad were calculated. The ILS II in comparison reported ranges between 37 and 45 % for all tested brakes, with the reference bake system Br1F exhibiting a ratio of 42 % for the LM pad and a slightly higher ratio of 45 % for the NAO pad [43]. While the general ranges of $PM_{2.5}/PM_{10}$ ratios are in good accordance to the data from the ILS II, the lower values for the LM pads in comparison to the reference

brake can be explained by the different vehicle simulation parameters, since the temperature plays an important role in the emission patterns of brake systems, with higher temperatures resulting in smaller particle diameters [1]. The higher wheel load/disc mass factor of the ILS II system requires a 10°C higher average brake disc temperature, favoring the generation of $PM_{2.5}$ in comparison to PM_{10}. This effect also explains the higher $PM_{2.5}/PM_{10}$ ratio of the NAO pad that was tested on the custom-built dynamometer, since this pad showed higher maximum brake disc temperature of 122 °C, compared to 114.6 °C of the LM pad during testing.

The measured total particle number (TPN) and solid particle number (SPN) emissions for the LM pad were 2.33 (TPN) and 2.51 (SPN) times higher than values of the ILS II, which reported an average TPN of 1.93 x 10^9 #/km/brake and a SPN of 2.19 x 10^9 #/km/brake [46]. For the NAO pad the PN emissions were 8.8 (TPN) and 8.3 (SPN) higher than the ILS II that measured 9.37 x 10^8 #/km/brake (TPN) and 1.03 x 10^9 #/km/brake (SPN) for their NAO pad. As discussed for the PM levels, the NAO pad tested as part of this thesis behaved more like a LM pad due to its high metal content. When comparing the NAO pad to the Br1Fa (LM) pad of the ILS II the obtained values result in 4.3 (TPN) and 3.9 (SPN) times higher PN emissions. While being several times higher, the PN emission levels obtained from the custom-built dynamometer can still be regarded as meaningful, since a wide variety of parameters such as temperature, wheel load/ disc mass factor, vehicle weight and brake pad compositions influence the PN levels [26], making it difficult to compare PN data obtained with different simulated vehicles, while also employing different friction partners. Furthermore, the brake dynamometer design heavily influences the PN, which is reflected by the high range of TPN reported by the ILS II, which ranged from 9.1×10^8 #/km/brake to 1.1×10^{10} #/km/brake for the seven tested brakes and differed substantially within the 16 participating labs, with the reference LM pad varying approximately within a factor of 5 between the lowest and the highest tested TPN [46].

From the obtained PM and PN results it can be concluded, that the custom-built brake dynamometer yielded feasible results, even though it deviates slightly from the GTR24 specifications in its enclosure design. With this the task 2 defined in the scope, which featured the development of a testing setup capable of reproducibly generating realistic emissions for physical and chemical characterization of brake wear particles can be considered as fulfilled. EFs for PM_{10}, $PM_{2.5,}$ SPN and TPN for the studied LM and NAO pads averaged over three WLTP brake cycles are summarized in Table 5-2, while the time resolved TPN plotted against the speed profile of the WLTP brake are illustrated in Figure 5-2.

Table 5-2: PN and PM EFs of the analyzed LM and NAO brake pads at the brake and vehicle level

Brake pad	Emission level	TPN #/km	SPN #/km	PM_{10} mg/km	$PM_{2.5}$ mg/km
LM	Single brake	4.51 ± 0.06 x 10^9	5.49 ± 0.11 x 10^9	5.03 ± 0.05	1.81 ± 0.03
	Vehicle	1.37 ± 0.02 x 10^{10}	1.65 ± 0.03 x 10^{10}	15.08 ± 0.14	5.42 ± 0.08
NAO	Single brake	8.26 ± 0.1 x 10^9	8.50 ± 0.21 x 10^9	5.43 ± 0.14	2.41 ± 0.08
	Vehicle	2.50 ± 0.03 x 10^{10}	2.55 ± 0.06 x 10^{10}	16.29 ± 0.43	7.24 ± 0.24

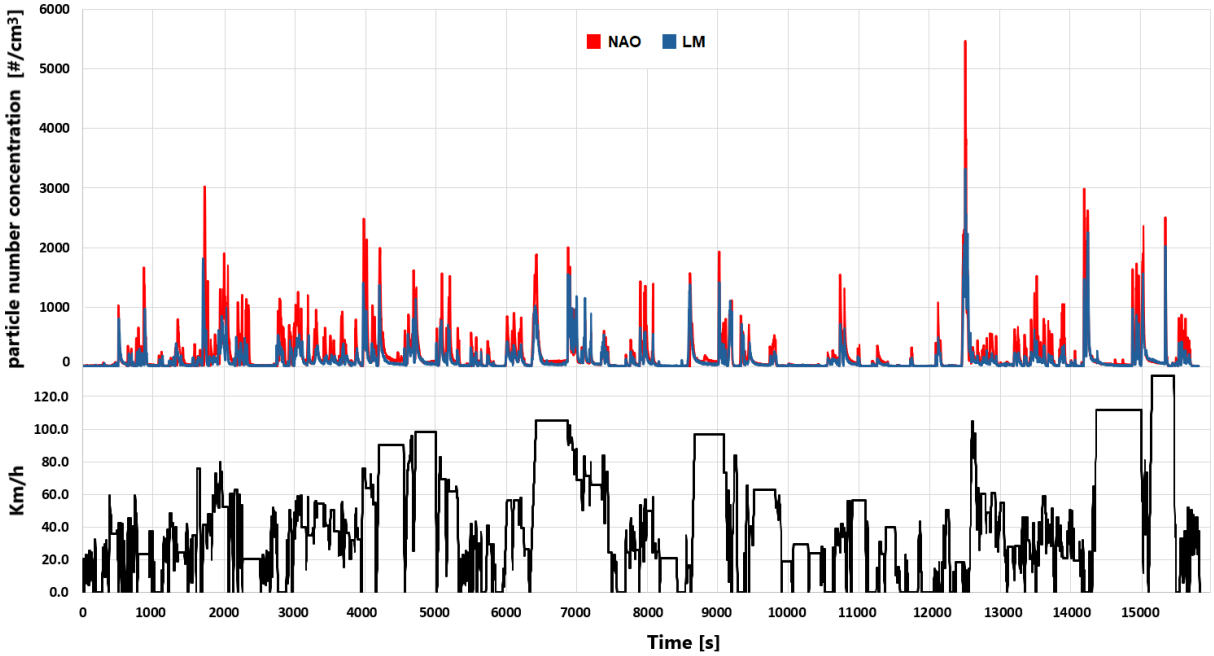

Figure 5-2: TPN emissions of LM & NAO pads plotted against the WLTP brake speed profile

Size characterization of brake wear NEEs by electrical mobility of particles (DMS 500) displayed a bimodal PN size distribution with a geometric mean diameter (GMD) of 123 nm for the LM pad and 143 nm for the NAO pad. Both pads displayed a second mode at 86 nm, however, the peak was more pronounced for the NAO pad. Several studies in literature reported PN peaks in the range of 70 to 100 nm [27, 96, 97]. The OPS showed the mode of the particles between 300 and 400 nm, with steeply declining PN levels above 400 nm. While the OPS can theoretically detect particles above 300 nm, its counting efficiency is limited for particles smaller than 500 nm, due to its measurement principle being based on laser scattering properties [98]. Below 500 nm the data from the DMS 500 can be regarded as more accurate and the OPS, therefore, served as measurement instrument of larger particles, since the DMS 500 can only operate up to 1 µm. The NAO pad produced a larger share of smaller particles compared to the LM pad, visible from the data obtained from the DMS 500, while the OPS showed no equal increase in large particles. This is also reflected by the higher $PM_{2.5}/PM_{10}$ ratio and the higher TPN and SPN values for the NAO pad, since small particles often have a large influence on PN, however, a negligible influence on PM. The majority of particles was found between 40 and 300 nm, with a considerable fraction of PN in the nanoparticle range and the GMD slightly above. Several studies also reported particles in the range of 10 to 30 nm for strong braking events linked to exceeding the critical temperature of the brake leading to condensation of ultrafine particles in the cooling air [26–28]. Since the WLTP brake cycle features comparably moderate temperatures, with the highest measured temperature in this study being just above 120 °C, these peaks were not observed. PN size distributions for LM and NAO pads obtained by DMS 500 and OPS are shown in Figure 5-3..

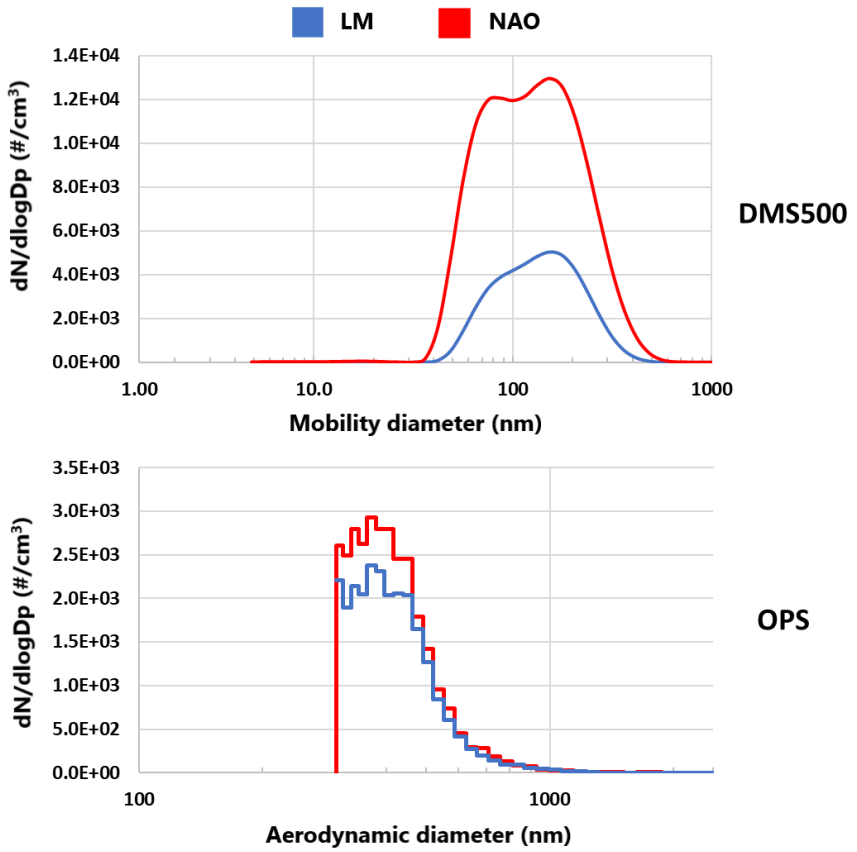

Figure 5-3: Size distributions for LM & NAO pads averaged over the WLTP brake cycle measured via DMS500 (5-1000 nm) and OPS (300-2500 nm)

ICP-MS/MS analysis of filter samples showed similar elemental compositions for PM_{10} and $PM_{2.5}$, suggesting a uniform chemical composition over the coarse (PM_{10}) and fine ($PM_{2.5}$) size range. For this reason, the following discussion of ICP-MS/MS data is only focused on PM_{10} data. The only noticeable exception to this observation was an enrichment of Sn in the $PM_{2.5}$ fraction of the LM pad, with Sn concentrations increasing from 0.78 ± 0.05 wt.% in the PM_{10} fraction to 1.03 ± 0.01 wt.% in the $PM_{2.5}$ fraction. The enrichment of certain elements, like Cu, Sn and Zn was attributed to their comparably low melting points by Kukutschová et al. [26], favoring the generation of nanoparticles. This effect was only observed for Sn, which has the lowest melting temperature of the metals at only 232°C. Qi and Day demonstrated, that temperatures at the tribological interface can be substantially higher than average brake disc temperatures, with the interface temperature in their study reaching 400°C, even though the average disc temperature was measured at 120°C [99].

Significant chemical changes from the initial brake lining material to the emitted wear particles were observable for both pad types. The LM pad originally contained 23.90 ± 0.35 wt.% of Fe, while its PM_{10} samples contained an average of 54.85 ± 0.85 wt.%. Higher Fe concentrations in filter samples were most likely caused by mixing of emitted pad wear particles with wear from the brake disc, which featured Fe concentrations of 81.79 ± 2.35 wt.%. This hypothesis is further supported by the trends of other heavy metal concentrations, such as Mn, which increased from 0.1 ± 0.0 wt.% in the LM bulk material to 0.29 ± 0.0 wt.% in filter samples due to higher concentrations of 0.56 ± 0.01 wt.% in the brake disc. A similar shift in the opposite direction in elemental compositions was also observed for

other heavy metals, such as Cu, which showed a decrease in Cu concentrations from 0.50 ± 0.04 wt.% in the LM pad to 0.29 ± 0.00 wt.% in the PM_{10} samples, caused by the lower Cu concentration of only 0.28 ± 0.01 wt.% in the brake disc. The mixing effect was most noticeable for Zn concentrations in LM samples, which lowered from 5.57 ± 0.20 % in the brake lining material to 1.46 ± 0.03 % in PM_{10} samples, due to the absence of Zn in the brake disc, which contained only 0.03 ± 0.02 % on average.

The elemental composition of filter samples obtained from the NAO pad exhibited even higher Fe contents than LM samples, suggesting an increased contribution of brake disc wear. Fe concentrations of 58.13 ± 1.39 % were found for the PM_{10} samples. These results let the manufacturers pad type classification as a NAO pad appear questionable, since the elemental composition would rather justify classification as a LM pad, which also matched the experimentally observed EFs. Evidently, brake lining type classifications offer only a rough estimation of the emission behavior and the chemical composition of pads should preferably be also addressed, when comparing the behavior of the types. General rules, stating that NAO pads produce less emissions than other types [49, 100] might be correct on average, but should be treated with care for the comparison of individual pads, since no clear rules for the classification of types apply.

The hypothesis of a strong brake disc contribution in NAO samples was further supported by Cu contents, which increased from 0.01 ± 0.00 wt.% in the bulk material to 0.21 ± 0.01 % (PM_{10}) and 0.20 ± 0.01 % ($PM_{2.5}$) of Cu in filter samples. Similar to the LM pads, the opposite effect of elemental contents decreasing due to mixing effects was observed. Initial Mg concentrations in the NAO pad were found at 9.62 ± 0.08 wt.% and lowered to 1.63 ± 0.02 wt.% in the PM_{10} samples, with the disc containing only 0.01 ± 0.00 wt.% of Mg.

A second visible effect that originated from contribution of brake disc wear, was the decrease in chemical difference from NAO and LM bulk samples to filter samples. While bulk brake lining materials initially had distinct differences in their elemental compositions, these differences diminished in filter samples of the two pads.

Significant changes in elemental compositions due to braking processes are well reported in the literature and are not only attributed to mixing with brake disc wear, but also to other factors, such as thermal degradation of the polymeric binding matrix at high temperatures, tribo-oxidation and other processes [21, 26, 101].

Both pads contained low amounts of Cu, which were compliant with Cu regulations of the US EPA. While the LM pad contained 0.5 ± 0.04 wt.% of Cu, which is the exact limit value for copper in the U.S. from 2025 onwards, the NAO pad contained only 0.01 ± 0.00 wt.%. This reduction is a positive trend in modern brake pad formulations, due to the increased toxicity of Cu nanoparticles [102] and their severe effects on the environment [103]. Former studies have reported accumulation of large amounts of Cu in oceans [4] and watersheds [2] mainly caused by brake wear contribution, with older pad formulations frequently displaying Cu contents between 5 and 15 % [4, 26].

Results from ICP-MS/MS analysis of bulk brake lining and disc material are summarized in Table 5-3, while the elemental compositions of PM_{10} and $PM_{2.5}$ samples are listed in Table 5-4.

Table 5-3: Elemental composition of brake bulk lining and brake disc material measured via ICP-MS/MS

Element wt. %	LM Pad	NAO Pad	Brake disc
Fe	23.90 ± 0.35	13.86 ± 1.06	81.79 ± 2.35
Cu	0.50 ± 0.04	0.01 ± 0.00	0.28 ± 0.01
Cr	0.37 ± 0.02	0.04 ± 0.00	0.22 ± 0.01
Mn	0.10 ± 0.00	0.07 ± 0.01	0.56 ± 0.01
Al	0.48 ± 0.03	1.56 ± 0.03	0.08 ± 0.02
Zn	5.57 ± 0.20	0.05 ± 0.02	0.03 ± 0.02
Ba	1.59 ± 0.02	0.02 ± 0.00	0.00 ± 0.00
Mg	4.12 ± 0.09	9.62 ± 0.08	0.01 ± 0.00
Ni	0.02 ± 0.00	0.01 ± 0.00	0.08 ± 0.00
V	0.01 ± 0.00	0.03 ± 0.00	0.01 ± 0.01
Mo	0.01 ± 0.00	0.00 ± 0.00	0.03 ± 0.00
Sn	2.86 ± 0.15	0.19 ± 0.04	0.08 ± 0.02
Total wt. % of heavy metals	33.83 ± 0.79	15.80 ± 1.16	83.18 ± 2.44

Table 5-4: Elemental composition of brake wear particles from LM and NAO filter samples analyzed via ICP-MS/MS

Element mass %	LM Pad		NAO Pad	
	PM_{10}	$PM_{2.5}$	PM_{10}	$PM_{2.5}$
Fe	54.85 ± 0.85	54.46 ± 1.15	58.13 ± 1.39	57.19 ± 1.80
Cu	0.29 ± 0.00	0.28 ± 0.00	0.21 ± 0.01	0.20 ± 0.01
Cr	0.61 ± 0.01	0.60 ± 0.01	0.13 ± 0.00	0.13 ± 0.00
Mn	0.29 ± 0.00	0.29 ± 0.00	0.31 ± 0.01	0.31 ± 0.01
Al	0.26 ± 0.01	0.24 ± 0.00	0.36 ± 0.00	0.28 ± 0.01
Zn	1.46 ± 0.03	1.45 ± 0.02	0.05 ± 0.01	0.01 ± 0.02
Ba	0.41 ± 0.01	0.40 ± 0.01	0.01 ± 0.00	0.00 ± 0.00
Mg	0.90 ± 0.04	0.90 ± 0.03	1.63 ± 0.02	1.72 ± 0.09
Ni	0.05 ± 0.00	0.05 ± 0.00	0.05 ± 0.00	0.05 ± 0.00
V	0.01 ± 0.00	0.01 ± 0.00	0.01 ± 0.00	0.01 ± 0.00
Mo	0.02 ± 0.00	0.02 ± 0.00	0.03 ± 0.00	0.03 ± 0.00
Sn	0.78 ± 0.05	1.03 ± 0.01	0.02 ± 0.00	0.02 ± 0.00
Total % of heavy metals	58.80 ± 0.97	58.61 ± 1.21	58.94 ± 1.42	57.97 ± 1.85

Based on ICP-MS/MS and gravimetric results PM_{10} and $PM_{2.5}$ EFs were calculated for heavy metals, which are depicted in Figure 5-4. Average PM_{10} EFs for Fe, which were found at 8.27 ± 0.12 mg/km (LM) and 9.47 ± 0.22 mg/km (NAO) were significantly higher than values reported in the literature review by Grigoratos and Martini, which summarized EFs for iron of up to 1 mg/km for light duty vehicles [1], highlighting the need to put older studies into context of modern GTR24 compliant measurements.

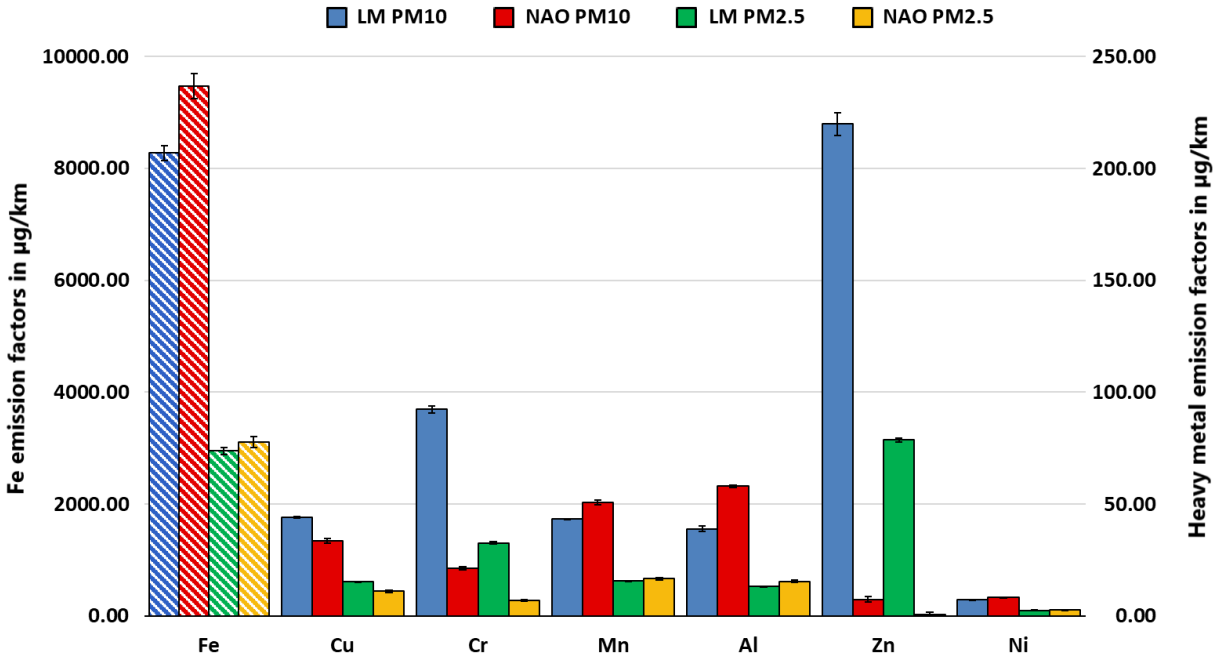

Figure 5-4: Heavy metal EFs at the vehicle level. Hatched bars for iron levels are plotted on the left Y-Axis, while solid bars for other heavy metals are plotted on the right Y-Axis. Modified with permission from Neukirchen et al. [52]

SEM/EDX analysis was conducted on cut-outs from both brake pad bulk materials and showed highly inhomogeneous distribution of elements. While large flakes of Fe were visible in the LM pad, the NAO pad displayed a higher abundance of steel fibers. Steel fibers tend to increase abrasive wear of brake rotors [104], which is in good agreement with ICP-MS/MS results, which suggested an increased rotor wear contribution to the elemental composition. Primary plateaus, which originate from wear resistant compounds in the pad, such as steel fibers, as well as secondary plateaus, formed from compacting debris [1], were visible in both samples as part of the generated tribolayer [105, 106]. Elemental maps of the two materials are shown in Figure 2-2 in chapter 2.1.1.

Particles from brake wear samples exhibited rough edges typical for samples from abrasion processes. Two distinct shapes were commonly observed in all samples via SEM analysis and were found for both pad types. The predominant type of morphology was spherically shaped with rough edges and was found in all size ranges. The second type of particles showed a flake like morphology, with the upper and lower surfaces showing a less ruptured and smoother structure, while the surrounding edges were jagged and ruptured. Flake like structures, which Wahlström et al. [107] attributed to wear from the brake disc due to the absence of typical brake markers, such as Ti, Cu and Al, were primarily found for particles > 1 µm. However, SEM/EDX analysis also revealed flakes showcasing high concentrations of

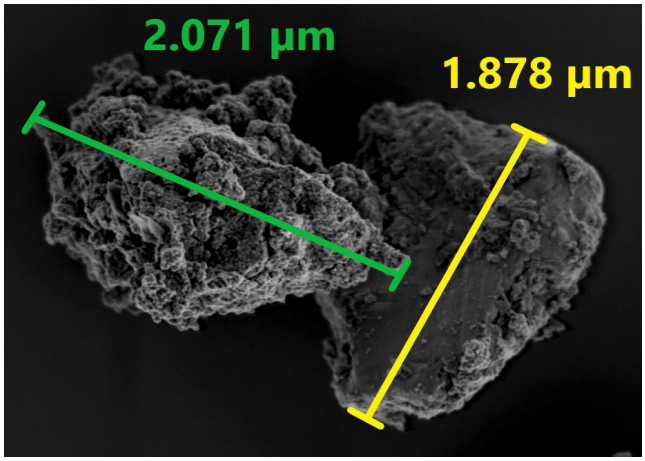

Figure 5-5: SEM micrograph of spherical (green) and flake-like (yellow) shaped particles commonly found in brake-wear samples. Particles shown originated from the LM brake pad. Reprinted with permission from Neukirchen et al. [52]

brake markers, such as Zn, which were not present in the bulk ICP-MS/MS analysis of the brake disc, contradicting the hypothesis, that flake-like structures originate from brake discs. Instead, flake like particles exhibited similar chemical compositions as spherical particles. Common morphologies of brake wear particles from an LM sample are depicted in Figure 5-5.

EDX analysis showed Fe concentrations in the range of 43 to 75 %, O contents between 19 and 39 % and C with 2.5 to 32 % in all samples. Only a few particles with Fe concentrations matching the initial Fe contents of the two analyzed brake pads and the brake disc were found. Instead, most particles in samples of both pads showed Fe concentrations between 50 and 60 %, which is similar to the average Fe contents found with ICP-MS/MS.

Variance of elemental compositions were large, with no apparent trend regarding distributions among different sizes, which is in good agreement with ICP/MS-MS results, which indicated a strong chemical similarity of PM_{10} and $PM_{2.5}$ samples. This observation proved true even into the nanoparticle size range, as observed with SEM/EDX, which showed particles as small as 30 nm consisting of 50 % of Fe or more.

Only a few particles with Fe concentrations matching the initial Fe contents of the two analyzed brake pads and the brake disc were found. Instead, most particles in samples of both pads showed Fe concentrations between 50 and 60 %, which is similar to the average Fe contents found with ICP-MS/MS. This is contradictory to the assumption, that the Fe contents found with ICP-MS/MS are the result of a mixture of highly Fe containing particles from the brake rotor and particles containing lower amounts of Fe from the pads. Instead, this would favor the hypothesis of strong chemical changes for both friction partners, with effects like thermal degradation of organic substances enhancing the Fe concentrations of particles from the pads and processes like tribo-oxidation lowering the Fe content of disc wear particles. The severance of such effects is visible in Figure 5-6, which gives an overview of morphologies and elemental compositions of NAO particles, were particle F contained 74.1 % of Fe and 0.7 % of Mg, while particle G comprised 70.6 % of Fe and 1.6 % of Mg. The presence of Mg, which was found at 0.01% in the ICP/MS-MS analysis of the brake disc, indicates the NAO pad as origin of these particles. The NAO pad itself contained only 13.86 ± 1.06 % of Fe (based on ICP-MS/MS), however, emitted particles showed Fe concentrations up to 75 %. Most likely, particles with such high Fe concentrations originate from wear of highly Fe containing compounds of the brake pad, such as the frequently observed steel fibers and are not a result of chemical changes.

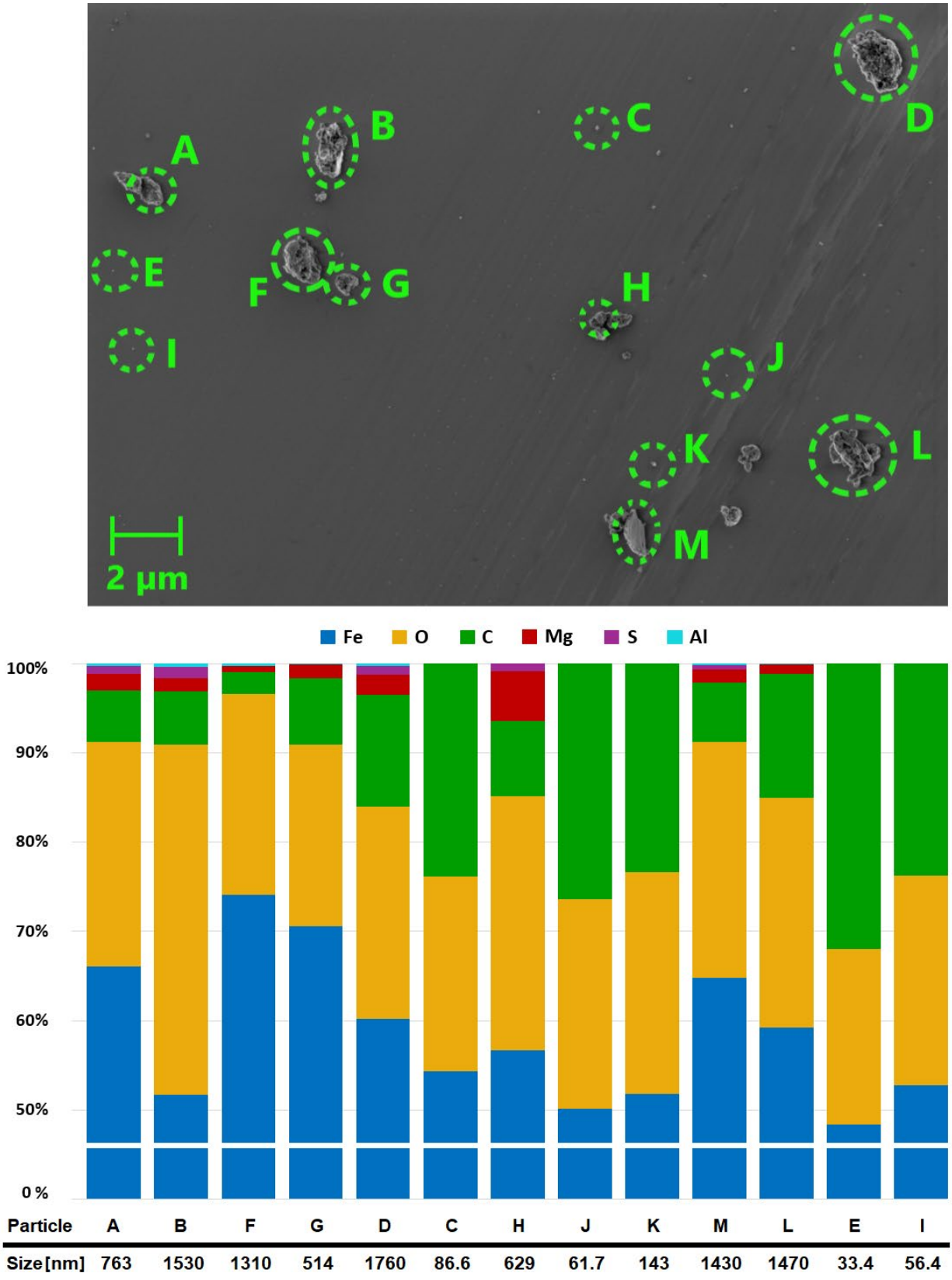

Figure 5-6: SEM overview and bar chart of elemental compositions, derived from the associated EDX spectra of NAO particles on a Si wafer measured at 5 kV. Reprinted with permission from Neukirchen et al. [52]

5.3 Subway studies

Mobile measurements in the Munich subway system showed a high spatial variability of PM, which steeply increased towards the city center upon entering of the tunnel system. Highest concentrations occurred at transfer stations, with the highest train frequencies. Train frequency also proved to be the main influencing factor for temporal variance, as seen from the analysis of intraday trends obtained from repetitions of the same route in the morning, noon and afternoon. PM concentrations were highest during morning and afternoon repetitions, due to the increased train frequency, which was 5 min during rush hours and 10 min at noon. Inter-day comparison revealed a low variance with relatively stable concentrations over different days of the week and seasons, showcasing the confined nature of subway systems, which undergo little interaction with the outside environment.

Overall, the spatial variability of PM proved to be more important than temporal differences, with platform design being responsible for the air quality of a certain station. PM levels were heavily influenced by the depth of the platforms, their ventilation, as well as the available air for mixing of the particles. Larger, more open designs exhibited lower PM concentrations, while smaller stations with the same train frequency showed increased PM levels. Furthermore, the temporal PM variability of smaller stations was higher, due to the lower air volume available for mixing resulting in more noticeable changes in air quality. PM dynamics inside the trains were found to be high, due to rapid air exchange with stations. Old train types, with windows for ventilation showed only slightly increased PM levels, indicating no, or poor filtration of the automated ventilation systems in modern trains.

The highest PM levels from repeated measurements were found at the deepest platform of the central station (CS-U2), with averaged PM_{10} values of 220 ± 32 µg/m^3, while the U-Bahn station CS-U1 located one floor above this platform, had an average concentration of 174 ± 40 µg/m^3. Overall PM levels at platforms of the U5 line ranged from 59 - 220 µg/m^3 (PM_{10}), 27–80 µg/m^3 ($PM_{2.5}$) and 9 – 21 (PM_1) µg/m^3, respectively. In comparison typical levels during train rides of the same line ranged from 73 to 170 µg/m^3 (PM_{10}), 29–59 µg/m^3 ($PM_{2.5}$), 8 - 19 µg/m^3 (PM_1). Air quality recommendations by the WHO were exceeded at almost all stations, highlighting the need for countermeasures for the reduction of PM levels in subway systems. High PM levels in the Munich subway system were presumably caused by inadequate ventilation of platforms and tunnels.

In contrast to PM levels, the PN levels were not observed to be elevated in the subway system. Only in a few cases increased PN levels occurred, which were attributed to outdoor traffic-related particles entering the subway platform, indicating that ambient air was not the dominant source of PM in the tunnel system. PM and PN levels measured in trains and on platforms were compared to average values of ambient urban background measurements. A maximum increase to outdoor levels by factors of 17.7 (PM10), 47 (PM2.5) and 28.5 (PM1) was observed for PM, however, the maximum PN enrichment factor was only 1.4 and PN levels were often lower than ambient values. Figure 5-7 displays the dynamics of PM_{10}, $PM_{2.5}$, PM_1 and PN concentrations, showing the steep increase in PM levels upon entering the tunnel system (indicated with orange dashed line). As visible, PM_{10} concentrations steadily increased while traveling towards the city center. A heatmap illustrating the spatio-temporal variability of PM and PN concentrations is given in Figure 5-8, with colors illustrating the enrichment factors compared to averaged ambient urban background measurements.

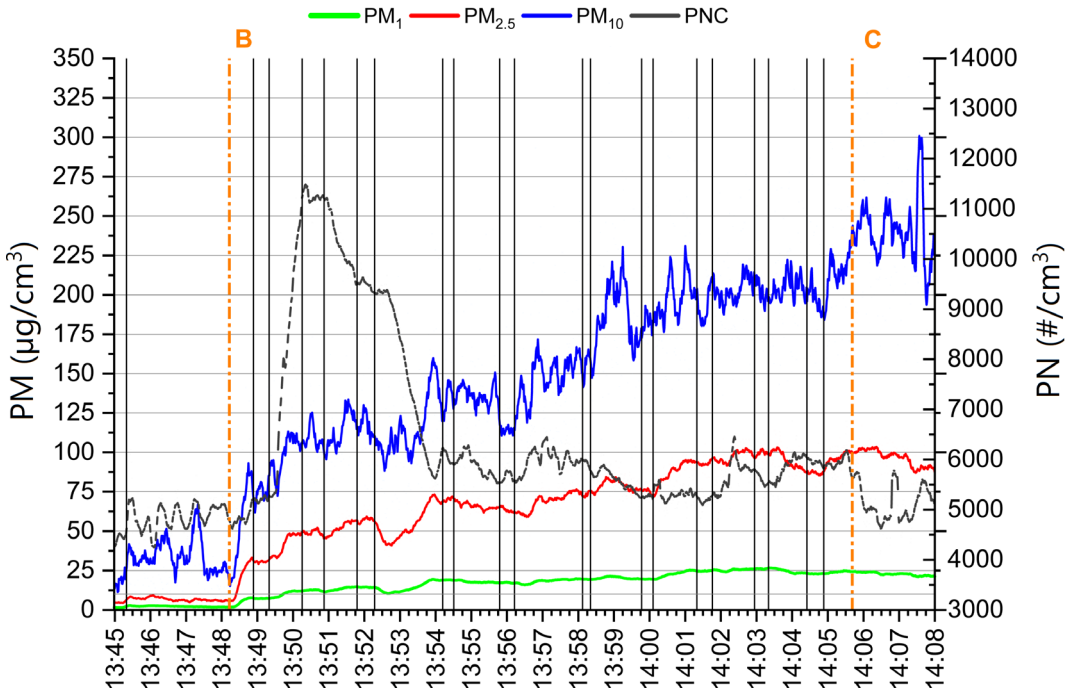

Figure 5-7: PM and PN concentration dynamics during subway rides. First vertical black line represents the entering of the train, orange dashed line indicates entering of the tunnel system and solid black lines show door opening/closing at the stations. Modified with permission from Bendl, Neukirchen et al. [63]

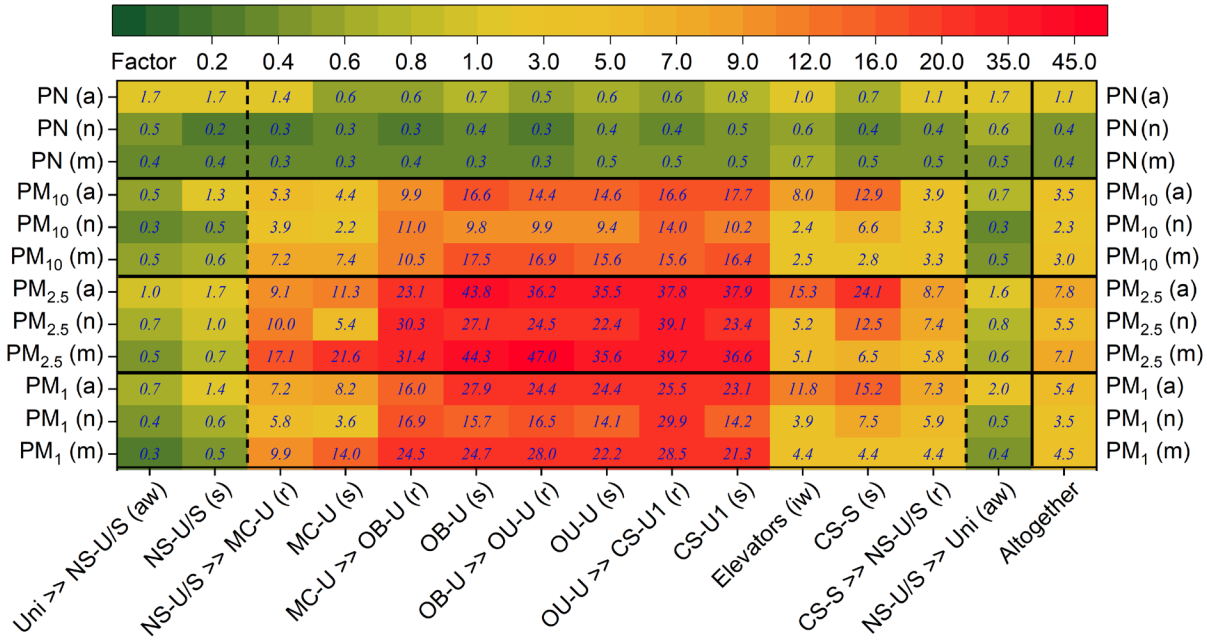

Figure 5-8: Spatio-temporal variability of PM and PN concentrations during repetitions in the morning (m), noon (n) and afternoon (a). Each route is divided into ambient walk (aw), indoor walk (iw), stationary measurements at platforms (s) and rides by the train (r). Dashed lines indicate entering and exiting of the train. Heatmap represents the ratio of the average absolute concentrations of each part of the route, compared to the overall average of a typical ambient walk (urban PM background). Last column "Altogether" represents the average from the whole route. Overview of the route, as well as station name abbreviations are listen in Bendl, Neukirchen et al. [63]. Figure modified with permission from Bendl, Neukirchen et al. [63]

ICP-MS/MS analysis of samples from stationary measurements at the central station (CS-U1) showed a large fraction of $PM_{2.5}$ to consist of Fe, with Fe concentrations of 67 µg/m^3 accounting for 69 % of $PM_{2.5}$. The highest Fe concentrations were observed during a scouting ride on November 5, 2021, with Fe reaching up to 123 µg/m^3 in the total PM, while the highest observed concentration during urban background reference walks was 2.6 µg/m^3 (October 26, 2021). Other abundantly found metals were Mn, Cr and Cu, however Cu contents in the Munich subway were lower than reported for other cities [108, 109], which is most likely due to the absence of Cu catenaries, since the Munich subway utilizes a third-wheel design with steel current collector shoes.

Manual SEM analysis of subway samples revealed almost identical morphologies as brake wear particles. The flake-like morphology frequently observed for brake wear was also commonly found in large subway wear particles, while the spherical type was less common and, instead, particles showed an elongated, splintery shape. The rough and jagged surfaces were similar to brake wear, suggesting similar modes of generations. SEM micrographs of subway wear particles are provided in Figure 5-9, with images 1 and 3 displaying flakes and images 2 and 4 showing splinters.

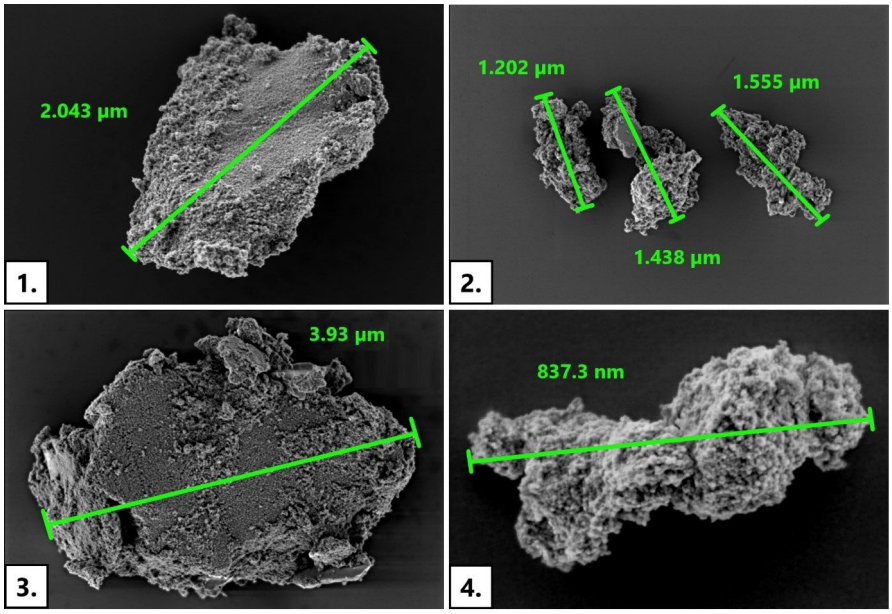

Figure 5-9: SEM micrographs of characteristic iron oxide particles found in the Munich subway system. Modified with permission from Neukirchen et al. [65]

Based on results from automated SEM high resolution imaging, conducted via the Zeiss Zen core software, equivalent aerodynamic diameters (D_A) were calculated, which showed subway particles predominantly in the submicron size, with the mode of the PN between 200 and 300 nm. The OPS in comparison showed the mode of particles at 300–400 nm and differed to the SEM/EDX based distributions, most likely due to the lowered counting efficiency of laser scattering based instruments at lower particle sizes (for a more detailed explanation see chapter 5.2). Another possible explanation is the difference between measured and calculated values, since the automated imaging yields shape information based on a 2D image, which are projected and extrapolated to the 3D particle. Such calculations naturally are less precise; however, the data quality was judged to be sufficient for analyzing trends in the assigned classes and to assess the chemical composition of certain size ranges.

Size distributions observed via the Zen core (all particles) and Aztec Features (iron oxides) softwares, as well as the OPS are plotted in Figure 5-10. Size distributions were normalized to account for differences in measurements, since automated imaging generally provides a value with the unit number or number per area, while online measurements yield results with the unit number per volume. Size distributions of overall particles showed a similar trend as the size distributions of iron oxide particles, with a noticeable deviation around 1 µm where the transition between the two automated SEM/EDX measurement sizes occurred and can most likely be attributed to the different signal responses and, therefore, different rates of recognized particles for measurements at 5 kV and 15 kV.

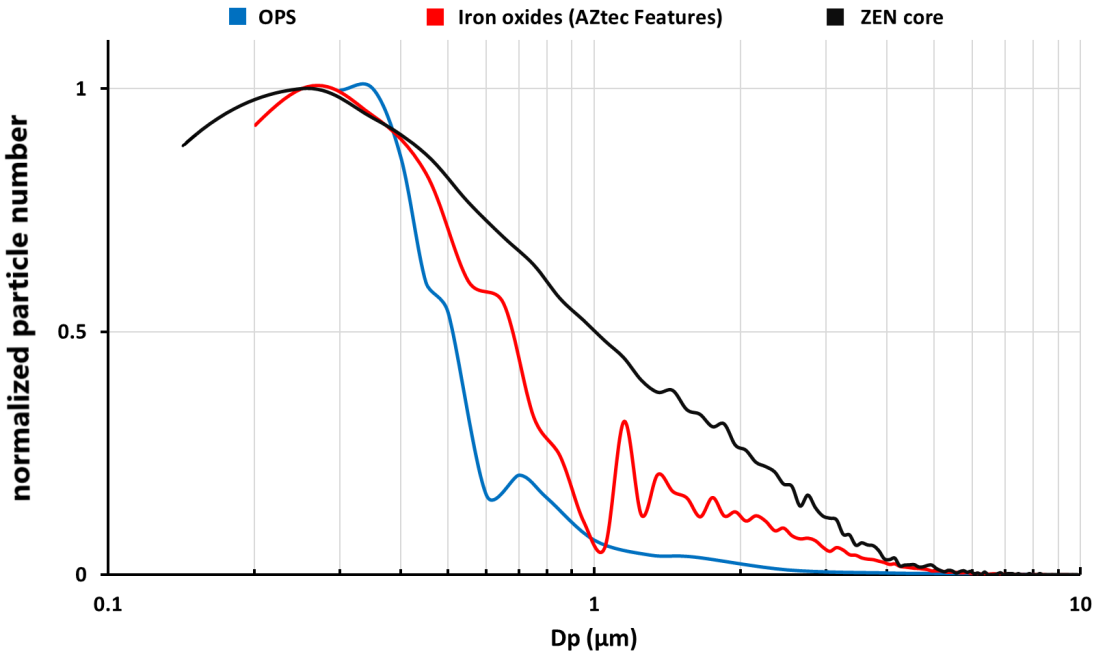

Figure 5-10: Size distributions of particles from 19/07/2022 measured via ZEN core (all particles), Aztec Features (iron oxides) and online size distribution obtained by OPS.- Reprinted with permission from Neukirchen et al. [65]

Initial results from the automated SEM/EDX classification contained several artifacts originating mainly from scratches in the surface of the silica wafers and from the pores of the filters, which were removed manually by deleting features that had no elemental data associated to them. After this data-clean-up process, the automated imaging process was capable of classifying up to 99 % of the over 200,000 analyzed particles, showing a robust measurement and classification method.

All three sample types consisted predominantly of highly ferruginous particles. Particles ≥1 µm measured on filters at 15 kV (F15) contained 92.78 ± 1.05 % of iron oxides, with an additional 4.28 ± 1.49 % belonging to the three steel subclasses, resulting in a total of 97.06 ± 0.64 % of iron-rich particles. Particles between 200 and 1000 nm on filters measured at 5 kV (F5) were classified with 63.30 ± 10.47 % of iron-rich particles, containing 62.69 ± 10.16 % of iron-oxides and only 0.61 ± 0.32 % of steel particles. The last sample type were particles ≥1 µm on Si wafers measured at 15 kV (W15), which showed iron oxides at 84.93 ± 5.48 % with an additional 8.75 ± 2.23 % of steel particles, totaling at 93.68 ± 3.28 % of iron-rich particles. W15 samples contained a higher share of steel particles than

F15 samples, which is most likely due to the application of a different classification scheme that was more suitable for distinguishing between iron oxides and steel types.

Iron oxide particles showed Fe contents averaging between 49.58 and 66.30 %, as well as high O values, from 27.37 to 45.53 % on average. C and Si showed a wide spread of concentrations, which is visible from the standard deviations, that often exceeded the average values by several times. Other elements, mostly S, Cu, Na, Ca, Mg, Al and K, were also detected, but only at average concentrations below 0.2 wt. % for individual elements.

Elemental compositions of iron oxides for the three sample types are summarized in Table 5-5. High C contents, visible from W15 samples suggest an origin from brake pads instead of a low steel source, which would be attributed to the rails and wheels [23], for the iron oxide particles. This hypothesis is in good agreement with results from EDX analysis of brake wear from the custom-built dynamometer, which exhibited similar elemental compositions (for comparison see Figure 5-6 in chapter 5.2)

Table 5-5: Average elemental compositions of iron oxides for filter and wafer samples.

Element	Wt. % for F15	Wt. % for W15	Wt. % for F5
Fe	66.30 ± 6.88	58.13 ± 6.63	49.58 ± 14.14
O	32.58 ± 6.00	27.37 ± 3.17	45.53 ± 13.06
C	ND	14.13 ± 4.51	ND
Si	0.80 ± 1.31	ND	4.39 ± 2.67
Other elements	1.12 ± 5.32	0.36 ± 3.10	66.30 ± 6.88

Apart from Fe rich and steel particles several other classes like carbonaceous particles were detected in all sample types. Particles assigned to the carbonaceous class were the third most abundant class after iron oxides and steel particles and were most noticeable in F5 samples, averaging at 23.62 ± 14.61 %. Since C was not measured in filter samples (F15 & F5) the classification was based on the assumption, that particles featuring O contents of > 75 wt.% and in whose spectra no other elements were present, have to contain large amounts of C, in order to be solid enough to withstand the electron beam. However, this classification is only an assumption and only W15 samples measured the C content of particles, allowing a more distinct analysis of this class. Carbonaceous particles can be linked to outside traffic sources, however, only minor amounts of soot chains, which act as typical markers for incomplete combustion processes, were observed.

Carbonaceous particles were mainly found in the submicron size range with an average D_A of 385 ± 136 nm, but also to some degree in the size range of 1388 ± 804 nm (W15) to 1641 ± 354 nm (F15). These particles were most likely formed from abrasion of the brake matrix, since their morphological characteristics matched those of brake wear and an average Fe content of 7.53 ± 5.21 wt.% and 0.27 ± 0.51 wt.% of Cu. Carbonaceous particles also showed a large temporal variance, with abundances of samples from the three analyzed days ranging from 10.31 to 43.97 % in F5 samples. While iron oxide and carbonaceous particle classes suggested a high contribution of brake wear to the PM, particles with distinct chemical profiles that could be directly associated to brake wear

were comparably low. Only 0.05 ± 0.01 % (F15) and 0.09 ± 0.05 % (W15) of particles were associated to the two brake wear subclasses $BaSO_4$ and SbS_3, with F5 samples showing no brake wear particles. However, the analysis of brake wear from the custom-built brake dynamometer also rarely showed particles containing these additives and instead contained large amounts of particles fitting the iron oxide class. Unfortunately, the chemical compositions of iron oxides were to generic to allow a more detailed allocation of particle sources. The complete absence of the brake wear class in F5 samples was attributed to the insufficient EHT of 5 kV, which is not able to quantitatively excite the Lα line of Ba, while the M-line normally observable at 5 kV overlapped with the L-Lines of Fe, which was ubiquitous in the samples.

Aside from Fe, other heavy metals indicated by the non-Fe oxides and non-Fe metals classes were distributed primarily in the submicron size range. Non-ferrous oxides were present at concentrations of 0.25 ± 0.15 % (F15), 2.00 ± 1.44 % (F5), and 0.09 ± 0.03 % (W15), while non-ferrous metals were found at 0.10 ± 0.01 % (F15), 0.14 ± 0.07 % (F5) and 0.90 ± 0.30 % (W15). Most heavy metal bearing particles were found to consist of Cu and are normally attributed to sparking at the catenary-pantograph interface in the subway context [24]. The trains in the Munich subway are, however, connected to the power conducting third-rail through steel current collectors [110], eliminating Cu catenaries as possible source of such particles. F5 samples, which contained the most Cu, showed significantly higher levels of Cu metal and oxide particles on one day (19/7/2022) with Cu oxides reaching a level of 4.04 % in the F5 sample, indicating a strong temporal variance of these particles. A SEM/EDX mapping of particles from a F15 sample is given in Figure 5-11, showing the distribution of elements.

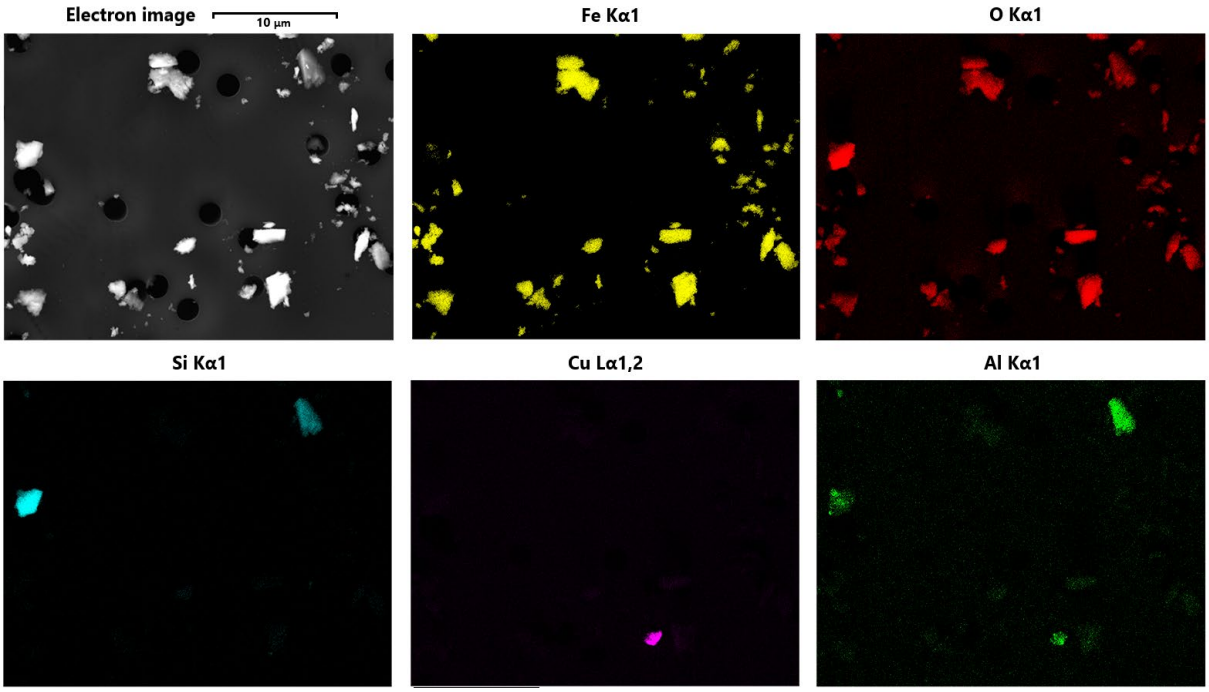

Figure 5-11: SEM/EDX mapping of subway particles on a F15 sample measured at 15 kV. Modified with permission from Neukirchen et al. [65]

Overall Cu concentrations in the Cu oxide and Cu metal subclasses ranged from 5 – 99 %, with average concentrations between 22.12 and 36.83 % of Cu for the three sample types. While the general amount of Cu rich particles was comparably low, their high temporal variance is of importance, since inhalation of Cu particles is regarded as highly toxic [16]. Furthermore, Cu was distributed mainly among small particles and manual EDX analysis also confirmed its presence as nanoparticles, which can penetrate deeply into the lung [111]. Average elemental compositions of Cu rich particles are listed in Table 5-6 and a nanoparticle belonging to the Cu metal class is depicted in Figure 5-12.

Table 5-6: Elemental composition of Cu rich particles found in the Munich subway

Element	Filter 15 kV	Wafer 15 kV	Filter 5 kV
Cu	30.38 ± 28.02	36.83 ± 23.36	22.12 ± 17.84
O	29.05± 9.87	12.78 ± 9.25	51.78 ± 16.39
Fe	37.90 ± 23.79	14.92 ± 19.93	10.86 ± 13.23
C	ND	29.15 ± 13.3	ND
Si	1.12 ± 1.99	ND	14.39 ± 8.15
other Elements	2.68 ± 6.50	6.32 ± 16.34	0.85 ± 3.29

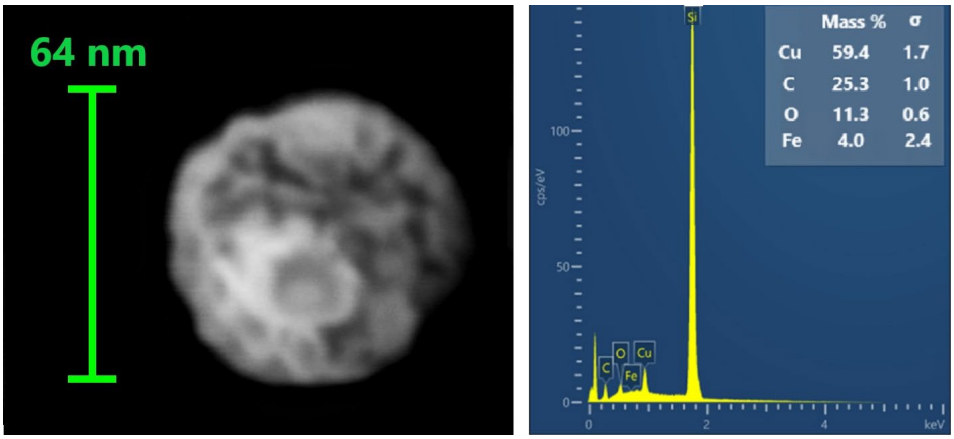

Figure 5-12: Cu nanoparticle found in wafer sample from 19/7/2022. Left: SEM micrograph Right: EDX spectrum. Modified with permission from Neukirchen et al. [65]

Non-anthropogenic sources of particles were also found in the subway, which were mainly of geological origin. Overall 0.57 ± 0.07 % (F15) and 1.99 ± 0.66 % (F5) of particles were assigned to silica, aluminosilicates and other various silicate types. The wafer classification scheme did not contain the silicate classes, since Si was excluded for measurements on Si wafers. Furthermore, salts and carbonates were detected at 0.69 ± 0.24 % (F15), 0.77 ± 0.66 % (F5) and 0.97 ± 0.47 % (W15), which were dominated by calcium carbonate. These soil derived particles were presumably brought into the subway system by commuters or were transported to the platforms via ventilation from the streets above. Classification results for all three sample types are depicted in Figure 5-13 showing the distribution of particle types in the Munich subway system.

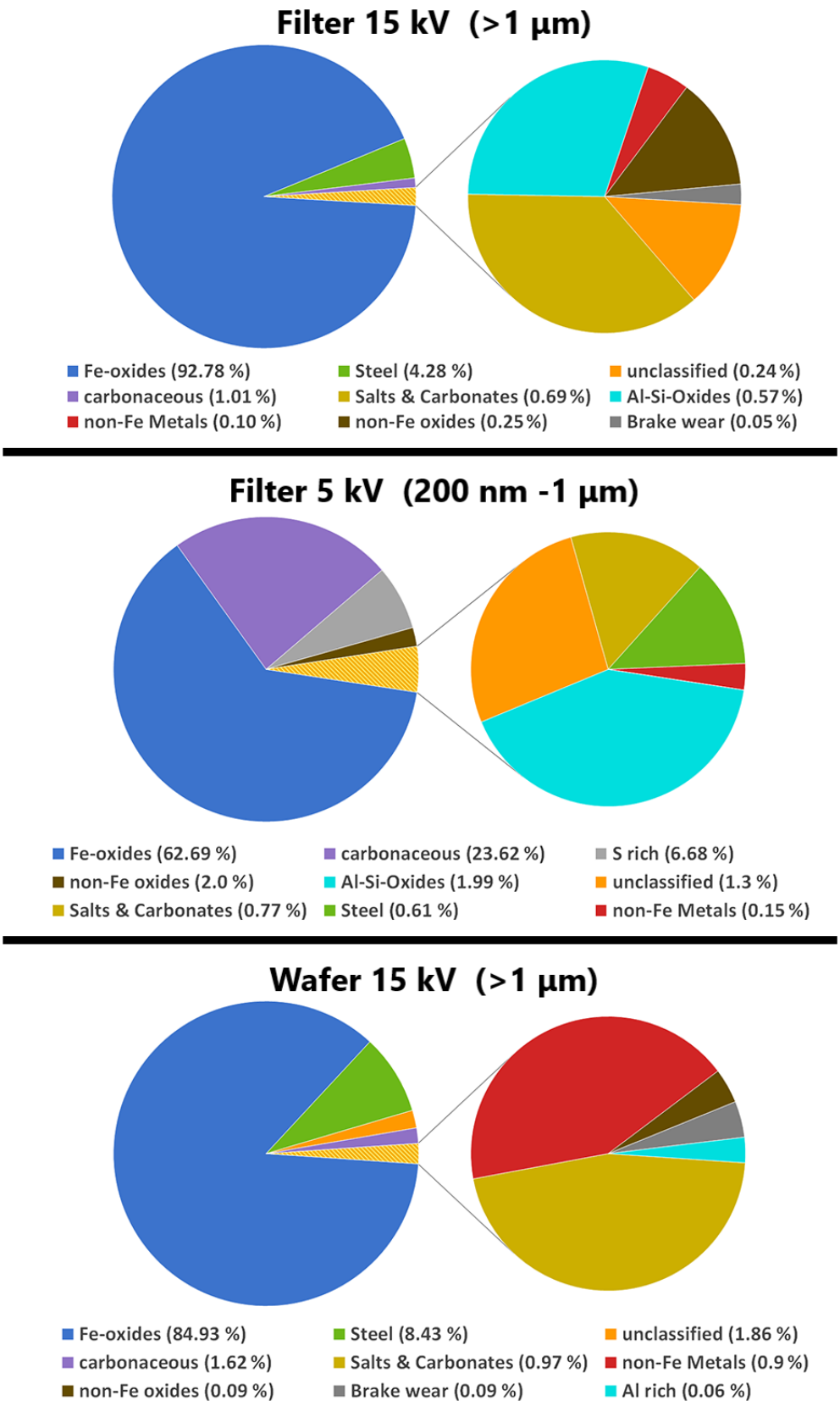

Figure 5-13: Automated SEM/EDX classification results for subway samples. Modified with permission from Neukirchen et al. [65]

6 Conclusion & Outlook

While NEES are of rapidly growing interest to researchers and regulatory authorities, their characterization still remains a challenging problem, mostly due to the lack of adequate and comparable sampling methodologies. Using a custom-built GTR 24 derived brake dynamometer, as well as an automated SEM/EDX imaging approach this thesis focused on the comprehensive elemental, physical and morphological characterization of metalliferous wear particles from automotive brakes under real world derived conditions and railways via mobile measurements in the Munich subway system. For this purpose, a variety of analytical methods was developed and tested regarding their applicability for the defined tasks.

The custom-built brake dynamometer showed emission factors, that were well comparable with the most recent ILS II and exceeded future maximum values at least twice. High contributions of wear from the brake disc were observed throughout samples and particles from both analyzed brake pad types showed similar characteristics. Almost all specifications of the GTR24 were implemented into the final dynamometer design, with deviations being only present in the shape and orientation of the brake enclosure.

Comprehensive air quality characterization in the Munich subway systems was achieved, using a mobile measurement system in combination with an automated SEM/EDX imaging algorithm and proved to be a fast and thorough way to determine the aerosol composition of certain micro-environments and to identify hotspots in specific systems. A high spatial variability in PM levels was observed in the Munich subway, while temporal differences were mainly caused by varying train frequencies. PM levels were up to 47 times higher than ambient reference measurements outside the subway, indicating a poor ventilation in the tunnels. The automated imaging algorithm yielded reliable classification of up to 99% of the over 200,000 analyzed particles, with up to 97 % of particles ≥1 µm and 63 % of particles ≤1 µm being classified as iron rich.

SEM analysis showed rough edged particles with large surface areas for both particle sources that often showed flake like (both sources) and elongated, splintery (subway), or spherical (brake wear) shapes. Even though larger particles > 1µm are normally attributed to abrasion derived processes, both sources displayed significant amounts of small particles, with average GMDs of brake wear found at 123 nm & 143 nm and subway emissions ranging between 200 – 300 nm. PM of both NEE sources was dominated by Fe, with average Fe concentrations in the $PM_{2.5}$ fraction of the brake pads of 54 % and 57 % and up to 69 % in subway samples. Other heavy metals, such as Cu, Zn, Sn and Cr were found for both brake and railway emissions and were present in all size ranges, even in nanoparticles.

While this thesis was able to give a comprehensive overview of the physical and morphological properties, as well as the elemental composition of metalliferous particles generated by automotive brakes and subways, many analytical challenges in the context of NEE still remain. Primarily the development of standardized sampling methodologies for other sources of NEE, like tire abrasion is of importance. For this purpose, the custom-built brake dynamometer, that was built as part of this thesis, was designed in a way to allow for an easy implementation of a tire module in the future, which will be the next step in the associated research project. Furthermore, the mobile measurement system with an automated SEM/EDX imaging approach can also be used to analyze the contribution of other NEE sources, such as road, brake and tire wear particles in other environments by further enhancing the methodology, e.g. retrofitting gas phase instrumentation into the mobile system and by establishing more classes for the automated assignment via the SEM/EDX imaging algorithm.

References

1. Grigoratos T, Martini G. Non-exhaust traffic related emissions - Brake and tyre wear PM: literature review. JRC Science and policy reports 2014. doi:10.2790/21481.
2. Sinclair Rosselot K. Copper Released from Brake Lining Wear in the San Francisco Bay Area. Process Profiles. 2006.
3. Haselden A, Christoforou C, Schlautman M. Characterization of airborne brake wear debris, final report. 2006.
4. Hulskotte JHJ, van der Gon HACD, Visschedijk AJH, Schaap M. Brake wear from vehicles as an important source of diffuse copper pollution. Water Sci Technol. 2007;56:223–31. doi:10.2166/wst.2007.456.
5. Lau WWY, Shiran Y, Bailey RM, Cook E, Stuchtey MR, Koskella J, et al. Evaluating scenarios toward zero plastic pollution. American Association for the Advancement of Science. 23.07.2020.
6. Wagner S, Hüffer T, Klöckner P, Wehrhahn M, Hofmann T, Reemtsma T. Tire wear particles in the aquatic environment - A review on generation, analysis, occurrence, fate and effects. Water Research. 2018;139:83–100. doi:10.1016/j.watres.2018.03.051.
7. Hua X, Wang D. Tire-rubber related pollutant 6-PPD quinone: A review of its transformation, environmental distribution, bioavailability, and toxicity. J Hazard Mater. 2023;459:132265. doi:10.1016/j.jhazmat.2023.132265.
8. Tian Z, Zhao H, Peter KT, Gonzalez M, Wetzel J, Wu C, et al. A ubiquitous tire rubber–derived chemical induces acute mortality in coho salmon. American Association for the Advancement of Science. 03.12.2020.
9. Walther E, Bogdan M. A novel approach for the modelling of air quality dynamics in underground railway stations. Transportation Research Part D: Transport and Environment. 2017;56:33–42. doi:10.1016/j.trd.2017.07.014.
10. Beck-Speier I, Kreyling WG, Maier KL, Dayal N, Schladweiler MC, Mayer P, et al. Soluble iron modulates iron oxide particle-induced inflammatory responses via prostaglandin E(2)synthesis: In vitro and in vivo studies. Part Fibre Toxicol. 2009;6:34. doi:10.1186/1743-8977-6-34.
11. Lay JC, Bennett WD, Ghio AJ, Bromberg PA, Costa DL, Kim CS, et al. Cellular and biochemical response of the human lung after intrapulmonary instillation of ferric oxide particles. Am J Respir Cell Mol Biol. 1999;20:631–42. doi:10.1165/ajrcmb.20.4.3355.
12. O'Day PA, Pattammattel A, Aronstein P, Leppert VJ, Forman HJ. Iron Speciation in Respirable Particulate Matter and Implications for Human Health. Environmental Science & Technology. 2022;56:7006–16. doi:10.1021/acs.est.1c06962.
13. Cooper RG. Zinc toxicology following particulate inhalation. Indian Journal of Occupational and Environmental Medicine. 2008;12:10–3. doi:10.4103/0019-5278.40809.
14. Hussain S, Khan M, Sheikh TMM, Mumtaz MZ, Chohan TA, Shamim S, Liu Y. Zinc Essentiality, Toxicity, and Its Bacterial Bioremediation: A Comprehensive Insight. Front Microbiol. 2022;13:900740. doi:10.3389/fmicb.2022.900740.
15. Gad SC. Acute and chronic systemic chromium toxicity. Science of The Total Environment. 1989;86:149–57. doi:10.1016/0048-9697(89)90201-5.

16. Hejazy M, Koohi MK, Bassiri Mohamad Pour A, Najafi D. Toxicity of manufactured copper nanoparticles - A review. Nanomedicine Research Journal. 2018;3:1–9. doi:10.22034/nmrj.2018.01.001.
17. Fussell JC, Franklin M, Green DC, Gustafsson M, Harrison RM, Hicks W, et al. A Review of Road Traffic-Derived Non-Exhaust Particles: Emissions, Physicochemical Characteristics, Health Risks, and Mitigation Measures. Environmental Science & Technology. 2022;56:6813–35. doi:10.1021/acs.est.2c01072.
18. Scerri MM, Weinbruch S, Delmaire G, Mercieca N, Nolle M, Prati P, Massabò D. Exhaust and non-exhaust contributions from road transport to PM10 at a Southern European traffic site. Environ Pollut. 2023;316:120569. doi:10.1016/j.envpol.2022.120569.
19. Grana M, Toschi N, Vicentini L, Pietroiusti A, Magrini A. Exposure to ultrafine particles in different transport modes in the city of Rome. Environ Pollut. 2017;228:201–10. doi:10.1016/j.envpol.2017.05.032.
20. Jung H-J, Kim B, Ryu J, Maskey S, Kim J-C, Sohn J, Ro C-U. Source identification of particulate matter collected at underground subway stations in Seoul, Korea using quantitative single-particle analysis. Atmospheric Environment. 2010;44:2287–93. doi:10.1016/j.atmosenv.2010.04.003.
21. Olofsson U, Olander L. On the identification of wear modes and transitions using airborne wear particles. Tribology International. 2013;59:104–13. doi:10.1016/j.triboint.2012.01.013.
22. Piscitello A, Bianco C, Casasso A, Sethi R. Non-exhaust traffic emissions: Sources, characterization, and mitigation measures. Sci Total Environ. 2021;766:144440. doi:10.1016/j.scitotenv.2020.144440.
23. Font O, Moreno T, Querol X, Martins V, Sánchez Rodas D, Miguel E de, Capdevila M. Origin and speciation of major and trace PM elements in the Barcelona subway system. Transportation Research Part D: Transport and Environment. 2019;72:17–35. doi:10.1016/j.trd.2019.03.007.
24. Zhou H, Duan F, Liu Z, Chen L, Song Y, Zhang Y. Study on electric spark discharge between pantograph and catenary in electrified railway. IET Electrical Syst in Trans. 2022;12:128–42. doi:10.1049/els2.12043.
25. macrovector / freepik. Free Vector | Isometric and colored city composition banner with tram station and big green button vector illustration. 04.10.2024. https://www.freepik.com/free-vector/isometric-colored-city-composition-banner-with-tram-station-big-green-button-vector-illustration_7199822.htm#fromView=search&page=1&position=23&uuid=397a8a45-d10c-41b0-954e-fc95b3daacbb. Accessed 4 Oct 2024.
26. Kukutschová J, Moravec P, Tomášek V, Matějka V, Smolík J, Schwarz J, et al. On airborne nano/micro-sized wear particles released from low-metallic automotive brakes. Environ Pollut. 2011;159:998–1006. doi:10.1016/j.envpol.2010.11.036.
27. Mathissen M, Scheer V, Vogt R, Benter T. Investigation on the potential generation of ultrafine particles from the tire–road interface. Atmospheric Environment. 2011;45:6172–9. doi:10.1016/j.atmosenv.2011.08.032.
28. Garg BD, Cadle SH, Mulawa PA, Groblicki PJ, Laroo C, Parr GA. Brake Wear Particulate Matter Emissions. Environmental Science & Technology. 2000;34:4463–9. doi:10.1021/es001108h.
29. International Council on clean transportation 2024. Euro 7: The new emission standard for light- and heavy-duty vehicles in the European Union;2024.

30. Morgan J, Bell R, Jones AL. Endogenous doesn't always mean innocuous: a scoping review of iron toxicity by inhalation. J Toxicol Environ Health B Crit Rev. 2020;23:107–36. doi:10.1080/10937404.2020.1731896.
31. Kanti Das T, Wati MR, Fatima-Shad K. Oxidative Stress Gated by Fenton and Haber Weiss Reactions and Its Association With Alzheimer's Disease. Arch Neurosci 2014. doi:10.5812/archneurosci.20078.
32. Bachler G, Losert S, Umehara Y, Goetz N von, Rodriguez-Lorenzo L, Petri-Fink A, et al. Translocation of gold nanoparticles across the lung epithelial tissue barrier: Combining in vitro and in silico methods to substitute in vivo experiments. Part Fibre Toxicol. 2015;12:18. doi:10.1186/s12989-015-0090-8.
33. Fortoul T, V. Rodríguez-Lara, A. González-Villalva, M. Rojas-Lemus, L. Colín-Barenque, P. Bizarro-Nevares, et al. Health Effects of Metals in Particulate Matter. 2015.
34. Hopkins LE, Laing EA, Peake JL, Uyeminami D, Mack SM, Li X, et al. Repeated Iron-Soot Exposure and Nose-to-brain Transport of Inhaled Ultrafine Particles. Toxicologic pathology. 2018;46:75–84. doi:10.1177/0192623317729222.
35. Pretorius E, Kell DB. Diagnostic morphology: biophysical indicators for iron-driven inflammatory diseases. Integr Biol (Camb). 2014;6:486–510. doi:10.1039/c4ib00025k.
36. Pretorius E, Bester J, Vermeulen N, Lipinski B, Gericke GS, Kell DB. Profound morphological changes in the erythrocytes and fibrin networks of patients with hemochromatosis or with hyperferritinemia, and their normalization by iron chelators and other agents. PLOS ONE. 2014;9:e85271. doi:10.1371/journal.pone.0085271.
37. Ghio AJ, Dailey LA, Richards JH, Jang M. Acid and organic aerosol coatings on magnetic nanoparticles increase iron concentrations in human airway epithelial cells. Inhalation Toxicology. 2009;21:659–67. doi:10.1080/08958370802406282.
38. Maher BA, González-Maciel A, Reynoso-Robles R, Torres-Jardón R, Calderón-Garcidueñas L. Iron-rich air pollution nanoparticles: An unrecognised environmental risk factor for myocardial mitochondrial dysfunction and cardiac oxidative stress. Environ Res. 2020;188:109816. doi:10.1016/j.envres.2020.109816.
39. Sobolewski M, Conrad K, Marvin E, Eckard M, Goeke CM, Merrill AK, et al. The potential involvement of inhaled iron (Fe) in the neurotoxic effects of ultrafine particulate matter air pollution exposure on brain development in mice. Part Fibre Toxicol. 2022;19:56. doi:10.1186/s12989-022-00496-5.
40. Stueckle TA, Davidson DC, Derk R, Kornberg TG, Schwegler-Berry D, Pirela SV, et al. Evaluation of tumorigenic potential of CeO2 and Fe2O3 engineered nanoparticles by a human cell in vitro screening model. NanoImpact. 2017;6:39–54. doi:10.1016/j.impact.2016.11.001.
41. Gasser M, Riediker M, Mueller L, Perrenoud A, Blank F, Gehr P, Rothen-Rutishauser B. Toxic effects of brake wear particles on epithelial lung cells in vitro. Part Fibre Toxicol. 2009;6:30. doi:10.1186/1743-8977-6-30.
42. European parliament. Euro 7: Deal on new EU rules to reduce road transport emissions Parlament; 27.08.2024.
43. Grigoratos T, Mathissen M, Vedula R, Mamakos A, Agudelo C, Gramstat S, Giechaskiel B. Interlaboratory Study on Brake Particle Emissions—Part I: Particulate Matter Mass Emissions. Atmosphere. 2023;14:498. doi:10.3390/atmos14030498.

44. Grigoratos T, Martini G. Brake wear particle emissions: a review. Environmental science and pollution research international. 2015;22:2491–504. doi:10.1007/s11356-014-3696-8.
45. Mathissen M, Grigoratos T, Lahde T, Vogt R. Brake Wear Particle Emissions of a Passenger Car Measured on a Chassis Dynamometer. Atmosphere. 2019;10:556. doi:10.3390/atmos10090556.
46. Mathissen M, Grigoratos T, Gramstat S, Mamakos A, Vedula R, Agudelo C, et al. Interlaboratory Study on Brake Particle Emissions Part II: Particle Number Emissions. Atmosphere. 2023;14:424. doi:10.3390/atmos14030424.
47. Thorpe A, Harrison RM. Sources and properties of non-exhaust particulate matter from road traffic: a review. Science of The Total Environment. 2008;400:270–82. doi:10.1016/j.scitotenv.2008.06.007.
48. Chan D, Stachowiak GW. Review of automotive brake friction materials. Proceedings of the Institution of Mechanical Engineers, Part D: Journal of Automobile Engineering. 2004;218:953–66. doi:10.1243/0954407041856773.
49. Woo S-H, Jang H, Na MY, Chang HJ, Lee S. Characterization of brake particles emitted from non-asbestos organic and low-metallic brake pads under normal and harsh braking conditions. Atmospheric Environment. 2022;278:119089. doi:10.1016/j.atmosenv.2022.119089.
50. EBC Brakes. Types Of Brake Pads – Which Is Best?; 22.04.2021.
51. US EPA. Copper-Free Brake Initiative | US EPA. 2015. https://www.epa.gov/npdes/copper-free-brake-initiative. Accessed 13 May 2024.
52. Neukirchen C, Saraji-Bozorgzad M, Mäder M, Mudan A, Czasch P, Becker J, et al. Comprehensive Elemental and Physical Characterization of Vehicle Brake Wear Emissions from Two Different Brake Pads Following the Global Technical Regulation Methodology.
53. Xu B, Hao J. Air quality inside subway metro indoor environment worldwide: A review. Environ Int. 2017;107:33–46. doi:10.1016/j.envint.2017.06.016.
54. Chang L, Chong WT, Wang X, Pei F, Zhang X, Wang T, et al. Recent progress in research on PM2.5 in subways. Environ Sci Process Impacts. 2021;23:642–63. doi:10.1039/d1em00002k.
55. Karlsson HL, Ljungman AG, Lindbom J, Möller L. Comparison of genotoxic and inflammatory effects of particles generated by wood combustion, a road simulator and collected from street and subway. Toxicology Letters. 2006;165:203–11. doi:10.1016/j.toxlet.2006.04.003.
56. Karlsson HL, Holgersson A, Möller L. Mechanisms related to the genotoxicity of particles in the subway and from other sources. Chemical Research in Toxicology. 2008;21:726–31. doi:10.1021/tx7003568.
57. Roy D, Lyou ES, Kim J, Lee TK, Park J. Commuters health risk associated with particulate matter exposures in subway system – Globally. Building and Environment. 2022;216:109036. doi:10.1016/j.buildenv.2022.109036.
58. Bachoual R, Boczkowski J, Goven D, Amara N, Tabet L, On D, et al. Biological Effects of Particles from the Paris Subway System. Chemical Research in Toxicology. 2007;20:1426–33. doi:10.1021/tx700093j.
59. Minguillón MC, Reche C, Martins V, Amato F, Miguel E de, Capdevila M, et al. Aerosol sources in subway environments. Environ Res. 2018;167:314–28. doi:10.1016/j.envres.2018.07.034.
60. Mugica-Álvarez V, Figueroa-Lara J, Romero-Romo M, Sepúlveda-Sánchez J, López-Moreno T. Concentrations and properties of airborne particles in the Mexico City subway system. Atmospheric Environment. 2012;49:284–93. doi:10.1016/j.atmosenv.2011.11.038.

61. Moreno T, Martins V, Querol X, Jones T, BéruBé K, Minguillón MC, et al. A new look at inhalable metalliferous airborne particles on rail subway platforms. Sci Total Environ. 2015;505:367–75. doi:10.1016/j.scitotenv.2014.10.013.
62. Martins V, Moreno T, Mendes L, Eleftheriadis K, Diapouli E, Alves CA, et al. Factors controlling air quality in different European subway systems. Environ Res. 2016;146:35–46. doi:10.1016/j.envres.2015.12.007.
63. Bendl J, Neukirchen C, Mudan A, Padoan S, Zimmermann R, Adam T. Personal measurements and sampling of particulate matter in a subway – Identification of hot-spots, spatio-temporal variability and sources of pollutants. Atmospheric Environment. 2023;308:119883. doi:10.1016/j.atmosenv.2023.119883.
64. Cartenì A, Cascetta F, Henke I, Molitierno C. The role of particle resuspension within PM concentrations in underground subway systems. Int. J. Environ. Sci. Technol. 2020;17:4075–94. doi:10.1007/s13762-020-02780-3.
65. Neukirchen C, Meiners T, Bendl J, Zimmermann R, Adam T. Automated SEM/EDX imaging for the in-depth characterization of non-exhaust traffic emissions from the Munich subway system. Sci Total Environ. 2024;915:170008. doi:10.1016/j.scitotenv.2024.170008.
66. Xu B, Yu X, Gu H, Miao B, Wang M, Huang H. Commuters' exposure to PM2.5 and CO2 in metro carriages of Shanghai metro system. Transportation Research Part D: Transport and Environment. 2016;47:162–70. doi:10.1016/j.trd.2016.05.001.
67. Querol X, Moreno T, Karanasiou A, Reche C, Alastuey A, Viana M, et al. Variability of levels and composition of PM_{10} and $PM_{2.5}$ in the Barcelona metro system. Atmos. Chem. Phys. 2012;12:5055–76. doi:10.5194/acp-12-5055-2012.
68. Yang F, Kaul D, Wong KC, Westerdahl D, Sun L, Ho K, et al. Heterogeneity of passenger exposure to air pollutants in public transport microenvironments. Atmospheric Environment. 2015;109:42–51. doi:10.1016/j.atmosenv.2015.03.009.
69. Shakya KM, Saad A, Aharonian A. Commuter exposure to particulate matter at underground subway stations in Philadelphia. Building and Environment. 2020;186:107322. doi:10.1016/j.buildenv.2020.107322.
70. Targino AC, Krecl P, Brimblecombe P, Oukawa GY, Danziger Filho JE, Moreno FL. Spatio-temporal variability of airborne particulate matter in the São Paulo subway. Building and Environment. 2021;189:107526. doi:10.1016/j.buildenv.2020.107526.
71. Reimer L. Scanning Electron Microscopy: Springer Berlin Heidelberg; 1998.
72. Nanoscience Instruments. Scanning Electron Microscopy | Nanoscience Instruments. 10.07.2024. https://www.nanoscience.com/techniques/scanning-electron-microscopy/. Accessed 21 Aug 2024.
73. Ul-Hamid A. A Beginners' Guide to Scanning Electron Microscopy: Springer; 2018.
74. Nobili F, Staffolani A. Methods, instruments and techniques | Structural analysis: Scanning electron microscopy. In: Reference Module in Chemistry, Molecular Sciences and Chemical Engineering: Elsevier; 2013. doi:10.1016/B978-0-323-96022-9.00212-7.
75. Williams DB, Carter CB. Transmission electron microscopy: A textbook for materials science C 2009. New York: Springer. doi:10.1007/978-0-387-76501-3.
76. Handbook of X-ray and Gamma-ray Astrophysics: Springer Nature Singapore; 2022.

77. Bertin EP. Principles and Practice of X-Ray Spectrometric Analysis. Boston, MA: Springer US; 1975.
78. Drouin D, Couture AR, Gauvin R. “Casino V2.0 : An Advance Simulation Tool for Scanning Electron Microscope Users”. Microsc Microanal. 2001;7:684–5. doi:10.1017/S1431927600029494.
79. Vacchi A. Silicon Drift Detectors. In: Handbook of X-ray and Gamma-ray Astrophysics: Springer Nature Singapore; 2022. p. 1–53. doi:10.1007/978-981-16-4544-0_18-1.
80. Fiorini C, Kemmer J, Lechner P, Kromer K, Rohde M, Schülein T. A new detection system for x-ray microanalysis based on a silicon drift detector with Peltier cooling. Rev. Sci. Instrum. 1997;68:2461–5. doi:10.1063/1.1148169.
81. Oxford Instruments. Silicon Drift Detectors Explained. OINA/SDDExplained/0212; 2012.
82. Ahmed S. Effect of light and temperature on the characteristics of PIN and SDD diode and their comparison using ATLAS/ Silvaco. Graduate Research Theses & Dissertations. 2015.
83. ThermoFisher Scientific. State-of-the-art EDS: An introduction to elemental analysis with ChemiSEM Technology. BR0116-EN-08-2021; 2012.
84. Oxford Instruments. What Dead Time you should choose for your EDS / EDX analysis? - Oxford Instruments. 18.08.2024. https://www.oxinst.com/blogs/what-dead-time-you-should-choose-for-your-eds-/-edx-analysis. Accessed 18 Aug 2024.
85. EDAX. Dead-Time Optimization for High Productivity Data Analysis.
86. Liao Y. Practical electron microscopy and database: An Online Book; 2006.
87. Statham PJ. Pile-Up Correction for Improved Accuracy and Speed of X-Ray Analysis. Microchim Acta. 2006;155:289–94. doi:10.1007/s00604-006-0558-1.
88. Gray AL. The ICP as an ion source—origins, achievements and prospects. Spectrochimica Acta Part B: Atomic Spectroscopy. 1985;40:1525–37. doi:10.1016/0584-8547(85)80176-2.
89. McCurdy E, Woods G. MS/MS Operation with ICP-QQQ: Redefining ICP-MS Reaction Mode Performance Since 2012. Agilent ICP-MS Journal. 2022, May, Issue 88. Agilent Technologies, Inc. 5994-4801EN.
90. Agilent Technologies. Octopole Collision/Reaction Cell and Helium mode. 5994-1172EN; 2020.
91. May TW, Wiedmeyer RH. A table of polyatomic interferences in ICP-MS. Atomic Spectroscopy 1998. doi:10.46770/AS.1998.05.002.
92. Agilent Technologies. Principles of ICP Tandem Mass Spectrometry (ICP-MS/MS). 5994-4929EN; 2022.
93. Netzplan U-Bahn München.svg – Wikipedia. 04.11.2023. https://de.m.wikipedia.org/wiki/Datei:Netzplan_U-Bahn_M%C3%BCnchen.svg. Accessed 4 Nov 2023.
94. U-Bahn München. U-Bahnhof Hauptbahnhof (U4, U5). 04.11.2023. https://www.u-bahn-muenchen.de/netz/bahnhoefe/ho/. Accessed 4 Nov 2023.
95. Dulude J. Selecting the Best ICP Sample Introduction System: MJH Life Sciences; 2008.
96. Perrenoud A, Gasser M, Rutishauser BR, Gehr P, Riediker M. Characterisation of nanoparticles resulting from different braking behaviours. IJBNN. 2010;1:17. doi:10.1504/IJBNN.2010.034123.

97. Wahlström J, Söderberg A, Olander L, Jansson A, Olofsson U. A pin-on-disc simulation of airborne wear particles from disc brakes. Wear. 2010;268:763–9. doi:10.1016/j.wear.2009.11.014.
98. Vasilatou K, Wälchli C, Koust S, Horender S, Iida K, Sakurai H, et al. Calibration of optical particle size spectrometers against a primary standard: Counting efficiency profile of the TSI Model 3330 OPS and Grimm 11-D monitor in the particle size range from 300 nm to 10 µm. Journal of Aerosol Science. 2021;157:105818. doi:10.1016/j.jaerosci.2021.105818.
99. Qi HS, Day AJ. Investigation of disc/pad interface temperatures in friction braking. Wear. 2007;262:505–13. doi:10.1016/j.wear.2006.08.027.
100. Giechaskiel B, Grigoratos T, Dilara P, Karageorgiou T, Ntziachristos L, Samaras Z. Light-Duty Vehicle Brake Emission Factors. Atmosphere. 2024;15:97. doi:10.3390/atmos15010097.
101. Limmer F, Brooks PC, Gilkeson C, Kosarieh S, Barton DC. Tribo-oxidation of a brake friction couple under varying sliding conditions. Tribology International. 2023;185:108536. doi:10.1016/j.triboint.2023.108536.
102. Karlsson HL, Gustafsson J, Cronholm P, Möller L. Size-dependent toxicity of metal oxide particles--a comparison between nano- and micrometer size. Toxicology Letters. 2009;188:112–8. doi:10.1016/j.toxlet.2009.03.014.
103. Sandahl JF, Baldwin DH, Jenkins JJ, Scholz NL. A sensory system at the interface between urban stormwater runoff and salmon survival. Environmental Science & Technology. 2007;41:2998–3004. doi:10.1021/es062287r.
104. Park SB, Cho KH, Jung S, Jang H. Tribological properties of brake friction materials with steel fibers. Met. Mater. Int. 2009;15:27–32. doi:10.1007/s12540-009-0027-6.
105. Neis PD, Ferreira NF, Fekete G, Matozo LT, Masotti D. Towards a better understanding of the structures existing on the surface of brake pads. Tribology International. 2017;105:135–47. doi:10.1016/j.triboint.2016.09.033.
106. Kim KI, Lee H, Kim J, Oh KH, Kim KT. Wear Behavior of Commercial Copper-Based Aircraft Brake Pads Fabricated under Different SPS Conditions. Crystals. 2021;11:1298. doi:10.3390/cryst11111298.
107. Wahlström J, Olander L, Olofsson U. Size, Shape, and Elemental Composition of Airborne Wear Particles from Disc Brake Materials. Tribol Lett. 2010;38:15–24. doi:10.1007/s11249-009-9564-x.
108. Babu P, Khare M, Goyal R. Chemical Characterization of Airborne Particles Collected in an Underground Metro Station Platform in Delhi City. AJS. 2015;3:45–54. doi:10.30958/ajs.3-1-4.
109. Kim C-H, Yoo D-C, Kwon Y-M, Han W-S, Kim G-S, Park M-J, et al. A study on characteristics of atmospheric heavy metals in subway station. Toxicol Res. 2010;26:157–62. doi:10.5487/TR.2010.26.2.157.
110. U-Bahn München. Stromversorgung. 19.09.2023. https://www.u-bahn-muenchen.de/betrieb/stromversorgung/. Accessed 19 Sep 2023.
111. Costa A, Pinheiro M, Magalhães J, Ribeiro R, Seabra V, Reis S, Sarmento B. The formulation of nanomedicines for treating tuberculosis. Adv Drug Deliv Rev. 2016;102:102–15. doi:10.1016/j.addr.2016.04.012.

List of Figures and Tables

Figures

Tables

Contribution to scientific publications

First Authorships

The following manuscripts were contributed by Carsten Neukirchen as the first author and published in peer-reviewed journals. Carsten Neukirchen's contribution is declared below.

Title: Automated SEM/EDX imaging for the in-depth characterization of non-exhaust traffic emissions from the Munich subway system

Authors: Neukirchen, C.; Meiners, T.; Bendl, J.; Zimmermann, R.; Adam, T.

Journal: Science of The Total Environment

Year: 2023

DOI: https://doi.org/10.1016/j.scitotenv.2024.170008

Carsten Neukirchen conceived and designed the majority of the study, created the criteria for the automated imaging algorithm, performed a large part of the experiments, processed and evaluated the data, and wrote the majority of the manuscript.

Submitted:

Title: Comprehensive elemental and physical characterization of vehicle brake wear emissions from two different brake pads following the Global Technical Regulation methodology

Authors: Neukirchen, C.; Saraji-Bozorgzad, M.; Mäder, M.; Mudan, A.; Czasch, P.; Becker, J.; Di Bucchianico, S.; Trapp, C.; Zimmermann, R.; Adam, T.

Journal: Journal of Hazardous Materials

Year: 2025

DOI: https://doi.org/10.1016/j.jhazmat.2024.136609

Carsten Neukirchen conceived and designed the majority of the study, helped in designing and building the brake dynamometer, developed and applied the analytical techniques, processed and evaluated their data, and wrote the majority of the manuscript.

Co-authorships:

Title: Personal measurements and sampling of particulate matter in a subway – Identification of hot-spots, spatio-temporal variability and sources of pollutants

Authors: Bendl, J.; Neukirchen, C.; Mudan, A.; Padoan, S.; Zimmermann, R.; Adam, T.

Journal: Atmospheric Environment

Year: 2023

DOI: https://doi.org/10.1016/j.atmosenv.2023.119883

Carsten Neukirchen performed and evaluated the SEM/EDX experiments, revised and wrote parts of the manuscript and participated in the literature review.

Title: Trace Elements in PM2.5 Shed Light Over Saharan Dust Incursions Over Munich Airshed in Spring 2022

Authors: Padoan, S.; Zappi, A.; Bendl, J.; Herrmann, T.; Mudan, A.; Neukirchen, C.; Brattich, E.; Tositti, L; Adam, T.

Journal: Environmental Science: Atmospheres

Year: 2024

DOI: https://doi.org/10.1039/D4EA00092G

Carsten Neukirchen performed and evaluated the SEM/EDX experiments and revised and wrote minor parts of the manuscript.

Title: Detailed Gaseous and Particulate Emissions of an Allison 250-C20B Turboshaft Engine

Authors: Rohkamp, M.; Rabl, A.; Gündling, B.; Saraji-Bozorgzad, M.; Mull, C.; Bendl, J.; Neukirchen, C.; Helcig, C.; Adam, T.; Gümmer, V.; Hupfer, A.

Journal: Journal of Engineering for Gas Turbines and Power

Year: 2023

DOI: https://doi.org/10.1115/1.4063693

Carsten Neukirchen performed and evaluated the SEM analysis, revised and wrote minor parts of the manuscript.

Title: Gaseous and Particulate Matter (PM) Emissions from a Turboshaft-Engine using different Blends of Sustainable Aviation Fuel (SAF)

Authors: Rohkamp, M.; Rabl, A.; Neukirchen, C.; Bendl, J.; Saraji-Bozorgzad, M.; Helcig, C.; Adam, T.; Hupfer, A.

Journal: submitted to Aerosol Science & Technology

Year: submitted on 22.08.2024

DOI: TBD

Carsten Neukirchen performed and evaluated supporting SEM analysis and revised parts of the manuscript.

Title: Red and green laser powder bed fusion of pure copper in combination with chemical post-processing for RF cavity fabrication

Authors: Mayerhofer, M.; Brenner, S.; Dickmann, M.; Doppler, M.; Gruber, S.; Helm, R.; Lopez, E.; Maier, V.; Mitteneder, J.; Neukirchen, C.; Nedeljkovic-Groha, V.; Reinarz, B.; Schuch, M.; Stepien, L.; Dollinger, G.

Journal: Instruments

Year: 2024

DOI: https://doi.org/10.3390/instruments8030039

Carsten Neukirchen performed and evaluated the SEM/EDX experiments, conducted parts of the literature research and revised the chapter about chemical impurities in the manuscript

List of related Publications and Data

Publication 1

Automated SEM/EDX imaging for the in-depth characterization of non-exhaust traffic emissions from the Munich subway system

Neukirchen, C.; Meiners, T.; Bendl, J.; Zimmermann, R.; Adam, T.

Sci. Total Environ. (2023). https://doi.org/10.1016/j.scitotenv.2024.170008

Supplementary Information Publication 1

Publication 2

Comprehensive elemental and physical characterization of vehicle brake wear emissions from two different brake pads following the Global Technical Regulation methodology

Neukirchen, C.; Saraji-Bozorgzad, M.; Mäder, M.; Mudan, A.; Czasch, P.; Becker, J.; Di Bucchianico, S.; Trapp, C.; Zimmermann, R.; Adam, T.

Journal of Hazardous Materials (2025) https://doi.org/10.1016/j.jhazmat.2024.136609

Supplementary Information Publication 2

Publication 3

Personal measurements and sampling of particulate matter in a subway – Identification of hot-spots, spatio-temporal variability and sources of pollutants

Bendl, J.; Neukirchen, C.; Mudan, A.; Padoan, S.; Zimmermann, R.; Adam, T.

Atmos. Environ. (2023). https://doi.org/10.1016/j.atmosenv.2023.119883

Supplementary Information Publication 3

Publication 1

Science of the Total Environment 915 (2024) 170008

Contents lists available at ScienceDirect

Science of the Total Environment

journal homepage: www.elsevier.com/locate/scitotenv

Automated SEM/EDX imaging for the in-depth characterization of non-exhaust traffic emissions from the Munich subway system

Carsten Neukirchen [a,d], Thorsten Meiners [b], Jan Bendl [a,e,*], Ralf Zimmermann [c,d], Thomas Adam [a,c]

[a] University of the Bundeswehr Munich, Faculty for Mechanical Engineering, Institute of Chemical and Environmental Engineering, Werner-Heisenberg-Weg 39, 85577 Neubiberg, Germany
[b] Oxford Instruments GmbH, Borsigstraße 15 A, 652025 Wiesbaden, Germany
[c] Joint Mass Spectrometry Center (JMSC) at Comprehensive Molecular Analytics (CMA), Department Environmental Health, Helmholtz Munich, Gmunder Str. 37, 81379 München, Germany
[d] Joint Mass Spectrometry Center (JMSC) at Chair of Analytical Chemistry, Institute of Chemistry, University of Rostock, Albert-Einstein-Strasse 27, 18059 Rostock, Germany
[e] Institute for Environmental Studies, Faculty of Science, Charles University, Benátská 2, 128 01 Prague, Czech Republic

HIGHLIGHTS

- Majority of particles formed from abrasion of brakes, rails and wheels.
- 94–97 % of ≥1 μm and 63 % of particles ≤1 μm classified as highly ferruginous.
- Heavy metal particles found also in the ultrafine size range.
- Particle number mode detected between 200 and 300 nm.
- The utilized method classifies up to 99 % of over 200,000 particles.

GRAPHICAL ABSTRACT

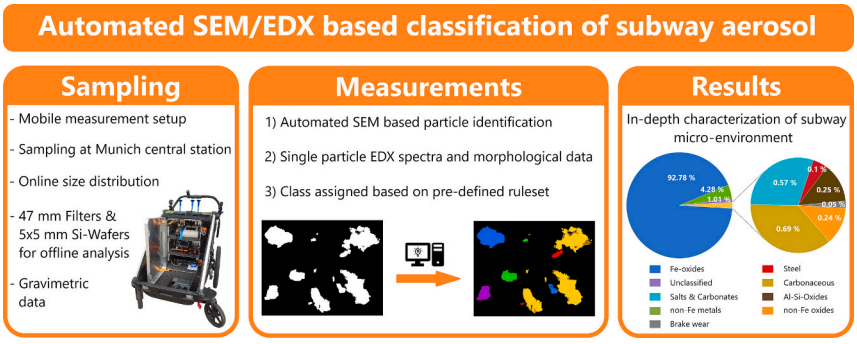

ARTICLE INFO

Editor: Hai Guo

Keywords:
Automated particle classification
Train emissions
Personal exposure

ABSTRACT

A SEM/EDX based automated measurement and classification algorithm was tested as a method for the in-depth analysis of micro-environments in the Munich subway using a custom build mobile measurements system. Sampling was conducted at platform stations, to investigate the personal exposure of commuters to subway particulate matter during platform stays. EDX spectra and morphological features of all analyzed particles were automatically obtained and particles were automatically classified based on pre-defined chemical and morphological boundaries. Source apportionment for individual particles, such as abrasion processes at the

Abbreviations: AR, Aspect ratio; BSE, Backscattered electrons; EAD, Equivalent aerodynamical diameter; ECD, Equivalent circular diameter; EPD, Equivalent perimeter diameter; EDX, Energy-dispersive X-ray spectroscopy; EHT, Electron high tension; FePM, Iron rich particulate matter; ICP-MS, Inductively coupled plasma mass spectrometry; NEE, Non-exhaust emissions; NP, Nanoparticle; OPS, Optical particle sizer; PC, Polycarbonate; PM, Particulate matter; PNC, Particle number concentration; ROS, Reactive oxygen species; SEM, Scanning electron microscopy; SI, Supplementary information.

* Corresponding author at: University of the Bundeswehr Munich, Faculty for Mechanical Engineering, Institute of Chemical and Environmental Engineering, Werner-Heisenberg-Weg 39, 85577 Neubiberg, Germany.
E-mail address: jan.bendl@unibw.de (J. Bendl).

https://doi.org/10.1016/j.scitotenv.2024.170008
Received 19 November 2023; Received in revised form 27 December 2023; Accepted 6 January 2024
Available online 12 January 2024

Elemental composition
Algorithm-based particle classification
Scanning electron microscopy

wheel-brake interface, was partially possible based on the established particle classes. An average of 98.87 ± 1.06 % of over 200,000 analyzed particles were automatically assigned to the pre-defined classes, with 84.68 ± 16.45 % of particles classified as highly ferruginous. Manual EDX analysis further revealed, that heavy metal rich particles were also present in the ultrafine size range well below 100 nm.

1. Introduction

Exhaust particle emissions have long been known to be harmful and to cause diseases, such as inflammatory lung diseases and lung cancer (Ghio et al., 2012; Totlandsdal et al., 2010). With modern day regulations becoming stricter, exhaust emissions have declined throughout the last decades reaching a point where automotive non-exhaust emissions (NEE), such as brake and tyre abrasion, have surpassed engine exhaust emissions as largest traffic derived contributors to urban PM_{10} pollution (Grigoratos and Martini, 2014). Some NEE's like automotive brake and tyre particles, which will be included for the first time in the upcoming EURO 7 norm, are currently undergoing legislatory processes (Storch et al., 2023), however, most of them are still unregulated. Nonetheless NEE's are of rapidly growing interest for researchers worldwide, which is due to their potential as environmental pollutants and hazardous substances. NEE's are mainly abrasion derived particles, formed from braking processes or friction between wheels and roads/rails. While tyre abrasion particles contribute greatly to the microplastic problem (Knight et al., 2020), other NEE's released from brake pads and train steel wheels and rails consist mainly of heavy metals (Font et al., 2019; Grigoratos and Martini, 2015). Particles bearing high quantities of heavy metals are known to induce chronic respiratory diseases and to facilitate lung cancer via the formation of reactive oxygen species (ROS) through the Fenton reaction causing DNA damage in the respiratory tract (Kanti Das et al., 2014). Small particles are of special concern with $PM_{2.5}$ being able to penetrate deep into the lungs and particles smaller than 0.1 μm depositing in the alveoli, eventually reaching the bloodstream via the blood-air barrier (Bachler et al., 2015). Furthermore metal containing nanoparticles (NP) were found to penetrate to the central nervous system via uptake and transport in the olfactory nerve via the nasal route (Hopkins et al., 2018; T. Fortoul et al., 2015) causing pro-inflammatory responses (Trickler et al., 2014) as well as apoptosis due to increased cytotoxicity of heavy metals (Niska et al., 2015).

While most techniques for elemental analysis, such as conventional ICP-MS, are capable of measuring trace quantities of elements in whole samples, they cannot distinguish, whether a certain element is distributed homogenously among all particles or if high quantities are present in a small number of particles. While recently more specialized techniques, such as single particle ICP-MS with time-of-flight based detection for chemical characterization of particles arise, they are still limited regarding their measurable size range (Laborda et al., 2014) and are generally more applicable to the analysis of aqueous and powder samples, instead of aerosols, which are normally sampled on filters. In contrast, EDX analysis provides spectra for thousands of individual particles regardless of their source, thus offering the possibility of addressing the homogeneity of complex environmental samples. This benefit is of special interest for the characterization of subway aerosols, where highly redox active, copper-rich particles derived from sparking at the catenary-pantograph-interface (Font et al., 2019) as well as abrasion derived metallic and oxidic iron particles frequently occur (Bendl et al., 2023; Font et al., 2019). Especially copper NP quantities are critical in closed, poorly ventilated environments like subways, given that they are considered to be among the most toxic particles in mammals (Hejazy et al., 2018). In addition to their size and the chemical composition, form factors play an important role in particle toxicity. While the health impact of inhalable iron oxide particles is commonly regarded as low, subway emissions have been shown to be of increased cytotoxicity (Jung et al., 2012; Loxham and Nieuwenhuijsen, 2019) linked to the large surface area of abrasion derived particles, which often exhibit rough and splintery edges (Moreno et al., 2015).

Automated Imaging software offers a powerful solution for the characterization of large amounts of individual features rendering them an ideal tool for morphology-based particle characterization with the SEM. If a particle is identified, its morphological data is automatically measured and a subsequent EDX measurement is triggered by the software supplying additional chemical data used for classification. A set of classification boundaries is then applied to the dataset sorting the analyzed features into pre-defined categories. Parameters utilized for classification can either be directly measured geometrical values, such as the length (also known as maximum feret diameter) and the perimeter of a particle, or calculated values like the equivalent circular diameter (ECD) and the aspect ratio as well as the elemental composition. This approach can be utilized to accomplish a variety of objectives, such as analyzing the homogeneity of particles, or solving so called "needle in a haystack" problems, where small quantities of particles of interest (e.g. copper particles from sparking at the catenary/ third-rail type power supply) are scattered among a large number of other particles. Furthermore, the Imaging Software ZEN core (Carl Zeiss) was used to obtain high-resolution morphological data for the bulk of the particles.

The aim of this study was to demonstrate a new approach in detailed elemental analysis of particles using automated SEM/EDX, which allows almost all particles captured on the filter to be analyzed separately for their elemental composition and morphology, and to be classified based on the data obtained. This approach could have wide applications in aerosol research and air quality measurement. We have demonstrated this method in the context of mobile air quality measurements in the Munich subway (Bendl et al., 2023), assessing the personal exposure of commuters to harmful compounds such as heavy metals at the subway platform. To the best of our knowledge, there is no published study on individual particle compositions in subway systems worldwide with a data-set of comparable size with over 200,000 particles automatically analyzed and classified yielding detailed results with a statistically relevant sample size.

2. Methods and materials

2.1. Sampling and studied location

All samples were collected in the Munich subway (Germany) in the middle of the platform of the central station, called "Hauptbahnhof" (line U4/U5), at exactly the same spot. As a housing for all the instruments, a self-made mobile measuring system consisting of an aluminum ventilated box with omni-directional inlets (801565, TSI), located in the breathing zone height of a seated person was used (Bendl et al., 2023). The platform is located below ground in a depth of - 22 m (DB Netz AG, 2023). A map of the Munich subway system with a photo of the sampling site highlighted in the map, as well as the mobile measurement device used in this study are shown in Fig. 1.

Sample 1 was collected on 17/5/2022 (14:08–17:08) using a pump with a constant flowrate of 8.5 lpm (SG10-2, GSA) and a $PM_{2.5}$ pre-impactor (Sioutas, SKC; $PM_{2.5}$ fraction). Sample 2 was collected using the same set-up on 19/7/2022 (20:33–23:21), but without the pre-impactor (PM_{total} fraction). Sample 3 was collected on 28/8/2023 (14:06–20:06) without any pre-impactor (PM_{total} fraction) over a longer period of time, therefore, a sampler with a lower flow rate of 2 lpm was used (BiVOC2V2, Holbach) to make sure that filters were not overloaded. The method can operate in a wide range of particle concentrations, as long as there are enough particles on a filter to be statistically

representative and individual particles are present, which do not overlap due to overloading.

Particles were sampled on 47 mm polycarbonate (PC) track-etched filters (Whatman, Nuclepore, 2 μm pore-size), with five silica wafers (p-type boron dotted 5 × 5 mm, Ted Pella Inc.) placed on-top of each filter, situated in vertically positioned filter-holders so that wafers were at fixed positions over the whole sampling time.

To prevent contaminations, sampling for gravimetric analysis was performed using an additional identical pump (SG10-2, GSA), 47 mm filter holder, and a PC filter, which was weighed prior and after sampling using a micro-balance (Cubis MCA2.7S-2S00-F, Sartorius) and pre-conditioned (45 % RH, 22 °C) for 24 h in a weighing chamber (pureGMC 18-EPA1065) with a corona discharger for filter charge neutralization (Bendl et al., 2023).

All flowrates of the pumps were set/checked using a mass flow meter (4043H, TSI).

2.2. Online particle measurements

During the sampling period, the PM size-distribution in the range of 0.3–10 μm was measured with a resolution of 1 Hz via an Optical Particle Sizer (OPS 3330, TSI). On-line data was corrected based on gravimetry with a factor of 2.11 (Bendl et al., 2023). Particle number concentrations (PNC) in the range of 10–700 nm were measured in 1 Hz using a DISCmini from Testo.

2.3. Sample preparation

Samples with a diameter of 12 mm were cut from each filter and were transferred to SEM pin stubs with conductive high purity EDX suitable double-sided carbon adhesive pads in-between (Spectro-Tabs, Plano GmbH company). Silica wafers were secured to SEM pin stubs with conductive silver paint (EM-Tec AG15, Micro to Nano). Wafers and filter punches were then stored in a desiccator under vacuum for 24 h to ensure removal of volatile components that would otherwise contaminate the system. The wafer surface was left unaltered, while filter samples were coated with a conductive carbon layer of approximately 10 nm, to minimize charging effects during analysis. Surface coating was applied with a Q150T ES Plus sputter device (Quorum technologies) utilizing a woven carbon fiber string (density 1.55 g/m, Quorum technologies) in pulsed cord evaporation mode.

2.4. SEM/EDX analysis

SEM micrographs were taken with the Inlens and SE2 detectors of a Gemini Sem 360 (Carl Zeiss) field emission SEM at acceleration voltages of 0.75–1.5 kV. Manual EDX analysis was conducted with an UltimMax 40 EDX detector (Oxford Instruments). Additionally, samples were measured via the manufacturers Software ZEN core EM 3.5 to obtain high resolution morphological data for the calculation of size and shape descriptors. Particles were imaged with a 5 nm pixel size with a minimum particle length of 100 nm and a minimum breath of 50 nm.

Automated SEM/EDX measurements were conducted with a Zeiss Gemini 450 SEM equipped with an UltimMax 170 EDX detector and an UltimExtreme windowless EDX detector from Oxford Instruments. The UltimMax 170 is an ultra large area Silicon Drift Detector (170 mm^2 detection area) equipped with a thin polymer window allowing high count rates and, therefore, short acquisition times. The UltimExtreme is a 100 mm^2 windowless detector with an optimized geometry and electron trap allowing to reach very small detector to sample distances and thus large solid angles. It is optimized for low kV analysis and reaches high count rates compared to conventional detectors, even with low beam currents. The Software AZtec Feature (Version 6.0) was used for automated detection of particles based on their mean gray value measured with a backscatter electron detector (BSE). The electron yield of a common BSE detector strongly depends on the mean atomic number of the analyzed material (Čalkovský et al., 2023). In this way, particles can be easily separated from the substrate (in this work carbon adhesive pads and Si wafer) by gray values of the BSE detector, if particles are heavier or lighter than the substrate. The automated particle analysis was carried out at 15 kV for all samples as well as at 5 kV for the carbon pad samples in order to reduce the interaction volume of the incoming

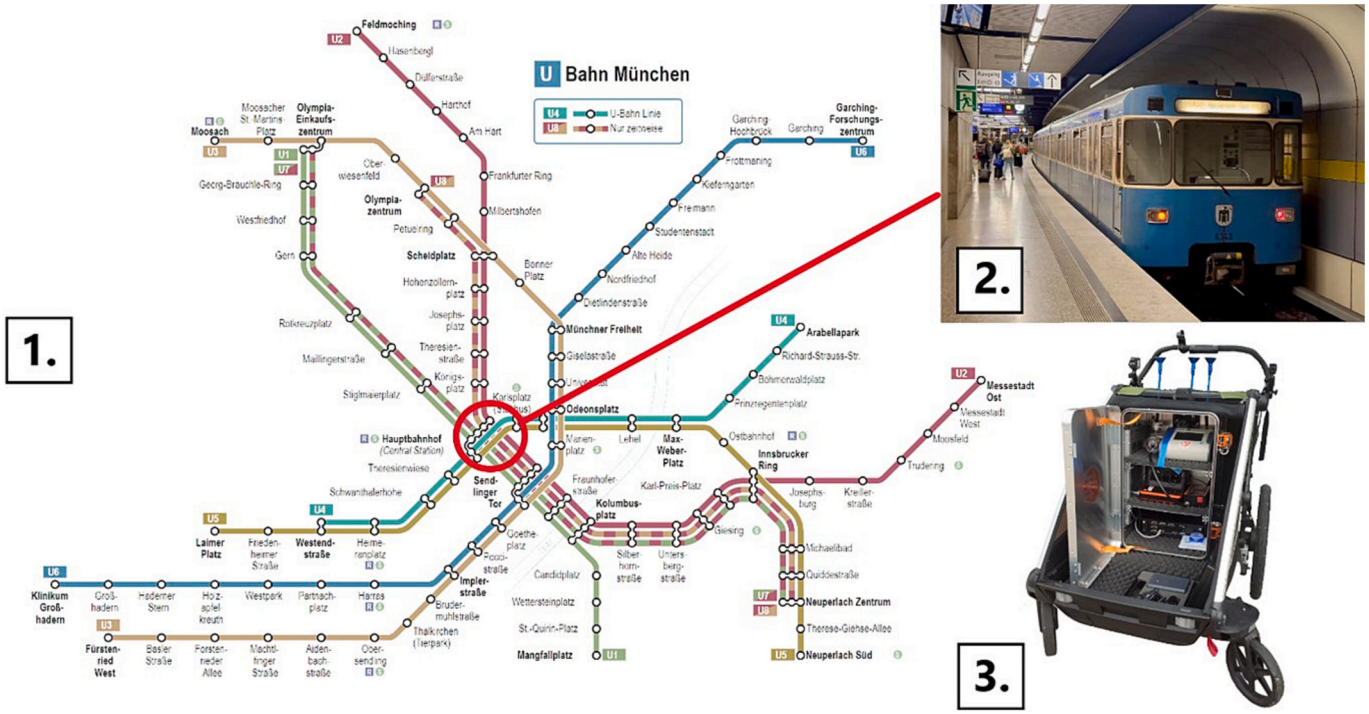

Fig. 1. Studied area and mobile measurement system. 1. Map of the Munich subway system (Wikipedia, 2023) 2. Platform of U4/U5 at the Munich central station (U-Bahn München, 2023b) 3. Mobile measurement system used in this study.

electrons to optimize the analysis for particles sizes well below 1 μm. At 15 kV the UltimMax 170 and at 5 kV the UltimExtreme was used to collect the X-Ray data. Measurements with 15 kV were conducted with a 2 nA beam current. Image acquisition settings were chosen so that 1 μm sized particles are described by at least 5 pixels. The smallest particles measured are 770 nm in diameter (ECD), which corresponds to 3 pixels in the image. EDX Spectra were acquired for 0.3 s per particle, which results in approximately 40.000 counts. Measurements with 5 kV were also conducted with a 2 nA beam current. Image acquisition settings were chosen so that 200 nm sized particles, which is also the smallest particle size that was measured, are described by at least 5 pixels. The EDX spectra were acquired for 2 s per particle, which results in approximately 200,000 counts. The longer acquisition was chosen to measure a significant number of X-rays coming from the small particles. The overlap in particle counts from 770 nm to 1 μm for filter measurements at 15 kV and 5 kV was manually deleted from the 15 kV dataset to avoid double counting of particles. The overlapping size region was measured intentionally for normalization between the rates of automated particle recognition, later used for compiling size distributions.

The classification scheme was built and developed based on a modified version of the technical cleanliness scheme provided by Oxford Instruments GmbH. To address the differences between carbon coated particles on filters and particles on silica wafers, as well as differences due to particle sizes, three different versions of the scheme were developed. Table S3 and Table S4 in the supplementary information (SI) list the boundaries and rulesets for each class of the three schemes. Classes were established based on a thorough scan of literature, to represent the particle types that can be expected in the subway environment, such as iron oxides and copper particles. Several classes like the critical fibers class, which scans for asbestos like fibers and the geological origin class scanning for silicates, salts and carbonates, were also established since these classes are of general interest to public health or offer insight into the interaction between the outside world and the subway environment. In total 10 main classes were defined during this stage, which were later divided into 31 subclasses, to allow for a more accurate distinction. For example, the brake wear class was subdivided into the two classes barium sulfate ($BaSO_4$) and antimony trisulphide (SbS_3), since these are common additives used in the manufacturing of brake pads (Grigoratos and Martini, 2015). Finally, three rejection classes were integrated into the scheme to discard particles larger than the investigated size range of a sample (only 5 kV measurements on filters) and artifacts caused from sample preparation, such as scratches in the wafer structure and particles from the conductive silver paint (only wafer measurements).

Morphological descriptors such as the particles maximum (X_{Fmax}) and minimum (X_{Fmin}) feret diameter, area A, perimeter p and dynamic shape factor x were directly obtained from the ZEN core and AZtec Features Software, while other parameters, such as the equivalent perimeter diameter (EPD), aspect ratio (AR), extent bulkiness, compactness, circularity, roundness and solidity were calculated based on Eqs. (1) to (8) from the ISO 21363:2020. These values can be used to address a particles shape, giving a numeric value that can be directly compared to other particles.

$$ECD = \sqrt{\frac{4\,A}{\pi}} \tag{1}$$

$$EPD = \frac{p}{\pi} \tag{2}$$

$$AR = \frac{x_{Fmin}}{x_{Fmax}} \tag{3}$$

$$extent\ bulkiness = \frac{A}{x_{Fmin}\ x_{Fmax}} \tag{4}$$

$$compactness = \frac{\sqrt{\frac{4\,A}{\pi}}}{x_{Fmax}} \tag{5}$$

$$circularity = \frac{ECD}{EPD} = \sqrt{\frac{4\,\pi\,A}{p^2}} \tag{6}$$

$$roundness = compactness^2 \tag{7}$$

The Zen core software additionally calculated the so-called convex hull, which is the smallest convex set containing a given geometric object. With this data the solidity and the convexity of particles were calculated, given the Eqs. (8) and (9) with the area of the convex hull A_C and the perimeter of the convex hull P_C.

$$solidity = \frac{A}{A_C} \tag{8}$$

$$convexity = \frac{P_C}{P} \tag{9}$$

Furthermore, the equivalent aerodynamic diameter D_A was calculated based on the ECD, the particle density p_p and the particles dynamic shape factor via Eq. (8) given by Hinds (Hinds and Zhu, 2022). This value is commonly used in aerosol research and allows for a direct comparison of particle size data measured via a SEM to data obtained from other devices such as an OPS.

$$D_A = ECD\ \sqrt{\frac{p_p}{p_0\ x}} \tag{10}$$

For particles measured via the ZEN core software, additional data regarding the legendre ellipse was also recorded. The legendre ellipse is an ellipse with the centre in the object's centroid and with the same geometrical moments up to the second order as the original object area (Besterci et al., 2001). These values were used to calculate the ellipticity, elongation and dispersion of particles according to Eqs. (11) and (12) provided by Besterci (Besterci et al., 2001), where a is the semi-mayor and b the semi-minor of the legendre ellipse.

$$ellipticity = \frac{a}{b} \tag{11}$$

$$elongation = log_2\left(\frac{a}{b}\right) \tag{12}$$

Table S1 in the SI shows an overview of the shape describing morphological features for different particle shapes to give a better understanding of the meaning of each parameter. Morphological data was acquired utilizing the extended particle analyzer feature from the BioVoxxel plugin (Brocher, 2022) via the ImageJ image analysis software. These morphological descriptors address a variety of parameters that are relevant for the characterization of particle morphology. Descriptors like the AR, ellipticity, extent bulkiness as well as the compactness and the roundness give a general understanding of the form of a particle, while other parameters like the solidity and the circularity describe the surface of a particle.

3. Results and discussion

3.1. Online measurements & gravimetric analysis

The online data obtained from stationary platform measurements are listed in Table 1. In summary, PM and PNC concentrations were comparable for all three samples at the Hauptbahnhof U4/U5 platform, despite the different sampling times. As discussed in our previous study (Bendl et al., 2023), the PNC were similar to ambient background levels at our suburban reference station located on the University campus (*GPS: 48°04'37.5"N 11°38'21.2"E)* and its vicinity using walking measurements. This observation, coupled with the absence of active

Table 1
Online data from platform stationary measurements obtained via OPC and DISCmini.

Date	PM in μg m^{-3}			PNC in $\#/cm^{-3}$	size mode in nm
	PM_{10}	$PM_{2.5}$	PM_1		
17/5/2022	231 ± 52	96 ± 10	25 ± 3	6099 ± 630	56 ± 3
19/7/2022	218 ± 50	85 ± 8	26 ± 2	7857 ± 713	54 ± 3
28/8/2022	181 ± 32	105 ± 24	29 ± 5	5074 ± 1111	64 ± 7

ventilation in the Munich subway system, and the location of the surveyed subway platform in the city centre with substantial traffic, leads us to conclude that the air exchange rate with the ambient air is relatively low. This aligns with the findings of Kumar et al., 2023, and suggest a low influence of traffic-related particles. The subway was identified as a dominant source of PM on the platform, with high concentrations of coarse particles. While the size mode of the PNC was outside of the range measured via the automated SEM/EDX approach, the data from DISCmini showed that there was no noticeable increase in the ultrafine fraction when entering the Munich subway system (Bendl et al., 2023). Overall PM levels on the platform were relatively stable over the sampling period suggesting that the samples were representative. Only small fluctuations in concentrations were observed, while short term $PM_{2.5}$ and PM_{10} peaks were associated with particle resuspension caused by incoming trains and piston effects (Bendl et al., 2023).

Simultaneous sampling for gravimetric analysis was performed on PC, PTFE and quartz filters and the $PM_{2.5}$ mass concentrations were 100.2 ± 4.13, 103.2 ± 1.65 and 102.9 ± 5.66 μg m^{-3}. Based on the comparison between gravimetry and on-line measurements, the average $PM_{2.5}$ effective density was estimated to be 2.1 g cm^{-3}, which was used as a correction factor for on-line PM data. This gravimetric approach also confirmed that $PM_{2.5}$ collection on PC filters is comparable to quartz and PTFE filters (Bendl et al., 2023).

3.2. SEM/EDX analysis

High resolution automated morphological measurements on PC filters conducted via Zen core listed particles predominantly in the submicron size, with the mode of the particle number between 200 and 300 nm, with similar distributions for the three different days. The size distribution from the 19/7/2022 measured via ZEN core as well as the size distribution of the iron oxides measured via AZtec Features and the online OPS size distribution for the same day are plotted in Fig. 2. Since automated imaging generally provides a value with the unit number or number per area, while online measurements yield results with the unit number per volume, these values were normalized to allow for comparison of these size distributions by normalizing the peak of each distribution to the value of 1. Size distributions of overall particles showed a similar trend as the size distributions of iron oxide particles, with a noticeable deviation around 1 μm where the transition between the two automated SEM/EDX measurement sizes occurred and can most likely be attributed to the different signal responses and, therefore, different rates of recognized particles for measurements at 5 kV and 15 kV. The online OPS size distribution showed the mode of particles at 300–400 nm and differed to the other distributions, most likely due to the lowered counting efficiency of laser scattering based instruments at lower particle sizes (Heim et al., 2008) and the lowest measurable size of 300 nm with the used instrument.

The dataset showed that the majority of particles was still in the size range measurable via automated SEM/EDX imaging, thus proving the validity of classification data for the Munich subway system. Manual EDX analysis furthermore confirmed that there were no apparent differences in elemental composition between small particles compared to particles above the set threshold for automated SEM/EDX analysis of 200 nm. Even though the online PNC size mode was found around 50 nm, there was no significant increase of PNC concentrations inside and outside of the subway system (Bendl et al., 2023), suggesting that the subway system does not produce copious amounts of ultrafine particles.

Particle shapes revealed an elongation of particles, which is expressed by their average aspect ratios of 0.66 ± 0.13 (17/5/2022 and 28/8/2022) and 0.65 ± 0.13 (19/7/2022) as well as their roundness of 0.55 ± 0.14 (17/5/2022 and 19/7/2022) and 0.56 ± 0.13 (28/8/2022). These values are further supported by the results for the legendre ellipse, which showed an average elongation of 0.68 ± 0.41 (17/5/2022), 0.69 ± 0.40 (19/7/2022) and 0.66 ± 0.39 (28/8/2022) and an ellipticity of 0.65 ± 0.16 (17/5/2022 and 28/8/2022) and 0.64 ± 0.16 (19/7/2022). The surfaces of analyzed particles were mainly rough with a largely increased surface area generally attributed to formation via abrasion processes. The roughness of particle surfaces is expressed by their average circularity of 0.78 ± 0.12 (17/5/2022), 0.79 ± 0.11 (19/7/2022) and 0.81 ± 0.10 (28/8/2022) as well as the solidity of 0.87 ± 0.08 (17/5/2022), 0.88 ± 0.07 (19/7/2022), and 0.88 ± 0.06 (28/8/2022). Table 2 summarizes the morphological data for subway particles on PC filters measured via ZEN core. Overall morphological data showed high intra-sample variance with almost no inter-sample variance suggesting that different modes of particles are generated from the same source with little seasonal influence. Considering that indoor environments are less susceptible to weather and temperature changes the neglectable seasonal variance that was observed between samples can be considered as reasonable.

Automated SEM/EDX based imaging of subway aerosols classified the majority of particles as iron rich particulate matter (FePM). The initial classification, however, contained several artifacts originating mainly from scratches in the surface of the silica wafers and from the pores of the filters. A manual correction of the dataset was therefore conducted, where particles that had no elemental data associated to them were deleted. Initial results showed average values of unclassified particles at 3.29 ± 3.77 % for the three wafer samples (W15), 0.71 ± 0.22 % for the three filter samples measured at 15 kV (F15), and 11.74 ± 4.21 % for the fine particle fraction <1 μm of the same filter samples measured at 5 kV (F5), which was lowered via manual data cleanup to 0.24 ± 0.05 % (F15), 1.86 ± 1.36 % (W15) and 1.30 ± 0.45 % (F5). Fig. 2 shows the average percentages of the assigned classes for all three F15 samples. Further diagrams of the average classification percentages for F5 and W15 samples can be found in the SI in Fig. S3 and Fig. S4 together with Table S2, which shows the number of particles found in each sample. Standard deviations shown for percentages of particle classification indicate the variance between the three sampling days.

In total, 92.78 ± 1.05 % of all particles (F15) were assigned to the iron oxide class, while 4.28 ± 1.49 % belonged to the three steel subclasses resulting in a total of 97.06 ± 0.64 % of iron-rich particles. The average iron oxide percentage for W15 samples was slightly lower at 84.93 ± 5.48 % with an additional 8.75 ± 2.23 % of steel particles totaling at 93.68 ± 3.28 % of iron-rich particles. The differences between these two sample types can be explained by the usage of two different classification schemes that were applied to the samples, which included Si percentages for the filter samples and C percentages for the wafer samples resulting in particles falling below, or exceeding a certain class threshold. F5 samples consisted of a total of 63.30 ± 10.47 % of iron-rich particles, with 62.69 ± 10.16 % of all particles classified as iron-oxides and only 0.61 ± 0.32 % of steel particles. F5 samples showed a large amount of iron bearing particles in the submicron size range, however, the results were significantly lower than for particles ≥1 μm in diameter (F15 samples), which is due to the higher number of carbonaceous particles in these samples. Zhang et al. (2022) stated that iron was found in >75 % of particles (90 particles per sample) in Beijing, China, while Jung et al. (2010) reported that 75–91 % of all analyzed subway particles (300 particles per sample) in Seoul, South Korea were

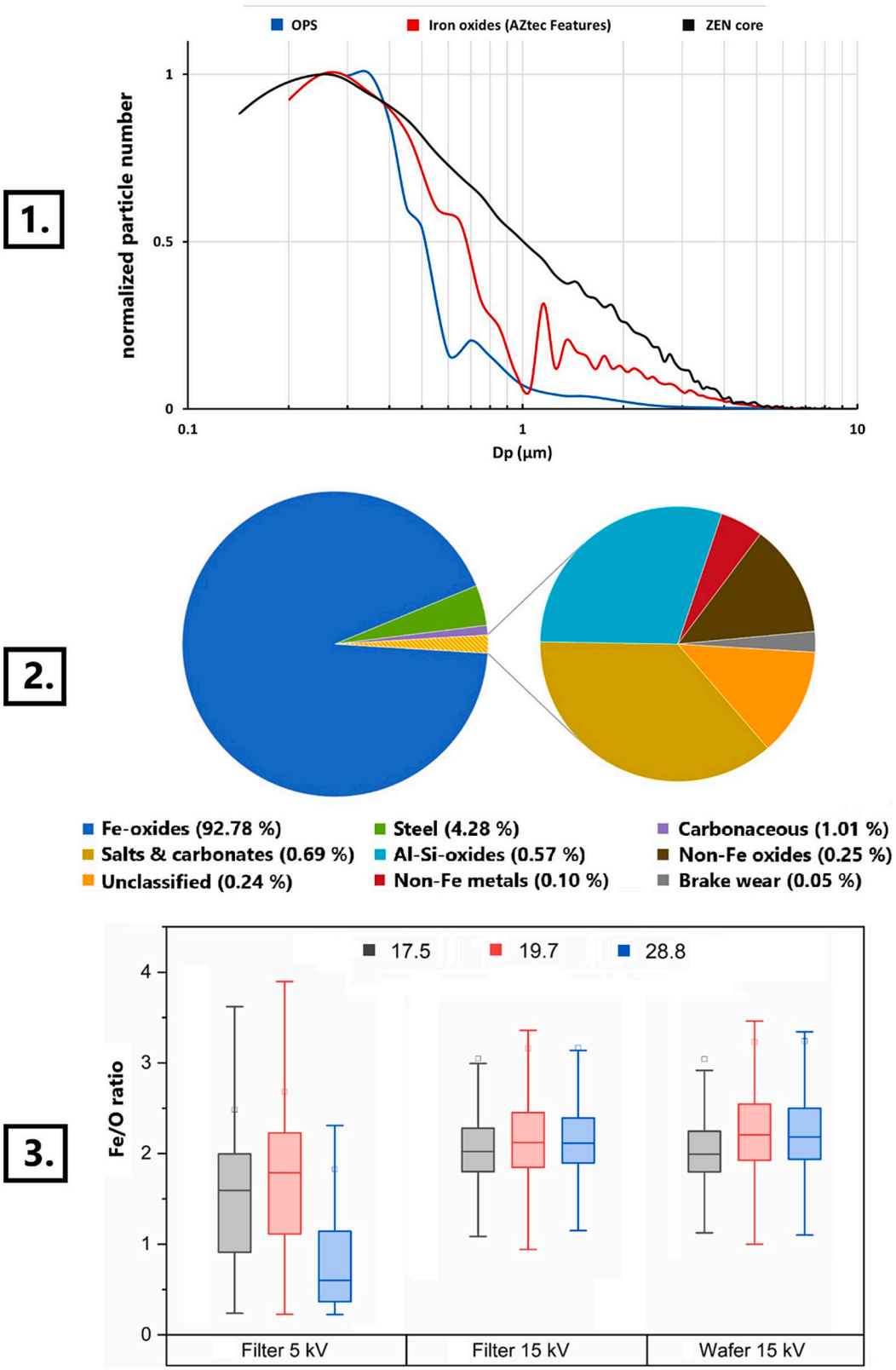

Fig. 2. Statistical information obtained via automated imaging. 1. Size distributions of particles from 19/07/2022 measured via ZEN core, iron oxides measured via Aztec Features and online size distribution obtained by OPS. Highest numbers for size bins were normalized to 1 for easier comparison of different techniques. 2. Average classification results of particles larger than 1 µm for filter samples measured at 15 kV. 3. Fe/O ratios of particles classified as iron oxides.

Table 2
Morphological descriptors for subway particles on filter samples measured via the ZEN core Software.

Descriptor	17/5/2022			19/7/2022			28/8/2022		
Particle count	45,640			68,447			87,287		
AR	0.66	±	0.13	0.65	±	0.13	0.66	±	0.13
Extent bulkiness	0.66	±	0.07	0.66	±	0.07	0.67	±	0.06
Compactness	0.74	±	0.10	0.74	±	0.09	0.75	±	0.09
Circularity	0.78	±	0.12	0.79	±	0.11	0.81	±	0.10
Roundness	0.55	±	0.14	0.55	±	0.14	0.56	±	0.13
Solidity	0.87	±	0.08	0.88	±	0.07	0.88	±	0.06
Convexity	0.90	±	0.08	0.91	±	0.08	0.92	±	0.07
Ellipticity	0.65	±	0.16	0.64	±	0.16	0.65	±	0.16
Elongation	0.68	±	0.41	0.69	±	0.40	0.66	±	0.39

iron-rich. Higher percentages of FePM in the Munich subway can be explained by the lower proportion of Cu rich particles due to the usage of a third-rail type power supply, instead of a copper catenary and the comparably low part of geological/ soil derived particles caused by the depth of the subway station at which samples were drawn and lower air exchange with the ambient air. These results suggest a similar origin of iron rich particles in the subway systems all over the world.

Fig. 3 contains six SEM micrographs of typical iron oxide particles found in the Munich subway system showcasing their overall form and surface topography. Fig. 3.1 and Fig. 3.3 depict flake like iron-oxide particles, which were commonly found throughout all samples, predominantly for particles >2 μm. Iron oxide particles exhibited rough and often splintery shapes with large surface areas due to the jagged edges often found on abrasion derived particles. This is expressed by their

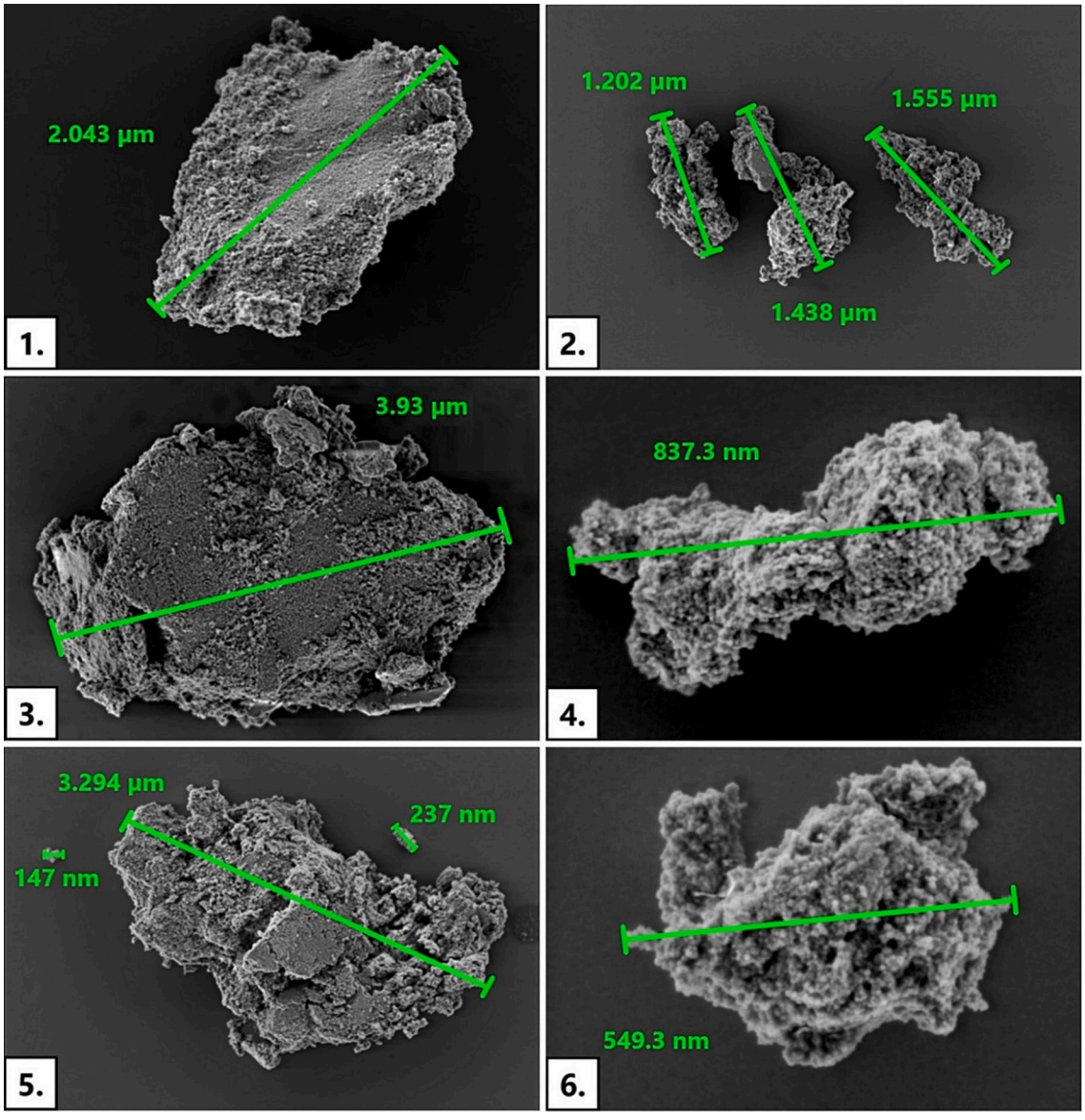

Fig. 3. SEM micrographs of characteristic iron oxide particles found in the Munich subway system.

circularity of 0.87 ± 0.12 (F15 and W15), and 0.88 ± 0.11 (F5). However, due to the comparably low magnification used for automated SEM/EDX imaging, an underestimation of particles perimeter is likely due to the limited number of pixels describing a particle. This is in accordance with the significantly lower circularity of all particle classes of 0.80 ± 0.11 determined with Zen core, which utilized a higher magnification for measurements. Since almost all particles found were classified as iron-oxide particles, the value obtained via ZEN core can be regarded as more probable.

The average aspect ratios for iron oxide particles were 0.62 ± 0.13 (F15), 0.60 ± 0.13 (W15), and 0.63 ± 0.12 (F5) indicating an elongation of particles, which is visible in Fig. 3.2 and Fig. 3.4 as splintery particles, mainly found in the <2 μm size range. This fact is also represented by the average roundness of iron oxide particles of 0.46 ± 0.11 for particles >1 μm and 0.49 ± 0.11 for particles <1 μm as well as an extent bulkiness of 0.60 ± 0.10 (F15), 0.61 ± 0.10 (W15), and 0.62 ± 0.09 (F5). Iron oxide particles were found in a fine mode at 484 ± 198 nm and a coarse mode at 1534 ± 1024 nm (W15) and 1853 ± 796 nm (F15). Morphological descriptors for iron oxide particles are summarized in Table 3.

Particles classified as iron oxides consisted almost exclusively of iron and oxygen with 14.13 ± 4.51 wt% of carbon (based on wafer samples) and 0.8 ± 1.31 wt% (F15) to 4.39 ± 2.67 wt% (F5) of Si. Other elements, mostly S, Cu, Na, Ca, Mg, Al and K, were also detected, but only at average concentrations below 0.2 wt% for individual elements. These values are in good agreement with data from Kumar et al. (2023) and Moreno et al. (2015) who reported elemental compositions for iron rich particles of 40.16–64.69 wt% for Fe, 9.08–32.47 wt% for O, 1.96–19.52 wt% for C, and 1.05–8.47 wt% for Si. Table 4 shows the average elemental composition of iron oxide particles for the three sample types. Furthermore the data obtained via SEM/EDX is in good agreement with results published in our previous study (Bendl et al., 2023) obtained via ICP-MS for the same days, which showed iron concentrations accounting for up to 69 wt% of the $PM_{2.5}$ fraction for the 17/5/2022.

The high average carbon percentages found in iron oxide particles suggests that most of these particles originated from brake pads instead of a low steel source, which would be attributed to the rails and wheels as well as the third rail power conductor (Font et al., 2019; U-Bahn München, 2023a). The high oxygen contents, which align neither with the chemical composition of cast iron nor with steel, can be explained by the high temperatures at the brake during particle formation facilitating rapid oxidation in the environment (Wang et al., 2016). Fe/O ratios of iron oxide particles <1 μm were less uniform than for those >1 μm indicating a wider spread of oxidation levels in the submicron size range. The average Fe/O ratio for small iron oxide particles was lower than for larger iron oxide particles, which is presumably linked to their higher surface area rendering them more susceptible to oxidation, while the fraction of the oxidized surface layer in comparison to the unoxidized Fe core also increases. Furthermore, there might be a slight underestimation of iron contents in small particles due to the lower EHT of 5 kV limiting the quantification of iron to the Lα line instead of the more accurate Kα line. Fig. 2 shows the Fe/O ratios for iron oxide particles for all sample types.

Metallic iron and steel particles, which also held a high share of subway particles at percentages between 0.61 and 8.75 % of all particles, where especially present in W15 samples. Filter samples consisted almost exclusively of low alloy steel and metallic iron particles with 99.77 ± 0.01 % (F15) and 100.00 % (F5), which is due to the less accurate distinction between steel types without measured carbon contents for these samples. The average D_A of steel particles in W15 samples was 2146 ± 1287 nm with a distribution of 94.50 ± 1.84 % of low alloy steel and metallic iron, 4.78 ± 1.82 of high alloy steel, and 0.72 ± 0.26 % of Cr-steel. These steel particles are attributed to abrasion of train wheels and rails (Moreno et al., 2015), which are commonly made of R260 or similar steel types (Aniołek and Herian, 2011).

While automated SEM/EDX analysis classified the majority of particles >200 nm as iron rich, even smaller particles of highly ferrous nature were present in the samples. Manual SEM/EDX analysis also revealed iron concentrations of similar levels compared to >200 nm subway particles in NPs ranging from 30 nm to 200 nm. Concentrations obtained from these measurements, which were obtained at 5 kV, are less accurate due to the beam partially piercing the particle and subsequently exciting the underlying filter or wafer. Nonetheless, based on a simulation of the penetration depth of electrons in a Fe_2O_3 substrate at an EHT of 5 kV calculated via the Monte Carlo software (Fig. S1 and Fig. S2 in SI), they can be considered reliable enough to give an estimation of the elemental composition of particles <200 nm. From a toxicologic viewpoint these particles, especially those NP in the sub 100 nm range, are considered to be critical due to their ability to reach the bloodstream via deposition in the alveoli followed by translocation throughout the whole body (Morawska and Buonanno, 2021; Thorley et al., 2014). Additionally, NPs were reported to be transported across the olfactory epithelium leading to accumulation in the brain (Hopkins et al., 2018; T. Fortoul et al., 2015). Fig. 4 shows a 68 nm iron oxide particle with its corresponding EDX spectrum as well as other small heavy metal rich particles found in the samples.

FePM is generally considered less toxic than particles containing other heavy metals such as Cu, however, FePM was shown to significantly impair human health following inhalation in several studies (Beck-Speier et al., 2009; Lay et al., 1999). While Fe can be generally considered as innocuous if ingested orally due to bounding of iron to proteins and chelating in the digestive system that prevent the generation of ROS (Morgan et al., 2020), the lung does not possess a pathway for coping with large amounts of unliganded ferrous or ferric iron (Ghio et al., 2009). Carcinogenic potential of long-term exposure to low-dose Fe_2O_3 nanoparticles resulting in neoplastic-like transformation of human small airway epithelial cells via formation of ROS was reported by Stueckle et al. (2017) emphasizing the significance of sub 100 nm iron rich particles in the subway, to which commuters are exposed on a daily base. Furthermore, particles formed by physical abrasion, mainly grinding and crushing, are suggested to exhibit significantly different toxicological responses compared to combustion derived Fe particles, such as fly ash, due to their rough, often flake like shape (Morgan et al., 2020). Generation of ROS from heavy metals via Fenton-like reactions requires the metal proportion of particles to be soluble putting a large significance on bioavailability of heavy metal rich PM (Longo et al., 2016; Zhang et al., 2008). Increased toxicity for subway FePM was reported in several studies (Jung et al., 2012; Loxham and

Table 3
Morphological descriptors for iron oxide particles obtained via the Aztec Features software.

Descriptor	Wafer 15 kV			Filter 15 kV			Filter 5 kV		
ECD in nm	1534	±	1024	1853	±	796	484	±	198
EPD in nm	1936	±	1813	2256	±	1380	572	±	288
D_A in nm	1832	±	976	2200	±	808	606	±	230
AR	0.60	±	0.13	0.62	±	0.13	0.63	±	0.12
extent bulkiness	0.61	±	0.10	0.60	±	0.10	0.62	±	0.09
compactness	0.67	±	0.09	0.67	±	0.09	0.70	±	0.08
circularity	0.87	±	0.12	0.87	±	0.12	0.88	±	0.11
roundness	0.46	±	0.11	0.46	±	0.11	0.49	±	0.11

Table 4
Average elemental compositions of iron oxides for filter and wafer samples.

Element	Wt% for Filter 15 kV			Wt% for Wafer 15 kV			Wt% for Filter 5 kV		
C	ND			14.13	±	4.51	ND		
O	32.58	±	6.00	27.37	±	3.17	45.53	±	13.06
Si	0.80	±	1.31	ND			4.39	±	2.67
Fe	66.30	±	6.88	58.13	±	6.63	49.58	±	14.14
Other elements	1.12	±	5.32	0.36	±	3.10	4.88	±	6.46

Nieuwenhuijsen, 2019) with a twofold increase in DNA damage compared to Fe_2O_3 or Fe_3O_4 particles alone (Karlsson et al., 2008). An investigation of various PM sources including wood combustion, tyre wear, street PM and subway particles conducted by Karlsson et al. (2006) showed subway aerosol as the most genotoxic with significantly increased DNA damage, which cannot solely be explained by enlarged surface areas, but was attributed by them to a highly reactive surface of these particles. Additionally, iron rich PM is often accompanied by other heavy metals, such as Cu, Mn, Cr and V, further enhancing its potential to generate ROS compared to pure iron and iron oxide particles. Furthermore, the small clearance between trains and the tunnel walls leads to resuspension of sedimented particles via the so called "piston-effect", which can temporarily cause high particle concentrations in the surrounding air by pushing the air in front of the trains and creating a strong suction behind them (Walther and Bogdan, 2017). These short-term exposures to high PM concentrations might be reduced in the Munich subway system compared to other cities, by the usage of a specialized vacuum train called "VakTrak, which is used to clean the track bed from waste and debris and filters out resuspended particles down to 100 nm (Trambahn.de, 2023). Additionally, the Munich transport network (MVG) operating the subway is planning the installation of platform screen doors in the future (mvg.de, 2023), which some studies showed to mitigate commuters' exposure (Kim et al., 2012; Son et al., 2013).

While these iron oxide and steel particles are well reported in the literature and are linked to abrasion at the rail-wheel-brake interface (Moreno et al., 2015) other distinct chemical profiles linked to the emission of subway trains were only scarcely found. Except from iron oxide and steel particles, the third most abundant class was carbonaceous particles present at concentrations of 1.01 ± 0.15 % (F15), 23.62 ± 14.61 % (F5), and 2.35 ± 1.62 % (W15). While carbonaceous particles are normally related to automotive traffic, only minor amounts of soot chains, typical for the incomplete combustion of fuels, were found in all samples. Instead, carbonaceous particles were almost exclusively found in the submicron size range with an average aerodynamic diameter of 385 ± 136 nm, but also to some degree in the size range of 1388 ± 804 nm (W15) to 1641 ± 354 nm (F15). Automated classification of carbonaceous particles, however, is only accurate for Wafer samples since no carbon was measured in filter samples and the classification was based on the assumption that particles consisting of >75 wt% of O have to be carbonaceous in order to be solid, since all other elements except C were measured. Furthermore, manual EDX measurements confirmed that these particles were in fact carbonaceous and present in high quantities, even though their carbon content could not be accurately quantified. The small fraction of carbonaceous particles (F5) showed similar morphological characteristics as iron oxide (Yang et al., 2016) particles with an average roundness of 0.43 ± 0.12 and a circularity of 0.84 ± 0.13. These values indicate a similar, abrasion derived source, possibly generated from frictional wear of graphite contact blocks used in the current collectors of third-rail type power supplies (Yang et al., 2016) or from other sources, such as electric motor brushes employed in newer trains as well as brake pads (Moreno et al., 2015).

Font (Font et al., 2019) analyzed motor brushes used in the Barcelona subway system, which showed Zn, Ti, Ba, Sn, and Cr as the main impurities of the carbon nanotubes, which are employed in these brushes. Carbonaceous particles in F5 samples contained 7.53 ± 5.21 wt % of Fe and 0.27 ± 0.51 wt% of Cu with no other metal concentrations above the limit of detection for EDX analysis. This elemental composition, even though actual values are most likely lower due to the missing carbon content in these samples, contradicts motor brushes as main source of carbonaceous particles in the Munich subway environment and points towards brake wear as the most likely source. The fact that submicronic carbonaceous particles contained iron and copper also renders the assumption that these particles might be artifacts from the sputtering process improbable. The F5 sample from the 28.8 showed especially high amounts of carbonaceous particles in the submicron fraction indicating a high temporal variability of these particles with a total range of 10.31 % (19.7) to 43.97 % (28.8).

Heavy metal bearing particles, linked to wear and abrasion of brake pads, such as $BaSO_4$ and SbS_3 (Grigoratos and Martini, 2015), were also present at concentrations of 0.05 ± 0.01 % at an average size of 2286 ± 936 nm (F15) and 0.09 ± 0.05 % at an average size of 1459 ± 416 nm (W15). F5 samples did not show significant amounts of brake wear particles due to the general lack of Sb rich particles in all subway samples and the insufficient EHT to excite the Lα line of the more frequently occurring Ba. Since the M-line of Ba, which can be observed at an EHT of 5 kV, is overlapping with the L-Lines of Fe, it could not be used for determination of Ba presence due to the ubiquitous nature of Fe in the subway environment. Abbasi et al. (2012) reported peaks for railway break wear in the ultra-fine size range at around 100 nm; two fine peaks - one dominant at 300–400 nm and one at 500–600 nm - and a coarse peak at 3–7 μm, which were found under all test conditions. In contrast, Hagino et al. (2016) showed the coarse peak in the range of 1.2–3.5 μm. Furthermore, Iijima et al. (2007) showed that heavy metals associated to brake wear are predominantly found in the coarse fraction. This is in good accordance with data from the Munich subway, which showed the carbonaceous fraction of brake wear at 385 ± 136 nm and the heavy metal rich brake wear fraction in the coarse mode between 1459 ± 416 nm – 2286 ± 936 nm.

Average heavy metal concentrations, except for iron were present at low levels, however, they were found to be distributed inhomogeneously throughout the samples. Fig. 5 depicts an EDX map of the F15 sample from 28/8/2022 illustrating the distribution of metals such as Cu and Al.

Classification results listed non-ferrous metal rich particles at percentages of 0.10 ± 0.01 % (F15), 0.14 ± 0.07 % (F5) and 0.90 ± 0.30 % (W15) for the non-ferrous metals and 0.25 ± 0.15 % (F15), 2.00 ± 1.44 % (F5), and 0.09 ± 0.03 % (W15) for non-ferrous oxides. Most of these heavy metal containing particles were classified as metallic copper or copper oxide particles and are often attributed by literature to sparking at the catenary-pantograph interface, often consisting of Cu alloys (Zhou et al., 2022). However, these catenary-pantograph type power collectors are not utilized in the Munich subway. Wafer samples contained an average of 0.42 ± 0.02 % of copper rich particles, while filter samples contained at average 0.31 ± 0.14 % (F15) and 2.11 ± 1.52 % (F5). Samples taken on the 19/7/2022 showed significantly higher levels of Cu metal and oxide particles with Cu oxides reaching a level of 4.04 % in the F5 sample. These results show that while average numbers of Cu rich particles are fairly low, they can temporally reach high dosages, causing potential threads to commuters' health. Third-rail type power supplies, which are also used in the Munich subway, consists of either a graphite or a copper current collector (Yang et al., 2016) and might, therefore, contribute to copper rich emissions in subway tunnels. However, given

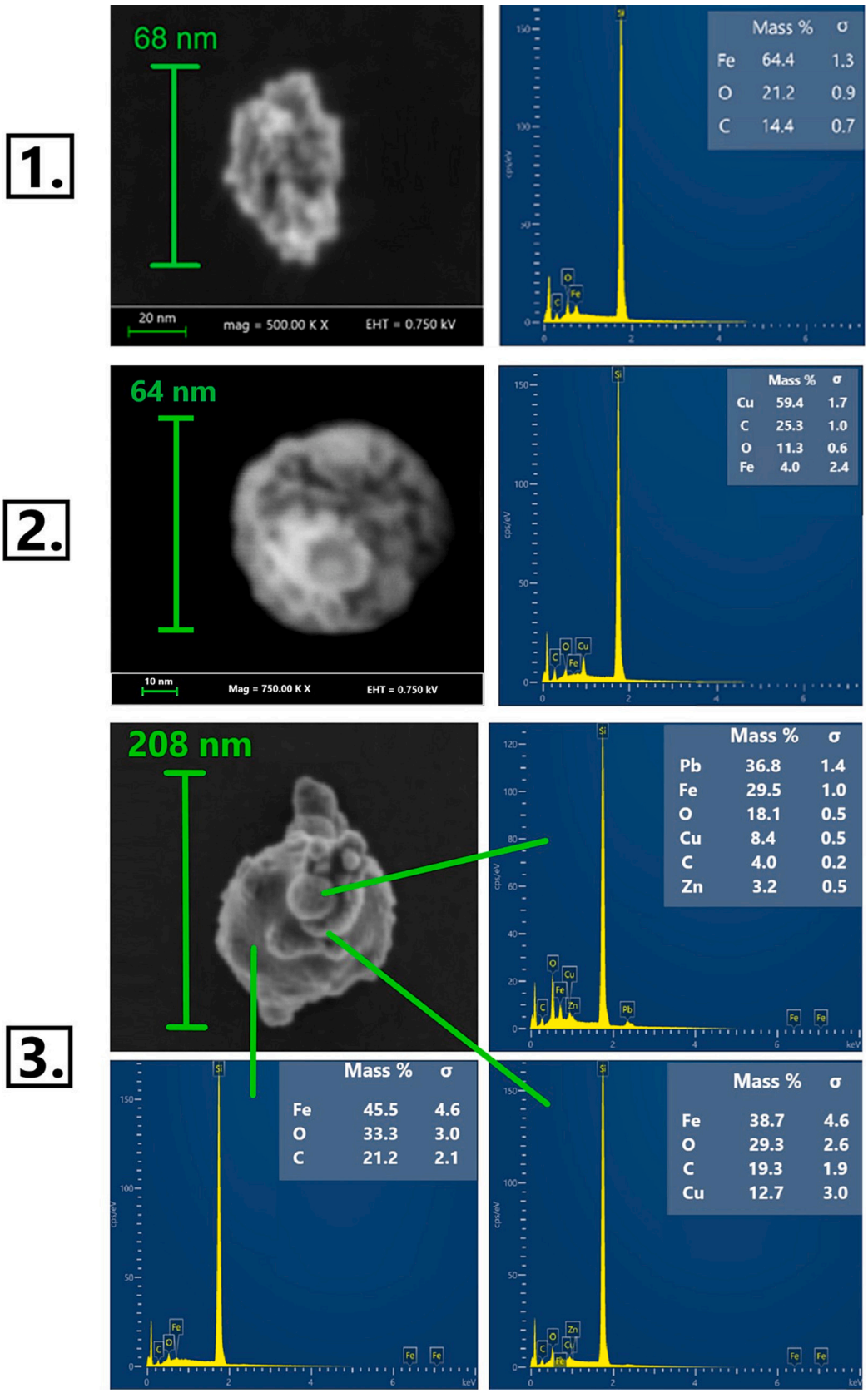

Fig. 4. Manual EDX data of small particles taken at 5 kV. 1. 68 nm iron oxide particle found in wafer sample from 28/8/2022. 2. 64 nm copper oxide particle found in wafer sample from 19/7/2022. 3. 208 nm iron oxide particle with Cu and Pb encrustations found in wafer sample from 28/8/2022.

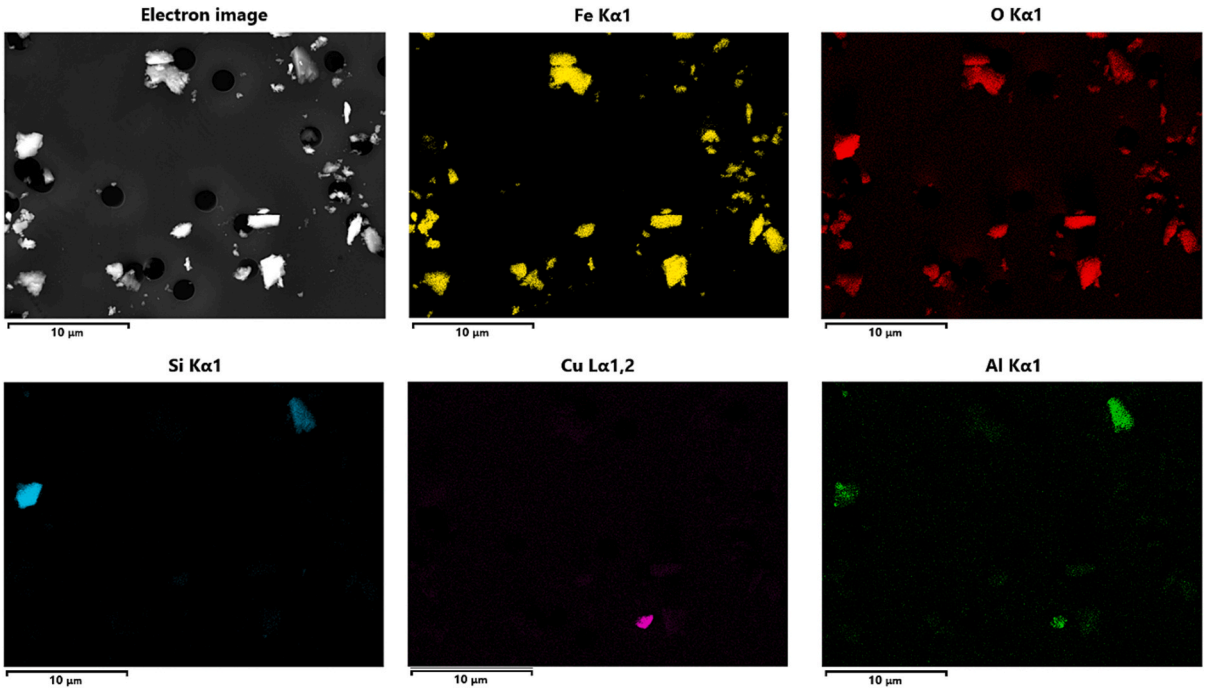

Fig. 5. EDX overview of sample from 28/8/2022 at 15 kV.

the low levels of copper in comparison to other subway systems (Bendl et al., 2023), it is likely that the current collectors are made of graphite, which is in good agreement with the high levels of carbonaceous particles found in the Munich subway system. These results point towards brake wear as the most likely source of copper in the subway tunnels, which is commonly used as marker for automotive brake wear (Grigoratos and Martini, 2015).

Cu particles found in the Munich subway system were found in two size modes. Cu particles in F15 and W15 samples had a particle size between 2029 ± 741 nm (F15) and 1432 ± 589 nm (W15) while the majority of Cu particles was found in F5 samples at an average particle size of 445 ± 191 nm. The average elemental compositions for the combined Cu oxides and Cu metal classes for all samples are given in Table S5 in the SI. These copper rich particles can be considered as critical to the human health since particles between 1 and 2.5 µm end up in terminal bronchi (Sankhe et al., 2019) and particles smaller 1 µm can even reach the pulmonary alveoli (Costa et al., 2016), where the generation of ROS can induce several diseases (Boukhenouna et al., 2018; Kanti Das et al., 2014). Especially temporary high concentrations, such as in the F5 sample from the 19/7/2022, where 4.04 % of all particles were copper rich, are critical considering that respirable copper particles are considered to be the most toxic heavy metal bearing particles in mammals (Hejazy et al., 2018). Fig. 4.2 contains a SEM micrograph of a 64 nm copper particle, together with its associated EDX spectrum highlighting the high mass percentages of copper that could be found even in particles smaller than 100 nm.

Apart from pure copper oxides, some iron-oxide particles were observed to contain encrustations of other heavy metals, such as Cu and Pb. An exemplary SEM micrograph of a 208 nm particle with its EDX spectra is shown in Fig. 4.3. For these particles, which contain a variety of heavy metals, the overall toxicity is hard to predict, however, studies suggest that the toxicity is higher than the sum of the toxicity of the individual heavy metals. Sun et al. reported that mixed heavy metals in $PM_{2.5}$ samples from smeltery districts in China showed an increased rate of apoptosis in A549 cells compared to the single metals (Sun et al., 2022).

Furthermore, non-anthropogenic sources of particles, mostly of geological origin, were observed in the Munich subway system. A total of 0.57 ± 0.07 % (F15) and 1.99 ± 0.66 % (F5) was assigned to silica, aluminosilicates and other various silicate types, while none were found in wafer samples, which is due to the fact that Si was excluded from these samples. These soil derived particles were presumably brought into the subway system by commuters or were transported to the platforms via ventilation from the streets above. The second most prominent detected non-anthropogenic particle source was the salts and carbonates class at 0.69 ± 0.24 % (F15), 0.77 ± 0.66 % (F5) and 0.97 ± 0.47 % (W15) dominated by calcium carbonate.

4. Conclusions

Automated SEM based morphological analysis of subway particles showed a high intra-sample variance, but almost no variance between samples, which were taken at the same place at different time and seasons suggesting the same dominant source, which is relatively stable over time. Particles found in the Munich subway system displayed rough edged splintery surfaces, indicated by their average circularity of 0.78 to 0.81, as well as an average solidity of 0.87 to 0.88. The main mode of the particle number was observed in the size range from 100 to 300 nm peaking at 175–200 nm. Two main types of particle morphologies, a flake like shape for particles >2 µm and an elongated shape for particles <2 µm, were predominantly found throughout all samples.

Of the over 200,000 particles analyzed via automated SEM/EDX imaging, 98.87 ± 1.06 % were automatically assigned to the pre-defined classes. Automated SEM/EDX based classification of the subway aerosol revealed the highly ferruginous nature of subway particles compliant with literature from other subway systems around the globe. In total, 84.68 ± 16.45 of all particles were found to be of iron rich nature with an average Fe concentration of these particles of 49.58–66.30 % depending on the particle size. Other heavy metals, mainly copper oxides, were found either as pure particles or as encrustations embedded into larger iron oxide particles. These high levels of Fe rich and other heavy metal bearing particles, which were also found in the size range well below 100 nm, could pose a threat especially to vulnerable groups, such as pregnant women and old and young people, if they are exposed to subway aerosol for prolonged periods of time.

These results highlight the desirability of reducing commuters'

exposure, for which other studies showed the installation of platform protection doors as one of the feasible mitigations. Another feasible mitigation to limit the exposure to short-term high particle concentrations due to the piston-effect might be improvement of the ventilation system and a more frequent removal of sedimented particles via specialized vacuum trains.

The suitability of automated SEM/EDX based imaging was demonstrated for the in-depth characterization of micro-environments, such as non-exhaust emissions. The technique described in this paper can be used to address the homogeneity of a wide variety of different emission sources, or to study their contribution to complex environmental samples. It can be used stand-alone or as a complement to other filter analysis techniques, such as ICP-MS, where the added value is mainly information on the distribution of elements in different particle sizes, which can have a major impact on health risks.

CRediT authorship contribution statement

Carsten Neukirchen: Writing – review & editing, Writing – original draft, Visualization, Investigation, Data curation, Conceptualization. **Thorsten Meiners:** Writing – review & editing, Writing – original draft, Validation, Software, Investigation, Data curation, Conceptualization. **Jan Bendl:** Writing – review & editing, Writing – original draft, Validation, Resources, Methodology, Investigation, Formal analysis, Data curation, Conceptualization. **Ralf Zimmermann:** Writing – review & editing, Writing – original draft, Validation, Supervision, Project administration, Funding acquisition. **Thomas Adam:** Writing – review & editing, Validation, Supervision, Resources, Project administration, Funding acquisition, Formal analysis, Conceptualization.

Declaration of competing interest

The authors declare that they have no known competing financial interests or personal relationships that could have appeared to influence the work reported in this paper.

Data availability

Data will be made available on request.

Acknowledgments

This research is funded by dtec.bw – Digitalization and Technology Research Center of the Bundeswehr [project LUKAS and MORE]. Dtec.bw is funded by the European Union – NextGenerationEU. This research was also supported by the project ULTRHAS – ULtrafine particles from TRansportation – Health Assessment of Sources, a project funded under the EU's Research and Innovation programme Horizon 2020, Grant Agreement No. 955390. We acknowledge financial support by Universität der Bundeswehr München.

Appendix A. Supplementary data

Supplementary data to this article can be found online at https://doi.org/10.1016/j.scitotenv.2024.170008.

References

2023 Netzplan U-Bahn München.svg – Wikipedia. https://de.m.wikipedia.org/wiki/Datei:Netzplan_U-Bahn_M%C3%BCnchen.svg (accessed 04 November 2023).

Abbasi, S., Jansson, A., Olander, L., Olofsson, U., Sellgren, U., 2012. A pin-on-disc study of the rate of airborne wear particle emissions from railway braking materials. Wear 284-285, 18–29. https://www.sciencedirect.com/science/article/pii/S0043164812000257.

Aniołek, K., Herian, J., 2011. The structure, properties and a resistance to abrasive wear of railway sections of steel with a different pearlite morphology. IOP Conf. Ser. Mater. Sci. Eng. 22 (1), 12012. https://doi.org/10.1088/1757-899X/22/1/012012.

Bachler, G., Losert, S., Umehara, Y., Goetz, N. von, Rodriguez-Lorenzo, L., Petri-Fink, A., et al., 2015. Translocation of gold nanoparticles across the lung epithelial tissue barrier: combining in vitro and in silico methods to substitute in vivo experiments. Part. Fibre Toxicol. 12 (1), 18. https://doi.org/10.1186/s12989-015-0090-8.

Beck-Speier, I., Kreyling, W.G., Maier, K.L., Dayal, N., Schladweiler, M.C., Mayer, P., et al., 2009. Soluble iron modulates iron oxide particle-induced inflammatory responses via prostaglandin E(2)synthesis: In vitro and in vivo studies. Part. Fibre Toxicol. 6, 34. https://doi.org/10.1186/1743-8977-6-34.

Bendl, J., Neukirchen, C., Mudan, A., Padoan, S., Zimmermann, R., Adam, T., 2023. Personal measurements and sampling of particulate matter in a subway – identification of hot-spots, spatio-temporal variability and sources of pollutants. Atmos. Environ. 308, 119883. https://www.sciencedirect.com/science/article/pii/S1352231023003096.

Besterci, M., Käerdi, H., Kulu, P., Mikli, V., 2001. Characterization of powder particle morphology. Proc. Estonian Acad. Sci. Eng. 7 (1), 22. https://doi.org/10.3176/eng.2001.1.03.

Boukhenouna, S., Wilson, M.A., Bahmed, K., Kosmider, B., 2018. Reactive oxygen species in chronic obstructive pulmonary disease. Oxidative Med. Cell. Longev. 2018, 5730395. https://www.hindawi.com/journals/omcl/2018/5730395/.

Brocher, 2022. biovoxxel/BioVoxxel-Toolbox: BioVoxxel Toolbox. Zenodo.

Čalkovský, M., Müller, E., Gerthsen, D., 2023. Quantitative analysis of backscattered-electron contrast in scanning electron microscopy. J. Microsc. 289 (1), 32–47. https://doi.org/10.1111/jmi.13148.

Costa, A., Pinheiro, M., Magalhães, J., Ribeiro, R., Seabra, V., Reis, S., et al., 2016. The formulation of nanomedicines for treating tuberculosis. Adv. Drug Deliv. Rev. 102, 102–115. https://doi.org/10.1016/j.addr.2016.04.012.

DB Netz AG, 2023. Stationsbau - 2. Stammstrecke München. https://www.2.stammstrecke-muenchen.de/stationsbau.html. (Accessed 15 September 2023).

Font, O., Moreno, T., Querol, X., Martins, V., Sánchez Rodas, D., Miguel, E. de, et al., 2019. Origin and speciation of major and trace PM elements in the Barcelona subway system. Transp. Res. Part D: Transp. Environ. 72 (1506–1516), 17–35. https://www.researchgate.net/publication/334141687_Origin_and_speciation_of_major_and_trace_PM_elements_in_the_Barcelona_subway_system.

Fortoul, T., Rodríguez-Lara, V., González-Villalva, A., Rojas-Lemus, M., Colín-Barenque, L., Bizarro-Nevares, P., et al., 2015. Health effects of metals in particulate matter. https://www.semanticscholar.org/paper/Health-Effects-of-Metals-in-Particulate-Matter-Fortoul-Rodr%C3%ADguez-Lara/9e1dcb26db219f654d2ab5e1a1c301fe25a25661.

Ghio, A.J., Dailey, L.A., Richards, J.H., Jang, M., 2009. Acid and organic aerosol coatings on magnetic nanoparticles increase iron concentrations in human airway epithelial cells. Inhal. Toxicol. 21 (8), 659–667. https://doi.org/10.1080/08958370802406282.

Ghio, A.J., Smith, C.B., Madden, M.C., 2012. Diesel exhaust particles and airway inflammation. Curr. Opin. Pulm. Med. 18 (2), 144–150. https://journals.lww.com/co-pulmonarymedicine/fulltext/2012/03000/Diesel_exhaust_particles_and_airway_inflammation.10.aspx.

Grigoratos, T., Martini, G., 2014. Non-exhaust traffic related emissions – Brake and tyre wear PM. 1831-9424. https://publications.jrc.ec.europa.eu/repository/handle/JRC89231.

Grigoratos, T., Martini, G., 2015. Brake wear particle emissions: a review. Environ. Sci. Pollut. Res. 22 (4), 2491–2504. https://pubmed.ncbi.nlm.nih.gov/25318420/.

Hagino, H., Oyama, M., Sasaki, S., 2016. Laboratory testing of airborne brake wear particle emissions using a dynamometer system under urban city driving cycles. Atmos. Environ. 131, 269–278. https://www.sciencedirect.com/science/article/pii/S135223101630125X.

Heim, M., Mullins, B.J., Umhauer, H., Kasper, G., 2008. Performance evaluation of three optical particle counters with an efficient "multimodal" calibration method. J. Aerosol Sci. 39 (12), 1019–1031. https://doi.org/10.1016/j.jaerosci.2008.07.006.

Hejazy, M., Koohi, M.K., Pour, Bassiri Mohamad, A., Najafi, D., 2018. Toxicity of manufactured copper nanoparticles - a review. Nanomed. Res. J. 3 (1), 1–9. http://www.nanomedicine-rj.com/article_31894.html.

Hinds, W.C., Zhu, Y., 2022. Aerosol Technology: Properties, Behavior, and Measurement of Airborne Particles. Wiley, Hoboken, NJ.

Hopkins, L.E., Laing, E.A., Peake, J.L., Uyeminami, D., Mack, S.M., Li, X., et al., 2018. Repeated iron–soot exposure and nose-to-brain transport of inhaled ultrafine particles. Toxicol. Pathol. 46 (1), 75–84. https://www.ncbi.nlm.nih.gov/pmc/articles/PMC6405220/.

Iijima, A., Sato, K., Yano, K., Tago, H., Kato, M., Kimura, H., et al., 2007. Particle size and composition distribution analysis of automotive brake abrasion dusts for the evaluation of antimony sources of airborne particulate matter. Atmos. Environ. 41 (23), 4908–4919. https://www.sciencedirect.com/science/article/pii/S1352231007001409.

Jung, H.-J., Kim, B., Ryu, J., Maskey, S., Kim, J.-C., Sohn, J., et al., 2010. Source identification of particulate matter collected at underground subway stations in Seoul, Korea using quantitative single-particle analysis. Atmos. Environ. 44 (19), 2287–2293. https://www.sciencedirect.com/science/article/pii/S1352231010002852.

Jung, M.H., Kim, H.R., Park, Y.J., Park, D.S., Chung, K.H., Oh, S.M., 2012. Genotoxic effects and oxidative stress induced by organic extracts of particulate matter (PM 10) collected from a subway tunnel in Seoul, Korea. Mutat. Res. 749 (1–2), 39–47. https://www.sciencedirect.com/science/article/pii/S1383571812002690.

Kanti Das, T., Wati, M.R., Fatima-Shad, K., 2014. Oxidative stress gated by Fenton and Haber Weiss reactions and its association with Alzheimer's disease. Arch. Neurosci. 2 (3) https://doi.org/10.5812/archneurosci.20078.

Karlsson, H.L., Ljungman, A.G., Lindbom, J., Möller, L., 2006. Comparison of genotoxic and inflammatory effects of particles generated by wood combustion, a road

simulator and collected from street and subway. Toxicol. Lett. 165 (3), 203–211. https://www.sciencedirect.com/science/article/pii/S0378427406001238.
Karlsson, H.L., Holgersson, A., Möller, L., 2008. Mechanisms related to the genotoxicity of particles in the subway and from other sources. Chem. Res. Toxicol. 21 (3), 726–731. https://doi.org/10.1021/tx7003568.
Kim, K.-H., Ho, D.X., Jeon, J.-S., Kim, J.-C., 2012. A noticeable shift in particulate matter levels after platform screen door installation in a Korean subway station. Atmos. Environ. 49, 219–223. https://www.sciencedirect.com/science/article/pii/S1352231011012453.
Knight, L.J., Parker-Jurd, F.N.F., Al-Sid-Cheikh, M., Thompson, R.C., 2020. Tyre wear particles: an abundant yet widely unreported microplastic? Environ. Sci. Pollut. Res. 27 (15), 18345–18354. https://doi.org/10.1007/s11356-020-08187-4.
Kumar, P., Zavala-Reyes, J.C., Kalaiarasan, G., Abubakar-Waziri, H., Young, G., Mudway, I., et al., 2023. Characteristics of fine and ultrafine aerosols in the London underground. Sci. Total Environ. 858 (Pt 1), 159315. https://www.sciencedirect.com/science/article/pii/S0048969722064142.
Laborda, F., Bolea, E., Jiménez-Lamana, J., 2014. Single particle inductively coupled plasma mass spectrometry: a powerful tool for nanoanalysis. Anal. Chem. 86 (5), 2270–2278. https://doi.org/10.1021/ac402980q.
Lay, J.C., Bennett, W.D., Ghio, A.J., Bromberg, P.A., Costa, D.L., Kim, C.S., et al., 1999. Cellular and biochemical response of the human lung after intrapulmonary instillation of ferric oxide particles. Am. J. Respir. Cell Mol. Biol. 20 (4), 631–642. https://doi.org/10.1165/ajrcmb.20.4.3355.
Longo, A.F., Feng, Y., Lai, B., Landing, W.M., Shelley, R.U., Nenes, A., et al., 2016. Influence of atmospheric processes on the solubility and composition of iron in Saharan dust. Environ. Sci. Technol. 50 (13), 6912–6920. https://doi.org/10.1021/acs.est.6b02605.
Loxham, M., Nieuwenhuijsen, M.J., 2019. Health effects of particulate matter air pollution in underground railway systems - a critical review of the evidence. Part. Fibre Toxicol. 16 (1), 12. https://doi.org/10.1186/s12989-019-0296-2.
Morawska, L., Buonanno, G., 2021. The physics of particle formation and deposition during breathing. Nat. Rev. Phys. 3 (5), 300–301. https://www.nature.com/articles/s42254-021-00307-4.
Moreno, T., Martins, V., Querol, X., Jones, T., BéruBé, K., Minguillón, M.C., et al., 2015. A new look at inhalable metalliferous airborne particles on rail subway platforms. Sci. Total Environ. 505, 367–375. https://pubmed.ncbi.nlm.nih.gov/25461038/.
Morgan, J., Bell, R., Jones, A.L., 2020. Endogenous doesn't always mean innocuous: a scoping review of iron toxicity by inhalation. J. Toxicol. Environ. Health B Crit. Rev. 23 (3), 107–136. https://doi.org/10.1080/10937404.2020.1731896.
mvg.de, R., 2023. Entlastungsspange U9 | Münchner Verkehrsgesellschaft mbH. https://www.mvg.de/ueber/mvg-projekte/bauprojekte/u9.html (accessed 18 September 2023).
Niska, K., Santos-Martinez, M.J., Radomski, M.W., Inkielewicz-Stepniak, I., 2015. CuO nanoparticles induce apoptosis by impairing the antioxidant defense and detoxification systems in the mouse hippocampal HT22 cell line: protective effect of crocetin. Toxicology 29 (4), 663–671. https://www.sciencedirect.com/science/article/pii/S0887233315000211.
Sankhe, K., Khan, T., Bhavsar, C., Momin, M., Omri, A., 2019. Selective drug deposition in lungs through pulmonary drug delivery system for effective management of drug-resistant TB. Expert Opin. Drug Deliv. 16 (5), 525–538. https://doi.org/10.1080/17425247.2019.1609937.
Son, Y.-S., Salama, A., Jeong, H.-S., Kim, S., Jeong, J.-H., Lee, J., et al., 2013. The effect of platform screen doors on PM10 levels in a subway station and a trial to reduce PM10 in tunnels. ajae 7 (1), 38–47. https://doi.org/10.5572/ajae.2013.7.1.038.
Storch, L., Hamatscheck, C., Hesse, D., Feist, F., Bachmann, T., Eichler, P., et al., 2023. Comprehensive Analysis of Current Primary Measures to Mitigate Brake Wear Particle Emissions from Light-Duty Vehicles. 2073-4433 14(4), 712. https://publications.jrc.ec.europa.eu/repository/handle/JRC133217.
Stueckle, T.A., Davidson, D.C., Derk, R., Kornberg, T.G., Schwegler-Berry, D., Pirela, S.V., et al., 2017. Evaluation of tumorigenic potential of CeO2 and Fe2O3 engineered nanoparticles by a human cell in vitro screening model. NanoImpact 6, 39–54. https://www.sciencedirect.com/science/article/pii/S2452074816300994.
Sun, S., Zheng, N., Wang, S., Li, Y., Hou, S., An, Q., et al., 2022. Inhalation bioaccessibility and risk assessment of metals in PM2.5 based on a multiple-path particle dosimetry model in the Smelting District of Northeast China. Int. J. Environ. Res. Public Health 19 (15). https://www.ncbi.nlm.nih.gov/pmc/articles/PMC9331668/.
Thorley, A.J., Ruenraroengsak, P., Potter, T.E., Tetley, T.D., 2014. Critical determinants of uptake and translocation of nanoparticles by the human pulmonary alveolar epithelium. ACS Nano 8 (11), 11778–11789. https://pubmed.ncbi.nlm.nih.gov/25360809/.
Totlandsdal, A.I., Cassee, F.R., Schwarze, P., Refsnes, M., Låg, M., 2010. Diesel exhaust particles induce CYP1A1 and pro-inflammatory responses via differential pathways in human bronchial epithelial cells. Part. Fibre Toxicol. 7 (1), 41. https://doi.org/10.1186/1743-8977-7-41.
Trambahn.de, 2023. U-Bahn Fahrzeuge | trambahn. https://www.trambahn.de/u-bahn fahrzeuge (accessed 18 September 2023).
Trickler, W.J., Lantz-McPeak, S.M., Robinson, B.L., Paule, M.G., Slikker, W., Biris, A.S., et al., 2014. Porcine brain microvessel endothelial cells show pro-inflammatory response to the size and composition of metallic nanoparticles. Drug Metab. Rev. 46 (2), 224–231. https://doi.org/10.3109/03602532.2013.873450.
U-Bahn München, 2023a. Stromversorgung. https://www.u-bahn-muenchen.de/betrieb/stromversorgung/ (accessed 19 September 2023a).
U-Bahn München, 2023b. U-Bahnhof Hauptbahnhof (U4, U5). https://www.u-bahn-muenchen.de/netz/bahnhoefe/ho/ (accessed 04 November 2023b).
Walther, E., Bogdan, M., 2017. A novel approach for the modelling of air quality dynamics in underground railway stations. Transp. Res. Part D: Transp. Environ. 56, 33–42. https://www.sciencedirect.com/science/article/pii/S1361920917301487.
Wang, B.-Q., Liu, J.-F., Ren, Z.-H., Chen, R.-H., 2016. Concentrations, properties, and health risk of PM2.5 in the Tianjin City subway system. Environ. Sci. Pollut. Res. 23 (22), 22647–22657. https://doi.org/10.1007/s11356-016-7444-0.
Yang, C., Cai, G., Li, X., Bo, J., 2016. Study on third rail current collector shoes wear of metro trains. In: International Conference on Logistics, Informatics and Service Sciences (LISS), pp. 1–4. https://doi.org/10.1109/LISS.2016.7854552.
Zhang, Y., Schauer, J.J., Shafer, M.M., Hannigan, M.P., Dutton, S.J., 2008. Source apportionment of in vitro reactive oxygen species bioassay activity from atmospheric particulate matter. Environ. Sci. Technol. 42 (19), 7502–7509. https://doi.org/10.1021/es800126y.
Zhang, M., Shao, L., Jones, T., Feng, X., Ge, S., Yang, C.-X., et al., 2022. Atmospheric iron particles in PM2.5 from a subway station, Beijing, China. Atmos. Environ. 283, 119175. https://www.sciencedirect.com/science/article/pii/S1352231022002400.
Zhou, H., Duan, F., Liu, Z., Chen, L., Song, Y., Zhang, Y., 2022. Study on electric spark discharge between pantograph and catenary in electrified railway. IET Electr. Syst. Trans. 12 (2), 128–142. https://doi.org/10.1049/els2.12043.

Supplementary Information publication 1

Table S1: Morphological data for different shaped particles calculated via the BioVoxxel plugin in the ImageJ software

particle shape					
aspect ratio	1.00	0.70	0.91	0.50	0.50
extent bulkiness	0.79	0.71	0.69	0.80	0.74
compactness	1.00	0.8	0.90	0.71	0.69
circularity	1.00	0.89	0.89	0.88	0.73
roundness	1.00	0.64	0.80	0.51	0.47
solidity	1.00	1.00	1.00	1.00	0.86
convexity	1.00	1.00	1.00	1.00	0.90
ellipticity	1.00	1.00	1.05	2.00	1.91
elongation	0.00	0.00	0.07	1.00	0.93

Table S2: Number of particles found per sample measured via AZtec Features (Oxford)

	Particles found per sample		
Date	**W15**	**F15**	**F5**
17/5/2022	21622	31895	5426
19/7/2022	7765	31400	10194
28/8/2022	17789	61544	11121

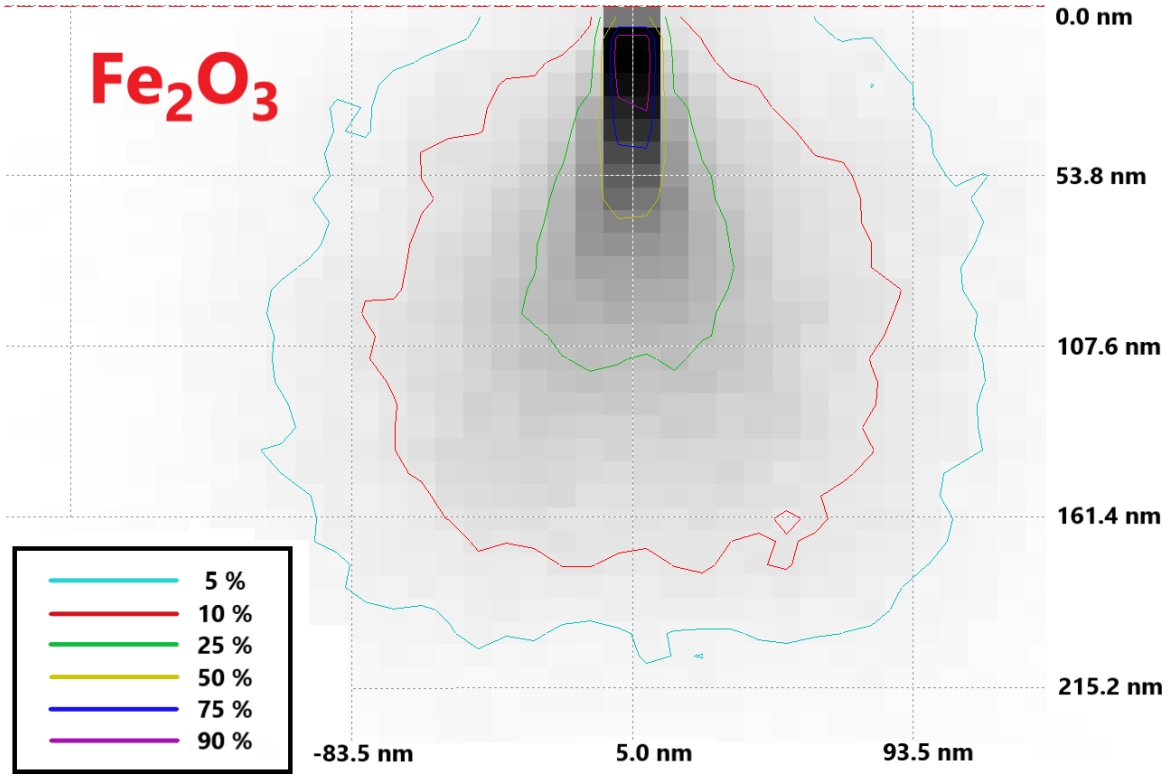

Figure S1: Energy-by-position distribution of a 5 kV electron beam in a Fe_2O_3 substrate, simulated via the trajectories of 2500 electrons in the Monte Carlo Software.

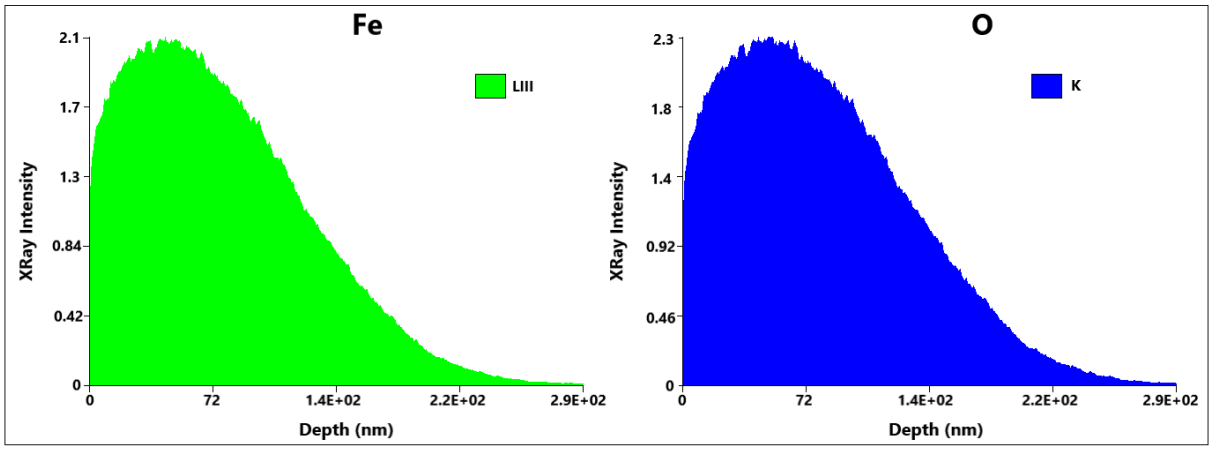

Figure S2: X-ray intensity of Fe and O as a function of the penetration depth of a 5 kV electron beam in a Fe_2O_3 substrate, simulated via the trajectories of 2500 electrons in the Monte Carlo Software.

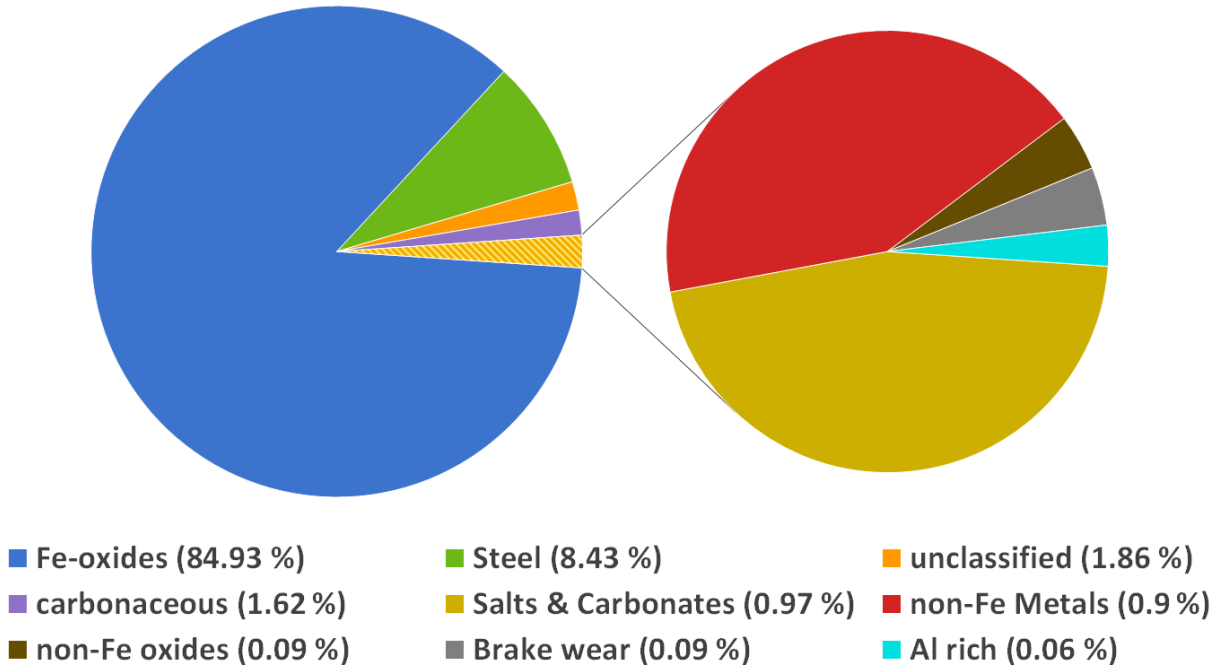

Figure S3: Average classification values for W15 samples

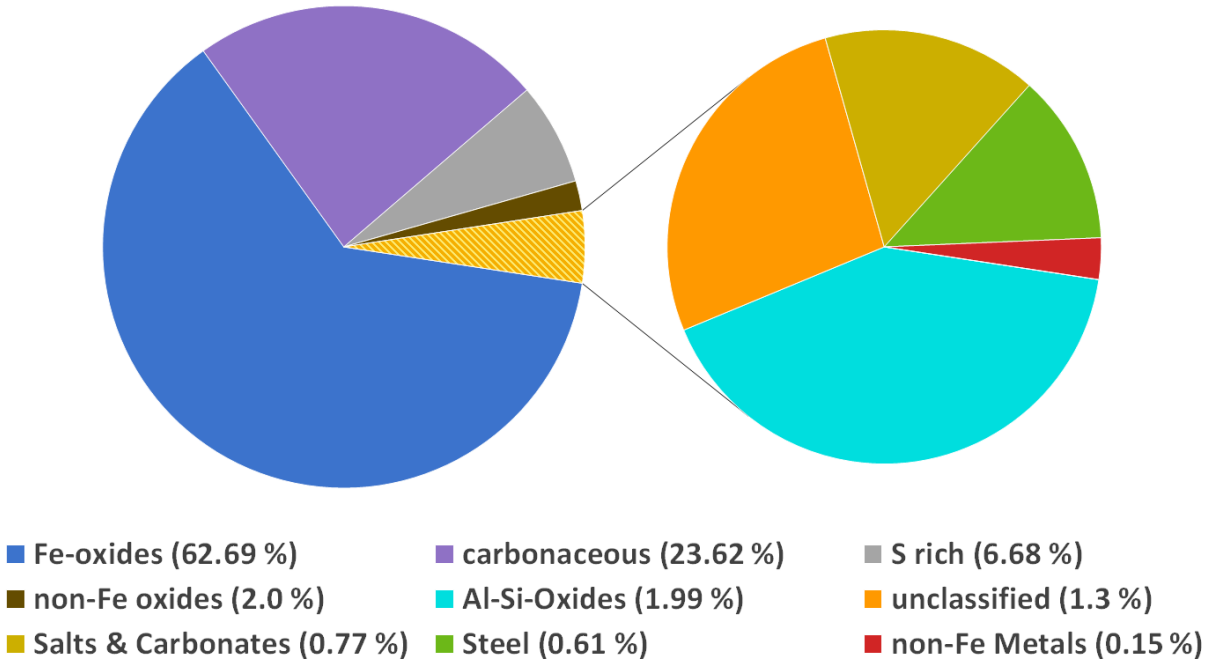

Figure S4: Average classification results of particles smaller than 1 µm for filter samples measured at 5 kV

Table S3: Classification scheme for particles on PC filters measured at 5 kV and 15 kV

Class	Subclass	Criteria	Min	Max	Special rule
Oversized (F5 only)		D_A (µm)	1	100	Reject if matched (F5 samples only)
Non-ferrous metals	Class rule	Oxygen	20	100	Exclude if matched
	Cu	Copper	5	100	Must be detected
	W	Tungsten	2	100	Must be detected
	Ti	Titanium	5	100	Must be detected
	Sn	Tin	5	100	Must be detected
		Copper	5	100	Exclude if matched
	Pb	Lead	5	100	Must be detected
		Copper	5	100	Exclude if matched
	Cd	Cadmium	1	100	Must be detected
Brake wear	Class rule	Sulphur	1	100	Must be detected
	SbS_3	Antimony	1	100	Must be detected
	$BaSO_4$	Barium	1	100	Must be detected
Ferrous metals	Class rule	Oxygen	20	100	Exclude if matched
		Iron	5	100	Must be detected
	Steel - Low alloy	Nickel	2	100	Exclude if matched
		Manganese	0	4	
		Chromium	0	1.5	
	Steel - Cr	Manganese	1	100	Exclude if matched
		Chromium	1	20	Must be detected
		Nickel	2	100	Exclude if matched
	Steel - High alloy	Nickel	2	100	Must be detected
		Chromium	2	100	Must be detected
Al Alloys	Class rule	Aluminium	75	100	Must be detected
		Oxygen	10	100	Exclude if matched
		Manganese	0	5	
	Al	Magnesium	0	0.5	
		Aluminium	75	100	Must be detected
		Silicon	0	0.5	
	Al (Mg)	Magnesium	0.5	5	Must be detected
		Silicon	0	1	
	Al (Mg,Si)	Magnesium	0.5	10	Must be detected
		Silicon	0.5	10	Must be detected
Non-ferrous oxides	Class rule	Oxygen	20	100	Must be detected
		Iron	30	100	Exclude if matched
	Ba-oxide	Barium	1	100	Must be detected
		Titanium	1	100	Exclude if matched
		Sulfur	1	100	Exclude if matched
	Ti-oxide	Titanium	5	75	Must be detected
	Zr-oxide	Zirconium	10	75	Must be detected
		Silicon	5	100	Exclude if matched
	Zn-oxide	Zinc	15	50	Must be detected
	Cu-oxide	Cu	5	100	Must be detected

Table S3: Classification scheme for particles on PC filters measured at 5 kV and 15 kV (continued)

Class	Subclass	Criteria	Min	Max	Special rule
Iron oxide		Iron	18	100	Must be detected
		Oxygen	20	100	Must be detected
Al-Si-Oxides	Class rule	Oxygen	20	100	Must be detected
	Al-Oxide	Aluminium	15	100	Must be detected
		Silicon	5	100	Exclude if matched
		Iron	5	100	Exclude if matched
		Copper	5	100	Exclude if matched
		Tungsten	2	100	Exclude if matched
	Si-Oxide	Silicon	15	100	Must be detected
		Aluminium	1	50	Exclude if matched
		Iron	20	100	Exclude if matched
	Silicates	Aluminium	5	100	Must be detected
		Silicon	5	100	Must be detected
		Copper	5	100	Exclude if matched
		Tungsten	2	100	Exclude if matched
	Zircon	Zirconium	5	100	Must be detected
		Silicon	5	100	Must be detected
		Iron	30	100	Exclude if matched
Salts & carbonates	Class rule	Silicon	10	100	Exclude if matched
	Salt	Chlorine	5	100	Must be detected
		Aluminium	5	100	Exclude if matched
		Copper	5	100	Exclude if matched
		Zinc	5	100	Exclude if matched
		Cadmium	1	100	Exclude if matched
		Iron	5	100	Exclude if matched
	$CaSO_4$	Calcium	5	100	Must be detected
		Sulfur	5	100	Must be detected
		Oxygen	20	100	Must be detected
		Silicon	5	100	Exclude if matched
		Chlorine	10	100	Exclude if matched
	$CaCO_3$ & CaO	Oxygen	20	100	Must be detected
		Sodium	0	15	
		Sulfur	0	2	
		Calcium	10	60	Must be detected
		Silicon	10	100	Exclude if matched
	Al-chloride	Silicon	10	100	Exclude if matched
		Chlorine	10	100	Must be detected
		Aluminium	10	100	Must be detected
	Nitrates	Oxygen	60	100	Must be detected
		Nitrogen	15	50	Must be detected
Critical fibers		Aspect ratio	3	250	Must be detected
		Lenght (µm)	5	100	Must be detected
Carbonaceous		Oxygen	75	100	Must be detected

Table S4: Classification scheme for particles found on Si wafers measured at 15 kV

Class	Subclass	Criteria	Min	Max	Special rule
Wafer		Oxygen	95	100	reject if matched
Ag-paint		Silver	10	100	reject if matched
Non-ferrous metals	Class rule	Oxygen	20	100	Exclude if matched
	Cu	Copper	5	100	Must be detected
	W	Tungsten	2	100	Must be detected
	Ti	Titanium	5	100	Must be detected
	Sn	Tin	5	100	Must be detected
		Copper	5	100	Exclude if matched
	Pb	Lead	5	100	Must be detected
		Copper	5	100	Exclude if matched
	Cd	Cadmium	1	100	Must be detected
Brake wear	Class rule	Sulfur	1	100	Must be detected
	SbS_3	Antimony	1	100	Must be detected
	$BaSO_4$	Barium	1	100	Must be detected
Ferrous metals	Class rule	Oxygen	20	100	Exclude if matched
		Iron	5	100	Must be detected
	Steel - Low alloy	Nickel	2	100	Exclude if matched
		Manganese	0	4	
		Chromium	0	1.5	
	Steel - Cr	Manganese	1	100	Exclude if matched
		Chromium	1	20	Must be detected
		Nickel	2	100	Exclude if matched
	Steel - High alloy	Nickel	2	100	Must be detected
		Chromium	2	100	Must be detected
Al Alloys	Class rule	Aluminium	75	100	Must be detected
		Oxygen	10	100	Exclude if matched
		Manganese	0	5	
	Al	Magnesium	0	0.5	
	Al (Mg)	Magnesium	0.5	5	Must be detected
Non-ferrous oxides	Class rule	Oxygen	20	100	Must be detected
		Iron	30	100	Exclude if matched
	Ba-oxide	Barium	1	100	Must be detected
		Titanium	1	100	Exclude if matched
		Sulfur	1	100	Exclude if matched
	Ti-oxide	Titanium	5	75	Must be detected
	Zr-oxide	Zirconium	10	75	Must be detected
	Zn-oxide	Zinc	15	50	Must be detected
	Cu-oxide	Cu	5	100	Must be detected
Iron oxide		Iron	18	100	Must be detected
		Oxygen	20	100	Must be detected

Table S4: Classification scheme for particles found on Si wafers measured at 15 kV (continued)

Al-Oxides		Oxygen	20	100	Must be detected
		Aluminium	15	100	Must be detected
		Iron	5	100	Exclude if matched
		Copper	5	100	Exclude if matched
Class	Subclass	Criteria	Min	Max	Special rule
Salts & carbonates	Salt	Chlorine	5	100	Must be detected
		Aluminium	5	100	Exclude if matched
		Copper	5	100	Exclude if matched
		Zinc	5	100	Exclude if matched
		Cadmium	1	100	Exclude if matched
		Iron	5	100	Exclude if matched
	$CaSO_4$	Calcium	5	100	Must be detected
		Sulfur	5	100	Must be detected
		Oxygen	20	100	Must be detected
		Chlorine	10	100	Exclude if matched
	$CaCO_3$ & CaO	Oxygen	20	100	Must be detected
		Sodium	0	15	
		Sulfur	0	2	
		Calcium	10	60	Must be detected
	Al-chloride	Chlorine	10	100	Must be detected
		Aluminium	10	100	Must be detected
	Nitrates	Oxygen	60	100	Must be detected
		Nitrogen	15	50	Must be detected
Critical fibers		Aspect ratio	3	250	Must be detected
		Length (µm)	5	100	Must be detected
Carbonaceous	Organic carbon	Oxygen	10	60	Must be detected
		Carbon	40	90	Must be detected
		Oxygen + Carbon	90	100	Must be detected
	Elemental carbon	Oxygen	99	100	Must be detected

Table S5: Elemental composition of Cu rich particles found in the Munich subway

Concentration in wt. %	**Filter 15 kV**	**Wafer 15 kV**	**Filter 5 kV**
Cu	30.38 ± 28.02	36.83 ± 23.36	22.12 ± 17.84
O	29.05 ± 9.87	12.78 ± 9.25	51.78 ± 16.39
Fe	37.90 ± 23.79	14.92 ± 19.93	10.86 ± 13.23
C	ND	29.15 ± 13.3	ND
Si	1.12 ± 1.99	ND	14.39 ± 8.15
other Elements	2.68 ± 6.50	6.32 ± 16.34	0.85 ± 3.29

Journal of Hazardous Materials 482 (2025) 136609

Contents lists available at ScienceDirect

Journal of Hazardous Materials

journal homepage: www.elsevier.com/locate/jhazmat

Comprehensive elemental and physical characterization of vehicle brake wear emissions from two different brake pads following the Global Technical Regulation methodology

Carsten Neukirchen [a,b], Mohammad Reza Saraji-Bozorgzad [a], Michael Mäder [c], Ajit Paul Mudan [a], Philipp Czasch [c], Johannes Becker [b,d], Sebastiano Di Bucchianico [b,d,e], Christian Trapp [f], Ralf Zimmermann [b,d,e], Thomas Adam [a,d,*]

[a] University of the Bundeswehr Munich, Faculty for Mechanical Engineering, Institute of Chemistry and Environmental Engineering, Werner-Heisenberg-Weg 39, 85577 Neubiberg, Germany
[b] Joint Mass Spectrometry Center at Chair of Analytical Chemistry, Institute of Chemistry, University of Rostock, Albert-Einstein-Strasse 27, 18059 Rostock, Germany
[c] HDC Blueprints GmbH, Am Hohen Rain 4, 86529 Schrobenhausen, Germany
[d] Joint Mass Spectrometry Center at Comprehensive Molecular Analytics (CMA), Environmental Health Center, Helmholtz Munich, Ingolstädter Landstrasse 1, 85764 Neuherberg, Germany
[e] Department Life, Light & Matter, University of Rostock, Albert Einstein Strasse 25, 18059 Rostock, Germany
[f] University of the Bundeswehr Munich, Faculty for Mechanical Engineering, Institute of Energy and Power Train Technology, Werner-Heisenberg-Weg 39, 85577 Neubiberg, Germany

HIGHLIGHTS

- PM_{10} emission factors defined for two brake pads.
- More than half of the mass of PM_{10} emitted as iron.
- Geometric mean diameter found in the nanometer range.
- High emissions of heavy metals such as Fe, Cu, Cr, Sn, Mn and Zn.
- Large emission contribution from wear of the brake disc observed.

GRAPHICAL ABSTRACT

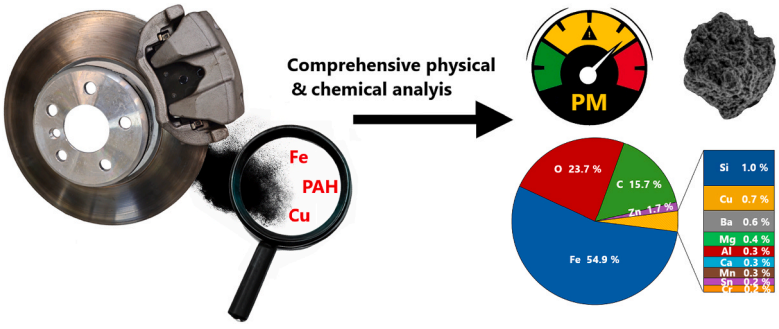

Abbreviations: ALI, Air-liquid interface; CPC, Condensation particle counter; CVS, Constant volume sampler; EDX, Energy-dispersive X-ray spectroscopy; GMD, Geometric mean diameter; GTR24, United Nations global technical regulation No.24; ICP-MS/MS, Inductively coupled plasma tandem mass spectrometry; ILS II, Global interlaboratory study; LM, Low metallic; NAO, Non-asbestos organic; NEE, Non-exhaust emissions; OEM, Original equipment manufacturer; OPS, Optical particle sizer; PAH, Polycyclic aromatic hydrocarbons; PC, Polycarbonate; PM, Particulate matter; PMP, Particle measurement programme; PNC, Particle number concentration; ROS, Reactive oxygen species; SEM, Scanning electron microscopy; SI, Supplementary information; SPC, Solid particle counter; SPN, Solid particle number; TPC, Total particle counter; TPN, Total particle number; UNECE, United Nations Economic Commission for Europe; WLTP, Worldwide Harmonized Light Vehicle Test Procedure; BR1Fa, ILS II brake 1 with brake pad a; BR1Fb, ILS II brake 1 with brake pad b.

* Corresponding author at: University of the Bundeswehr Munich, Faculty for Mechanical Engineering, Institute of Chemistry and Environmental Engineering, Werner-Heisenberg-Weg 39, 85577 Neubiberg, Germany,.
E-mail address: thomas.adam@unibw.de (T. Adam).

https://doi.org/10.1016/j.jhazmat.2024.136609
Received 26 September 2024; Received in revised form 14 November 2024; Accepted 19 November 2024
Available online 20 November 2024

ARTICLE INFO

Keywords:
EURO 7
GTR24
Brake wear
Non-exhaust emissions
Inductively coupled plasma mass spectrometry
Scanning electron microscopy
Chemical composition

ABSTRACT

Non-exhaust emissions have gained increasing attention during the last years, with the upcoming EURO 7 regulation defining maximum PM_{10} emission factors for tire and brake emissions for the first time. This study, therefore, focusses on broadening the knowledge on chemical composition and physical characteristics of brake dust to define emission factors for heavy metal and organic pollutants. Particles from two pads were analyzed utilizing the Worldwide Harmonised Light Vehicle Test Procedure (WLTP) brake cycle. Geometric mean diameters for both pads were found with a bimodal distribution in the ultrafine range. PM_{10} emission factors of 15.1 ± 0.1 mg/km and 16.3 ± 0.4 mg/km were measured, which is 2.15 and 2.32 times higher than upcoming maximum permitted emission factor of 7 mg/km. On average 54.9 % and 58.1 % of PM10 was emitted as iron, with a wide variety of Fe concentrations between 43 – 75 % by mass found in individual particles. Other heavy metals, such as Cu, Cr, Mn and Zn, were also found and a high contribution of wear from the brake disc was noticeable, based on the elemental composition. Fe emission factors calculated from the WLTP brake cycle were 8–9 times higher than previously reported values in literature, while Cu levels were significantly lower based on recent trends in brake pad formulations. Four different PAH were detected even at the relatively low temperatures that are common for the WLTP brake test cycle.

1. Introduction

Automotive emissions derived from combustion engines have long been the focus of many researchers worldwide and underwent significant reduction due to regulatory measures by governments in the last decades [1]. However, non- exhaust emissions have long been disregarded in this discussion, even though they contribute a large fraction to traffic emissions. It is estimated that in the year 2016 non-exhaust emissions made up 73 % of traffic derived PM_{10} emissions [2], with brake emissions contributing between 16 to 55 % of non-exhaust emissions, heavily depending on the braking frequency of vehicles at the studied location [3]. For these reasons, non-exhaust emissions (NEE) from automotive traffic have gained increasing attention, which is reflected by the fact that the upcoming EURO 7 norm will define maximum emission factors for particles originating from brakes and tires for the first time [4]. Furthermore, many studies are dealing with their toxicological impact and human health risks without a consensus on consistent setups [2]. Indeed, comparability of these studies has been lacking due to the huge differences in the used test setups, which range from pin-on-disc tribometers, to brake dynamometers with various designs, to "real-world driving scenarios" and environmental studies ([5]; Mathissen et al., 2019). For this reason, the particle measurement programme (PMP) of the United Nations Economic Commission for Europe (UNECE) has developed the United Nations Global Technical Regulation No. 24 (GTR24) for more comparable brake emission measurements, utilizing a uniform test cycle in the form of the Worldwide Harmonized Light Vehicle Test Procedure (WLTP) brake cycle, as well as a strict measurements procedure with defined maximum allowed deviations for speed, temperature and a range of other relevant parameters. The brake temperature plays a crucial role in emission testing [5], which is why applied vehicle parameters, like the weight of the brake disc in comparison to the vehicle weight are very important. This is accounted for by the GTR 24 via the implementation of four different groups of wheel load to disc mass ratios, which each have a different target range of the brake temperature. Such measures facilitate a more controlled testing procedure, which greatly enhance the comparability of studies. Type approval on GTR24 compliant brake dynamometers will be mandatory starting from 2026, with the EURO 7 norm defining maximum allowed PM_{10} emission factors of 3 mg/km for pure electric vehicles, 7 mg/km for internal combustion engines and hybrid cars, as well as 11 mg/km for internal combustion engine vans. These emission factors will be further lowered to 3 mg/km for all light-duty vehicles in 2035 [6].

Common brake pad formulations, such as so called low metallic (LM) pads often contain metal contents around 10 – 30% of mass, while the softer non-asbestos organic (NAO) pads generally contain lower amounts of metals [7]. Additional differences in brake pad formulations arise from local legal regulations, most prominently the EPA's Memorandum of Understanding on Copper Mitigation in Watershed and Waterways [8], which limits the amounts of asbestiform fibers, chromium(VI)-salts, mercury and lead to 0.1%, cadmium compounds to 0.01% and copper to 5% of weight from 2021, with further restrictions that allow a maximum amount of copper of 0.5% starting in 2025. The usage of different friction pairings with varying brake pads and brake discs, influences the emission behavior of a brake system. For example, NAO pads normally release less PM, however they facilitate a higher wear of the brake disc, due to higher contents of abrasive fibers [5].

The need for legal restrictions of heavy metal concentrations originating from brake wear, as well as the demand to monitor compliance with such regulations is supported by literature, which lists brake wear as major contributor to ambient particulate Cu levels. A study conducted within "The Brake Pad Partnership" estimated emission factors for the nine sub-watersheds in the San Francisco bay area of 53.8 tonnes of Cu/year as airborne emissions, plus an additional 50.4 tonnes of Cu/year released to roadways [9], while a study from Hulskotte estimated that 2.4 kilotons of Cu are deposited to surface waters annually and that up to 75% of the atmospheric copper input in the North Sea may be due to brake wear [10].

Particles formed via abrasion of brake discs and pads have been found to be a potential threat, not only to the environment, but also to human health, since they contain high amounts of heavy metals such as Fe and Cu, a variety of other heavy metals, and minerals like anatase or graphite [11,12]. Airborne copper particles entering the human respiratory system, are expected to be toxic, with studies particularly pointing out the cytotoxic effects of copper nanoparticles in human alveolar models [13], while iron rich particles are often falsely disregarded as innocuous. This assumption is based on the fact that the human body has numerous pathways of dealing with large contents of Fe, preventing the generation of ROS by chelating the unbound iron if digested orally (Morgan et al., 2020), however, the lung does not possess pathways of dealing with large amounts of unliganded iron species (Ghio et al., 2009). Several studies have shown severe health impacts following inhalation of iron rich particles, particularly from PM mixtures containing reduced and oxidized iron (Beck-Speier et al., 2009; Lay et al., 1999; O'Day et al., 2022). The carcinogenic potential of long-term exposure to low-dose Fe_2O_3 nanoparticles resulting in neoplastic-like transformation of human small airway epithelial cells via formation of ROS was reported, as well as the potential neurotoxic and cardiovascular effects of iron-rich PM [14-16]. The chemical composition of brake-abrasion particles is thus related to their toxicological potential and their ability to induce oxidative stress, pro-inflammatory responses and DNA damage resulting in concerns for the human health [17]. For instance, increasing metal content of brake wear particles also increased tight junction damage, thus possibly decreasing lung epithelial barrier functions via intracellular formation of reactive oxygen species [18]. Abrasion derived particles are known to exhibit different toxicological responses compared to combustion derived Fe particles, often due to

rough and flake like shapes (Morgan et al., 2020). Studies on the toxicity of subway aerosol, which is similar in its chemical and morphological properties (Bendl et al., 2023) have revealed increased cytotoxicity and a twofold increase in DNA damage compared to Fe_2O_3 or Fe_3O_4 particles, attributed to the increased and highly active surface of these particles (Karlsson et al., 2006; Loxham and Nieuwenhuijsen, 2019). Furthermore, while ambient concentrations of low-metallic brake pad formulations did not induce biological responses in a multicellular in vitro model of lung, the presence of anatase in non-asbestos formula was associated with decreased cell viability and pro-inflammatory activity following pseudo-air-liquid-interface exposures [11].

While the EURO 7 regulation focusses on PM_{10} emission values, smaller particles can also be generated during the braking process. Garg et al. reported the fraction of ultrafine particles of up to 33% of the airborne PM [19], which are not addressed in the EURO 7 legislation. Smaller particle sizes are of special concern, since the PM2.5 fraction is able to penetrate deep into the lungs and particles smaller than 0.1 μm can even deposit in the alveoli, from where they eventually reach the bloodstream via the blood-air barrier [20]. Metal containing nanoparticles are reportedly also able to penetrate to the central nervous system via the nasal route, followed by uptake and transport in the olfactory nerve [21,22].

Apart from heavy metals and minerals, brake wear emissions can emit other known pollutants, such as polycyclic aromatic hydrocarbons (PAH) and other harmful organic compounds, formed via thermal degradation of organic substances. The high local temperatures at the tribological interface of the brake can facilitate thermal degradation of the organic binding matrix, which is usually composed of modified phenol-formaldehyde resins [5]. Gasser et al. also reported an increased release of pro-inflammatory mediator interleukin-8 during strong braking, which they attributed to organic compounds and black carbon [18]. So far little is known on the organic emissions of brake wear and only a few studies have investigated this topic [23].

Due to the metallic nature of brake wear and the large differences in elemental composition in different brake lining types, not only the generated particle mass and numbers, but also the concentrations of heavy metals in particles is of utmost importance to assess the potential health threats of a specific pad. For this purpose, inductively coupled plasma tandem mass spectrometry (ICP-MS/MS) is a suitable technique for sensitive quantification of a large variety of elements in filter samples, as well as bulk brake lining material. Furthermore, the distribution of elements throughout different size ranges is important for the evaluation of potential health impairing effects. For this purpose, SEM/EDX analysis is a beneficial orthogonal technique for the detection of elements like Si and C that are not accessible by conventional ICP-MS/MS analysis, providing additional information about the distribution and homogeneity of brake wear markers over different size ranges.

The aim of this study was the comprehensive physical and elemental characterization of brake dust, emitted under standardized conditions, as close to those defined by the GTR24, providing a broader understanding of the chemical composition and the distribution of environmental and health impairing pollutants among different size ranges from coarse to ultrafine. To our knowledge this is the first in-depth characterization of brake dust on a modern dynamometer design exceeding the scope of measurements defined within the GTR24.

2. Methods and Materials

2.1. Brake dyno setup and test cycle procedure

Brake wear measurements were conducted utilizing a custom-built brake dyno (manufacturers: AiP automotive for construction and design; HDC Blueprints for Project management, automatization, construction and operation) designed to fulfill the specifications in the GTR24 [24] by the PMP of the UNECE. All requirements for the design of the brake dyno, except for the orientation of the brake housing, which is located vertical instead of horizontal, and the symmetry of the housing, which is slightly asymmetrical at the exit point. A constant volume sampler (CVS) was utilized to maintain a consistent cooling air flow throughout emission tests and isokinetic nozzles were installed in front of all sampling probes. Images of the brake dyno and its compartments are depicted in Fig. 1.

Original 330 mm by 24 mm brake discs, as well as a brake caliper fitting a 17-inch tire rim, were supplied by the original equipment manufacturer (OEM) of the simulated vehicle and were utilized for all measurements. The specifications for the simulated vehicle can be found in Table S1 in the supplementary information (SI). Whenever new brake pads were installed, brake discs were also changed to new discs. LM brake pads were directly supplied by the OEM and were tested together with commercially available NAO pads from the aftermarket. Thermoelements for monitoring brake disc temperatures were embedded according to the GTR24 with data being obtained with 10 Hz resolution. The WLTP brake cycle, comprising 303 individual brake events, was utilized for brake emission tests.

As required by the GTR24 a minimum of five WLTP brake cycles were conducted for the bedding of newly installed brake discs and pads before testing. The cooling air flow of the system was adjusted according to the GTR24, by determining the wheel load to disc mass ratio and measuring the corresponding temperatures during Trip #10 of the WLTP brake. Results from the cooling air speed adjustment, as well as the specific values for the simulated vehicle requested by the GTR24 are listed in Table S2 in the SI, while the brake disc temperatures during the WLTP brake cycle are plotted in Fig. S1 in the SI. Based on these results the CVS was set to a flow rate of 540 m^3/h for the LM pad and 720 m^3/h for the NAO pad.

2.2. Online measurements, gravimetry & filter sampling

The measurement setup for the determination of brake wear emissions and toxicity is illustrated in Fig. 2. All measurements required by the GTR24, except for the total particle counter (TPC), were conducted in the brake test cell, whereas all additional instruments were located in the control room outside of the test cell and were connected via two 12 mm outer diameter stainless steel tubes, depicted as green & red lines in Fig. 2.

A condensation particle counter (CPC) (SPC-D-19, AiP automotive), equipped with a catalytic stripper and a built-in dilution system, with a dilution factor of 1:100, acted as solid particle counter (SPC).

The green line was diluted 1:25 via a portable dilution system (Dekati eDiluter Pro, Dekati Ltd.), providing suitable particle concentrations for the downstream instrumentation. Clean air for dilution was supplied via a zero-air generator (AADCO 737–15, Tisch Environmental Inc.) to avoid contamination and influence on measurements results. A second CPC (Grimm 5420, Grimm Aerosol Technik GmbH & Co. KG,) was utilized as TPC and additional filter sampling for chemical analysis was conducted via a gravimetric filter holder (Dekati eFilter, Dekati Ltd.). Particle size-distributions in the range of 0.3 – 2.5 μm were measured with a resolution of 0.5 Hz via an Optical Particle Sizer (OPS) (Aerosol Particle Size Spectrometer LAP 322, Topas GmbH),

The red line was connected without any dilution to a Fast Aerosol Sizer (DMS500 Mk II, Cambustion Ltd.), measuring size distributions in the range of 5 nm – 1 μm with a resolution of 1 Hz.

Samples were drawn on a variety of filter materials. PTFE membrane filter discs with a diameter of 47 mm (Teflo 2 μm, 47 mm, Pall Corporation) were used for gravimetric measurements and ICP-MS analysis and were loaded in the PM_{10} and $PM_{2.5}$ filter holders, installed in the brake test cell. The Dekati eFilter was set to a flow of 10 L/min for sampling on 47 mm quartz fibre filters (Whatman QMA 47 mm, Cytiva), which were used for analysis of PAHs and 47 mm polycarbonate (PC) track-etched filters (Whatman, Nucleopore, 2 μm pore-size) for SEM/EDX analysis. For SEM/EDX analysis silica wafers (p-type boron dotted 5 ×5 mm, Ted Pella Inc.) and pure Nb substrates (EM-Tec NB12, ø

Fig. 1. Images from the initial installation of the custom-built brake dyno for emission measurements. 1. Brake enclosure 2. Sampling point, filter holder location and closet housing the SPC 3. CVS system.

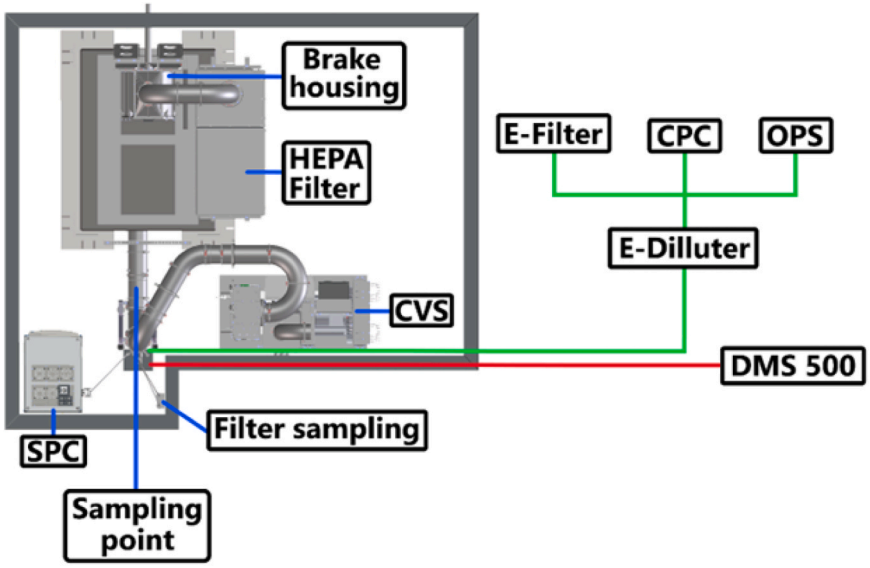

Fig. 2. Setup for the brake wear measurement campaign (top view). Sampling line 1 (green) was equipped with a $PM_{2.5}$ cyclone at the inlet, while sampling line 2 (red) was equipped with a PM_{10} cyclone, followed by a PM_1 cyclone for the DMS500. All instruments on the green line were diluted 1:25 by the E-Diluter. The DMS500 connected to the red line measured undiluted.

12 ×0.1 mm, 99.99 % Nb, Micro to Nano) were placed on top of the filters. These additionally sampled substrates were used for a variety of benefits giving a holistic overview of the sample. Silica wafers show a smooth, polished surface and excellent conductivity, offering a good substrate for high-resolution micrographs, excelling in the analysis of nanoparticles, while Nb plates are a more suitable medium for EDX analysis of small particles, where a portion of the electron beam can pierce the particles and excite x-ray transitions from the underlying substrate, falsifying the data. Both sample types potentially suffer from being a passive sampling approach, therefore being prone to altered size distributions of sampled particles. PC filters were also analyzed to compare particles found on Si wafers and Nb plates to an unaltered size distribution, ensuring a representative analysis. All analysed filters of the same type originated from the same batch. At least three blank filters were analysed for every filter type with each measurement technique.

Gravimetry was carried out by weighing filters before and after each WLTP brake cycle, using a micro-balance (Cubis MCA2.7S-2S00-F, Sartorius). Before each weighing filters were pre-conditioned at a relative humidity of 45 % and a temperature of 22 °C for 24 h in a climate-controlled chamber (pureGMC 18-EPA1065), equipped with a corona discharger for filter charge neutralization.

2.3. ICP-MS/MS analysis

Bulk material analysis of both brake pads, as well as the brake disc were carried out by grinding powder samples from the top layer of new pads. A tungsten carbide grinder was utilized to generate these powders, to avoid possible contamination with iron and other metals originating from the tools.

Loaded PTFE filters and powder samples were digested with a microwave assisted pressure digestion according to the VDI regulation 2267 [25] by placing the samples in PTFE vessels and adding 8 ml of 69 % HNO_3 (Rotipuran Supra, Carl Roth GmbH + Co. KG), followed by 2 ml of H_2O_2 (Rotipuran, Carl Roth GmbH + Co. KG),) and 10 µl of a mixed internal standard solution (100 µg/ml Bi, Ge, In, ^{4}Li, Lu, Rh, Sc, Tb, Agilent Technologies). Sealed samples were then heated in a ventilated microwave (MARS 5, CEM) following a pre-defined temperature gradient for 180 min. Before the analysis samples were diluted to a final volume of 50 ml with Millipore water (18.2 MΩ·cm at 25 °C) and filtered with syringe filters (Whatman Puradisc, pore size 0.2 µm, Cytiva).

Analysis was conducted with an Agilent 8900 triple quadrupole ICP-MS/MS. During the analysis a constant volume of an Yttrium standard

solution (High-Purity Standards) with a concentration of 0.5 mg/L was added via a peristaltic pump and a T-piece, to assess the signal drift and plasma stability. The utilized reaction gases and measured *m/z* values for ICP-MS/MS analysis are listed in Table S3 in the SI.

2.4. SEM/EDX analysis

SEM/EDX analysis of bulk brake wear linings was carried out by cutting small samples of approximately 5 × 10×5 mm from the friction surface of each pad. Prior to sampling the bedding process of 5 WLTP brake cycles was carried out to remove the brake in coating present on the NAO sample and to obtain a representative sample for a bedded brake pad.

Samples with a diameter of 12 mm were cut from PC filters and were transferred to SEM pin stubs with conductive high purity EDX suitable double-sided carbon adhesive pads in-between (Spectro-Tabs, Plano GmbH). Silica wafers and Niobium plates were secured to SEM pin stubs with conductive silver paint (EM-Tec AG15, Micro to Nano). Samples were then stored in a desiccator under vacuum for at least 24 h to ensure removal of volatile components hindering analysis. Wafer and Nb plate samples were left unaltered, while filter samples were coated with a thin carbon layer of approximately 10 nm, to minimize charging effects during analysis. A Q150T ES Plus sputter device (Quorum technologies) with a woven carbon fiber string (density 1.55 g/m, Quorum technologies) was used in pulsed cord evaporation mode for the application of a conductive carbon layer of approximately 10 nm.

SEM micrographs were taken with the Inlens and SE2 detectors of a Gemini Sem 360 (Carl Zeiss) field emission SEM at acceleration voltages of 0.75 – 1.5 kV. EDX analysis was conducted with an Ultim Max 40 EDX detector (Oxford Instruments) equipped with a thin polymer detector window and a Silicon drift detector, granting the ability to measure low-Z elements (Z > 6). EDX analysis of particles with a geometric diameter > 200 nm was carried out with an acceleration voltage of 12 kV, while particles smaller than 200 nm were analysed with 5 kV, to minimize piercing of the electron beam through the particles. The chosen acceleration voltages were based on simulations of electron penetration depths and X-ray excitation responses of particles in the Monte Carlo Casino software, as demonstrated in a previous study on brake- and rail wear particles emitted by subway trains [26].

At least 25 particles were measured for each filter and substrate type and in total more than 100 particles were analyzed for each brake pad.

2.5. GC-MS/MS analysis

From each quartz fiber filter five punches with a diameter of 8 mm were cut and extracted with 980 µl of acetone and 20 µl of a 5 µg/ml internal standard solution (PAH Analyzer Calibration Sample Kit, Agilent) containing five deuterated PAHs, in an ultrasonic bath for 60 min. Before analysis samples were filtered with PVDF syringe filters with a 0.2 µm pore size (Rotilabo®, Carl Roth) to remove particles prior to the injection into the system.

Filter extracts were measured for 27 different particle bound PAHs via an Agilent 8890/7000D triple quadrupole GC-MS/MS PAH analyzer with H_2 as carrier gas and an Agilent DB-EUPAH, 20 m × 0.18 mm, 0.14 µm column following the application note 5994–2192EN by the manufacturer [27]. An average recovery rate of 79.7 % was calculated for 12 PAHs by extraction of a certified reference material (ERM-CZ100 – Fine dust PM10-like, Joint Research Centre of the European Commission). The individual recovery rates for the individual PAHs are listed in Table S4 in the SI. Final PAH concentrations were obtained by correcting the measured concentrations for each PAH in the extracts with the corresponding recovery rate if applicable and with the average recovery rate for those where no value was available.

3. Results and discussion

3.1. Online measurements & gravimetric analysis

The averaged PM emission factors for three runs at the brake and vehicle level conducted with LM and NAO brake pads are listed in Table 1. PM data of the tested single front brake was multiplied with the volumetric flow of the CVS and was divided by the sampling air flow of the filters. The obtained total PM emissions during the WLTP brake cycle were then divided by a factor of 192, which is the total driven distance during the cycle in km, to obtain single front brake emission factors. The formula used for calculating emission factors (EF) of the front brake is given in Eq. 1.

$$EF_{front\ brake} = \frac{Flow_{CVS} \quad * PM}{Flow_{Filters} \quad * \quad 192\ km} \tag{1}$$

Vehicle level emission factors were calculated from emission factors (EF) of the single front brake following Eq. 2, which is adopted from the GTR 24. A standard brake force distribution (FAF) between front and rear axle with a share of the braking force applied to the front axle of 66 % of the total braking force was utilized, which is also the normal distribution of the simulated vehicle. The FAF is further multiplied by a factor of 0.5, since the brake force on the front axle is shared between the two front brakes. A friction braking share coefficient (c) of 1.0 was applied, which refers to the amount of electric recuperation in the deceleration of the vehicle, which is 1.0 per definition for vehicles with only an internal combustion engine.

$$EF_{vehicle} = \frac{EF_{front\ brake}}{FAF * \quad 0.5} * c \tag{2}$$

The LM pad emission factors at the vehicle level were found at 15.1 ± 0.1 mg/km of PM_{10}, which is 2.2 times higher than upcoming maximum permitted emission factor of 7 mg/km, while the NAO pad was 2.3 times higher than permitted from 2026 onwards, with a PM_{10} emission factor of 16.3 ± 0.4. The OEM LM pad showed single brake emission factors of 5.0 ± 0.1 mg/km for PM_{10} and of 1.8 ± 0.0 mg/km for $PM_{2.5}$. These values are well comparable to the most recent global interlaboratory study (ILS II), which reported average emission factors of 5.0 mg/km for PM_{10} and 1.9 mg/km for $PM_{2.5}$ with the friction pairing ILS II brake 1 with pad a (BR1Fa) with a LM pad and a slight lighter simulated vehicle weight of 1600 kg [28]. However, when comparing the average single brake emission factors of the aftermarket NAO pad, which was measured at 5.4 ± 0.1 mg/km of PM_{10} and 2.4 ± 0.1 mg/km of $PM_{2.5}$, to the values reported for the ILS II brake 1 with brake pad b (Br1Fb), which is the same vehicle as Br1Fa, but equipped with a NAO pad, emissions were significantly higher. For NAO pads Grigoratos et al. [28] reported an average of 2.2 mg/km of PM_{10} and 0.8 mg/km of $PM_{2.5}$, which is only 40.5 % of PM_{10} and 33.2 % of $PM_{2.5}$ found in this study. The ILS-II was chosen as reference point for PM and PN data, since it was the only study with a GTR compliant brake dynamometer at the time of this study. The Br1Fa and Br1Fb friction

Table 1
PN and PM emission factors of LM and NAO brake pads on the brake and vehicle level.

Brake pad	Emission level	TPN #/km	SPN #/km	PM_{10} mg/km	$PM_{2.5}$ mg/km
LM	Single front brake	4.51 ± 0.06 × 10^9	5.49 ± 0.11 × 10^9	5.0 ± 0.1	1.8 ± 0.0
	Vehicle	1.37 ± 0.02 × 10^{10}	1.65 ± 0.03 × 10^{10}	15.1 ± 0.1	5.4 ± 0.1
NAO	Single front brake	8.26 ± 0.1 × 10^9	8.50 ± 0.21 × 10^9	5.4 ± 0.1	2.4 ± 0.1
	Vehicle	2.50 ± 0.03 × 10^{10}	2.55 ± 0.06 × 10^{10}	16.3 ± 0.4	7.2 ± 0.2

pairings were deemed the most comparable, due to used vehicle weight and availability of data for both LM ad NAO pads. Observed differences can be partially attributed to differences in the simulated vehicle, wheel load to disc mass ratios and utilized friction pairing, the most likely explanation is the high metal content that was measured in the NAO brake lining of 15.8 %, which is unusual for such pad formulations (for further discussion see chapter 3.2 ICP-MS/MS analysis in the results section). When comparing the aftermarket NAO pads emission factors to those of an LM pad, which from the chemical characterization of the bulk brake lining material appears to be a more suitable classification for the pad, the results are again in a similar range compared to the ILS II. The obtained emission factors resulted in average $PM_{2.5}/PM_{10}$ ratios of 0.36 for the LM and 0.44 for the NAO pad, which is lower for the LM pad than the values of 0.42 to 0.45 reported by the ILS II. Since the temperature has a large influence on the emitted particle size [5], with higher temperatures resulting in smaller particles, the lower values for the LM pad are to be expected when comparing to the BR1Fa with a 10 °C higher required average braking temperature based on differences in wheel load to disc mass ratio. The NAO pad also reached a slightly higher maximum temperature of 122 °C, compared to 114.6 °C of the LM pad, which could explain the shift in emissions towards smaller particles.

The measured total particle number (TPN) and solid particle number (SPN) emissions averaged over three runs for the LM and the NAO pad are listed in Table 1 and the average measured particle #/cm^3 for individual WLTP brake cycles, measured by the SPC are given in Table S5 in the SI. PN emissions from the LM pad were 2.3 (TPN) and 2.5 (SPN) times higher than values of the ILS II, which reported a TPN of 1.93×10^9 #/km/brake and a SPN 2.19×10^9 #/km/brake on average [29]. For the NAO pad the emission were 8.8 (TPN) and 8.3 (SPN) higher than the ILS II that measured 9.37×10^8 #/km/brake (TPN) and 1.03×10^9 #/km/brake (SPN) for the BR1Fb. However, as discussed for the PM values, the NAO pad can be better compared to the ILS BR1Fa due to its high metal content, which would result in 4.3 (TPN) and 3.9 (SPN) times higher PN emissions. Since numerous variables, such as brake temperature, formulation of the brake pad, the wheel to disc mass ratio and the weight of the simulated vehicle have a strong impact on emitted particle sizes and numbers [12], it is difficult to compare PN data of two different configurations, with different vehicles, friction pairings and dynos. This is also reflected by the high range of TPN reported by the ILS II, which ranged from 9.1×10^8 #/km/brake to 1.1×10^{10} #/km/brake for the 7 tested brakes.

In general, it can be concluded that the used brake dyno setup, albeit minimally deviating from GTR24, yielded feasible emission factors, suitable for physical and chemical investigations.

The time resolved TPN concentrations measured with a CPC are plotted against the speed profile of the WLTP brake in Fig. 3, showcasing the high impact of strong braking events and rapid successions of medium brake events on PN emissions. As visible in the graph, braking events resulted in distinct peaks, well distinguishable from the background noise even for weaker braking events.

The DMS 500 revealed similar bimodal PN size distributions for both pads. The geometric mean diameter (GMD) for the LM pad was 123 nm, while the NAO pad had a GMD of 143 nm. Both pads showed a second mode around 86 nm, which was more distinct for the NAO pad. This is in good agreement with several published studies, which reported peaks for the particle number around 70 to 100 nm [30-32]. The OPS showed the optical mode between 300 and 400 nm, with PN levels steeply declining above the 400 nm mark. The OPS, in contrast to the DMS 500, measured more particles in the size bin around 400 nm than around 300 nm, which is likely caused by the lower counting efficiency of OPS instruments for smaller particles [33]. Up to particle sizes of 500 nm the DMS 500 data can be regarded as more accurate, due to the measurement principle being based on the electric mobility of particles, instead of their light scattering properties. PN size distributions for LM and NAO pads obtained by DMS 500 and OPS are shown in Fig. 4. The NAO pad produced a larger share of smaller particles compared to the LM pad, visible from the data obtained from the DMS 500, while the OPS showed no equal increase in large particles. This is also reflected by the higher $PM_{2.5}/PM_{10}$ ratio and the higher TPN and SPN values for the NAO pad, since small particles often have a large influence on PN, however, a negligible influence on PM. Overall the majority of particles was distributed between 40 and 300 nm, with a considerable fraction in the ultrafine region, and the GMD slightly above the ultrafine region. Some

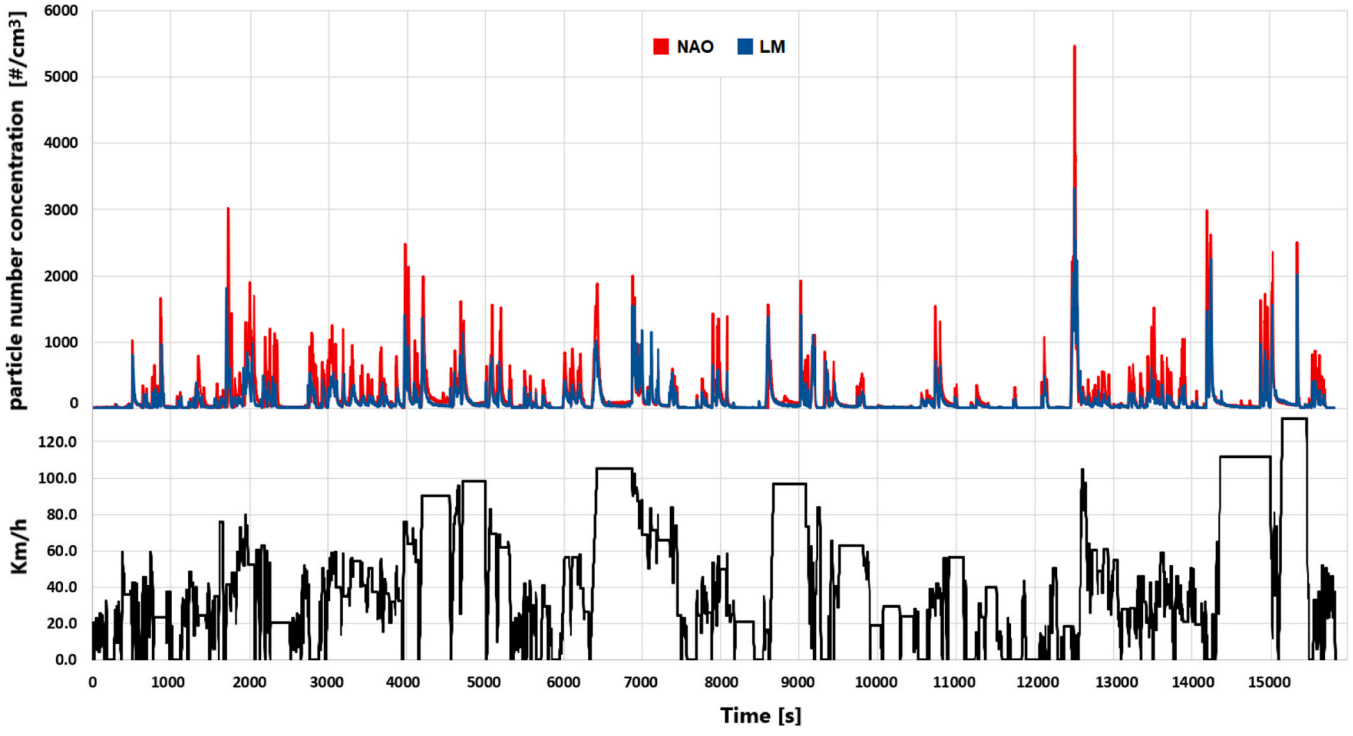

Fig. 3. TPN emissions of LM & NAO pads plotted against the WLTP brake speed profile.

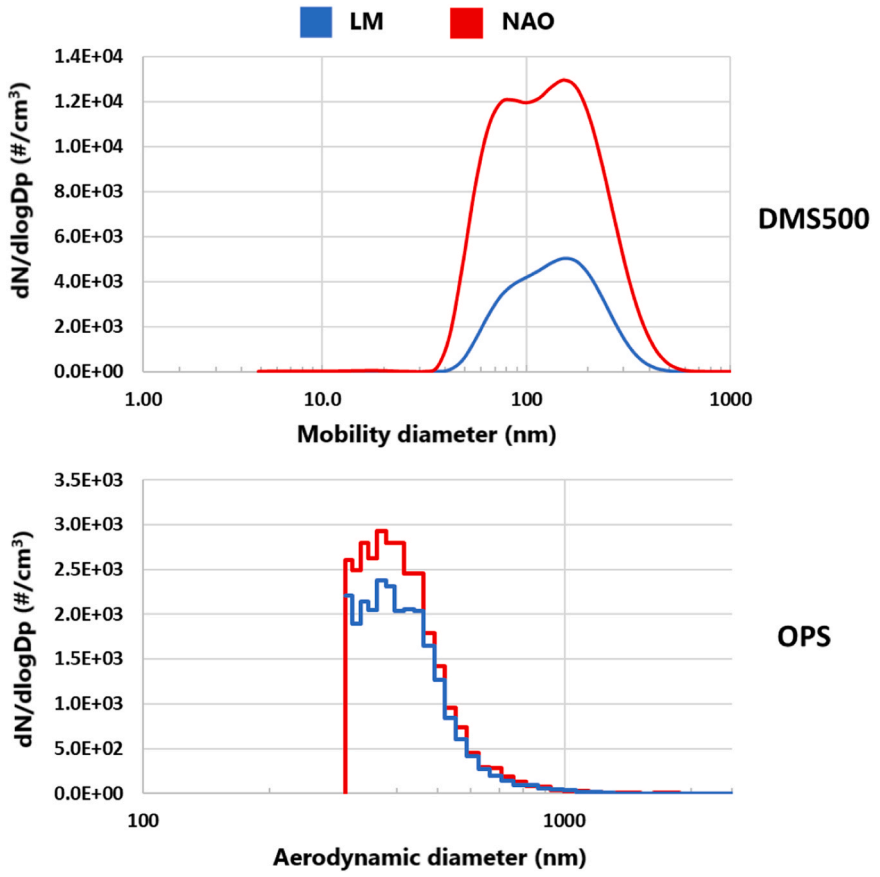

Fig. 4. Size distributions for LM & NAO pads averaged over the WLTP brake cycle measured via DMS500 (5–1000 nm) and OPS (300–2500 nm).

studies also reported smaller particles between 10 nm and 30 nm for strong braking events [30], which are linked to a critical temperature of the brake [12], where local temperatures at the friction interface are high enough to melt iron, leading to condensation of ultrafine particles in the cooling air stream [19]. Garg et al. further reported that 33 % of PM_{10} are emitted as ultrafine particles [19], showcasing the high abundance of small particles, which is in good agreement with results from this study. Since future amendments to the EURO 7 will feature maximum PN emission factors from 2030 onwards [4], such findings are not only critical regarding human health, but pose a large challenge to manufacturers, as ultrafine contribute greatly to PN emissions.

3.2. *ICP-MS/MS analysis*

The ICP-MS/MS analysis of bulk brake wear material and particles emitted during brake events, showed a significant difference in chemical composition for both brake pads. While the LM brake lining bulk material contained 23.9 ± 0.4 wt% of Fe, the particles in PM_{10} samples emitted by the LM pad averaged at 54.85 ± 0.85 wt%. The higher Fe content in filter samples can be explained by the fact that emitted particles are not solely originating from the brake pad, but are a mixture of wear from brake pad and brake disc. The Fe content of the utilized brake disc was measured at 81.8 ± 2.4 wt%, accounting for the elevated iron contents in the mixture of particles. This hypothesis is further supported by other heavy metal concentrations, such as Mn which increased from 0.1 ± 0.0 wt% in the LM bulk material to 0.29 ± 0.0 wt% in the filters, while the brake disc contained an average of 0.56 ± 0.01 wt% of Mn. The same shift in heavy metal concentrations was also observed in the opposite direction for several elements e.g. Cu, where the LM bulk material contained 0.50 ± 0.04 wt% of Cu, whereas the PM_{10} filter samples contained 0.29 ± 0.00 wt% of Cu and the brake disc only 0.28 ± 0.01 wt% of Cu. This trend is most noticeable for Zn concentrations, which lowered from 5.57 ± 0.20 % in the brake lining material to 1.46 ± 0.03 % in PM_{10} samples, most likely due to the absence of Zn in the brake disc, which contained only 0.03 ± 0.02 %. Such changes in elemental composition from the initial brake lining material to the emitted particles are well reported in literature and can not only be attributed to the abrasive wear of the brake disc, but also to a variety of other parameters, such as speed, severity and frequency of braking events and individual driving and braking behaviour [12,34]. Kukutschová listed the lower melting points of the common brake marker elements Cu, Zn and Sn compared to Fe as possible source for enrichment of mentioned metals in nanoparticles [12], while Österle proposed that local temperatures at the friction interface are high enough to cause thermal degradation, or even evaporation of the organic material [35], which would also account for elemental changes originating from the braking process.

ICP-MS/MS analysis of the NAO bulk material revealed average Fe contents of 13.9 ± 1.1 wt%. Such concentrations are unusually high for such a pad formulation and fit rather into the category of an LM pad, which generally contain between 10 - 30 % of Fe [7]. This result can also explain the high PM and PN emission factors found for this pad, since emission values of this pad were well in accordance with those of a LM pad formulation. The ICP-MS/MS results of the analyzed NAO pad showed, that manufacturers classifications of the brake pad types, which in most parts of the world is neither mandatory, nor regulated regarding their chemical composition, is not always sufficient to estimate the emission behavior of a certain brake pad.

Elemental compositions of PM_{10} filter samples showed an increased Fe content of 58.1 ± 1.4 %, which was even higher than the Fe content found in the LM samples, suggesting an increased wear of the brake disc. A high contribution of disc wear to the sampled particles is also

supported by the Cu contents measured in PM_{10} and $PM_{2.5}$ samples. The original brake lining material measured almost no copper, showing the impact of US EPAs restriction of copper usage in brake pads, while the emitted particles contained on average 0.21 ± 0.01 % (PM_{10}) and 0.20 ± 0.01 % ($PM_{2.5}$) of Cu.

Elemental compositions of the bulk brake lining material were similar to those found by Kukutschová, however, Cu concentrations were significantly lower than the reported 7.7 %, which can be attributed to changes in modern pads based on the ban on copper in the U.S [12].

Elemental compositions of PM_{10} and $PM_{2.5}$ filter samples for each pad were very similar showing an even distribution of elements over the coarse and fine size region. However, for Sn an enrichment in the $PM_{2.5}$ fraction of the LM pad was observed with 0.78 ± 0.05 wt% of Sn in the PM_{10} fraction and 1.03 ± 0.01 wt% in the $PM_{2.5}$ fraction. The effect was not present for the NAO pad, however, Sn concentrations were much lower than in the LM pad. Kukutschová et al. attributed the enrichment of certain elements such as Cu, Zn and Sn to the comparably low melting points of these metals, facilitating their potential to form nanoparticles at elevated temperatures [12]. This effect was only observable for Sn, which has an especially low melting point of 232 °C, which is plausible considering the generally low temperatures during the WLTP brake cycle. A second effect that was only noticeable for the LM pad was the enrichment of Cr. While the brake pad initially contained 0.37 ± 0.02 wt% and the brake disc 0.22 ± 0.01 wt% of Cr, the PM_{10} and $PM_{2.5}$ filters showed concentrations of 0.61 ± 0.01 wt% and 0.60 ± 0.01 wt% respectively. A general trend that was also observed, was the reduction in chemical differences in the composition of emitted particles for both PM_{10} and $PM_{2.5}$ in LM and NAO samples, due to mixing with wear from the brake disc, which was the same for both pads.

Fig. 5 illustrates the elemental changes from bulk materials to PM_{10} samples caused by the contribution of brake disc wear. The numerical values for chemical compositions of initial brake lining materials, as well as the cast iron brake disc measured via ICP-MS/MS, are listed in Table 2, while the chemical compositions in PM_{10} and $PM_{2.5}$ samples are given in Table 3.

Average emission factors for heavy metals were calculated from the gravimetric and ICP-MS/MS results and are plotted in Fig. 6, and the numerical values are listed in Table S6 in the SI. On average the PM_{10} emission factors of the LM pad were 8.3 ± 0.1 mg/km of Fe and 44.9 ± 0.3 µg/km of Cu, while the NAO pad exhibited emission factors of 9.5 ± 0.2 mg/km for Fe and 33.6 ± 1.1 µg/km of Cu. A literature review by Grigoratos and Martini summarized the emission factors for heavy metals reported in several studies and found Fe emission factors of up to 1 mg/km for light duty vehicles and Cu emission from 50 to 700 µg/km [5]. Results from this study were substantially higher than Fe emission factors reported in the literature review by Grigoratos and Martini, showing that the PM_{10} emission factors of previously published studies still have to be put into context with modern dyno designs and GTR24 compliant measurements.

Especially high copper emission values are of concern, considering its massive accumulation in the environment [10] and human exposure to airborne copper particles. Therefore, it is a positive trend that copper contents of brake pads are globally declining, most likely due to the EPA regulations. This can be seen by the analysis of the bulk brake lining material, which showed the compliance of both pads to the current regulations and the NAO pad being almost completely copper free. As a result of these changes in brake pad formulations current Cu emissions from brake pads might be overestimated, based on results of older

Table 2
Elemental composition of brake bulk lining and brake disc material measured via ICP-MS/MS.

Element wt%	LM Pad	NAO Pad	Brake disc
Fe	23.9 ± 0.4	13.9 ± 1.0	81.8 ± 2.4
Cu	0.50 ± 0.04	0.01 ± 0.00	0.28 ± 0.01
Cr	0.37 ± 0.02	0.04 ± 0.00	0.22 ± 0.01
Mn	0.10 ± 0.00	0.07 ± 0.01	0.56 ± 0.01
Al	0.48 ± 0.03	1.56 ± 0.03	0.08 ± 0.02
Zn	5.57 ± 0.20	0.05 ± 0.02	0.03 ± 0.02
Ba	1.59 ± 0.02	0.02 ± 0.00	0.00 ± 0.00
Mg	4.12 ± 0.09	9.62 ± 0.08	0.01 ± 0.00
Ni	0.02 ± 0.00	0.01 ± 0.00	0.08 ± 0.00
V	0.01 ± 0.00	0.03 ± 0.00	0.01 ± 0.01
Mo	0.01 ± 0.00	0.00 ± 0.00	0.03 ± 0.00
Sn	2.86 ± 0.15	0.19 ± 0.04	0.08 ± 0.02
S	2.84 ± 0.30	2.31 ± 0.04	0.12 ± 0.01
Total wt% of heavy metals	33.8 ± 0.8	15.8 ± 1.2	83.2 ± 2.4

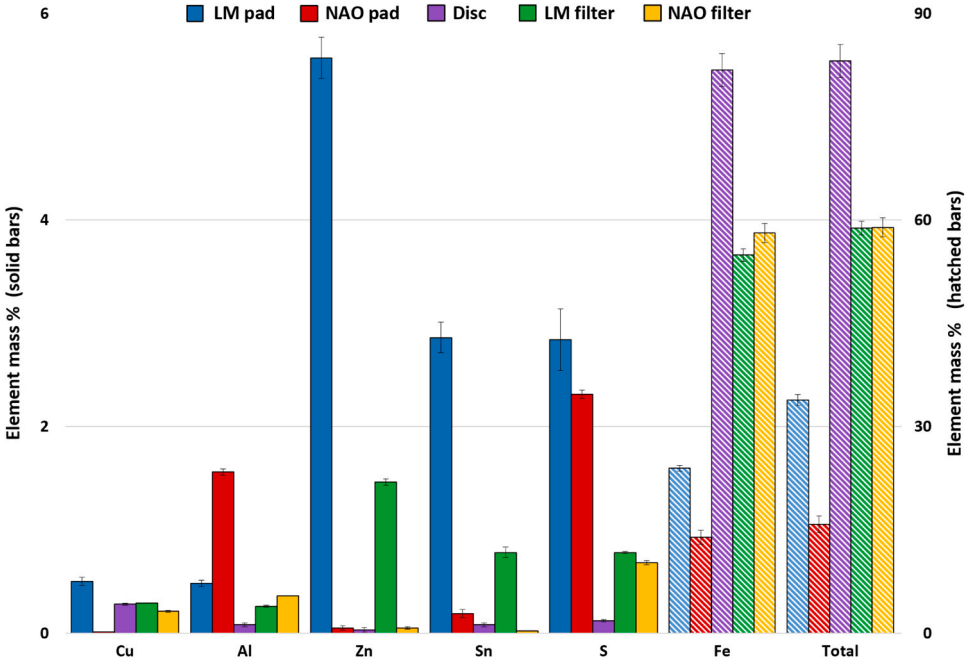

Fig. 5. Weight percentages for selected elements analyzed via ICP-MS/MS, illustrating the contribution of the brake disc to PM_{10} samples. Solid bars are plotted on the left Y-Axis, while hatched bars are plotted on the right Y-Axis.

Table 3
Elemental composition of brake wear particles from LM and NAO filter samples analyzed via ICP-MS/MS.

Element mass %	LM Pad		NAO Pad	
	PM_{10}	$PM_{2.5}$	PM_{10}	$PM_{2.5}$
Fe	54.9 ± 0.9	54.5 ± 1.2	58.1 ± 1.4	57.2 ± 1.8
Cu	0.29 ± 0.00	0.28 ± 0.00	0.21 ± 0.01	0.20 ± 0.01
Cr	0.61 ± 0.01	0.60 ± 0.01	0.13 ± 0.00	0.13 ± 0.00
Mn	0.29 ± 0.00	0.29 ± 0.00	0.31 ± 0.01	0.31 ± 0.01
Al	0.26 ± 0.01	0.24 ± 0.00	0.36 ± 0.00	0.28 ± 0.01
Zn	1.46 ± 0.03	1.45 ± 0.02	0.05 ± 0.01	0.01 ± 0.02
Ba	0.41 ± 0.01	0.40 ± 0.01	0.01 ± 0.00	0.00 ± 0.00
Mg	0.90 ± 0.04	0.90 ± 0.03	1.63 ± 0.02	1.72 ± 0.09
Ni	0.05 ± 0.00	0.05 ± 0.00	0.05 ± 0.00	0.05 ± 0.00
V	0.01 ± 0.00	0.01 ± 0.00	0.01 ± 0.00	0.01 ± 0.00
Mo	0.02 ± 0.00	0.02 ± 0.00	0.03 ± 0.00	0.03 ± 0.00
Sn	0.78 ± 0.05	1.03 ± 0.01	0.02 ± 0.00	0.02 ± 0.00
S	0.78 ± 0.01	0.78 ± 0.03	0.68 ± 0.02	0.71 ± 0.04
Total % of heavy metals	58.8 ± 1.0	58.6 ± 1.2	58.9 ± 1.4	58.0 ± 1.9

studies with other test setups and older brake linings types.

Fe rich particles are also reported to induce several adverse health effects following long-term inhalation [14-16]. This places further emphasis on the importance of the high PN of brake wear found in the submicron mode for both analyzed pads.

Additionally, brake dust is normally mixed with other heavy metals, such as Cu, Mn, Cr, Sn and V, complicating the assessment of the toxicological impact of such particles. Here especially the high Cr [36] and Zn [37] contents found in the LM pad, together with the higher percentages of Cu are of concern.

3.3. SEM/EDX analysis

SEM/EDX analysis of bulk material cut-outs showed a high inhomogeneity of the elemental distribution in both samples. The NAO pad displayed a more uniform distribution of iron throughout the sample, while the LM sample showed large flakes of iron. Furthermore, the NAO pad showed a higher abundance of steel fibres, which explains the more pronounced influence of brake disc wear on the chemical profile of emitted particles observed with ICP-MS/MS, since the addition of higher amounts of these fibres tends to increase rotor wear [38]. Primary plateaus, consisting of wear resistant compounds in the pad such as steel fibers and secondary plateaus, formed from compacted debris, were visible in both samples as part of the generated tribolayer [39,40]. Chemical mappings of LM and NAO bulk material cut-outs, with visible Fe flakes for the LM pad and a steel fibers in the NAO sample are shown in Fig. 7.

SEM micrographs of brake wear showed rough edged, splintery particles, typical for abrasion processes, which were found in all samples of both brake pads. Two main types of morphology, spherical and flake like particles, were commonly found throughout all samples. Flake like particles, shown with a yellow size marker in Fig. 8, were mainly found for particles > 1 µm, while spherical shaped particles, depicted in green, where found among all sizes. The images in Fig. 8 show particles from a LM sample, however, both pad types frequently displayed the two morphologies. Wahlström et al. attributed the flake like particle morphology to wear from the brake disc due to the absence of typical brake markers, such as Ti, Cu and Al [41]. However, SEM/EDX analysis also revealed flakes showcasing high concentrations of brake markers, such as Zn, which were not present in the bulk ICP-MS/MS analysis of the brake disc. Instead flake like particles exhibited similar chemical compositions as spherical particles.

EDX measurements showed high Fe contents in almost all particles, ranging between 43 % and 75 %. Two elements, C and O, were also found at high concentrations in all particles, with O ranging from 19 - 39 % and C from 2.5 - 32 %. An overview of morphologies and elemental compositions of NAO particles is given in Fig. 9, while a more detailed micrograph and elemental composition derived from the EDX spectra for a LM particle is presented in Fig. 10. Overall ranges of elements in particles were large, and no changes were observed in this spread across different analyzed sizes. This is in accordance with ICP-MS/MS data, which showed virtually no differences in PM_{10} and $PM_{2.5}$ samples. SEM/EDX analysis confirmed that this observation was true throughout all

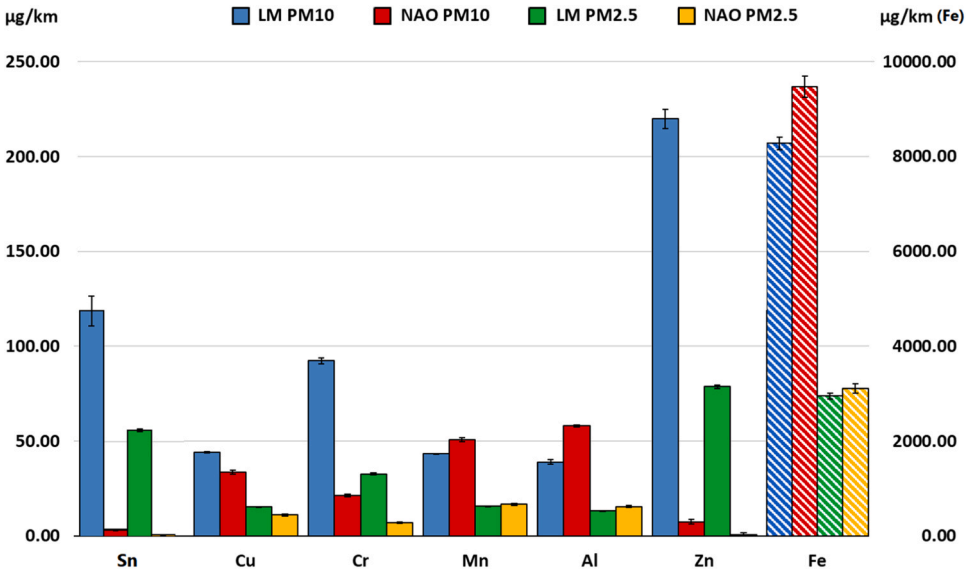

Fig. 6. Heavy metal emission factors at the vehicle level. Hatched bars for iron levels are plotted on the right Y-Axis, while solid bars are plotted on the left Y-Axis.

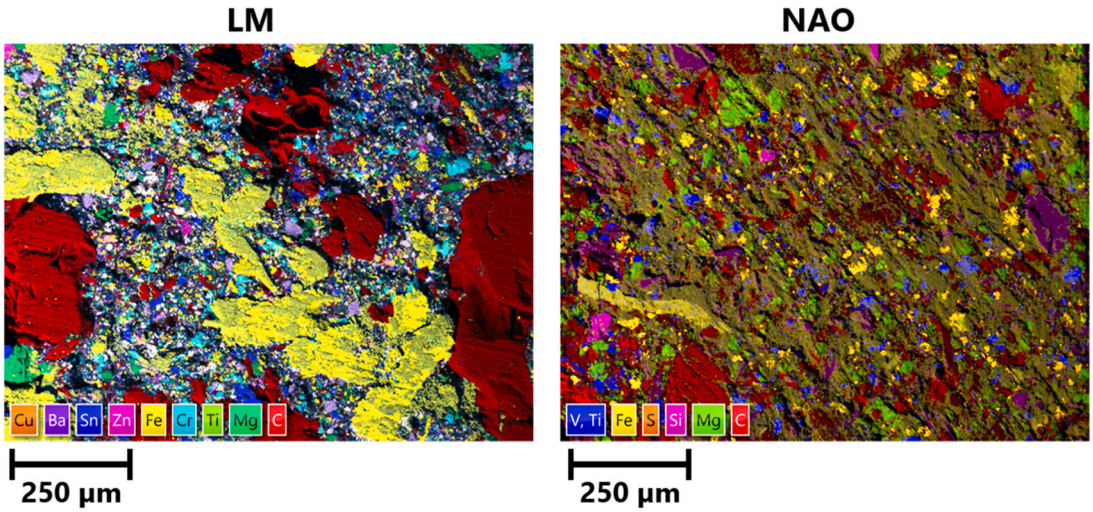

Fig. 7. Chemical mapping of bulk brake pad linings at 100 x magnification measured via SEM/EDX.

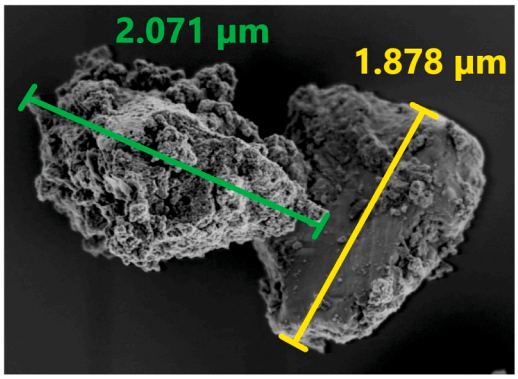

Fig. 8. SEM micrograph of spherical (green) and flake-like (yellow) shaped particles commonly found in brake-wear samples. Particles shown originated from the LM brake pad.

size ranges, even down to the ultrafine region, with particles as small as 30 nm consisting of 50 % of iron or more. These small particles are specifically of concern, since particles < 2.5 µm can penetrate deeply into the lung and nanoparticles smaller than 100 nm can eventually reach the bloodstream via entry route through the blood-air-barrier [20, 42], or uptake via the nasal route followed by translocation through the olfactory nerve [21,22].

Interestingly, only a few particles with Fe concentrations of 15 – 30 % and 80 – 90 % were found that matched the initial iron contents of the two analyzed brake pads and the brake disc. Instead, most particles in samples of both pads showed iron concentrations between 50 % and 60 %, which is similar to the average Fe contents found with ICP-MS/MS. This would contradict the hypothesis that the iron contents found with ICP-MS/MS are the result of a mixture of highly iron containing particles from the brake rotor and particles containing lower amounts of Fe from the pads and instead suggest strong changes in the chemical composition for both friction partners. This could potentially also explain the wide range of iron contents, with some effects enhancing the concentration of iron in the pads, like the thermal degradation of the polymeric binding matrix and, on the other hand, effects that lead to emission of particles with lowered Fe content from the brake disc, such as tribo-oxidation. The severance of these effects is visible for the particles F and G in Fig. 9. Particle F featured 74.1 % of Fe and 0.7 % of Mg, while particle G contained 70.6 % of Fe and 1.6 % of Mg. The presence of Mg implies that these particles originated from the NAO pad, since the brake disc contained only 0.01 % of Mg based on ICP-MS results. This would indicate that particles with Fe concentrations of up to 75 % are emitted by a pad that, on average, contained only 17.06 ± 0.66 % of iron (based on ICP-MS/MS). A feasible explanation for this phenomenon would be the chipping of highly Fe containing compounds of the pad, such as the observed steel fibres. As illustrated in Fig. 7 the pads displayed a heterogenous distribution of elements with visible iron rich flakes and fibers that can be abraded by mechanical processes from the tribolayer forming at the friction surface. However, only limited amounts of particles below the average Fe concentrations of the pads were found, which suggest that parts of the pad that are lower in iron still undergo significant changes in their composition, or that they are emitted in larger particles not captured on the filters.

3.4. GC-MS/MS analysis

Only 4 substances of the 27 measured PAH in the GC-MS/MS method were found in the filter samples of both brakes at concentrations above the LOD. 1-Methylphenanthrene was detected in LM and NAO samples, at concentrations below the LOQ, while Phenanthrene, Fluoranthene and Pyrene were found at quantifiable concentrations. In total, only 3 and 4 ring structures were observed under the WLTP brake, which is in agreement with results from Alves et al., who reported no detected PAH with five or more benzenic rings [23]. While the WLTP brake provides a wide range of driving conditions for emission measurements, not all real-world scenarios are represented by this cycle. In general- the WLTP brake comprises moderate brake temperatures, which can be exceeded by far in certain situations, such as long deceleration events when driving down a slope. PAH are normally formed at temperatures > 300 °C (Odinga et al., 2021) and can be released during strong braking events, or several braking events in a short succession, where high local temperatures are achieved at the friction interface. Qi and Day demonstrated that brake interface temperatures, which they reported around 400 °C, were substantially higher than average disc temperatures, which ranged around 120 °C (Qi and Day, 2007), by comparing an exposed wire thermocouple to a conventional sliding thermocouple. Especially in mountainous areas where long and steep declines are common, PAH emissions could potentially be significantly higher and also other polycyclic core structures, like 5 ring PAH could be generated.

The NAO pad emitted lower amounts of PAH under tested conditions, even though measured temperatures were higher than for the LM pad and a pad with higher organic content is prone to form more organic degradations products. However, this pad showed an uncommon chemical composition and a higher rotor wear was observed from ICP-MS/MS results. Furthermore, the higher cooling air flow could lead to

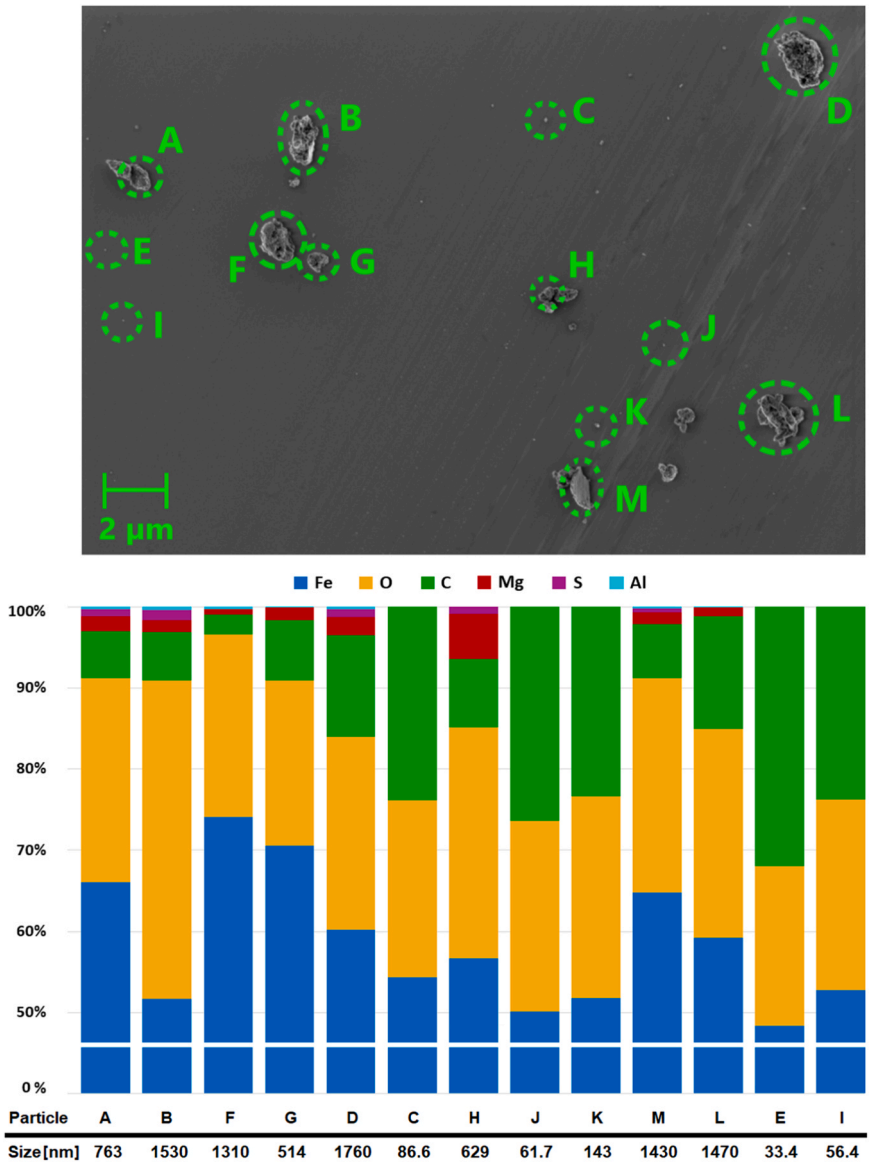

Fig. 9. SEM overview and bar chart of elemental compositions, derived from the associated EDX spectra of NAO particles on a Si wafer measured at 5 kV.

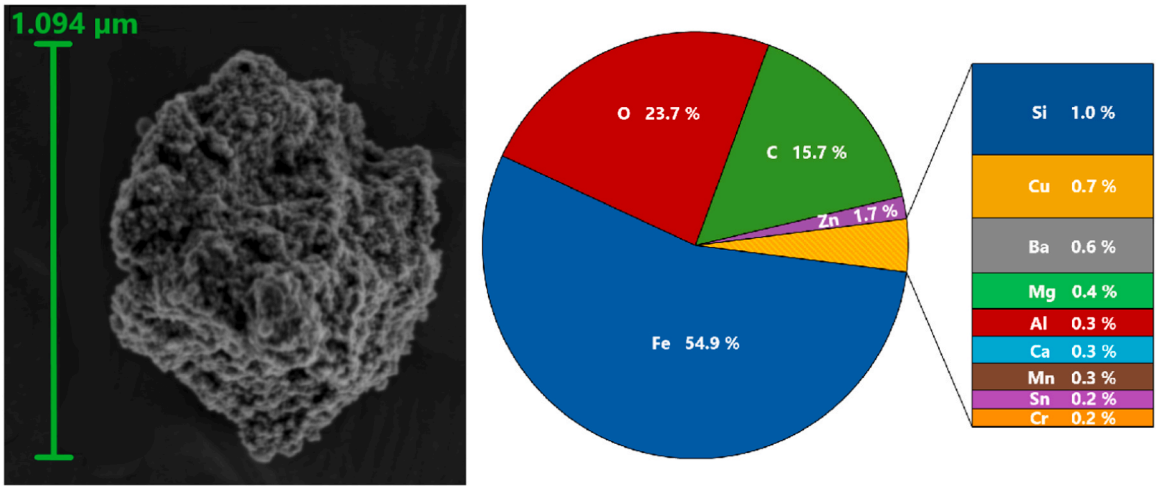

Fig. 10. SEM micrograph and pie chart derived from the associated EDX spectrum of a spherical LM particle on a Nb substrate measured at 12 kV.

changes in concentrations for volatile and semi volatile substances due to higher dilution in the tunnel. The PM_{10} and $PM_{2.5}$ emission factors of measured PAH at the vehicle level are listed in Table 4.

4. Conclusions

The custom-built brake dynamometer that was utilized in this study and which was tailored to fulfill the requirements of the GTR24 for the measurement of brake emissions as close as possible, yielded reliable and useful results. PM_{10} emission factors at the vehicle level were found at 15.1 ± 0.1 and 16.3 ± 0.4 mg/km, while $PM_{2.5}$ was found at 5.4 ± 0.1 and 7.2 ± 0.2 mg/km for the two tested brake pads. PN emitted from single brakes was measured in the range of 10^9 #/km with the geometric mean diameter found at 123 (LM pad) and 143 nm (NAO pad) and a second mode for both pads at 86 nm. The emission values of the tested LM pad were in accordance with data from the latest global interlaboratory study, while values obtained for the aftermarket bought NAO pad were unusually high due to an increased iron content of 13.9 %. When comparing the results to the class of LM pads, which fitted better from the chemical compositions the pad yielded comparable result, showing that manufacturers pad type classifications are not always sufficient in estimating emission levels of a certain brake pad.

Chemical analysis of the obtained brake dust revealed highly metallic particles with 54.9–58.1 % of PM_{10} emitted as iron and other heavy metals, such as Cu, Cr, Mn and Zn present in varying concentrations for the two pads. Based on the elemental distribution a high contribution from the wear of the brake disc was observed. Fe emission factors found in this study were 8–9 times higher than previously published studies from non GTR 24 compliant brake dynamometers. In contrast, this study indicates that current Cu emissions from brake pads might be overestimated, based on recent trends in brake pad formulations and differences in emission test setups.

SEM/EDX analysis revealed rough edged surfaces that are typical for abrasion derived particles, with two common morphologies, round and flake-like, displayed throughout all samples. EDX single particle elemental spectra showed high ranges of Fe found between 43 % and 75 % with no noticeable difference within the different size ranges.

Four different PAH species were identified in emissions from both pads, however, no 5-ring or larger PAH structures were found, probably due to the moderate temperatures of the WLTP brake test cycle.

Results from this study highlight the necessity of reducing brake wear emissions and put an emphasis on the importance of physical and chemical characterization of emitted particles. To our knowledge this is the first comprehensive characterization of brake dust, emitted from a GTR24 based brake dynamometer, providing a broader understanding of the chemical composition and the distribution of environmental and health impairing pollutants under standardized test procedures, opening new possibilities for developing policy responses to NEE.

Environmental Implication

Non-exhaust emissions presently pose the largest portion of particulate emissions from automotive traffic, with brake wear largely contribution to anthropogenic heavy metal emissions, such as Fe and Cu. Many studies have underlined the potential environmental and health impacts of brake wear, however, the detailed physical and chemical properties of brake wear particles under standardized, real-world conditions remain to be studied in-depth. For this reason, particles emitted from a well-controlled custom-built brake dyno were studied under the real-world driving conditions of the WLTP brake cycle to deepen the knowledge on the chemical and physical properties of brake wear.

CRediT authorship contribution statement

Mohammad Saraji-Bozorgzad: Writing – review & editing, Investigation, Conceptualization. **Carsten Neukirchen:** Writing – review & editing, Writing – original draft, Visualization, Validation, Methodology, Investigation, Formal analysis, Data curation, Conceptualization. **Ajit Mudan:** Investigation. **Michael Mäder:** Methodology, Investigation. **Ralf Zimmermann:** Supervision, Project administration, Funding acquisition. **Christian Trapp:** Supervision, Project administration, Funding acquisition. **Thomas Adam:** Supervision, Project administration, Funding acquisition. **Sebastiano Di Bucchianico:** Writing – review & editing, Writing – original draft. **Johannes Becker:** Writing – review & editing, Writing – original draft. **Philipp Czasch:** Methodology.

Table 4
PAH emission factors at the vehicle level calculated from PM_{10} and $PM_{2.5}$ filter samples. PAH stated as <LOQ were detected at concentrations above the LOD.

PAH in ng/km	LM Pad		NAO Pad	
	PM_{10}	$PM_{2.5}$	PM_{10}	$PM_{2.5}$
Phenanthrene	44.1 ± 5.6	< LOQ	31.9 ± 1.5	< LOQ
1-Methylphenanthrene	< LOQ	< LOQ	< LOQ	< LOQ
Fluoranthene	32.0 ± 2.8	17.5 ± 0.4	39.9 ± 0.7	18.9 ± 0.6
Pyrene	14.7 ± 1.3	3.8 ± 0.5	18.9 ± 0.6	10.0 ± 2.2

Declaration of Competing Interest

The authors declare the following financial interests/personal relationships which may be considered as potential competing interests. Thomas Adam reports financial support was provided by dtec.bw - NextGenerationEU. Thomas Adam reports financial support was provided by ULTRHAS - H2020. If there are other authors, they declare that they have no known competing financial interests or personal relationships that could have appeared to influence the work reported in this paper.

Acknowledgments

Funding: This work was funded by dtec.bw – Digitalization and Technology Research Center of the Bundeswehr [project MORE]. Dtec.bw is funded by the European Union – NextGenerationEU. This research was also supported by the project ULTRHAS – ULtrafine particles from TRansportation – Health Assessment of Sources, a project funded under the EU's Research and Innovation programme Horizon 2020, Grant Agreement No. 955390. We acknowledge financial support by Universität der Bundeswehr München.

GC-MS/MS analysis was supported by student Bastian Lorson, as part of his bachelor thesis.

Appendix A. Supporting information

Supplementary data associated with this article can be found in the online version at doi:10.1016/j.jhazmat.2024.136609.

Data availability

Data will be made available on request.

References

[1] Giechaskiel, B., Maricq, M., Ntziachristos, L., Dardiotis, C., Wang, X., Axmann, H., et al., 2014. Review of motor vehicle particulate emissions sampling and measurement: From smoke and filter mass to particle number. J Aerosol Sci 67, 48–86. ⟨https://www.sciencedirect.com/science/article/pii/S0021850213001961⟩.

[2] Fussell, J.C., Franklin, M., Green, D.C., Gustafsson, M., Harrison, R.M., Hicks, W., et al., 2022. A review of road traffic-derived non-exhaust particles: emissions, physicochemical characteristics, health risks, and mitigation measures. Environ Sci Technol 56 (11), 6813–6835. ⟨https://www.ncbi.nlm.nih.gov/pmc/articles/PMC9178796/⟩.

[3] Piscitello, A., Bianco, C., Casasso, A., Sethi, R., 2021. Non-exhaust traffic emissions: Sources, characterization, and mitigation measures. Sci Total Environ 766, 144440. ⟨https://www.sciencedirect.com/science/article/pii/S0048969720379717⟩.

[4] International Council on clean transportation 2024. Euro 7: The new emission standard for light- and heavy-duty vehicles in the European Union (Accessed 27 August 2024) 2024. ⟨https://theicct.org/wp-content/uploads/2024/03/ID-116-%E2%80%93-Euro-7-standard_final.pdf⟩.

[5] Grigoratos, T., Martini, G., 2014. Non-exhaust traffic related emissions - brake and tyre wear PM: literature review. JRC Sci Policy Rep. https://doi.org/10.2790/21481.

[6] European parliament, 2024. Euro 7: Deal on new EU rules to reduce road transport emissions Parlament.

[7] Grigoratos, T., Martini, G., 2015. Brake wear particle emissions: a review. Environ Sci Pollut Res Int 22 (4), 2491–2504. ⟨https://www.ncbi.nlm.nih.gov/pmc/articles/PMC4315878/⟩.

[8] US EPA, 2015. Copper-Free Brake Initiative | US EPA. ⟨https://www.epa.gov/npdes/copper-free-brake-initiative⟩ (accessed 13 May 2024).

[9] Sinclair Rosselot, K., 2006. Copper released from brake lining wear in the san francisco bay area. Process Profiles. ⟨www.suscon.org/pdfs/bpp/pdfs/BrakeSourcesReportFinal01-30-06a⟩.

[10] Hulskotte, J.H.J., van der Gon, H.A.C.D., Visschedijk, A.J.H., Schaap, M., 2007. Brake wear from vehicles as an important source of diffuse copper pollution. Water Sci Technol 56 (1), 223–231. https://doi.org/10.2166/wst.2007.456.

[11] Barosova, H., Chortarea, S., Peikertova, P., Clift, M.J.D., Petri-Fink, A., Kukutschova, J., et al., 2018. Biological response of an in vitro human 3D lung cell model exposed to brake wear debris varies based on brake pad formulation. Arch Toxicol 92 (7), 2339–2351. https://doi.org/10.1007/s00204-018-2218-8.

[12] Kukutschová, J., Moravec, P., Tomášek, V., Matějka, V., Smolík, J., Schwarz, J., et al., 2011. On airborne nano/micro-sized wear particles released from low-metallic automotive brakes. Environ Pollut (Barking, Essex 1987) 159 (4), 998–1006. ⟨https://www.sciencedirect.com/science/article/pii/S0269749110005476⟩.

[13] Karlsson, H.L., Gustafsson, J., Cronholm, P., Möller, L., 2009. Size-dependent toxicity of metal oxide particles–a comparison between nano- and micrometer size. Toxicol Lett 188 (2), 112–118. ⟨https://www.sciencedirect.com/science/article/pii/S0378427409001611⟩.

[14] Maher, B.A., González-Maciel, A., Reynoso-Robles, R., Torres-Jardón, R., Calderón-Garcidueñas, L., 2020. Iron-rich air pollution nanoparticles: an unrecognised environmental risk factor for myocardial mitochondrial dysfunction and cardiac oxidative stress. Environ Res 188, 109816. https://doi.org/10.1016/j.envres.2020.109816.

[15] Sobolewski, M., Conrad, K., Marvin, E., Eckard, M., Goeke, C.M., Merrill, A.K., et al., 2022. The potential involvement of inhaled iron (Fe) in the neurotoxic effects of ultrafine particulate matter air pollution exposure on brain development in mice. Part Fibre Toxicol 19 (1), 56. https://doi.org/10.1186/s12989-022-00496-5.

[16] Stueckle, T.A., Davidson, D.C., Derk, R., Kornberg, T.G., Schwegler-Berry, D., Pirela, S.V., et al., 2017. Evaluation of tumorigenic potential of CeO2 and Fe2O3 engineered nanoparticles by a human cell in vitro screening model. NanoImpact 6, 39–54. ⟨https://www.sciencedirect.com/science/article/pii/S2452074816300994⟩.

[17] Forest, V., Pourchez, J., 2023. Biological effects of brake wear particles in mammalian models: a systematic review. Sci Total Environ 905, 167266. https://doi.org/10.1016/j.scitotenv.2023.167266.

[18] Gasser, M., Riediker, M., Mueller, L., Perrenoud, A., Blank, F., Gehr, P., et al., 2009. Toxic effects of brake wear particles on epithelial lung cells in vitro. Part Fibre Toxicol 6 (1), 30. ⟨https://particleandfibretoxicology.biomedcentral.com/articles/10.1186/1743-8977-6-30⟩.

[19] Garg, B.D., Cadle, S.H., Mulawa, P.A., Groblicki, P.J., Laroo, C., Parr, G.A., 2000. Brake wear particulate matter emissions. Environ Sci Technol 34 (21), 4463–4469. https://doi.org/10.1021/es001108h.

[20] Bachler, Losert, G., Umehara, S., Goetz, Y., von, N., Rodriguez-Lorenzo, L., Petri-Fink, A., et al., 2015. Translocation of gold nanoparticles across the lung epithelial tissue barrier: Combining in vitro and in silico methods to substitute in vivo experiments. Part Fibre Toxicol 12 (1), 18. ⟨https://particleandfibretoxicology.biomedcentral.com/articles/10.1186/s12989-015-0090-8⟩.

[21] Fortoul, T., V. Rodríguez-Lara, A. González-Villalva, M. Rojas-Lemus, L. Colín-Barenque, P. Bizarro-Nevares et al., 2015. Health Effects of Metals in Particulate Matter. ⟨https://www.semanticscholar.org/paper/Health-Effects-of-Metals-in-Particulate-Matter-Fortoul-Rodr%C3%ADguez-Lara/9e1dcb26db219f654d2ab5e1a1c301fe25a25661#citing-papers⟩.

[22] Hopkins, L.E., Laing, E.A., Peake, J.L., Uyeminami, D., Mack, S.M., Li, X., et al., 2018. Repeated iron-soot exposure and nose-to-brain transport of inhaled ultrafine particles. Toxicol Pathol 46 (1), 75–84. ⟨https://pubmed.ncbi.nlm.nih.gov/28914166/⟩.

[23] Alves, C., Evtyugina, M., Vicente, A., Conca, E., Amato, F., 2021. Organic profiles of brake wear particles. Atmos Res 255, 105557. ⟨https://www.sciencedirect.com/science/article/pii/S0169809521001095⟩.

[24] UNECE, 2024. ECE/TRANS/WP.29/GRPE/2023/4 | UNECE - Proposal for a new UN GTR on Laboratory Measurement of Brake Emissions for Light-Duty Vehicles. ⟨https://unece.org/transport/documents/2023/01/informal-documents/clean-pmp-proposal-amend-ecetranswp29grpe20234⟩ (Accessed 15 March 2024).

[25] VDI 2267 Part 15:2019–12. Determination of suspended matter in ambient air - Measurement of the element concentration after sampling on filters - Determination of Al, As, Ba, Ca, Cd, Co, Cr, Cu, Fe, K, Mg, Mn, Na, Ni, Pb, Sb, Se, Sn, Tl, V, and Zn by GF-AAS, ICP-OES, or ICP-MS.

[26] Neukirchen, C., Meiners, T., Bendl, J., Zimmermann, R., Adam, T., 2024. Automated SEM/EDX imaging for the in-depth characterization of non-exhaust traffic emissions from the Munich subway system. Sci Total Environ 915, 170008. ⟨https://www.sciencedirect.com/science/article/pii/S0048969724001426⟩.

[27] Anastasia A. Andrianova and Bruce D. Quimby, Agilent Technologies. Optimized PAH Analysis Using Triple Quadrupole GC/MS with Hydrogen Carrier (Accessed 24 January 2024). ⟨https://www.agilent.com/cs/library/applications/application-polycyclic-aromatic-hydrocarbons-pah-gcms-gc-tq-gcmsms-5994–2192EN-agilent.pdf⟩.

[28] Grigoratos, T., Mathissen, M., Vedula, R., Mamakos, A., Agudelo, C., Gramstat, S., et al., 2023. Interlaboratory study on brake particle emissions—part i: particulate matter mass emissions. Atmosphere 14 (3), 498. ⟨https://www.mdpi.com/2073-4433/14/3/498⟩.

[29] Mathissen, M., Grigoratos, T., Gramstat, S., Mamakos, A., Vedula, R., Agudelo, C., et al., 2023. Interlaboratory study on brake particle emissions part ii: particle number emissions. Atmosphere 14 (3), 424. ⟨https://www.mdpi.com/2073-4433/14/3/424⟩.

[30] Mathissen, M., Scheer, V., Vogt, R., Benter, T., 2011. Investigation on the potential generation of ultrafine particles from the tire–road interface. Atmos Environ 45 (34), 6172–6179. ⟨https://www.sciencedirect.com/science/article/pii/S1352231011008569⟩.

[31] Perrenoud, A., Gasser, M., Rutishauser, B.R., Gehr, P., Riediker, M., 2010. Characterisation of nanoparticles resulting from different braking behaviours. IJBNN 1 (1), 17. https://doi.org/10.1504/IJBNN.2010.034123.

[32] Wahlström, J., Söderberg, A., Olander, L., Jansson, A., Olofsson, U., 2010. A pin-on-disc simulation of airborne wear particles from disc brakes. Wear 268 (5-6), 763–769. ⟨https://www.sciencedirect.com/science/article/pii/S0043164809006024⟩.

[33] Vasilatou, K., Wälchli, C., Koust, S., Horender, S., Iida, K., Sakurai, H., et al., 2021. Calibration of optical particle size spectrometers against a primary standard: Counting efficiency profile of the TSI Model 3330 OPS and Grimm 11-D monitor in the particle size range from 300 nm to 10 µm. J Aerosol Sci 157, 105818. ⟨https://www.sciencedirect.com/science/article/pii/S0021850221005498⟩.

[34] Olofsson, U., Olander, L., 2013. On the identification of wear modes and transitions using airborne wear particles. Tribology Int 59, 104–113. ⟨https://www.sciencedirect.com/science/article/pii/S0301679×12000382⟩.

[35] Österle, W., Griepentrog, M., Gross, T., Urban, I., 2001. Chemical and microstructural changes induced by friction and wear of brakes. Wear 251 (1-12), 1469–1476. ⟨https://www.sciencedirect.com/science/article/pii/S0043164801007852⟩.

[36] Gad, S.C., 1989. Acute and chronic systemic chromium toxicity. Sci Total Environ 86 (1-2), 149–157. ⟨https://www.sciencedirect.com/science/article/pii/0048969789902015⟩.

[37] Hussain, S., Khan, M., Sheikh, T.M.M., Mumtaz, M.Z., Chohan, T.A., Shamim, S., et al., 2022. Zinc essentiality, toxicity, and its bacterial bioremediation: a comprehensive insight. Front Microbiol 13, 900740. https://doi.org/10.3389/fmicb.2022.900740.

[38] Park, S.B., Cho, K.H., Jung, S., Jang, H., 2009. Tribological properties of brake friction materials with steel fibers. Met Mater Int 15 (1), 27–32. ⟨https://link.springer.com/article/10.1007/s12540-009-0027-6⟩.

[39] Kim, K.I., Lee, H., Kim, J., Oh, K.H., Kim, K.T., 2021. Wear behavior of commercial copper-based aircraft brake pads fabricated under different SPS conditions. Crystals 11 (11), 1298. ⟨https://www.mdpi.com/2073-4352/11/11/1298⟩.

[40] Neis, P.D., Ferreira, N.F., Fekete, G., Matozo, L.T., Masotti, D., 2017. Towards a better understanding of the structures existing on the surface of brake pads. Tribology Int 105, 135–147. ⟨https://www.sciencedirect.com/science/article/pii/S0301679×16303516⟩.

[41] Wahlström, J., Olander, L., Olofsson, U., 2010. Size, shape, and elemental composition of airborne wear particles from disc brake materials. Tribol Lett 38 (1), 15–24. ⟨https://link.springer.com/article/10.1007/s11249-009-9564-x⟩.

[42] Miller, M.R., Raftis, J.B., Langrish, J.P., McLean, S.G., Samutrtai, P., Connell, S.P., et al., 2017. Inhaled nanoparticles accumulate at sites of vascular disease. ACS Nano 11 (5), 4542–4552. https://doi.org/10.1021/acsnano.6b08551.

Supplementary Information publication 2

Table S 1: Parameters for the simulated vehicle

Parameter	Vehicle data
Vehicle type	SUV
Vehicle mass (including driver weight)	1895 kg
Wheel load (without driving resistance)	614.4 kg
Disc dimensions	330 mm x 24 mm
Wheel load/ Disc mass	64.2
Disc/ brake position	Front axle
Disc type	Gray cast iron - ventilated

Table S 2: Results from cooling air speed adjustment for LM and NAO pads

Dyno parameter	LM	NAO	GTR24 specification
WL/DM	64.2	64.2	$45 < WL/DM \leq 65$
Average brake temperature	56.9°C	55.3°C	55°C ≤
Initial brake temperature	57.8°C	57.3°C	75°C ± 25°C
Final brake temperature	86.5°C	88.9°C	115°C ± 35°C
Maximum temperature over WLTP	114.6	122.0	n.a.
Cooling air flow	540 m^3/h	720 m^3/h	300 m^3/h <

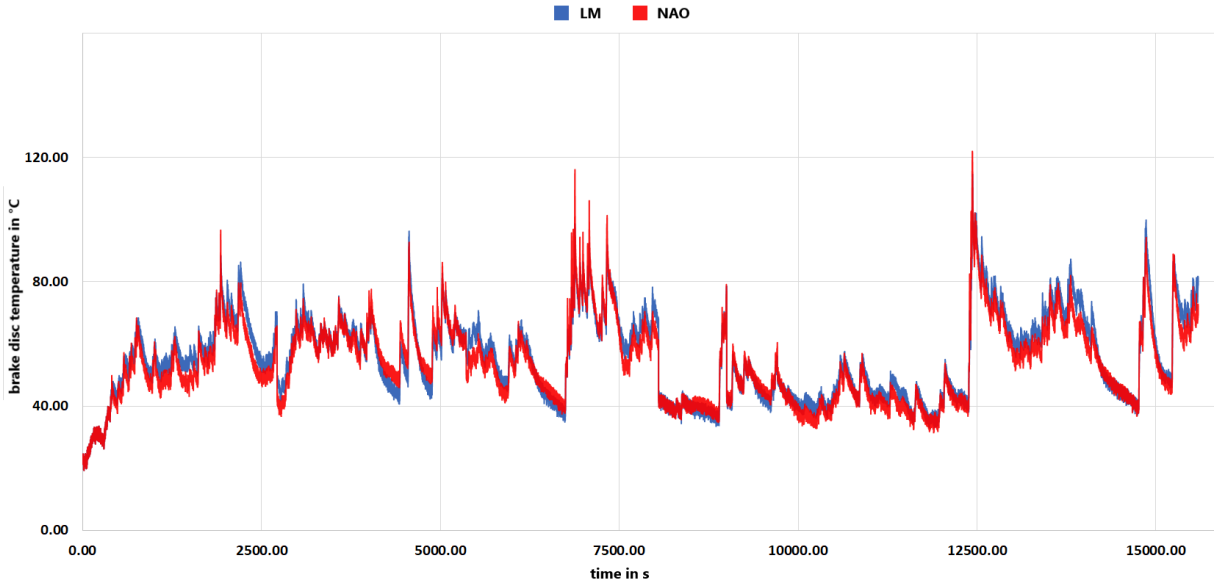

Figure S 1: Brake disc temperatures during the WLTP brake cycle

Table S 3: Reaction gases and measurement parameters for ICP-MS/MS analysis

Element	m/z Q1	Reaction gas Q2	m/z Q3
Mg	24	He	24
Al	27	He	27
S	32	O_2	48
V	51	NH_3	51
Cr	52	He	52
Mn	55	He	55
Fe	56	He	56
Co	59	NH_3	59
Ni	60	He	60
Cu	63	He	63
Zn	66	He	66
As	75	O_2	91
Mo	95	He	95
Sb	121	He	121
Ba	138	He	138

Table S 4: Recovery rates for PAHs calculated via extraction of certified reference material ERM-CZ100

PAH	Average recovery rate in %
Benzo[a]anthracene	74 ± 1.0

Benzo[a]pyrene	99 ± 4.0
Benzo[b]fluoranthene	94 ± 1.5
Benzo[j]fluoranthene	87 ± 3.1
Benzo[k]fluoranthene	113 ± 1.4
Indeno[1,2,3-c,d]pyrene	61 ± 1.0
Anthracene	81 ± 0.0
Benzo[g,h,i]perylene	63 ± 0.8
Chrysene	85 ± 0.7
Fluoranthene	65 ± 0.6
Phenanthrene	68 ± 0.5
Pyrene	66 ± 0.5
Average recovery rate for all specified PAH	79.6 ± 15.7

Table S 5: Average particle #/cm^3 of individual WLTP brake cycles measured by the SPC

Pad	**WLTP**	**#/cm^3**	**Average #/cm^3**
LM	1	470	429 ± 25
	2	417	
	3	404	
	4	424	
NAO	1	486	496 ± 9
	2	499	
	3	508	
	4	489	

Table S 6: Heavy metal emission factors at the vehicle level

Element	**LM**		**NAO**	
	PM10 µg/km	**PM2.5 µg/km**	**PM10 µg/km**	**PM2.5 µg/km**
Fe	8271 ± 128	2951 ± 62	9468 ± 226	3105 ± 97
Cu	43.9 ± 0.3	15.2 ± 0.2	33.6 ± 1.1	11.0 ± 0.5
Cr	92.3 ± 1.6	32.5 ± 0.6	21.3 ± 0.7	6.8 ± 0.3
Mn	43.2 ± 0.2	15.5 ± 0.2	50.5 ± 1.1	16.7 ± 0.5
Al	38.9 ± 1.3	13.2 ± 0.1	57.9 ± 0.5	15.4 ± 0.7

Zn	219.8 ± 5.2	78.6 ± 0.9	7.3 ± 1.3	0.7 ± 0.9
Sn	118.4 ± 7.8	55.9 ± 0.7	3.4 ± 0.4	1.0 ± 0.0
Ni	7.1 ± 0.1	2.5 ± 0.1	8.3 ± 0.1	2.7 ± 0.1

Publication 3

Atmospheric Environment 308 (2023) 119883

Contents lists available at ScienceDirect

Atmospheric Environment

journal homepage: www.elsevier.com/locate/atmosenv

Personal measurements and sampling of particulate matter in a subway – Identification of hot-spots, spatio-temporal variability and sources of pollutants

Jan Bendl [a,d,*], Carsten Neukirchen [a,c], Ajit Mudan [a], Sara Padoan [a,b], Ralf Zimmermann [b,c], Thomas Adam [a,b]

[a] University of the Bundeswehr Munich, Faculty for Mechanical Engineering, Institute of Chemical and Environmental Engineering, Werner-Heisenberg-Weg 39, 85577, Neubiberg, Germany
[b] Joint Mass Spectrometry Center (JMSC) at Comprehensive Molecular Analytics (CMA), Helmholtz Zentrum München, Ingolstädter Landstr. 1, 85764, Neuherberg, Germany
[c] Joint Mass Spectrometry Center (JMSC) at Chair of Analytical Chemistry, Institute of Chemistry, University of Rostock, Albert-Einstein-Strasse 27, 18059, Rostock, Germany
[d] Institute for Environmental Studies, Faculty of Science, Charles University, Benátská 2, 128 01, Prague 2, Czech Republic

HIGHLIGHTS

- Higher spatial than temporal variability of PM in the Munich subway system was observed.
- Significant differences in PM concentrations between platforms were found, with train frequency being a key factor.
- Iron oxide particles as products of rails and wheels abrasion dominated PM mass.
- Mobile measurements of subway systems effectively identify hot-spots and air quality.
- With the proposed methodology, subway systems can be comparably mapped for site-specific PM reduction measures.

GRAPHICAL ABSTRACT

ARTICLE INFO

Keywords:
Metro
Public transport
Indoor air quality
Personal exposure
Particulate matter
Elemental composition

ABSTRACT

A mobile measurement system for complex characterization of particulate matter (PM) was developed together with the proposed methodology and applied in the subway system of Munich, Germany. The main objectives were to observe the spatio-temporal variability of PM, personal exposure, identify hot-spots and pollution sources. Particle mass (PM_x) and number (PNC) concentrations, and equivalent black carbon (eBC) were measured at 0.1–1 Hz. On the *U5* subway line, PM_{10}, $PM_{2.5}$ and PM_1 concentrations at platforms ranged from 59 to 220, 27–80, and 9–21 μg m^{-3}, respectively. During rides towards downtown, average PM_{10}, $PM_{2.5}$ and PM_1 levels gradually increased from 8 to 220, 2 to 71 and 2–20 μg m^{-3}, respectively, with a similar dynamic of decrease on the return journey. Spatial variability of PM was generally more important than temporal, and

Abbreviations: PM, Particulate matter.

* Corresponding author. University of the Bundeswehr Munich, Faculty for Mechanical Engineering, Institute of Chemical and Environmental Engineering, Werner-Heisenberg-Weg 39, 85577, Neubiberg, Germany.
E-mail address: jan.bendl@unibw.de (J. Bendl).

https://doi.org/10.1016/j.atmosenv.2023.119883
Received 25 February 2023; Received in revised form 18 May 2023; Accepted 31 May 2023
Available online 1 June 2023

significant differences were observed between platforms. During the rides, air exchange between train and tunnel was high in both air-conditioned and old passively ventilated trains. Peak PM concentrations on platforms were associated with arriving/departing trains. Subway PNC were not significantly elevated, but a few cases of intake of traffic-related particles from outside were observed, otherwise air exchange was considered low. Generally, most of the aerosol mass was composed of iron corrosion products from rails and wheels (Fe up to 66 μg m^{-3} in $PM_{2.5}$). The effective density of $PM_{2.5}$ was 2.1 g cm^{-3}. Particles were classified as 75.4% iron oxides, 5.35% metallic Fe, 1.23% aluminosilicates and 17% carbon and oxygen rich particles. The iron oxide particles consisted predominantly of Fe (63.4 ± 8.7 wt%) and O (36.2 ± 8.2 wt%). To effectively monitor subway PM and reduce overall PM exposure, we propose to identify hot-spots using our methodology and focus on improving their ventilation, as well as installing filters in air-conditioned wagons.

1. Introduction

People in urban areas around the world spend a considerable amount of time commuting and often choose subway as the most sustainable and time-efficient environmentally friendly transport mode. However, personal exposure to harmful compounds within the transport microenvironment can pose a health risk (Cepeda et al., 2017). Even low concentrations of pollutants, such as ultrafine particles (UFP), can cause long-term adverse health effects (Schraufnagel, 2020). In general, the health effects of PM exposure ranging from respiratory diseases to cancer, result in significant impairment of quality of life, premature deaths and non-negligible economic impacts (World Health Organization, 2021). Minimizing exposure to PM in public transport is, therefore, necessary and in line with the objective of the United Nation's Sustainable Development Goal #11 (Huck, 2022) and the Guidelines for Developing and Implementing a Sustainable Urban Mobility Plan (Rupprecht Consult, 2019).

Subway stations and tunnels are a specific micro-environment dominated by non-exhaust emissions (NEE) from electric trains in relatively closed space. NEE are not yet regulated and systematically monitored like vehicle exhaust emissions. Nevertheless, PM_{10} and $PM_{2.5}$ concentrations in subways have been often found to exceed WHO ambient air quality guidelines (Xu and Hao, 2017; Chang et al., 2021). The negative health effects of subway PM have been proven in various studies. These include DNA damage caused most likely by the redox-active surfaces of metal-rich particles leading to oxidative stress (Karlsson et al., 2006, 2008), as well as inflammatory, toxicity and transient biological effects (Bachoual et al., 2007). Recent research has also revealed cancer risks associated with exposure to subway PM (Roy et al., 2022). However, not all mechanisms are fully understood yet.

The main sources of subway PM described in literature are abrasion from brakes (steel alloys containing chromium and nickel), rails and wheels (mostly iron) as well as rail catenary and pantographs (copper) with iron being dominant in $PM_{2.5}$ (Minguillón et al., 2018). Due to subway systems being enclosed environments, the effects of ventilation on air quality have been observed as well as other phenomena such as piston effects of trains, which resuspend settled dust (Martins et al., 2016; Cartenì et al., 2020).

Various studies focusing on personal exposure in the subway have been conducted (Querol et al., 2012; Yang et al., 2015; Xu et al., 2016; Shakya et al., 2020; Targino et al., 2021), however, the aim of this study is to present the most comprehensive approach to characterize subway PM exclusively using a custom-built mobile measurement system (followed by laboratory analysis). One of the aims was to propose a methodology to effectively identify hot-spots, measure the spatial and temporal dynamics of the aerosol, provide an indoor/outdoor PM comparison with respect to size distribution, elemental composition and morphology of the particles. In addition, personal exposure during typical rides and specific questions such as differences between old and new trains have been addressed.

Measurements were conducted in the Munich subway system, where there has been no published study to date. In our pilot study, on-line PM measurements were focused on PM_1, $PM_{2.5}$, PM_{10}, particle number concentration (PNC), equivalent black carbon (eBC) and lung deposited surface area (LDSA), which is a relatively new health-relevant metric combining alveolar deposition efficiency of particles with their surface area (Salo et al., 2021). Filter sampling for metal contents of PM analyzed by inductively coupled plasma mass spectrometry (ICP-MS) was performed either stationary at selected platforms or during typical journeys to assess citizen exposure. The morphology and elemental composition of individual particles were analyzed using scanning electron microscopy with energy dispersive X-ray spectroscopy (SEM-EDX).

2. Materials and methods

2.1. Study area

Mobile measurements were conducted in the area of Munich with 1.5 mio. inhabitants and an area of 311 km^2. Its subway system called *U-Bahn* consists of 8 lines (*U1-U8*), the first of which was completed in 1971. The total length of the rail network is about 95 km with 100 station platforms, tunnels with a maximum depth of 25 m and around 530 trains. In 2019, 429 million passengers used the subway for transportation, however, the numbers decreased due to the Covid-19 pandemic in 2020 (251 mio.) and 2021 (254 mio.; https://www.mvg.de/). Normally, the frequency of trains is 10 min, which shortens to 5 min during rush hours (7-9 am and 3-7 pm) and extends up to 30 min at the beginning (4 a.m.) and end (2 a.m.) of the service. Currently, three train types (A, B, C) with usually 6 cars are present, while only trains A (built 1967-1983) and C (build 2000 and later) were investigated. The "old" trains (A) have no ventilation system except for windows and the interior is separated into individual wagons while "new" trains (C) have ventilation, permanently closed windows and the interiors of three wagons are connected into one large volume. Focus of this study was on the line *U5* (Fig. S3 in SI), where "new" and "old" trains are randomly in operation. Trains are powered by a 750 V third rail made of low carbon steel (in the locations sampled) or aluminium. Outside of operating hours, the Munich Transport Service (MVG) occasionally uses a *Speno* train for grinding the rails and a special vacuum locomotive (VakTrak, New International Railways & SOCOFER) to clean the tracks from trash and sedimented particles using a blower and filtration system (*https://www.u-bahn-muenchen.de/*).

In Munich, the regional overground trains *S-Bahn* (*S1-S8*) often run in tunnels that are separated from the *U-Bahn* system with few exceptions. *S-Bahn* trains are ventilated with the possibility of opening the windows. The *S7* line was partially investigated in this study.

Hauptbahnhof (Munich Central Station) and *Ostbahnhof* are transfer stations to normal long-distance and regional trains.

Table 1 lists all stations included in this study along with abbreviations indicating *U-Bahn* (*U*), *S-Bahn* (*S*), or *railway* (*R*) stations. For example, the abbreviation *CS-R* stands for Munich central railway station and *CS-S* for Munich central station of *S-Bahn* trains. As there are two *U-Bahn* station platforms at the *Munich central station*, they are additionally numbered with the higher number indicating the deeper station (e.g. *CS-U2*). *NS-U/S* indicates the station *Neuperlach Süd* with a shared platform for *U-Bahn* and *S-Bahn*. The highlighted public transport map is in SI (Fig. S3) and all routes are shown in detail in Tables S2–S5.

2.2. Measurement strategy (proposed methodology)

The starting point of all personal measurements was at the Bundeswehr University Munich (GPS: 48°04′54.5″N 11°38′20.1″E) 1 km away from the terminal station *Neuperlach Süd* (*NS-U/S*, line *U5*), which is exceptionally above-ground. The ambient air quality station for reference measurements (section 2.6.) was located on the university campus.

The strategy of measurements and sampling is schematically reported in Fig. 1. As a first step, reference measurements in the surrounding area and different scouting rides within the subway were performed to identify hot-spots and to select typical routes for repetitions at different times of the day for the spatio-temporal variability of PM. Finally, stationary measurements were conducted with the mobile system at the center of the selected platforms to obtain information on the effects of arriving trains on the variability of PM. Therefore, the study was divided into the following experiments:

1) Mobile measurements of PM, PNC, and personal sampling for metals analysis (ICP-MS) on the university campus and surrounding urban micro-environments for reference (map of route in SI Fig. S2). A 1-h typical walking route **A** (Tables 2 and 3) was repeated 6 times and the new customized measurement system was tested
2) Scouting subway rides for PM, PNC observation, and identification of hot-spots (randomly selected routes **B, C, D, E**)
3) Repetition of the same ~1h long subway routes in the morning, noon and afternoon (selected based on previous results) to estimate daily variability (route **F**)
4) Stationary measurements and sampling (~3 h) at a platform identified as a hot-spot and considered to be a representative busy transfer station in the Munich city center for detailed characterization of particles using SEM/EDX and ICP/MS (**G**: platform *U5/U4* of Munich main train station *Hauptbahnhof CS-U1*). The dynamics of the particle emissions were linked to arriving trains
5) Another extended stationary sampling (6 h) for gravimetric analysis to calculate the specific density of PM used for the optical particle sizer (OPS) correction
6) Tracking of the differences in the dynamics of PM concentration between an old and a new type of subway train during the ride on the same track (line *U5*)

At the beginning and the end of each subway experiment, a minimum 20 min measurement walk (2 km) was taken between the university campus and the *NS-U/S* subway station to allow comparison with actual ambient urban PM levels. The mobile subway measurement routes (experiment 2 & 3) included train mid-section rides, stationary measurements simulating exposure of people waiting at selected platforms, and elevator rides. Platform measurements (experiment 4 & 5) were taken in the middle of the selected platform on designated passenger seats for the time necessary to obtain a sufficient number of data points. The operator documented the time at which trains entered and exited the station, and trains were categorized as old (o) and new (n), respectively. The *S-Bahn* platforms were measured similarly to *U-Bahn*. The investigation of the regional/long-distance train platform at the main station was conducted where most people gather and where small cafés and shops are also located. Sampling was done either cumulatively during the ride or at the selected platform (experiment 4).

Table 1
List of subway/train stations with abbreviations used in this study with average platform particulate matter (PMx), particle number concentration (PNC), equivalent black carbon (eBC) and UV-absorbing PM (UVPM) concentrations where the SD represents variability among measurements. For interpretation, design of the platform cross-section is indicated, where "P" is platform, "T" is track, "-" is direct transition and "|" indicate the separation of tracks/platform by a wall. Averages from ID 10-16 were not shown due to short measuring time.

ID	Name of the station	Abbr.	Lines	Type	Number of tracks (platform design)	PM_{10} (μg m^{-3})	$PM_{2.5}$ (μg m^{-3})	PM_1 (μg m^{-3})	PNC (pt cm^{-3})	eBC (ng m^{-3})	UVPM (ng m^{-3})	Size mode (nm)	No. of measurements
1	Neuperlach Süd	NS-U	U5, S7	overgr. (open w/ roof)	3 (T-P-T-T-P)	9 ± 5	3 ± 2	2 ± 2	7300 ± 7582	111 ± 117	620 ± 486	37 ± 19	7
2	Michaelibad	MC-U	U5	undergr.	2 (T-P-T)	59 ± 26	27 ± 14	9 ± 4	6547 ± 2419	4043 ± 1964	3236 ± 1353	40 ± 4	4
3	Ostbahnhof	OB-U	U5	undergr., transfer	2 (T-P-T)	205 ± 72	80 ± 18	21 ± 5	7470 ± 2773	9416 ± 3299	6840 ± 1694	43 ± 3	4
4	Odeonsplatz	OU-U	U4, U5	undergr., transfer	2 (T-P|P-T)	179 ± 52	70 ± 20	20 ± 6	6985 ± 1597	10540 ± 2628	6622 ± 1188	43 ± 2	4
5	Hauptbahnhof (over)	CS-U1	U4, U5	undergr., transfer	2 (T-P-T)	174 ± 40	66 ± 13	18 ± 4	8817 ± 2442	8648 ± 1469	6204 ± 562	40 ± 3	4
6	Hauptbahnhof (under)	CS-U2	U1, U2, U7, U8	undergr., transfer	4 (T-P-T-T-P-T)	220 ± 32	72 ± 7	20 ± 0.3	7175 ± 754	7845 ± 2560	6052 ± 723	46 ± 10	2
7	Hauptbahnhof Nord	CS-S	S1-4, S6-8	undergr., transfer	2 (P-T-P-T-P)	126 ± 89	42 ± 30	11 ± 7	6942 ± 1749	4616 ± 3053	3385 ± 2294	42 ± 7	4
8	Hauptbahnhof	CS-R	Railway	overgr. (semi-open), transfer	15 (large hall)	26 ± 9	11 ± 1	9 ± 1	7425 ± 4543	827 ± 401	1126 ± 707	48 ± 4	2
9	Innsbrucker Ring	IR-U	U2, U5	undergr., transfer	4 (T-P-T-T-P-T)	114 ± NA	48 ± NA	14 ± NA	5817 ± NA	7345 ± NA	5118 ± NA	46 ± NA	1
10	Therese-Giehse-Allee	TG-U	U5	undergr.	2 (T-P-T)	-	-	-	-	-	-	-	short
11	Neuperlach Zentrum	NZ-U	U5	undergr.	2 (T-P-T)	-	-	-	-	-	-	-	short
12	Quiddestrasse	QI-U	U5	undergr.	2 (T-P-T)	-	-	-	-	-	-	-	short
13	Max-Weber-Platz	MW-U	U4, U5	undergr.	2 (T-P-T-T-P-T)	-	-	-	-	-	-	-	short
14	Lehel	LH-U	U4, U5	undergr.	2 (T-P|P-T)	-	-	-	-	-	-	-	short
15	Karlsplatz (Stachus)	KA-U	U4, U5	undergr.	2 (T-P|P-T)	-	-	-	-	-	-	-	short
16	Theresienwiese	TW-U	U5	undergr.	2 (T-P-T)	-	-	-	-	-	-	-	short

2.3. Custom-built mobile measuring system

We developed a new mobile measurement system (Fig. S1 and full description in the SI) consisting of an actively ventilated, water-proof aluminum box with adjustable internal shelves, which serves as a housing for all online instruments and samplers. These are connected to omni-directional inlets (801565, TSI) by short conductive tubes. For underground measurements, the experimental box was attached to a frame rucksack, which was carried by the operator. While carried, the inlets in the breathing zone were at a distance of at least 20 cm from the operator to minimize personal cloud artifacts due to particles from clothing and hair (Licina et al., 2017). While riding the subway, the backpack was placed on a passenger seat, resulting in a measurement of the breathing zone of a seated person, similar to measurements on platforms. During reference ambient measurements, the box was secured in a modified stroller (Cab 2, Thule) to absorb vibrations. The temperature inside the box was kept within the operating range of the instruments to avoid discrepancies and extensive losses of volatile components from the samples.

2.4. On-line mobile measurements

PM size-distributions (OPS 3330, TSI) and PNC, the lung deposited surface area (LDSA) and size modes (DISCmini, Testo) were measured at 1 Hz resolution (0.2 Hz for OPS during platform measurements in one case), eBC and UVPM (MA200, Aethlabs; 150 mL min^{-1}, dual-spot) were measured at 0.1 Hz resolution. GPS coordinates were acquired at 1 Hz (64s, Garmin). Since GPS signal was not available in the subway, the time of door opening and closing was documented at each station with an accuracy of 1 s. All relevant events were noted or recorded with a cell

Table 2
Summary of on-line measurements (mean ± SD) of particle number concertation (PNC), particulate matter (PMx), lung deposited surface area (LDSA), equivalent black carbon (eBC), UV-absorbing PM (UVPM) and selected ratios during the sampling time for the metal analysis by ICP-MS for comparison. Routes B-F are described also in specific tables for each measurement based on the transects of the route (suppl. Tables S4–S10) to see the exact contribution of different environment.

Measurement	ID	Date	Duration	Start	Stop	PM_{10}	$PM_{2.5}$	PM_1	PNC	Size mode	LDSA	eBC	UVPM	$PM_{2.5}/PM_{10}$	$PM_1/PM_{2.5}$	eBC/UVPM
		DD-MM-YY	min.	hh:mm	hh:mm	μg m^{-3}	μg m^{-3}	μg m^{-3}	pt cm^{-3}	nm	μm^2 cm^{-3}	ng m^{-3}	ng m^{-3}			
Ambient walk 1	**A1**	19-10-21	91	15:35	17:06	16 ± 33	1.6 ± 1.0	0.9 ± 0.4	10352 ± 17752	37 ± 5	18 ± 10	371 ± 313	836 ± 325	0.1	0.5	0.4
Ambient walk 2	**A2**	26-10-21	74	14:21	15:35	8 ± 1	2.6 ± 0.8	1.2 ± 0.1	3262 ± 1373	47 ± 7	8 ± 3	401 ± 411	661 ± 443	0.3	0.5	0.6
Ambient walk 3	**A3**	26-10-21	67	15:46	16:53	9 ± 29	2.5 ± 0.7	1.1 ± 0.1	5963 ± 20012	53 ± 9	13 ± 11	31 ± 15	497 ± 266	0.3	0.4	0.1
Ambient walk 4	**A4**	27-10-21	81	7:50	9:11	15 ± 55	1.6 ± 1.7	0.7 ± 0.2	39615 ± 12525	22 ± 5	42 ± 10	1125 ± 751	1610 ± 755	0.1	0.4	0.7
Ambient walk 5	**A5**	27-10-21	77	9:25	10:42	15 ± 70	1.8 ± 1.9	0.7 ± 0.4	21653 ± 15180	29 ± 5	30 ± 11	NA ± NA	NA ± NA	0.1	0.4	NA
Ambient walk 6	**A6**	27-10-21	74	13:13	14:27	8 ± 17	1.8 ± 0.8	0.8 ± 0.1	5049 ± 1452	49 ± 3	14 ± 2	625 ± 437	709 ± 416	0.2	0.5	0.9
Subway scouting 1	**B**	04-11-21	97	7:17	8:54	137 ± 102	57 ± 39	17 ± 11	5550 ± 1922	41 ± 10	13 ± 5	7359 ± 5730	4659 ± 5015	0.4	0.3	1.6
Subway scouting 2	**C**	05-11-21	72	7:48	9:00	147 ± 119	51 ± 33	15 ± 8	12237 ± 5851	38 ± 6	24 ± 5	6906 ± 4445	4946 ± 2668	0.3	0.3	1.4
Subway scouting 3	**D**	17-11-21	101	8:47	10:28	109 ± 105	41 ± 32	14 ± 7	6998 ± 4236	44 ± 8	16 ± 7	4267 ± 4299	3369 ± 3074	0.4	0.3	1.3
Subway scouting 4	**E**	24-11-21	51	9:31	10:22	170 ± 71	59 ± 16	19 ± 4	6068 ± 2308	55 ± 5	19 ± 5	8423 ± 3624	5773 ± 2005	0.3	0.3	1.5
Subway route morning	**F1**	07-12-21	118	7:54	9:53	104 ± 89	41 ± 34	12 ± 9	6528 ± 3042	41 ± 7	14 ± 6	4560 ± 4313	3458 ± 2835	0.4	0.3	1.3
Subway route noon	**F2**	07-12-21	119	12:28	14:27	73 ± 58	29 ± 21	8 ± 6	5486 ± 2166	42 ± 8	13 ± 6	3707 ± 2913	3294 ± 2451	0.4	0.3	1.1
Subway route afternoon	**F3**	07-12-21	98	16:32	18:10	121 ± 82	45 ± 30	14 ± 8	13138 ± 6454	39 ± 5	27 ± 10	6022 ± 4402	4632 ± 2388	0.4	0.3	1.3
Platform sampling 1	**G1**	17-05-22	181	14:08	17:08	231 ± 52	96 ± 10	25 ± 3	6099 ± 630	56 ± 3	20 ± 1	8998 ± 2860	6919 ± 1499	0.4	0.3	1.3
Platform sampling 2	**G2**	19-07-22	164	20:36	23:20	218 ± 50	85 ± 8	26 ± 2	7857 ± 713	54 ± 3	25 ± 1	9967 ± 1153	7142 ± 772	0.4	0.3	1.4
Platform sampling 3	**G3**	28-08-22	360	14:06	20:06	181 ± 32	105 ± 24	29 ± 5	5074 ± 1111	64 ± 7	19 ± 2	5030 ± 608	4421 ± 478	0.6	0.3	1.1

phone camera for further data analysis. Temperature and relative humidity were measured sporadically by a data-logger with sensors (Almemo, Ahlborn or BiVOC2V2, Holbach).

The OPS was factory calibrated (TSI) with Polystyrene Latex (PSL) according to ISO 12501-1/4 and the dead time correction was used. As the density of the subway particles can differ significantly from the ambient air (Cha and Olofsson, 2018), corrections to the OPS were used for all measurements performed in the subway interiors and trains using gravimetric analysis by the external filter sampling (Section 2.5.1.). To avoid particle losses and minimize the time delay, the OPS was placed directly under the inlet.

Prior to each measurement, the instruments' flowrates were checked/calibrated using a mass flow meter (4043 H, TSI) as well as zero-filter checks (OPS), and automatic zero adjustments (DISCmini) were performed. The time was synchronized based on the GPS satellites.

2.5. Off-line measurements

For ICP-MS analysis, PM samples were collected on 47 mm quartz filters (preconditioned at 500 °C for 5 h) using the SG10-2 personal sampler (GSA) with a constant flowrate of 9 lpm and a filter holder with or without $PM_{2.5}$ pre-impactor (Sioutas, SKC; $PM_{2.5}$ or PM_{total}). The same filters were utilized for gravimetry prior to ICP-MS analysis. For quality assurance, two additional samples were taken simultaneously on 47 mm polycarbonate (PC) and 37 mm Teflon filters by additional SG10-2 samplers. For SEM-EDX analysis, BiVOC2V2 sampler (Holbach) with a constant flowrate of 2 lpm was used with a filter-holder and 47 mm PC filter, which also served as a support for 5 silica wafers (P-type boron dotted 5 × 5 mm). The samplers were calibrated using a mass flow meter (4043 H, TSI). Information on the filter material is given in Table S1 in SI. Time and duration of sampling are given in Table 3. Both blanks and field blanks were collected from each filter type.

2.5.1. Gravimetric analysis for correction of OPS data

Simultaneous 6h long sampling of $PM_{2.5}$ and PM_{total} for gravimetric analysis on three filter types (Section 2.5.) was performed on August 28, 2022 from 14:06 to 20:06 on the central part of the *U-Bahn* platform of the main train station *CS-U1* (line *U5/U4* with a 10 min interval on both lines). Filters were weighed prior and after sampling using a microbalance (Cubis MCA2.7S-2S00-F, Sartorius) and pre-conditioned (45% RH, 22 °C) for 24 h in a weighing chamber (pureGMC 18-EPA1065) with a corona discharge for filter deionization. All filters were weighed five times and the aerosol mass on the filter was calculated as the weight difference of the averages before and after the exposure. Then, the average 6-h PM mass concentration (μg m^{-3}) was calculated. For quality control, blank filters were weighed twice before and after exposure.

The OPS was measuring simultaneously at 0.2 Hz. The $PM_{2.5}$ mode from the entire sampling period was compared to the mode of gravimetric mass concentration from the PC, PTFE and quartz filter. The entire size range of the OPS from 0.3 to 10 μm (for underground measurements only) was then corrected by the correction factor:

$$OPS\ correction\ factor = \frac{c\ (g)}{c\ (OPS)} \quad (1)$$

where *c* (g) is the mass concentration of $PM_{2.5}$ from gravimetry and *c* (OPS) is the mode of $PM_{2.5}$ mass concentration from OPS.

2.5.2. Metal analysis using ICP-MS

Samples have been digested according to DIN 14902 (VDI 2267-part 15) by a Microwave speedwave ENTRY (Berghof) with a mixture of nitric acid (HNO_3, ultrapure grade, 69%) and hydrogen peroxide (H_2O_2, ultrapure grade 30%). Subsequently, samples have been diluted to a final volume of 50 mL with a final concentration of 5% of HNO_3. All the samples have been filtered utilizing a 0.2 μm syringe filter (Whatman Puradisc, 25 mm, 0.2 μm) and analyzed by Inductively Coupled Plasma

Table 3
Metal analysis by ICP-MS from mobile (A-G) and stationary (Ref) samples. Tables describing each transect and contribution of subway mobile measurements (B-F) are in the Supporting Information.

Measurement type	Reference ambient $PM_{2.5}$	Repetitions of the same ambient walk				Subway and railway scouting				Repetitions of a subway route at the same day			Subway platform stationary		Subway/ ambient
Route type/ stations	Station at UniBW	Urban PM background				NS-U, IR-U, OP-U, NS-U/S	OB-U, MC-U, NS-U/S	CS-U1, CS-U2, CS-R, OU-U	CS-U2, CS-U1, NS-U/S	NS-U/S, OB-U, OU-U, CS-R, CS-S, NS-U/S			CS-U1		Indoor/ outdoor ratio
ID	**Ref**	**A3**	**A4**	**A5**	**A6**	**B**	**C**	**D**	**E**	**F1**	**F2**	**F3**	**G1**	**G2**	**G1/Ref**
Sampling date	17-05-22	26-10-21	27-10-21	27-10-21	27-10-21	04-11-21	05-11-21	17-11-21	24-11-21	07-12-21	07-12-21	07-12-21	17-05-22	19-07-22	
Start sampling (hh:mm)	9:00	15:46	7:50	9:25	13:13	7:17	7:48	8:47	9:31	7:54	12:28	16:32	14:08	20:33	
Stop sampling (hh:mm)	9:00	16:53	9:11	10:42	14:27	8:54	9:00	10:28	10:22	9:53	14:27	18:10	17:08	23:21	
Sampling time (min.)	1440	67	82	78	74	97	72	102	51	118	119	97	180	168	
Sampled air (m^3)	641	0.60	0.74	0.70	0.67	0.88	0.65	0.91	0.46	1.07	1.07	0.88	1.53	1.43	
PM fraction	$PM_{2.5}$	PM_{tot}	PM_{tot}	PM_{tot}	PM_{tot}	PM_{tot}	PM_{tot}	PM_{tot}	PM_{tot}	PM_{tot}	PM_{tot}	PM_{tot}	$PM_{2.5}$	PM_{tot}	$PM_{2.5}$
Fe (μg m^{-3})	**0.073**	**2.6**	**1.6**	<LOQ	<LOQ	**115**	**123**	**20**	**122**	**56**	**49**	**91**	**67**	**171**	**911**
Mn (ng m^{-3})	**12.6**	**35**	**28**	**28**	<LOQ	**1045**	**1123**	**177**	**1113**	**523**	**503**	**804**	**617**	**1560**	**49**
Cr (ng m^{-3})	**1.2**	**205**	**159**	**154**	**180**	**420**	**448**	**151**	**786**	**306**	**215**	**384**	**197**	**484**	**163**
Cu (ng m^{-3})	**2.8**	**250**	**143**	**113**	**117**	**641**	**577**	**120**	**651**	**439**	**357**	**635**	**262**	**534**	**95**
Ni (ng m^{-3})	**0.51**	**232**	**73**	**57**	**109**	**317**	**308**	**76**	**683**	**206**	**141**	**245**	**146**	**344**	**286**
V (ng m^{-3})	**0.10**	<LOQ	<LOQ	<LOQ	<LOQ	<LOQ	<LOQ	<LOQ	<LOQ	<LOQ	<LOQ	<LOQ	<LOQ	**31**	NA
Pb (ng m^{-3})	**0.90**	**24**	**25**	**22**	<LOQ	<LOQ	<LOQ	<LOQ	**44**	**16**	<LOQ	**16**	<LOQ	**9**	NA
Mn to Fe (%)	17	1.3	1.8	NA	NA	0.91	0.91	0.89	0.91	0.93	1.03	0.88	0.92	0.91	
Cr to Fe (%)	1.7	7.9	9.9	NA	NA	0.37	0.36	0.76	0.64	0.55	0.44	0.42	0.30	0.28	
Cu to Fe (%)	3.8	9.6	8.9	NA	NA	0.56	0.47	0.60	0.53	0.78	0.73	0.70	0.39	0.31	
Ni to Fe (%)	0.7	8.9	4.5	NA	NA	0.28	0.25	0.39	0.56	0.37	0.29	0.27	0.22	0.20	

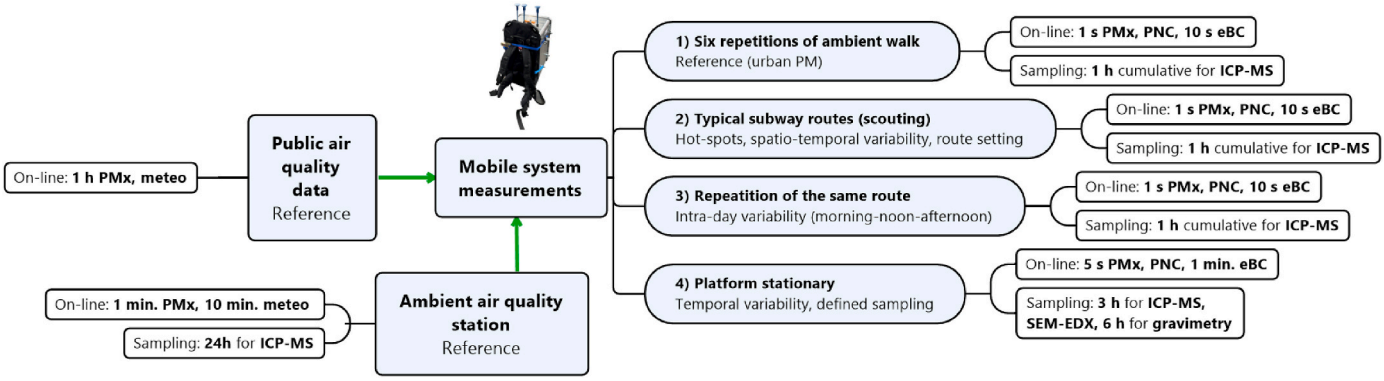

Fig. 1. Strategy of measurements and sampling of the subway micro-environment using the mobile measuring system; PNC, particle number concentration; PM, particulate matter; eBC, equivalent black carbon; ICP-MS, inductively coupled plasma mass spectrometry.

Mass Spectrometry (ICP-MS, Agilent Technologies 8900). Calibration standard curves for all measured elements were used for the quantification, as well as for the calculation of limits of detection (LOD) and quantification (LOQ). Three technical replicates have been performed for each sample, field and method blank. To check the extraction efficiency on each sample, prior to the digestion, a spike with a concentration of 20 μg L^{-1} of internal standard mix for ICP-MS systems was added. The constancy and the correctness of the analytical values of the used internal standard (ISTD) were checked in time through a control chart that documents the trend of the ISTD values.

2.5.3. Imaging and single particle elemental analysis using SEM-EDX

Samples used for analysis via SEM-EDX were stored in a desiccator under vacuum for 24 h to ensure removal of volatile components. Afterwards, 12 mm circular punches were cut from 47 mm PC filters, which were then transferred to 12 mm SEM pin stub sample holders with EDX suitable adhesive carbon pads in between. To minimize charging effects, the surface of the filters was coated in a Q150T ES Plus sputter device (Quorum technologies) with a thin carbon layer utilizing a woven carbon fiber string in pulsed cord evaporation mode.

Particles collected from subway stations were imaged with the built in Inlens and SE2 detectors of a Gemini Sem 360 (Carl Zeiss). EDX analysis was conducted with an Ultim Max 40 detector (Oxford instruments) at the optimum detector working distance of 8.5 mm. Usage of a silicon drift detector with a thin detector window ensured suitability for analysis of low-Z elements ($Z > 6$) such as C and O. The EHT was set to 5 kV for particles smaller than 0.5 μm to reduce the interaction volume of the beam, thus minimizing total passage of the beam through the particles with subsequent excitement of underlying materials such as the PC filter. Larger particles were measured with either 12 kV (particle sizes from 0.5 to 2.5 μm) or 20 kV acceleration voltage (particles >2.5 μm). Semi-quantitative EDX data was recorded for over 180 000 particles, followed by automated classification based on their main contributing elemental concentrations.

2.6. Reference stationary PM sampling and measurements

An air quality station on the university campus (GPS: 48°04′37.5″N 11°38′21.2″E) served as a reference for the subway measurements. A high-volume sampler (DHA-80, Digitel) with a $PM_{2.5}$ sampling head and a flowrate of 500 lpm was used to compare elemental composition between ambient air and in the subway. Daily 24-h samples starting at 9 a.m. were collected on 150 mm filters (Whatman QM-A, pre-conditioned for 5 h at 500 °C). PM size-distribution with 1 min time-resolution (APDA-372, Horiba with the Sigma-2 sampling head complying with VDI 2119-4, $PM_{2.5}$ according to EN14907 and PM_{10} EN 12341) and a weather station with 10 min data acquisition (Vantage 2 Pro, Davis) supported the interpretations.

2.7. Data analysis

On-line raw data were manually checked for potential errors caused by mobile use of instruments and processed in the manufacturer's software. PNC data from DISCmini were corrected for induction effects and cross-checked against a CPC (5416, Grimm) prior to the campaign. OPS data were corrected (see chapter 3.5.1.). BC and UVPM data (MA200, AethLabs) were smoothed using the Optimized Noise-reduction Averaging (ONA) algorithm with a smoothing factor of 0.01 (Hagler et al., 2011; Liu et al., 2021; Ji et al., 2022). When GPS signal was available, PNC and PM data were merged together with the GPS coordinates and plotted on maps using ArcGIS Pro software (ESRI). ICP-MS and SEM-EDX data were processed with the manufacturer's software.

3. Results and discussion

3.1. Reference ambient PM measurement (stationary and mobile)

For comparison with subway measurements, the average ambient concentrations of PM_1, $PM_{2.5}$ and PM_{10} on the university campus in May 2022 were 6 ± 4, 7 ± 4, 11 ± 5 μg m^{-3}, in July 2022 5 ± 3, 6 ± 4, 12 ± 7 μg m^{-3}, and in August 2022 5 ± 2, 7 ± 3, 11 ± 6 μg m^{-3}, respectively. At the same time, $PM_{2.5}$ values measured at the background station of the Bavarian Monitoring System for Air Quality (LÜB) in *Johanneskirchen* (Munich; *https://www.lfu.bayern.de/luft/immissionsmessungen/*), were 8 ± 4, 9 ± 4 and 9 ± 4 μg m^{-3} in May, July and August 2022, respectively. In October, November and December 2021, the $PM_{2.5}$ concentration in *Johanneskirchen* were 7 ± 4, 6 ± 5, 5 ± 5 μg m^{-3}, respectively. In summary, $PM_{2.5}$ levels on the campus were slightly lower than in the city. This confirms our reference site and its classification as an urban background station.

Six repetitions of the identical 1-h route in the vicinity of the station *Neuperlach Süd* (*NS-U/S*, see Fig. S2 with a detailed description in the SI) were used as comparison with the subway measurements (Fig. 4). They showed relatively high ambient spatio-temporal variability in PNC (Table 2) with the main road as the dominant source. Traffic strongly contributed to PNC values at the above-ground *U5* terminus *NS-U/S*. PNC were highest during the morning rush-hour (Ambient walk A4 and A5) and lowest in the early afternoon when traffic was reduced (A2, A6). According to DISCmini, the size mode ranged between 22 and 53 nm. PM_1 dynamics did not follow the PNC trend because ultrafine particles contribute little to the total mass concentration due to their low mass per particle. Furthermore, the OPS size range started at 300 nm. The PM_1/$PM_{2.5}$ ratio was similar for all 6 routes (0.4–0.5), which could indicate the same/similar dominant source of fine particles. PM_{10} had high SD (noise) due to the 1 Hz acquisition time and greater dynamics. Average eBC value between walks was 511 ± 417 ng m^{-3} and average ultraviolet

absorbing PM (UVPM) was 863 ± 525 ng m^{-3} with the highest value of 1.6 μg m^{-3} on October 27, when PNC was also highest. Since UVPM is an indicator of wood smoke and the measurements were taken during the heating season, domestic heating could contribute to the elevated background concentrations. The eBC/UVPM ratio was 0.7 on this day, otherwise, it varied from 0.1 to 0.9 between walks. The results of metal analysis by ICP-MS from the cumulative sampling can be found in Section 3.5.

3.2. Corrections of on-line subway measurements using gravimetry

The average $PM_{2.5}$ mass concentrations at the *CS-U1* platform (August 28, 2022, 14:06-20:06) calculated from PC, PTFE and quartz filters (simultaneous sampling) were 100.2 ± 4.13, 103.2 ± 1.65 and 102.9 ± 5.66 μg m^{-3}, respectively, with a median of 102.9 μg m^{-3}, whereas the $PM_{2.5}$ median measured on-line by the OPS was 48.8 μg m^{-3} (with a preset density 1 g cm^{-3} and default refractive index). Therefore, the correction factor of 2.11 from both medians was determined. This should roughly correspond to the average effective density of $PM_{2.5}$ in g cm^{-3}. However, as aerosol composition and particle structure vary over time, place and particle size, a more detailed measurement of effective density would be beneficial for precise correction. This aspect should be considered while comparing absolute values from on-line optical PM instruments among different studies but also within the same subway system due to different micro-environments. In Stockholm, precisely measured subway particle effective density was 1.87 ± 0.22 g cm^{-3}, which is in a similar range (Cha and Olofsson, 2018), however, the correction factors in Athens, Barcelona and Oporto suggest that there is high variability among subway systems (Martins et al., 2016), probably also in effective densities. One of the reasons could be different relative contributions of subway generated particles to PM e.g., due to different air exchange rates with the ambient environment and/or different emission patterns. During the same time, the PM_{total} concentration was 209.0 ± 7.79 μg m^{-3} (gravimetry) resulting in $PM_{total}/PM_{2.5}$ ratio of 2.1 (assuming zero sampling losses). Based on the corrected OPS, the PM_{10} concentration was 181 μg m^{-3} implying that particles larger than 10 μm in size should contribute about 28 μg m^{-3} to the PM_{total}. As a result, $PM_{2.5}/PM_{10}$ ratio was 0.6, PM_1/PM_{10} was 0.2, and $PM_1/PM_{2.5}$ was 0.3. The sampling was done on Sunday, however, the number of persons on the platform was comparable to weekdays (not quantified).

3.3. On-line PM subway measurements – general overview

Table 1 summarizes the average concentrations of PM, PNC, eBC and UVPM at selected underground and overground platforms of the *U-Bahn, S-Bahn* and railway main train station from all our measurements and lists the station abbreviations used in the figures.

The lowest PM mass concentrations were measured at *Michaelibad* (*MC-U*) with PM_{10}, $PM_{2.5}$, PM_1 = 59 ± 26, 27 ± 14, 9 ± 4 μg m^{-3}, respectively. The highest average concentrations were at the deeper *U-Bahn* platform of the *Hauptbahnhof* transfer station (*CS-U2*) with PM_{10}, $PM_{2.5}$, PM_1 = 220 ± 32, 72 ± 7 and 20 ± 0.3 μg m^{-3}, respectively. These values are concerning when compared to the WHO Air Quality Guidelines values of daily PM_{10} and $PM_{2.5}$ for outdoor air.

Table 2 shows the comparison between the different mobile and platform measurements, where **A1-A6** are repetitions of ambient walks, **B-E** are subway scouting trips, **F1-F3** are repetitions of the same ride in the morning, midday and afternoon, and **G1-G3** are several hours long stationary measurements on the *CS-U1* platform. The highest concentrations of PM_{10}, $PM_{2.5}$, PM_1 = 231 ± 52, 96 ± 10, 25 ± 3 μg m^{-3}, respectively, were recorded during the 3h long stationary measurement on May 17. This was in a similar range as at the Prague transfer station *Muzeum* with 214.8, 93.9 and 44.8 μg m^{-3} of PM_{10}, $PM_{2.5}$, PM_1, respectively (Cusack et al., 2015), however, the PM_1 in Munich was 2.3 times lower. The reason could be a lower contribution of ambient traffic-related particles to PM_1, which could be caused by both the reduced nearby traffic sources in Munich and/or lower air exchange with outside air (ventilation). This hypothesis is supported by the PNC values (Table 2, Fig. 4), which are, on average, at a similar level to the ambient urban background. This is also valid for LDSA and size-mode, both measured in the range of 10–300 nm and associated with PNC. $PM_{2.5}/PM_{10}$ ratio in the subway ranged from 0.4 to 0.6 and is higher than for ambient air (see Section 4.2.). Based on reviews of Carteni (Cartenì et al., 2020) and Chang (Chang et al., 2021) on subway PM in other cities, the highest average PM_{10} and $PM_{2.5}$ concentrations of 470 μg m^{-3} and 260 μg m^{-3}, respectively, were recorded on the platform in Stockholm in 2000 (Johansson and Johansson, 2003). In Rome in 2005, PM_{10} was 409 ± 22 μg m^{-3} (Perrino et al., 2015). High PM_{10} values were also observed in Seoul, Barcelona, Paris, Beijing, Milan, Budapest, Athens and other cities, while relatively low concentrations were determined in Naples, Sydney, and Turin (Cartenì et al., 2020).

The mean eBC concentration at the *CS-U1* platform was 8.0 ± 2.6 μg m^{-3} (**G1-G3**) and mean UVPM 6.2 ± 1.5 μg m^{-3}, which was significantly higher than in ambient air (during ambient walks **A1-A6** the mean eBC was 0.5 ± 0.4 μg m^{-3} and the highest values 2.5 ± 1.5 μg m^{-3} were recorded on December 7. 2021). Both eBC and UVPM correlated with PM measured by OPS. For comparison, in subway in Sao Paolo eBC were 11.33 ± 12.98 μg m^{-3} (Targino et al., 2021), in Helsinki 6.3 ± 1.8 μg m^{-3} (Aarnio et al., 2005), and in Montreal 4.6 ± 2.3 μg m^{-3} (van Ryswyk et al., 2017). Sources of BC are typically linked to combustion processes (e.g. diesel emissions), however, since we observed only minor amounts of soot-agglomerates via SEM in the Munich subway, we hypothesize that most of the eBC readings is caused by the interference of light absorbing iron oxide particles, which we identified as the major source of aerosol mass based on results from ICP-MS (Section 3.5.) and SEM-EDX (Section 3.6.). Moreover, PNC levels in the subway also suggested low intake of traffic related particles. Other sources of carbonaceous particles in the subway could be disc brake abrasion, as graphite is added to brake discs as a lubricant (Lyu and Olofsson, 2020), and carbon from electric motor brushes (Font et al., 2019). However, based on our SEM-EDX and ICP-MS analysis of trace elements typical for brake emissions, this cannot explain all eBC readings. Nevertheless, as the micro-aethalometer values correlated with the subway-PM measured by OPS, it was a good indicator of PM hot-spots. The possibility of micro-aethalometer artifacts in the subway has already been discussed (Midander et al., 2012; Targino et al., 2021) and we expect that interferences might affect published results from other subway studies. Therefore, this topic should be the subject of further investigation.

3.3.1. Subway scouting: hot-spots identification, effect of platform design on PM

Scouting rides (Table 2, **B-E**) represent various common trips of about 1h in the Munich subway system in November 2021 (same season as the reference ambient walks). As each of these routes was different, the exact routes are listed in SI (Tables S2–S8) with mean values of PM_{10}, $PM_{2.5}$, PM_1, PNC, eBC and UVPM for each transect (where the ambient walk is *aw*, the indoor walk *iw*, the subway ride *r*, and the platform stationary is *s*). The time of cumulative personal sampling for ICP-MS (section 3.5.) is marked in bold.

Based on these data, hot-spots were identified as transfer stations with higher train frequencies. The highest PM_{10} average values from repeated measurements (Table 1) were measured at *CS-U2,* the deepest of the *U-Bahn* platforms with values of 220 ± 32 μg m^{-3}, while the *U-Bahn* station *CS-U1* located above this platform, had an average concentration of 174 ± 40 μg m^{-3}. The depth of the station may play a role (Cartenì et al., 2015) but number of trains, station design (Table 1) and eventually ventilation seem to be responsible for the differences. *CS-U2*, with its four tracks not-separated by a wall, allows for a greater volume of mixing air compared to *CS-U1* with two tracks. The total train frequency is similar, but the peak-hour frequency at *CS-U2* is nearly twice as high. However, even with the same actual train frequency, PM_{10} concentrations at the *CS-U2* station were higher than at *CS-U1*

(Table S4). An interesting comparison is between the *U-Bahn* transfer station *Innsbrucker Ring* (*IR-U*, Table S2) with the lowest observed PM_{10} (114 μg m^{-3}, only one measurement) and *CS-U2* with the highest PM, which has almost the same platform design. Given that the difference in PM_{10} was approximately a factor of two when measured with similar actual train frequencies (Table S2, Table S4), it appears that *IR-U* is better ventilated. To investigate the difference in PM between two-track platforms, we compared *U-Bahn* station *Odeonsplatz* (*OU-U*, 179 ± 52 μg m^{-3}) with two tracks separated by a wall and *U-Bahn* station *CS-U1* with the shared platform mentioned above. As seen in Table 1, no significant difference in PM was observed. The measurements for these comparisons were not done simultaneously, but based on the standard deviations of repeated measurements at different times and even seasons, the concentrations were relatively stable. However, more measurements would be needed to accurately quantify the differences. Additional CO_2 measurements would help to investigate the effect of ventilation on PM. Another important hot-spot among the investigated routes was the *U-Bahn* transfer station *Ostbahnhof* (*OB-U*, 205 ± 72 μg m^{-3}), where $PM_{2.5}$ and PM_1 reached 80 ± 18 μg m^{-3} and 21 ± 5 μg m^{-3}, respectively. The busy *S-Bahn* underground station *Hauptbahnhof (CS-S*, a two-track platform with extended platforms on both sides of the tracks) yielded PM_{10} 236 ± 52 μg m^{-3} in the scouting measurement on November 24, 2021, but the mean value of the other investigations was 126 ± 89 μg m^{-3} and the lowest measured PM_{10} of 34 ± 21 μg m^{-3} on December 7, 2021 (Table S6). The neighboring *U-Bahn* stations *CS-U1* and *CS-U2* showed higher PM concentrations even at lower train frequencies. Because *S-Bahn* trains exit the tunnel to the surface 200 m beyond the *CS-S* station, it is probably better ventilated. More measurements would be needed to compare, which train emits/resuspends more particles.

In summary, the recommended PM levels for ambient air by the WHO (World Health Organization, 2021) were exceeded at almost all measurement sites and are, therefore, high for long-term exposure.

3.3.2. Repetition of the same route: intra-day variability, indoor/outdoor comparison

Based on the subway scouting rides (section 3.3.1.), a route was defined for repeated measurements. The heat-map (Fig. 4) summarizes the on-line measurements of the repetitions of the same route in the morning (*m*), noon (*n*) and afternoon (*a*) and shows how many times the concentrations of PM_1, $PM_{2.5}$, PM_{10}, PNC, eBC and UVPM were elevated on the specific transect of the route (x-axis) compared to the average concentrations of the reference ambient routes (section 3.1.). Ambient walking measurements (*aw*) at the beginning and end of each route show the deviation from the reference ambient measurement at a given time. Stationary measurements at selected platforms (*s*) and subway rides (*r*) are located between the dashed vertical lines indicating train boarding and exiting.

Generally, PM concentrations were highest during the morning and afternoon rush-hours and lowest during midday. Train frequency was a key factor, as it was 5 min in the morning (7-9 am) and afternoon (3-7 pm) rush-hours and 10 min during noon, which corresponds with measured PM (the morning measurement period occurred between 7:54-9:53 and the afternoon period between 16:32-18:10). Other factors may contribute to intra-day variability, such as the number of people moving on the platform, as discussed e.g. in the Shanghai study (Zhao et al., 2017).

At the stations (*s*) measured, the highest PM concentrations were generally at transfer stations with more lines and thus higher overall train and passenger frequencies. $PM_{2.5}$ concentrations at *OB-U* station were 44 times higher than ambient urban background levels. During the ride, the PM concentrations were usually greater in the tunnel than on the platforms. This was observed also in Prague (Braniš, 2006), but not in Barcelona (Martins et al., 2015). The tunnel was found to be a dominant source of PM and the quality/lack of train ventilation influenced how much PM entered the trains. Similar findings have been reported in Athens (Martins et al., 2016) and Naples (Cartenì et al., 2015). At *S-Bahn* platforms the PM concentrations were lower than at *U-Bahn* platforms as well as during *S-Bahn* trips. As discussed in Section 3.3., PNC inside trains and on platforms were generally at ambient levels. On elevators, all PM concentration decreased to the half while PNC values increased suggesting that there is a sufficient air exchange with the outside, which is more polluted by traffic in the city center.

To compare personal exposure, average time periods spent at the platforms and in the trains as well as average human breathing rates would need to be considered. In Barcelona, concentrations were higher at platforms, however, based on their calculations, the dose was double in trains due to the longer exposure time (Martins et al., 2016).

From the heat-map in Fig. 4, it is visible that spatial variability of PM is more important than temporal and the PM concentrations are raising when travelling from open-space terminus *NS* to the city.

Because no emissions from combustion processes have been observed at the majority of platforms, eBC and UVPM readings are most likely FePM interferences, as discussed in Section 3.3. However, the MA-200 instrument can explain the PM spatio-temporal variability similar to OPS. As the MA-200 has a suitable size for mobile measurements, its use for identifying hot-spots might be interesting and more detailed analysis of eBC and UVPM might be part of a future study.

3.3.3. Micro-scale PM spatio-temporal variability during the specific rides, old vs. new trains

Exemplarily, Fig. 2 shows the detailed variability of PM and PNC in 1 Hz resolution with a 10 s moving average (line). It represents the typical ride from the terminus *NS-U/S*, which is over-ground so ambient urban PM and PNC concentrations were present at the station and inside the train. This represents an ideal start for investigating the dynamics of concentrations inside the train and the behavior of PM in the tunnel system.

PM_{10} concentrations started to raise when the train entered the tunnel and reached about four times higher values within only 1 min until the next stop. The rapid exchange was accelerated by open windows in the wagon of the "old" train, which was empty. PM concentrations increased relatively uniformly throughout the entire ride to downtown. In less than 20 min, PM_{10} reached up to one order of magnitude higher levels at *U-Bahn* station *CS-U1* (city center). Opening the doors at the stations (indicated by vertical lines) typically caused an immediate slight decrease in PM_{10} concentrations as the air was exchanged and diluted. The largest decrease occurred at the *U-Bahn* station *IR*, which has an exceptionally large size and relative low concentration levels, as discussed in Section 3.3.1. The station itself did not serve as a significant sink for PM_{10} from the tunnel since concentrations rose sharply up- and downstream of the *IR* platform.

$PM_{2.5}$ and PM_1 were increasing gradually (slightly step-wise) with a similar trend, but the overall dynamics were lower with concentrations up to about 100 and 25 μg m^{-3}, respectively. PM_1 remained stable and the effects of the stations were negligible.

PNC did not follow the trend of PM and remained mostly at urban background levels, as shown previously (Table 2, Fig. 4). At the *U-Bahn* station *Neuperlach Zentrum* (*NZ-U*), PNC were around 11 500 pt cm^{-3}, which is appr. twice as high as the usual values in the *U-Bahn*. Most likely, traffic related particles were introduced into the subway system, since there is a large bus station, a shopping mall, and a relatively busy street above the *NZ-U* station. Interestingly, PNC were already rising at the previous subway stop. A similar situation on a smaller scale occurred at the next stop *U-Bahn* station *Quiddestrasse* (*QI-U*), and thereafter, the PNC decreased to "normal" levels within 2 min of travelling, while $PM_{2.5}$ continued to increase. The lower PNC in tunnels and stations in the city center might be caused by the lack of ventilation rather than absence of traffic-related particles above the subway.

The same experimental route was repeated with a new train (*n*) with air conditioning and closed windows (Fig. S6). First, on the way from *CS-U1* to the terminal station *NS-U/S* and then, after a short brake, back to the *CS-U1* platform with exactly the same train. The average

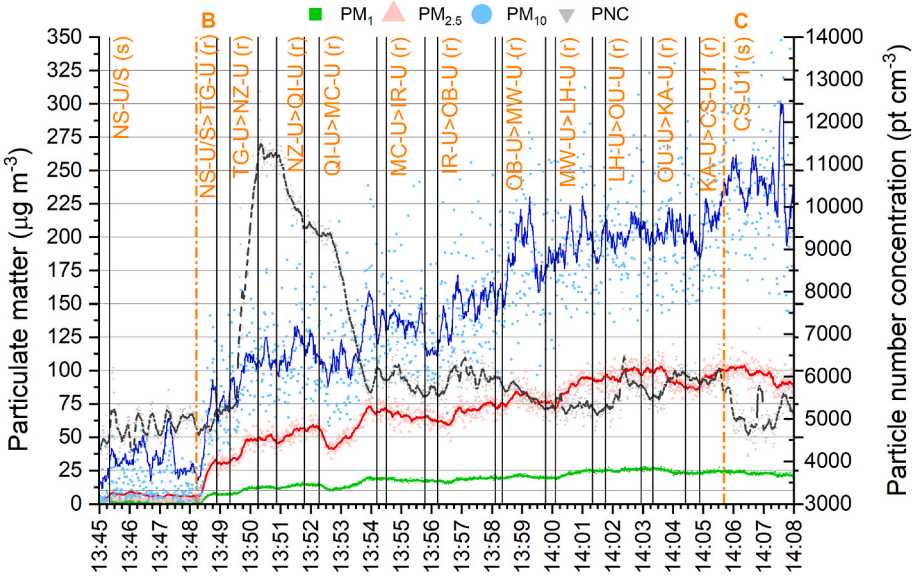

Fig. 2. PM_1, $PM_{2.5}$, PM_{10} and particle number concentration (PNC) dynamics during the ride (B) from the over-ground subway terminal station NS-U/S towards CS-U1 station by the old train (U5 line) on 17. 5. 2022. First vertical black line represents entering the train, which was waiting in the station (s), orange dashed line entering the tunnel and following black lines indicate door opening/closing at the stations (stations' abbreviations are above with indication of the direction of the ride (r), list of abbreviation is in the Table 1). Scatter represents 1s dynamics of concentrations and color lines are 10s moving averages. PM_x data of the part B and C were corrected based on the effective density of $PM_{2.5}$ (2.106 g cm^{-3}) measured at CS-U1 on 28. 8. 2022.

concentrations of PM_1, $PM_{2.5}$, PM_{10} were only 8-10% higher on the way from *CS-U1,* PNC were 2% higher. After the 40 min measurement at *CS-U1*, the same route to *NS-U/S* was repeated by an old train (o). Surprisingly, the difference in dynamics between old and new train in the same direction was only 7-12% for PM_1, $PM_{2.5}$, PM_{10} and 13% for PNC. The air conditioning systems seemed to be not efficient enough or were not equipped with air filters, which would clean the indoor air. Therefore, the air conditioning systems should be improved to achieve higher filtration efficiencies, such as in Barcelona (Querol et al., 2012).

3.4. PM dynamics on subway platforms during stationary measurements

As described in Section 4.2. and 4.3., PM concentrations measured stationary at the *U-Bahn* platform *CS-U1* were relatively stable in the range of 10^2 µg $m^{-3}$of PM_{10} (Table 2, Fig. 4). PM and PNC were illustrated in Fig. 3, which shows a 42-min representative section in order to investigate the source and what might influence the micro-dynamics. The columns indicate the time the train was in the station (*U5* in brown, *U4* in green), the arrow indicates the direction of travel (left: *Laimer Platz to Theresenwiese*, right: direction *NS-U/S to Arabellapark*).

Significant signals of PNC were associated with high numbers of people exiting the train (e.g. at 14:13-14:14), but the exact number was not noted. The signal decrease occurred relatively fast after departure of the train due to the wind caused by train movement (piston effect). The movement of the train is also affecting PM, probably due to the entering of polluted air from the tunnel. A similar behavior was described e.g. in Barcelona (Moreno et al., 2014). In some cases, when two trains left at the same time but in opposite directions (e.g. time 14:42-14:43 and 14:35), the PM_{10} concentration raised rapidly for a short time. In this

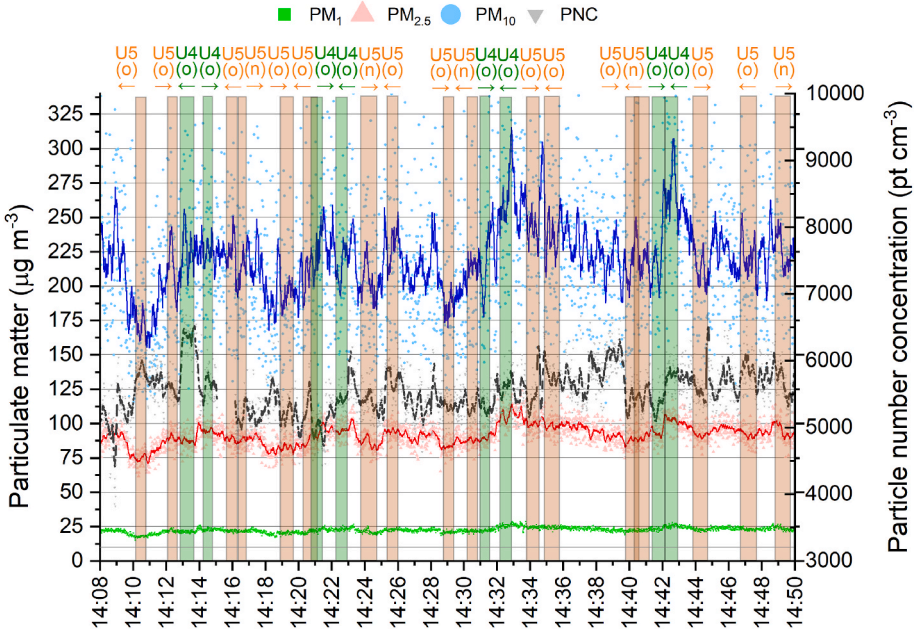

Fig. 3. Dynamics of PM_1, $PM_{2.5}$, PM_{10} and particle number concentration PNC (1s scatter) with 10s moving averages (color lines) at the Munich U4/U5 subway station CS1-U on 17. 5. 2022. Columns indicate trains in the station (arrival-departure), the line U4 (green) and U5 (brown) and the direction is indicated above (right arrow is towards NS U5/Arabelespark U4 station), "o" indicates the old train and "n" the new train.

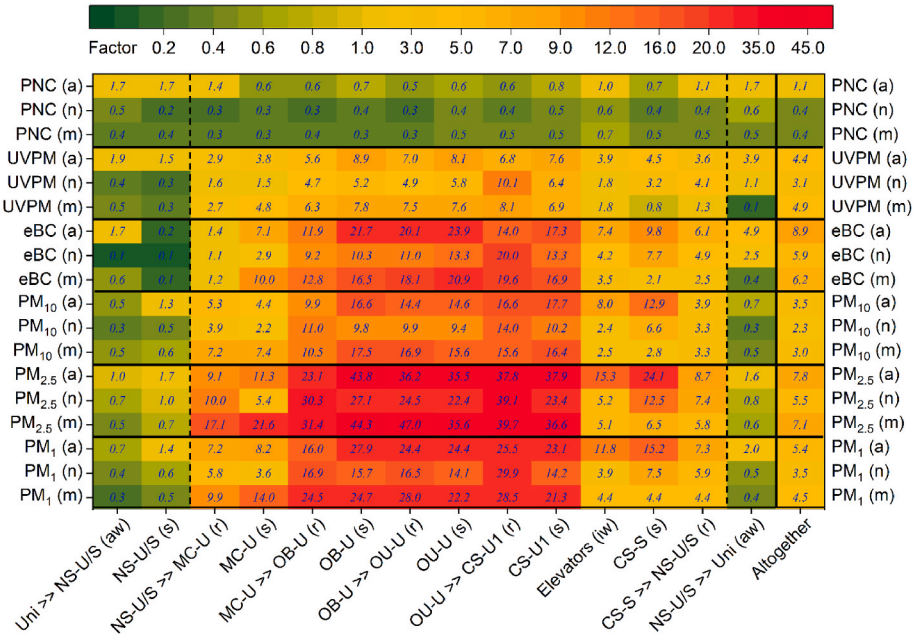

Fig. 4. Spatio-temporal variability of PM_1, $PM_{2.5}$, PM_{10}, equivalent black carbon (eBC), UV-absorbing PM (UVPM), particle number concentration (PNC) during the repetition of the same route in the morning (m), noon (n) and afternoon (a) on 12. 7. 2021. Each route is divided into ambient walk (aw), indoor walk (iw), stationary measurements at platforms (s) and rides by the train (r). Dashed line indicates entering and exiting the train. Heatmap represents the ratio of the average absolute concentrations of each part of the route to the overall average of 6 repetitions of a typical ambient walk (urban PM background) around the NS-U/S station. Last column "Altogether" represents the average from the whole route. Route starts and finishes at the campus of the Bundeswehr University (Uni) and consist of underground (U) and overground (S) stations listed in Table 1.

experiment, there was no significant difference in PM concentrations between new and old trains. Most likely, both trains resuspended PM similarly and any possible difference in emissions did not appear on the platform.

3.5. ICP-MS metal analysis

Table 3 shows the results of ICP-MS analysis for personal samples from 4 typical ambient walks (**A3-A6**) and 24-h reference stationary ambient air sampling using a high-volume sampler for comparison (**Ref**), 4 scouting subway routes (**B-E**), 3 repetitions of the same route (**F1-F3**), and two stationary platform measurements (**G1, G2**). All samples contain the PM_{total} fraction except **G1** and **Ref**, where it is $PM_{2.5}$. All routes are described in the previous chapters (Table 2 contains corresponding averages from on-line instruments) and additional parameters are available for comparison (Table 1, Tables S2–S8). In addition to Fe, Mn, Cr, Cu, Ni, V and Pb listed in Table 3, other elements were analyzed of which Na, Al, K, Zn and Ba were excluded from the dataset due to high blank concentrations. The reason for this could be the short sampling time, contamination and/or use of quartz filters. For other elements (Be, Mg, V, Co, As, Se, Ag, Cd, Sb and Th), both blanks and all samples were below the limit of detection (LOQ). This may be due to short sampling times and/or low concentrations in the air.

During the subway scouting rides, the highest concentrations of iron (Fe) in the PM_{total} fraction of 123 μg m^{-3} was recorded on November 5, 2021, while the highest concentration during the ambient walks was 2.6 μg m^{-3} on October 26. 2021. Fe was the dominating metal in the subway, as in other subway systems (Font et al., 2019; Chang et al., 2021; Ji et al., 2021). Subway scouting routes **B-E** yielded similar values with the exception of route **D**, which contained 48-min. measurements at the railway main train station (*CS-R*, Table S4). PM concentrations on the *CS-R* platform were close to ambient levels probably due to good ventilation. The Fe content per average aerosol mass followed a similar trend in all subway samples (on average about 1.7 compared to 0.2 in the ambient air). Further abundant metals were manganese (Mn), chromium (Cr), and copper (Cu). A significant increase in the subway was also observed for vanadium (V), however, most of the filters were below the LOQ.

Stationary measurements on the U-Bahn platform *CS-U1* revealed an Fe concentration of 67 μg m^{-3} in the $PM_{2.5}$ fraction on May 17, 2022 accounting for about 69% of $PM_{2.5}$ (Table 2). On July 19, 2022, the Fe concentration in PM_{total} was 171 μg m^{-3} while PM_{10} and $PM_{2.5}$ fractions were 218 ± 50 μg m^{-3} and 85 ± 8 μg m^{-3}, respectively. Therefore, most of the PM mass was formed by ferruginous particles (FePM).

The ratio of iron to other metals could provide information on the origin of the particles if compared to the corresponding ratios in materials subject to abrasion. The Mn/Fe ratio was 0.01 as in the Barcelona subway, where it was considered as a typical ratio for the origin of steel from wheels, rails and brakes (Moreno et al., 2015). The average ratios of different metals compared to Fe at *CS-U1* platform were 0.91% (Mn), 0.39% (Cr), 0.45% (Cu), 0.30% (Ni), 0.018% (V), respectively, while the usual composition of one of the most common rail steel R260 is: 0.92–1.07% (Mn), 0.03–0.12% (Cr), 0.01–0.12% (Cu), 0.01–0.08% (Ni), 0.002–0.011% (V), respectively. The variation for some elements may be due to the contribution of other sources or slightly different steel types used. Cu, Mn, Cr, and Ni are present in brake pads (with high variance), which are subject to wear (Font et al., 2019).

3.6. SEM-EDX imaging and single particle elemental analysis

The majority of subway particles analyzed via SEM exhibited a rough, splintery surface, oftentimes present as flakes (exemplary micrographs of characteristic particles are shown in Fig. 5a and Figs. S8-11Figs. S7–10 in the SI), which is in agreement with results of studies all over the world (Jung et al., 2012; Loxham et al., 2013; Moreno et al., 2015; Perrino et al., 2015; Wang et al., 2016; Grana et al., 2017; Chang et al., 2021; Guseva Canu et al., 2021). The uneven and rough edges found for most particles suggest that they are mainly derived from abrasion processes, most likely at the rail-wheel-brake interface (Kang et al., 2008; Byeon et al., 2015; Moreno et al., 2015; Perrino et al., 2015; Wang et al., 2016).

EDX analysis revealed that these particles consist predominantly of Fe (63.4 ± 8.67 wt%) and O (36.2 ± 8.2 wt%), with lower contents of Si (0.1 ± 0.9 wt%). Since filter samples used for EDX analysis were sputtered with a layer of carbon, no information on the concentration of carbon could be obtained. Moreno et al. (2015) reported element concentrations for iron-rich particles of 40.0–65.0 wt% for Fe, 9.0–32.5 wt % for O, 2.0–19.5 wt% for C, and 1.0–8.5 wt% for Si. While our findings are in agreement with their Fe and O ranges, the amounts of Si vary, which might be explained by the usage of different steel types for train

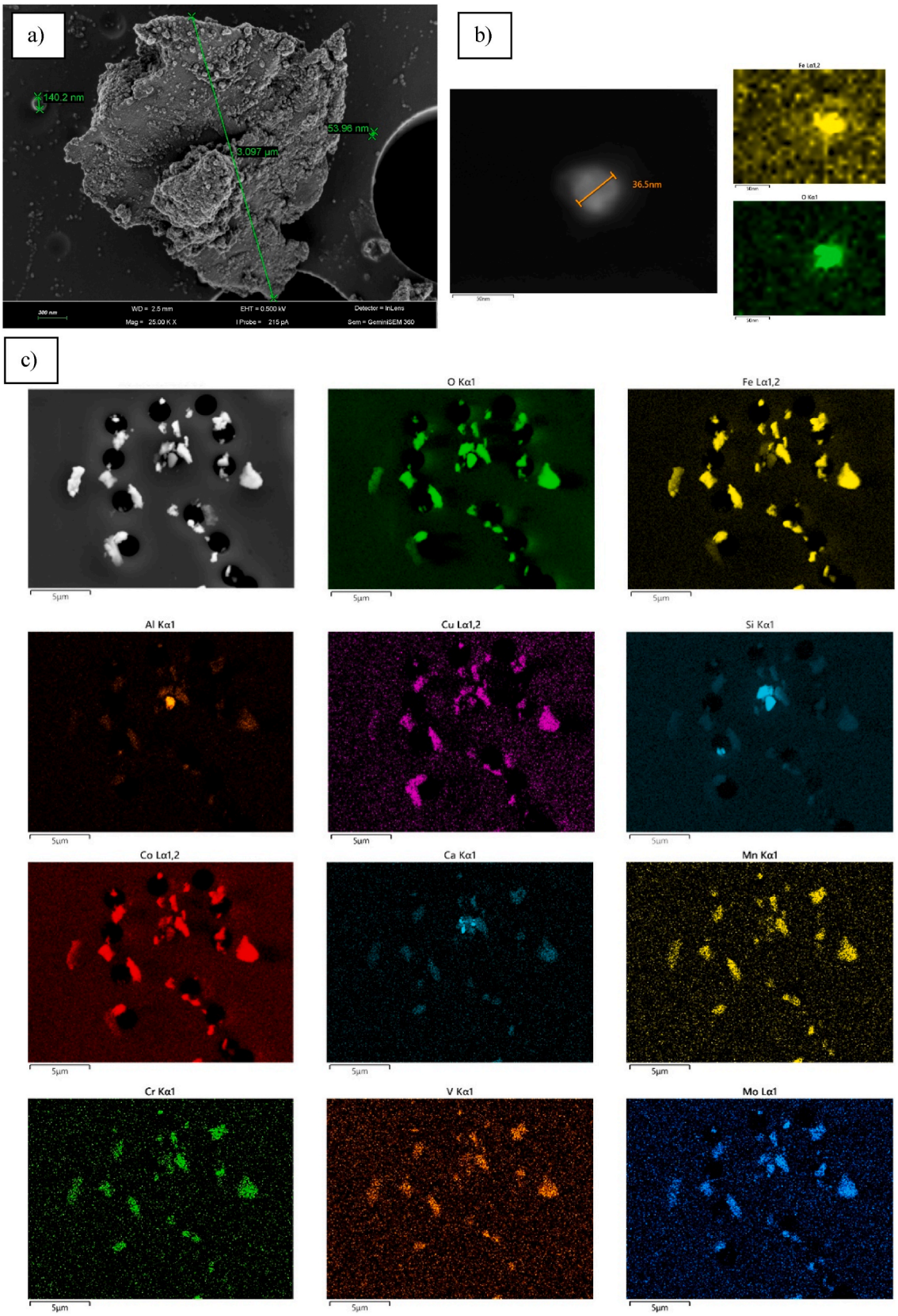

Fig. 5. a) SEM-micrograph of flake-like subway particle consisting predominantly of Fe and O with attached clusters of 20–30 nm sized spherical iron oxide and carbon containing particles, b) EDX mapping of 37 nm subway particle at 5 kV, c) EDX mapping of subway particles on a polycarbonate filter at 20 kV (size range of particles 200 nm–2.5 µm) Print in color.

rails and wheels in the Barcelona subway system, as well as differences in the composition of front and lateral brake pads between Munich and Barcelona.

Automated classification of EDX data showed that 75.43% of the >180 000 analyzed particles were made of iron oxides, while 5.35% consisted of metallic Fe and 1.23% belonged to geological, soil-derived particles. A total of 16.89% of all particles was not classified, however, large peaks for carbon and oxygen were observed in the spectra of these particles. This led to the assumption that these particles were mainly carbonaceous. Byeon et al. (2015) who used passive sampling reported values of 66 ± 9% for $PM_{2.5\text{-}1}$ in the Seoul subway system, while Jung et al. (2010) stated that 71 - 79% of all particles at stations without platform protection doors in Seoul consisted of iron-rich particles. These values are in accordance with our data highlighting the similarities in sampled subway aerosols around the globe.

The elemental distribution of Munich subway aerosol was similar for iron-rich particles of all analyzed sizes (250 nm - 5 μm) suggesting that the particles are originating from the same source. However, we observed that with decreasing particle size the ratio of iron to oxygen also decreased from Fe/O = 2.19 for particles of 5 μm to a ratio of Fe/O = 1.37 for particles of 250 nm. This can be explained by the increased ratio of surface area to volume of smaller particles, which facilitates oxidation processes at the surface of the particles.

Furthermore, clusters of nanoparticles adhering to larger ferruginous particles could be observed (Fig. 5), which were either iron-rich or of carbonaceous nature, and were also described by other research groups (Kang et al., 2008; Jung et al., 2010, 2012; Moreno et al., 2015). Iron oxide bearing nanoparticles were also found in an isolated form with their size ranging from 20 to 150 nm. An exemplary EDX mapping of a 37 nm iron oxide particle is given in Fig. 5b. Spherical Fe particles could originate from condensation of gaseous iron formed from sparking (Kang et al., 2008; Jung et al., 2010) while carbonaceous nanoparticles could be formed from oxidation of volatile organic compounds on the active metal surface of host particles (Kang et al., 2008; Moreno et al., 2015) or adhesion of soot particles from the outside air (Moreno et al., 2015; Grana et al., 2017). Graphite can also be found in brake pads and carbon particles can originate from electromotor brushes as discussed in Section 3.3. Literature suggests that iron oxides in the subway environment are present as hematite (Fe_2O_3), magnetite (Fe_3O_4) and maghemite (γ-Fe_2O_3) (Jung et al., 2012; Lu et al., 2015; Moreno et al., 2015), which we were not able to distinguish via EDX measurements.

Apart from the main elements Fe, O, and C the majority of particles in the subway aerosol was accompanied by trace elements such as Cu, Co, Mn, Cr, V, and Mo. These elements were also discovered by research groups world-wide (Kang et al., 2008; Jung et al., 2010; Midander et al., 2012; Moreno et al., 2015). Particles containing $BaSO_4$ or Sb that are attributed to brake wear and which were previously found in different subway systems (Kang et al., 2008; Moreno et al., 2015; Chang et al., 2021; Guseva Canu et al., 2021) were rare in the samples. In total, only 25 of >180 000 particles could be related to braking events via these metals. Fig. 5c shows an elemental mapping of subway particles on a PC filter.

While Munich subway aerosol (line *U5*) is similar in composition to subway systems in other cities, the often-reported Cu-rich particles, which are believed to originate from sparking and abrasion processes at the pantograph-catenary interface (Mugica-Álvarez et al., 2012; Moreno et al., 2015; Wang et al., 2016; Guseva Canu et al., 2021), were only scarcely observed in this study. In fact, only 220 of the total 182 020 particles analyzed were classified as Cu-rich and the reason might be that subway trains in Munich are powered by the third rail, which is made of low-carbon stainless steel at the sampled location (*https://www.u-bahn-muenchen.de/*).

Apart from iron-rich PM, several particles of supposedly geological origin were present in the samples. Particles attributed to this class consisted mainly of aluminium-magnesium silicates and quartz with occasional calcium carbonates, which is also described in the literature (Kang et al., 2008; Mugica-Álvarez et al., 2012; Byeon et al., 2015; Moreno et al., 2015; Perrino et al., 2015). These particles, as well as soot particles that were found in the samples, might entered the subway system by commuters or by mixing of in the subway generated aerosol with air from outside the system via ventilation (Kang et al., 2008; Mugica-Álvarez et al., 2012).

During the manual SEM-EDX analysis, we found several Fe-rich particles with layered structures interconnected by grooves. The structure and genesis of this particle type is unknown and has not been discussed in literature to our knowledge. A SEM micrograph and EDX spectra of one of the unknown particles, which consisted mainly of Fe, O, and C but also traces of Mn and Cr is given in Fig. S12 in the SI. The concentrations of Mn and Cr might indicate that the particle originated from some type of steel, however, its texture is not common for abrasion or evaporation derived particles but resembles more a crystalline structure. An additional EDX mapping of the particle class is given in Fig. S13 in the SI.

3.7. Summary

In the selected part of the *U-Bahn* subway line *U5*, PM_{10}, $PM_{2.5}$ and PM_1 concentrations at platforms ranged from 59 to 220, 27–80 and 9–21 μg m^{-3}, respectively. During typical trips, the average values ranged from 73 to 170, 29–59, 8 - 19 μg m^{-3}, respectively. The highest PM_{10} levels on the *CS-U2* platform were 231 ± 52 μg m^{-3}. Compared to WHO air quality recommendations, PM levels were generally high for long-term or repeated exposure, and mitigation measures for PM should be of great interest. The measured hot-spots could be classified as *very poor/extremely poor* compared to other subway systems (Cartenì et al., 2020). Most of the particle mass consisted of ferrous particles (FePM) from wheel and rail abrasion. Inadequate ventilation of platforms and tunnels is likely to be the cause of high PM levels. Probably for the same reason, subway PNC levels were not elevated even in the city center (10^3 - 10^4 pt cm^{-3}). Only a few cases of outdoor traffic-related particles with high PNC entering the subway platform were observed so ambient air was not the dominant source of PM.

Using mobile measurements, we observed a high spatial variability of PM among platforms and tunnel sections, which increased from the above-ground terminus *NS-U/S* towards downtown. The highest concentrations were measured at transfer stations with an overall high train frequency. The intra-day variability was mainly influenced by train frequency, so that PM concentrations were highest during the morning and afternoon rush-hour. Otherwise, concentrations at specific platforms were relatively stable over time (day of week, season). The same trend was observed from the eBC readings, but it is likely to be due to light-absorbing metal artifacts so further investigation of BC is needed.

The design of the station affected the concentrations – platforms with larger volumes tended to have lower PM concentrations than smaller with the same train frequency but the PM_{10} variability between these platforms was higher than on the double-track platforms. PM dynamics inside the train were high during rides due to the high air exchange with the outside tunnel. Old trains without air conditioning and with opened windows had slightly higher PM concentrations than new trains with air conditioning but the difference was less than 12% indicating poor or no filtration.

ICP-MS analysis quantified elevated levels of metals in the subway, particularly iron and metals present in the steel of the rails and wheels. Ferrous particles formed the majority of the aerosol mass. SEM-EDX analysis revealed the shape and size distribution of the metal particles. Trace elements typical for subways have been detected. The copper content in the Munich subway appeared to be lower than in other cities probably due to the absence of copper catenaries. Our results show that iron-rich particles and other metals are present even in the inhalable fraction of the aerosol, which could cause negative health effects. One of the described toxicological effects is the formation of reactive oxidative species (ROS) through the Fenton reaction, which can induce oxidative

stress (Kanti Das et al., 2014). However, most of the mass of these particles is formed by larger particles and not UFP, which can be deduced from the fact that PNC and LDSA in metro stations are not significantly elevated compared to ambient air values. Nevertheless, iron oxides nanoparticles around 30 nm were found. Given the potential association between iron nanoparticles and neurodegenerative diseases via the olfactory nerve entry route (Hopkins et al., 2018; Liu et al., 2018), toxicological investigations with real subway aerosol on this topic would be of interest.

To effectively mitigate air pollution, individual comprehensive measurements need to be made as subway systems can vary widely. While platform screen doors (PSD), air conditioning and other measures can reduce PM concentrations in the subway, they usually do not mitigate them completely (Chang et al., 2021; van Ryswyk et al., 2021). Measurements at selected platforms, as presented in other studies (Johansson and Johansson, 2003; Colombi et al., 2013; Moreno et al., 2014; Cusack et al., 2015; Chang et al., 2021), provide a comprehensive characterization of PM variability at one or several sites but often do not account for spatio-temporal variability in the wide variety of micro-environments during typical commuter rides. In addition, such campaigns can have high requirements on organization and equipment installation, which may be one reason why only a limited number of metro systems around the world have been characterized.

Based on our results, we propose to improve the air conditioning system of the new trains (ideally equipped with HEPA filters) and improve the ventilation of the platforms, but in such a way that there are no subway exhausts near busy streets or other sources of aerosol. More frequent dusting of the tracks and the best available brake system technology could also be beneficial. Wearing face-masks in subway could help to decrease the personal exposure from coarse particles as suggested by Ji et al. (2021), however, protection from nanoparticles is limited. Drivers and subway operators might be the most exposed to PM concentrations, so we propose to install air purifiers in the driver's cab.

The presented methodology for comprehensive air quality characterization in subways using a mobile measurement system has proven to be a fast and thorough way to determine the aerosol composition to which a subway passenger is exposed to. It can be used to map PM and PNC concentrations in different cities in a comparable manner by taking into account the high spatio-temporal variability of PM. Furthermore, realistic doses of specific pollutants can be calculated. This relatively low-cost approach typically requires no special preparations and measurements can be made rather effectively. Repeated trips can identify hot-spots and estimate personal exposure. Sampling for chemical analysis and particle imaging can reveal sources and potential health risks. In the future, it can be used to monitor potential air quality limits and the effectiveness of measures. The same system can also be used to compare different modes of transportation. Moreover, gas phase measurements and bioaerosol sampling can be added.

Funding sources

This research is funded by dtec.bw – Digitalization and Technology Research Center of the Bundeswehr [project LUKAS and MORE]. Dtec.bw is funded by the European Union – NextGenerationEU. This research was also supported by the project ULTRHAS – ULtrafine particles from TRansportation – Health Assessment of Sources, a project funded under the EU's Research and Innovation programme Horizon 2020, Grant Agreement No. 955390. We acknowledge financial support by Universität der Bundeswehr München.

CRediT authorship contribution statement

Jan Bendl: Conceptualization, Data curation, Formal analysis, Investigation, Methodology, Supervision, Visualization, Writing – original draft. **Carsten Neukirchen:** Formal analysis, Investigation, Methodology, Writing – original draft, Writing – review & editing. **Ajit Mudan:** Investigation. **Sara Padoan:** Investigation, Methodology, Writing – original draft. **Ralf Zimmermann:** Writing – review & editing. **Thomas Adam:** Conceptualization, Funding acquisition, Investigation, Methodology, Project administration, Resources, Supervision, Writing – review & editing.

Declaration of competing interest

The authors declare that they have no known competing financial interests or personal relationships that could have appeared to influence the work reported in this paper.

Data availability

Data will be made available on request.

Acknowledgement

Measurements were supported by students from the University of the Bundeswehr Munich M.Eng course Computer Aided Engineering (CAE): Ferdinand Lindenpütz, Moritz Tenckhoff, Rene Pfeiffer, Gregor Franke, Erik Milde. Construction of the measuring system was supported by the CAE master student Sören Möhrs.

Abbreviations

CPC	condensation particle counter
eBC	Equivalent Black Carbon
EC	Elemental Carbon
EDX	energy-dispersive X-ray spectroscopy
GPS	Global positioning system
ICP-MS	Inductively coupled plasma mass spectrometry
LDSA	lung deposited surface area
NEE	non-exhaust emissions
OC	Organic Carbon
ONA	Optimized Noise-Reduction Averaging
OPS	Optical particle sizer
PC	Polycarbonate
PAHs	Polycyclic Aromatic Hydrocarbons
PM	Particulate Matter
PM_x	particulate matter smaller than X μm in the aerodynamic diameter
PNC	particle number concentration
PSD	platform screed doors
SEM-EDX	Scanning electron microscopy with energy dispersive X-ray spectroscopy
SIA	secondary inorganic aerosols
UFP	ultrafine particles
UVPM	ultraviolet absorbing particulate matter

Appendix A. Supplementary data

Supplementary data to this article can be found online at https://doi.org/10.1016/j.atmosenv.2023.119883.

References

Aarnio, P., Yli-Tuomi, T., Kousa, A., Mäkelä, T., Hirsikko, A., Hämeri, K., Räisänen, M., Hillamo, R., Koskentalo, T., Jantunen, M., 2005. The concentrations and composition of and exposure to fine particles (PM2.5) in the Helsinki subway system. Atmos. Environ. 39, 5059–5066.

Bachoual, R., Boczkowski, J., Goven, D., Amara, N., Tabet, L., On, D., Leçon-Malas, V., Aubier, M., Lanone, S., 2007. Biological effects of particles from the paris subway system. Chem. Res. Toxicol. 20, 1426–1433.

Braniš, M., 2006. The contribution of ambient sources to particulate pollution in spaces and trains of the Prague underground transport system. Atmos. Environ. 40, 348–356.

Byeon, S.-H., Willis, R., Peters, T.M., 2015. Chemical characterization of outdoor and subway fine (PM(2.5-1.0)) and coarse (PM(10-2.5)) particulate matter in Seoul (Korea) by computer-controlled scanning electron microscopy (CCSEM). Int. J. Environ. Res. Publ. Health 12, 2090–2104.
Cartenì, A., Cascetta, F., Campana, S., 2015. Underground and ground-level particulate matter concentrations in an Italian metro system. Atmos. Environ. 101, 328–337.
Cartenì, A., Cascetta, F., Henke, I., Molitierno, C., 2020. The role of particle resuspension within PM concentrations in underground subway systems. Int. J. Environ. Sci. Technol. 17, 4075–4094.
Cepeda, M., Schoufour, J., Freak-Poli, R., Koolhaas, C.M., Dhana, K., Bramer, W.M., Franco, O.H., 2017. Levels of ambient air pollution according to mode of transport: a systematic review. Lancet Public Health 2, e23–e34.
Cha, Y., Olofsson, U., 2018. Effective density of airborne particles in a railway tunnel from field measurements of mobility and aerodynamic size distributions. Aerosol. Sci. Technol. 52, 886–899.
Chang, L., Chong, W.T., Wang, X., Pei, F., Zhang, X., Wang, T., Wang, C., Pan, S., 2021. Recent progress in research on PM2.5 in subways. Environmental science. Processes & impacts 23, 642–663.
Colombi, C., Angius, S., Gianelle, V., Lazzarini, M., 2013. Particulate matter concentrations, physical characteristics and elemental composition in the Milan underground transport system. Atmos. Environ. 70, 166–178.
Cusack, M., Talbot, N., Ondráček, J., Minguillón, M.C., Martins, V., Klouda, K., Schwarz, J., Ždímal, V., 2015. Variability of aerosols and chemical composition of PM 10 , PM 2.5 and PM 1 on a platform of the Prague underground metro. Atmos. Environ. 118, 176–183.
Font, O., Moreno, T., Querol, X., Martins, V., Sánchez Rodas, D., Miguel, E. de, Capdevila, M., 2019. Origin and speciation of major and trace PM elements in the Barcelona subway system. Transport. Res. Transport Environ. 72, 17–35.
Grana, M., Toschi, N., Vicentini, L., Pietroiusti, A., Magrini, A., 2017. Exposure to ultrafine particles in different transport modes in the city of Rome. Environmental pollution (Barking, Essex : 1987 228, 201–210.
Guseva Canu, I., Crézé, C., Hemmendinger, M., Ben Rayana, T., Besançon, S., Jouannique, V., Debatisse, A., Wild, P., Sauvain, J.J., Suárez, G., Hopf, N.B., 2021. Particle and metal exposure in Parisian subway: relationship between exposure biomarkers in air, exhaled breath condensate, and urine. Int. J. Hyg Environ. Health 237, 113837.
Hagler, G.S., Yelverton, T.L., Vedantham, R., Hansen, A.D., Turner, J.R., 2011. Post-processing method to reduce noise while preserving high time resolution in aethalometer real-time black carbon data. Aerosol Air Qual. Res. 11, 539–546.
Hopkins, L.E., Laing, E.A., Peake, J.L., Uyeminami, D., Mack, S.M., Li, X., Smiley-Jewell, S., Pinkerton, K.E., 2018. Repeated iron-soot exposure and nose-to-brain transport of inhaled ultrafine particles. Toxicol. Pathol. 46, 75–84.
Huck, W. (Ed.), 2022. Sustainable Development Goals. Nomos Verlagsgesellschaft mbH & Co. KG.
Ji, W., Li, X., Wang, C., 2021. Composition and exposure characteristics of PM2.5 on subway platforms and estimates of exposure reduction by protective masks. Environ. Res. 197, 111042.
Ji, W., Zhao, K., Liu, C., Li, X., 2022. Spatial characteristics of fine particulate matter in subway stations: source apportionment and health risks. Environmental pollution (Barking, Essex : 1987 305, 119279.
Johansson, C., Johansson, P.-Å., 2003. Particulate matter in the underground of Stockholm. Atmos. Environ. 37, 3–9.
Jung, H.-J., Kim, B., Malek, M.A., Koo, Y.S., Jung, J.H., Son, Y.-S., Kim, J.-C., Kim, H., Ro, C.-U., 2012. Chemical speciation of size-segregated floor dusts and airborne magnetic particles collected at underground subway stations in Seoul, Korea. J. Hazard Mater. 213–214, 331–340.
Jung, H.-J., Kim, B., Ryu, J., Maskey, S., Kim, J.-C., Sohn, J., Ro, C.-U., 2010. Source identification of particulate matter collected at underground subway stations in Seoul, Korea using quantitative single-particle analysis. Atmos. Environ. 44, 2287–2293.
Kang, S., Hwang, H., Park, Y., Kim, H., Ro, C.-U., 2008. Chemical compositions of subway particles in Seoul, Korea determined by a quantitative single particle analysis. Environ. Sci. Technol. 42, 9051–9057.
Kanti Das, T., Wati, M.R., Fatima-Shad, K., 2014. Oxidative stress gated by Fenton and haber weiss reactions and its association with alzheimer's disease. Arch Neurosci 2.
Karlsson, H.L., Holgersson, A., Möller, L., 2008. Mechanisms related to the genotoxicity of particles in the subway and from other sources. Chem. Res. Toxicol. 21, 726–731.
Karlsson, H.L., Ljungman, A.G., Lindbom, J., Möller, L., 2006. Comparison of genotoxic and inflammatory effects of particles generated by wood combustion, a road simulator and collected from street and subway. Toxicol. Lett. 165, 203–211.
Licina, D., Tian, Y., Nazaroff, W.W., 2017. Emission rates and the personal cloud effect associated with particle release from the perihuman environment. Indoor Air 27, 791–802.
Liu, J.-L., Fan, Y.-G., Yang, Z.-S., Wang, Z.-Y., Guo, C., 2018. Iron and alzheimer's disease: from pathogenesis to therapeutic implications. Front. Neurosci. 12, 632.
Liu, X., Hadiatullah, H., Zhang, X., Hill, L.D., White, A.H.A., Schnelle-Kreis, J., Bendl, J., Jakobi, G., Schloter-Hai, B., Zimmermann, R., 2021. Analysis of Mobile Monitoring Data from the microAeth® MA200 for Measuring Changes in Black Carbon on the Roadside in Augsburg, p. 13.
Loxham, M., Cooper, M.J., Gerlofs-Nijland, M.E., Cassee, F.R., Davies, D.E., Palmer, M.R., Teagle, D.A.H., 2013. Physicochemical characterization of airborne particulate matter at a mainline underground railway station. Environ. Sci. Technol. 47, 3614–3622.
Lu, S., Liu, D., Zhang, W., Liu, P., Fei, Y., Gu, Y., Wu, M., Yu, S., Yonemochi, S., Wang, X., Wang, Q., 2015. Physico-chemical characterization of PM2.5 in the microenvironment of Shanghai subway. Atmos. Res. 153, 543–552.
Lyu, Y., Olofsson, U., 2020. On black carbon emission from automotive disc brakes. J. Aerosol Sci. 148, 105610.
Martins, V., Cruz Minguillón, M., Moreno, T., Querol, X., Miguel, E. de, Capdevila, M., Centelles, S., Lazaridis, M., 2015. Deposition of aerosol particles from a subway microenvironment in the human respiratory tract. J. Aerosol Sci. 90, 103–113.
Martins, V., Moreno, T., Mendes, L., Eleftheriadis, K., Diapouli, E., Alves, C.A., Duarte, M., Miguel, E. de, Capdevila, M., Querol, X., Minguillón, M.C., 2016. Factors controlling air quality in different European subway systems. Environ. Res. 146, 35–46.
Midander, K., Elihn, K., Wallén, A., Belova, L., Karlsson, A.-K.B., Wallinder, I.O., 2012. Characterisation of nano- and micron-sized airborne and collected subway particles, a multi-analytical approach. Sci. Total Environ. 427–428, 390–400.
Minguillón, M.C., Reche, C., Martins, V., Amato, F., Miguel, E. de, Capdevila, M., Centelles, S., Querol, X., Moreno, T., 2018. Aerosol sources in subway environments. Environ. Res. 167, 314–328.
Moreno, T., Martins, V., Querol, X., Jones, T., BéruBé, K., Minguillón, M.C., Amato, F., Capdevila, M., Miguel, E. de, Centelles, S., Gibbons, W., 2015. A new look at inhalable metalliferous airborne particles on rail subway platforms. Sci. Total Environ. 505, 367–375.
Moreno, T., Pérez, N., Reche, C., Martins, V., Miguel, E. de, Capdevila, M., Centelles, S., Minguillón, M.C., Amato, F., Alastuey, A., Querol, X., Gibbons, W., 2014. Subway platform air quality: assessing the influences of tunnel ventilation, train piston effect and station design. Atmos. Environ. 92, 461–468.
Mugica-Álvarez, V., Figueroa-Lara, J., Romero-Romo, M., Sepúlveda-Sánchez, J., López-Moreno, T., 2012. Concentrations and properties of airborne particles in the Mexico City subway system. Atmos. Environ. 49, 284–293.
Perrino, C., Marcovecchio, F., Tofful, L., Canepari, S., 2015. Particulate matter concentration and chemical composition in the metro system of Rome, Italy. Environ. Sci. Pollut. Res. 22, 9204–9214.
Querol, X., Moreno, T., Karanasiou, A., Reche, C., Alastuey, A., Viana, M., Font, O., Gil, J., Miguel, E., de, Capdevila, M., 2012. Variability of levels and composition of PM_{10} and $PM_{2.5}$ in the Barcelona metro system. Atmos. Chem. Phys. 12, 5055–5076.
Roy, D., Lyou, E.S., Kim, J., Lee, T.K., Park, J., 2022. Commuters health risk associated with particulate matter exposures in subway system – globally. Build. Environ. 216, 109036.
Rupprecht Consult, 2019. Guidelines for Developing and Implementing a Sustainable Urban Mobility Plan, second ed., p. 168
Salo, L., Rönkkö, T., Saarikoski, S., Teinilä, K., Kuula, J., Alanen, J., Arffman, A., Timonen, H., Keskinen, J., 2021. Concentrations and size distributions of particle lung-deposited surface area (LDSA) in an underground mine. Aerosol Air Qual. Res. 21, 200660.
Schraufnagel, D.E., 2020. The health effects of ultrafine particles. Exp. Mol. Med. 52, 311–317.
Shakya, K.M., Saad, A., Aharonian, A., 2020. Commuter exposure to particulate matter at underground subway stations in Philadelphia. Build. Environ. 186, 107322.
Targino, A.C., Krecl, P., Brimblecombe, P., Oukawa, G.Y., Danziger Filho, J.E., Moreno, F.L., 2021. Spatio-temporal variability of airborne particulate matter in the São Paulo subway. Build. Environ. 189, 107526.
van Ryswyk, K., Anastasopolos, A.T., Evans, G., Sun, L., Sabaliauskas, K., Kulka, R., Wallace, L., Weichenthal, S., 2017. Metro commuter exposures to particulate air pollution and PM2.5-associated elements in three Canadian cities: the urban transportation exposure study. Environ. Sci. Technol. 51, 5713–5720.
van Ryswyk, K., Kulka, R., Marro, L., Yang, D., Toma, E., Mehta, L., McNeil-Taboika, L., Evans, G.J., 2021. Impacts of Subway System Modifications on Air Quality in Subway Platforms and Trains. Environmental science & technology. https://doi.org/10.1021/acs.est.1c00703.
Wang, B.-Q., Liu, J.-F., Ren, Z.-H., Chen, R.-H., 2016. Concentrations, properties, and health risk of PM2.5 in the Tianjin City subway system. Environ. Sci. Pollut. Res. Int. 23, 22647–22657.
World Health Organization, 2021. WHO Global Air Quality Guidelines: Particulate Matter (PM2.5 and PM10), Ozone, Nitrogen Dioxide, Sulfur Dioxide and Carbon Monoxide. WHO European Centre for Environment and Health, Bonn, Germany, p. 285.
Xu, B., Hao, J., 2017. Air quality inside subway metro indoor environment worldwide: a review. Environ. Int. 107, 33–46.
Xu, B., Yu, X., Gu, H., Miao, B., Wang, M., Huang, H., 2016. Commuters' exposure to PM2.5 and CO2 in metro carriages of Shanghai metro system. Transport. Res. Transport Environ. 47, 162–170.
Yang, F., Kaul, D., Wong, K.C., Westerdahl, D., Sun, L., Ho, K., Tian, L., Brimblecombe, P., Ning, Z., 2015. Heterogeneity of passenger exposure to air pollutants in public transport microenvironments. Atmos. Environ. 109, 42–51.
Zhao, L., Wang, J., Gao, H.O., Xie, Y., Jiang, R., Hu, Q., Sun, Y., 2017. Evaluation of particulate matter concentration in Shanghai's metro system and strategy for improvement. Transport. Res. Transport Environ. 53, 115–127.

Supplementary Information publication 3

Personal Measurements and Sampling of Particulate Matter in a Subway – Identification of Hot-spots, Spatio-temporal Variability and Sources of Pollutants

Jan Bendl[a,d,*], Carsten Neukirchen[a,c], Ajit Mudan [a], Sara Padoan[a, b], Ralf Zimmermann[b, c], Thomas Adam[a,b]

[a] University of the Bundeswehr Munich, Faculty for Mechanical Engineering, Institute of Chemical and Environmental Engineering, Werner-Heisenberg-Weg 39, 85577, Neubiberg, Germany

[b] Joint Mass Spectrometry Center (JMSC) at Comprehensive Molecular Analytics (CMA), Helmholtz Zentrum München, Ingolstädter Landstr. 1, 85764 Neuherberg, Germany

[c] Joint Mass Spectrometry Center (JMSC) at Chair of Analytical Chemistry, Institute of Chemistry, University of Rostock, Albert-Einstein-Strasse 27, 18059 Rostock, Germany

[d] Institute for Environmental Studies, Faculty of Science, Charles University, Benátská 2, 128 01 Prague, Czech Republic

*Corresponding author: jan.bendl@unibw.de (Jan Bendl)

Phone number: +49 89 6004 2473

Number of pages – 16

Number of figures – 15

Number of tables – 9

1.1 Development of the system for ambient/indoor spatio-temporal PM characterization

The measuring system was designed for mobile aerosol measurements and sampling, but can also be used for gas phase measurement and sampling. It can be placed inside the stroller/trailer for walking and cycling measurements, or attached to a frame-rucksack for walking measurement when a stroller cannot

be used. The box can also be attached to a car or other carriers, or even used as a stationary environmental enclosure.

It has a water-proof 71-liter, 4.4 kg aluminum box with external dimensions of L 59.5 x D 39.0 x H 38.0 cm, quality proved by the German Technical Inspection Association (TÜV), which is used sideways with door-like opening to the left side. Active ventilation is provided by two USB ventilators (diameter 25cm) on the backside, while one is in the bottom and the second one is in the top of the box. They are covered by a special grid preventing rain from entering the system. The upper ventilator is pushing out hot air while the lower ventilator is installed in the opposite direction (fig. S1). Ventilators are powered by a power bank and can be set to various speeds based on ambient temperatures. The aim is to keep inside the optimal temperature for instruments and samples to prevent malfunctions and losses of samples, especially volatile and semi-volatile compounds. The temperature in the box should always be slightly above outside temperature to prevent condensation in tubes/instruments, which is provided by natural heating of the instruments in operation. In some cases, heated inlet tubes can be additionally installed.

On the top of the box are 4 drilled holes with water-tide grommets for inlet installations. Omni-directional inlets (TSI) and the DISCmini (Testo) inlet are connected, but various other inlets can be used and further holes can be drilled/covered easily. When used in the stroller arrangement (in our case Thule Cab2 with brakes) the inlets are located exactly 100 cm above ground, which is in the breathing zone of a child. When used in a frame backpack, the inlets are in the breathing zone of an adult. Omnidirectional inlets should be used with a cap that prevents water from entering the hose.

Inside the box there are four rails made of ITEM profiles (profile 5, 20x10 mm) connected to the sides of the box (Fig. S1), with two adjustable shelves made of metal sheet (2 mm thickness), while the bottom is used as a third shelf. For optimal vibration damping, the foam originally intended for sound damping was used on the bottom of each shelf and on the sides. The instruments are optimally secured with a strap with a small ratchet. It was tested for the instruments used to avoid an undesirable increase in the amplitude of shaking, but effectively absorbed the vibrations.

In our case, the optical particle counter (OPS 3330, TSI) had to be placed at the top because larger particles are much more sensitive to losses, so the inlet is directly connected to the flexible conductive hose without having to bend it. In contrast, the DISCmini particle counter (Testo) can be placed on the bottom floor and the inlet tubing can be bent, since most particles are nanoparticles, which are not that sensitive to losses. The second floor is also used for filter holders and personal impactors (SIOUTAS, SKC). Pumps and computer are located on the bottom.

The GPS device and the instruments with the GPS sensor (Micro-Aethalometer MA200, AethLabs) must be located outside the box if they do not have an external antenna due to signal loss. Point-of-view cameras can be used for data analysis. The devices can be connected to a laptop/industrial computer with power supply to transmit the data directly and potentially display it in real time to the operator, or can even be remotely controlled via remote desktop using a GSM internet connection.

The basic requirements for setting up the device are the correct time according to GPS satellites, sufficient batteries/external power supply and data acquisition time set according to the measurement speed, where 1 Hz data is needed for cycling measurements, 1 or 5 Hz data for walking measurements. The GPS must always provide 1 Hz data in order to merge the data with all systems.

Attachment to the stroller is using a Velcro strap to its construction, while attachment to the backpack is by straps with ratchets and 4 eyelets on each side of the box.

Fig. S1: *Photo of the stroller (left) and the frame-rucksack (right) arrangement for walking measurements in the subway and used for other mobile aerosol measurements*

1.2 Stroller measurements of ambient air as a reference

The route for the ambient aerosol measurements as a reference to the subway mobile measurements was selected based on the following requirements:

1) The route must be around 1h long to observe enough micro-environments and have enough sample material on filter but, at the same time, the ambient PM background should not change significantly over the measuring time
2) The route should start and end at the same location to observe the change of background concentrations.
3) The route should be close to the long-term air quality monitoring station to allow data comparison.
4) Typical urban microenvironments should be included, e.g., busy and non-busy streets, highways, parks, residential areas, sports facilities, restaurants or kiosks (cooking emissions), schools, kindergartens, public buildings, et cetera.
5) It should be possible to repeat the same route for spatio-temporal variability, ideally also several times a day

In our case, these points were fulfilled by the route that mostly crosses the campus of the Bundeswehr University Munich (UniBW, Fig. S2), starting near the north gate to the west through administrative buildings towards the main gate with light traffic, then along the storage and sports facilities towards the Faculty of Mechanical Engineering with industrial machinery and in close proximity to the highway (southwest corner). Then back along the swimming pool, large parking lots with light traffic along the measuring station in the area of the University test circuit. The route continues through the student dorms (residential area) off campus where the cemetery is located. On the east side of the route is the end of the road tunnel, a busy intersection, and a road with heavy traffic and a 50 km/h speed limit where public transportation also operates. Buses also operate on the northern part of the roadway, but traffic there is milder and the speed limit is reduced to 30 km/h in the middle of the roadway.

The particle number concentration (PNC) best illustrates the variability due to traffic sources.

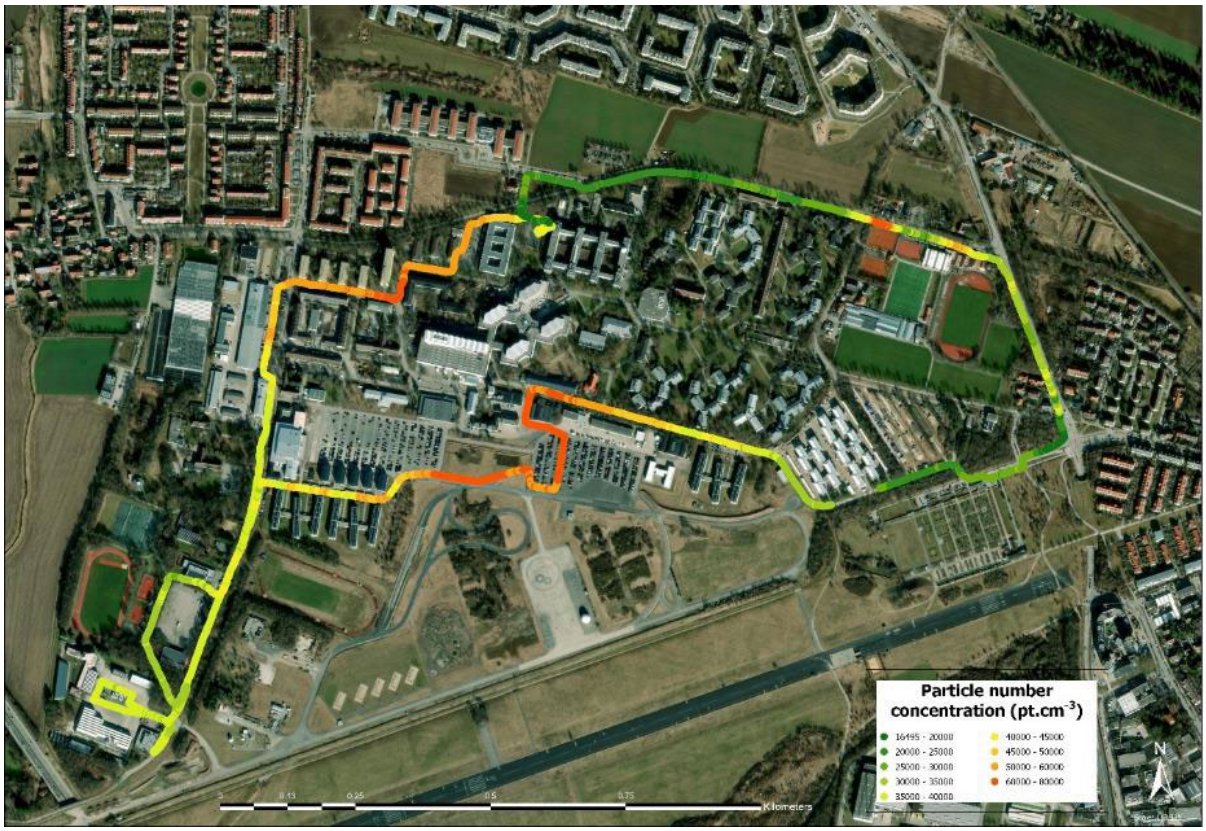

Fig. S2: *Spatio-temporal variability of particle number concentration during stroller measurement at Bundeswehr University Campus in Neubiberg, 27. 11. 2022 (7:50 – 9:11), samples for ICP-MS analysis were taken over the whole period of the walk (beginning is towards West)*

1.3 Subway mobile PM measurements

The stations included in this study are highlighted in the official public transport plan of the city of Munich (Fig. S3). For practical reasons, the study focused on the southern lines, but the city center was also included, so the selection of platforms and routes should be representative for the other lines, but further research is needed to confirm this assumption.

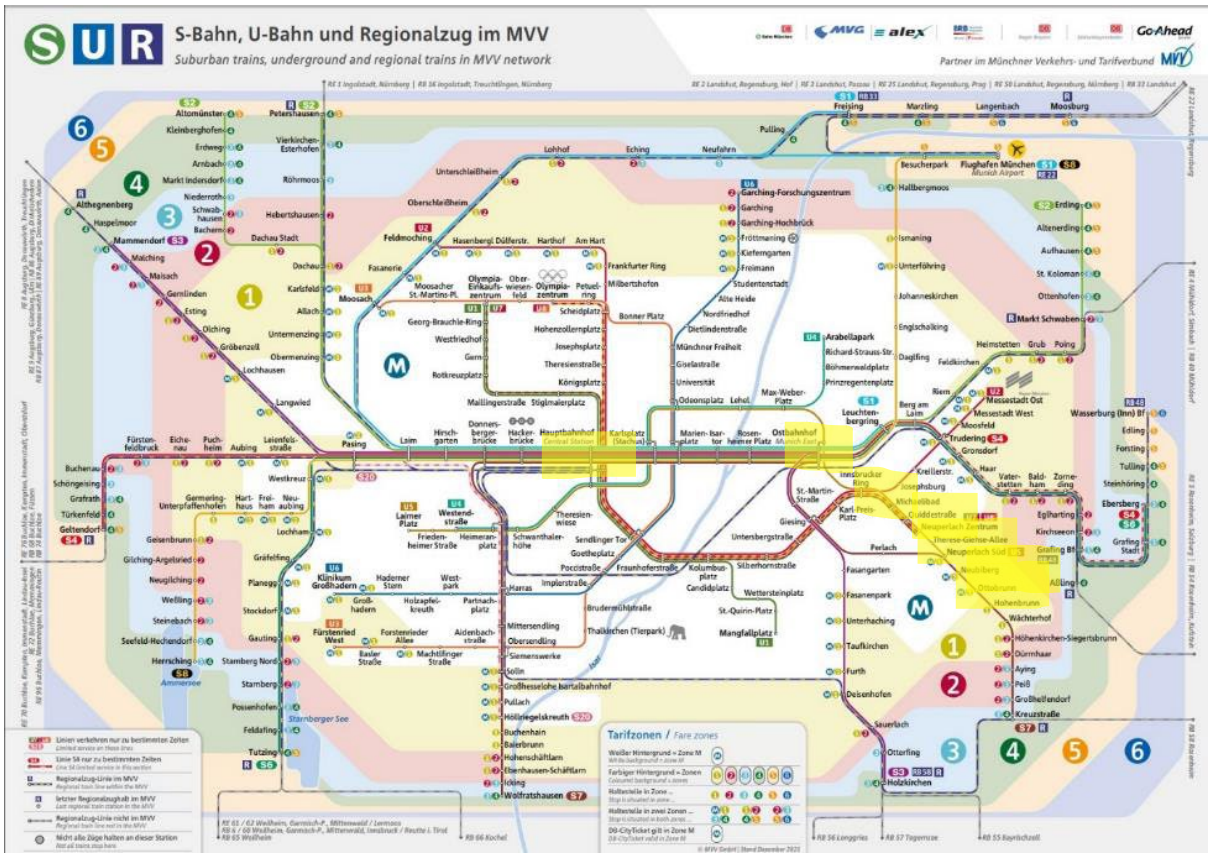

Fig. S3: *Plan of the Munich public transport system including the subway (U-Bahn), overground trains (S-Bahn) and trains (observed areas are highlighted), source: https://www.mvv-muenchen.de/*

Since concentrations change during the mobile measurements, each walk was divided into transects and the average values of selected parameters were recorded with standard deviations (Tab. S4-S10). In these tables, ambient walking measurements are listed at the beginning and end of each table to give an overview of the urban background. Then, the averages of stationary measurements (for at least several minutes to have enough data points), trips in the tunnel (*r*), and walks in the environment (*aw*) or indoors (*iw*) were recorded. The main purpose of these tables is to show the context of cumulative sampling (in bold) and other measured parameters for specific comparisons. The frequency of trains is calculated from the sum of all trains arriving at the station during the measurement period, therefore it does not correspond to the actual number of trains in a given hour. If the measurement time was too short for the information to be reliable, the number is preceded by a "~". This is also indicated before the measurement at the train station, where the number of arriving trains corresponds only to the adjacent platforms.

To illustrate the behavior of the aerosol and the transition from the ambient to the metro environment, see Fig. S2 on 17. 5. 2022 showing the PM_x and PNC dynamics during the walk from the university campus to the *NS* aboveground platform (A), where the PM_x concentration was similar to typical urban background levels and the PNC concentration was about 6000 pt cm^{-3}, with high short-term peaks due to traffic, the food kiosk, and a diesel engine at the construction site (around 1:40 pm). The black vertical line shows the approach to the old train with the windows open, since it was previously in the depot. The rate of increase in the 1-min. average is visible for PM_x particles, while PNC remains at a similar level. The dynamics of PM_{10} during the ride (B) is shown in greater detail in the Fig. 2 in the article. C represents 3-h long sampling periods and measurements at the main station, where concentrations are relatively stable. Some similarities in PNC and $PM_{2.5}$ variations were observed during this period; however, they do not overlap. In other cases, the opposite seems to be the case, such as at 15:40. A more

detailed look at the steady-state measurements is discussed in Section 4.5. Part D is the return trip to *NS-U/S* on the same train.

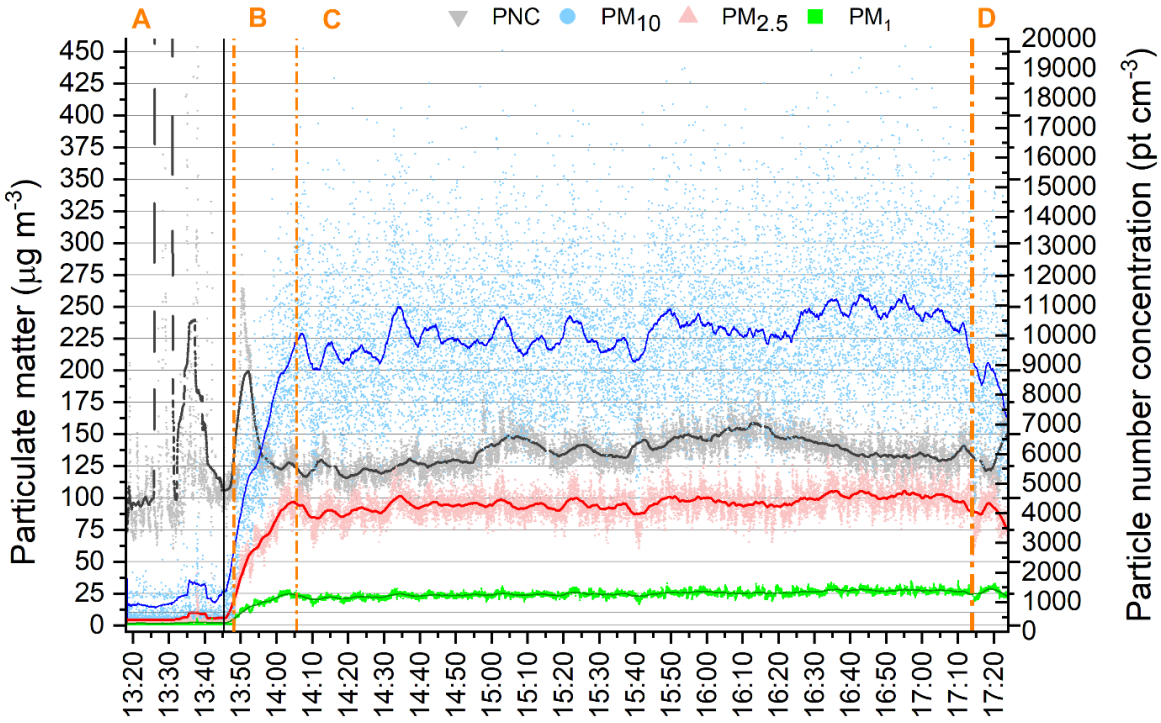

***Fig. S4**: Dynamics of PM_1, $PM_{2.5}$ and PM_{10} and particle number concentration PNC (1s scatter) with 5 min. moving average (bold line) during the walk from the UniBW campus to the subway station Neuperlach Süd NS-U/S (A), entering the train (black vertical line); ride by the old train with open windows (line U5) to the main train station CS-U1 (B); stationary measurements during 3-h long sampling at the CS-U1 platform (C), ride back to NS-U/S (D). 17. 5. 2022*

***Fig. S5**: PM_{10} variability (1 Hz) during the walk from the University campus to the subway station NS-U/S along the main street with higher traffic (A), waiting on the over-ground platform open to the ambient air and a ride into the tunnel by the old train (U5 line) with opened windows (B), 17. 5. 2022, 13:18 – 13:49*

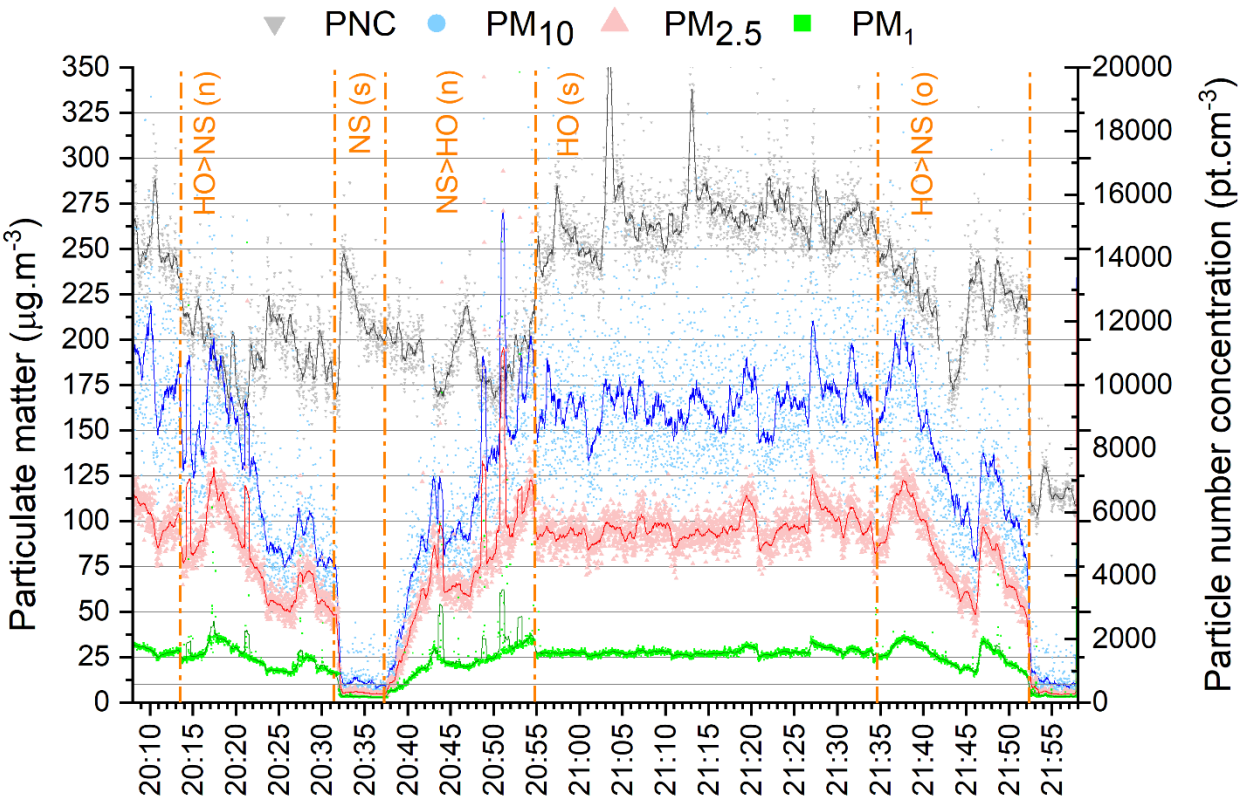

Fig. S6: *Comparison of the dynamics of PMx and particle number concentration (PNC) in 1s (scatter) and 30s moving average (color lines) during the way from underground station CS-U1 to over-ground terminal station NS-*U/S *by a new train (n) with air conditioning and back with exactly the same train. Stationary measurements (s) on the CS-U1 platform followed by the same way using the old train (o) with open windows to the tunnel on 28. 8. 2022.*

Tab. S1: *Sampling overview with the filter-material used*

Experiment	Purpose	Location	Fraction	Sampling	Flowrate (lpm)	Filter type	Filter vendor	LOT	Preconditioning
1	ICP-MS, gravimetry	Mobile/platform	PM_{total}	filter-holder with omni-directional inlet (TSI), SG10-2 (GSA) pump	9	Quartz 47 mm	Munktell ZEFA	3646	5h at 500°C
2	ICP-MS, gravimetry	Platform	$PM_{2.5}$	filter-holder with SKC pre-impactor and omni-directional inlet (TSI), SG10-2 (GSA) pump	9	Quartz 47 mm	Munktell ZEFA	3646	5h at 500°C
3	gravimetry	Platform	$PM_{2.5}$ and $PM_{>2.5}$	Sioutas impcator (SKC), two stages, SG10-2 (GSA) pump	9	PTFE 37 mm and 25 mm	SKC 225-1709 ($PM_{10-2.5}$) and Mitex ($PM_{2.5}$)	2153-7E5-306 and R8JA94705	without
4	SEM-EDX	Platform	PM_{total}	filter-holder with omni-directional inlet (TSI), Holbach BiVoc2 or SG10-2 (GSA) pump	2	Polycarbonate 47 mm	Whatman Nuclepore + silica wafers (p-type boron dotted)	A29752339	without

Tab. S2: *First scouting route (B) on 4. 11. 2021 segmented into units, where ">>" indicates movement from place to place and the abbreviations are the names of stations (university campus is Uni), which are listed in Table 1 in the article. In brackets, aw is ambient walk, s stationary, r ride. Average values and SD of particulate matter (PM_x), particle number concentration (PNC), equivalent black carbon (eBC) and UV absorbing PM (UVPM) are in the table. Concentration which are not reasonable due to the short acquisition time and low concentration are red. Sampling period for ICP-MS analysis is marked bold (7:17:02-8:54:25).*

ID	Location	Duration	Start	Stop	Train frequency	PM_{10}	$PM_{2.5}$	PM_1	PNC	eBC	UVPM
		min.	h:mm:ss	h:mm:ss	no. of trains (trains/hour)	µg m^{-3}	µg m^{-3}	µg m^{-3}	pt cm^{-3}	ng m^{-3}	ng m^{-3}
1	Uni >> NS-U/S (aw)	17	6:59:50	7:17:01		1 ± 7	0.3 ± 2	0.1 ± 0.1	3493 ± 8240	200 ± 347	182 ± 219
2	**NS-U/S (s)**	19	**7:17:02**	**7:36:15**	13 (41)	2 ± 5	0.6 ± 1	0.4 ± 0.9	5020 ± 3286	37 ± 0	146 ± 281
3	NS-U/S >> IR-U (r)	9	**7:36:16**	**7:45:20**		101 ± 62	44 ± 29	12 ± 8	4943 ± 1167	3330 ± 4223	3326 ± 2596
4	**IR-U (s)**	20	**7:45:21**	**8:05:15**	16 (48)	114 ± 45	48 ± 14	14 ± 4	5817 ± 1453	7345 ± 2350	5118 ± 1231
5	IR-U >> OU-U (r)	7	**8:05:16**	**8:12:20**		221 ± 62	102 ± 18	32 ± 5	4105 ± 542	13726 ± 3130	4980 ± 14684
6	**OU-U (s)**	25	**8:12:21**	**8:37:37**	11 (26)	240 ± 74	95 ± 18	27 ± 4	5820 ± 573	12507 ± 4304	7882 ± 2206
7	OU-U >> NS-U/S (r)	17	**8:37:38**	**8:54:25**		141 ± 77	60 ± 27	17 ± 8	6421 ± 1640	7502 ± 3833	4993 ± 2114
8	NS-U/S >> Uni (aw)	19	8:54:26	9:13:20		1 ± 3	0.2 ± 0.2	0.1 ± 0.0	4380 ± 11198	-136 ± 1176	172 ± 606

Tab. S3: *Second scouting route (C) on 5. 11. 2021 segmented into units, where ">>" indicates movement from place to place and the abbreviations are the names of stations (university campus is Uni), which are explained in Table 1 in the article. In brackets, aw is ambient walk, s stationary, r ride. Average values and SD of particulate matter (PM_x), particle number concentration (PNC), equivalent black carbon (eBC) and UV absorbing PM (UVPM) are in the table. Sampling period for ICP-MS analysis is marked bold (7:48:15-9:00:35).*

ID	Location	Duration	Start	Stop	Train frequency	PM_{10}	$PM_{2.5}$	PM_1	PNC	eBC	UVPM
		min.	h:mm:ss	h:mm:ss	no. of trains (trains/hour)	µg m^{-3}	µg m^{-3}	µg m^{-3}	pt cm^{-3}	ng m^{-3}	ng m^{-3}
1	Uni >> NS-U/S (aw)	21	6:56:00	7:17:00		10 ± 19	1 ± 3	0.4 ± 0.2	27630 ± 51683	117 ± 308	761 ± 782
2	**NS-U/S (s)**	7	7:17:01	7:23:45	2 (~17)	10 ± 11	1 ± 1	0.6 ± 0.1	11534 ± 1733	322 ± 153	1098 ± 356
3	NS-U/S >> OB-U (r)	24	7:23:46	7:48:15		66 ± 55	30 ± 16	12 ± 5	10033 ± 3272	5496 ± 2717	4207 ± 1677
4	**OB-U (s)**	20	**7:48:16**	**8:08:30**	8 (24)	293 ± 92	91 ± 16	24 ± 3	9625 ± 1020	12853 ± 2927	8411 ± 1656
5	Elevators (iw)	14	**8:08:31**	**8:22:45**		101 ± 91	32 ± 32	9 ± 9	21258 ± 7340	4929 ± 3596	3856 ± 2196
6	OB-U >> MC-U (r)	5	**8:22:46**	**8:27:35**		180 ± 57	72 ± 9	21 ± 2	10190 ± 1208	8866 ± 3559	6501 ± 1898
7	**MC-U (s)**	21	**8:27:36**	**8:48:50**	6 (17)	68 ± 28	31 ± 7	11 ± 2	9135 ± 736	5977 ± 2221	4214 ± 1596
8	MC-U >> NS-U/S (r)	7	**8:48:51**	**8:55:59**		100 ± 40	43 ± 11	14 ± 3	10601 ± 2153	7236 ± 2435	5046 ± 1794
9	NS-U/S >> Uni (aw)	32	**8:56:00**	9:27:30		10 ± 16	1 ± 2	1 ± 0.4	13251 ± 9145	1890 ± 1192	1647 ± 794

Tab. S4: *Third scouting route (D) on 17. 11. 2021 segmented into units, where ">>" indicates movement from place to place and the abbreviations are the names of stations (university campus is Uni), which are explained in Table 1 in the article. In brackets, aw is ambient walk, s stationary, r ride. Average values and SD of particulate matter (PM_x), particle number concentration (PNC), equivalent black carbon (eBC) and UV absorbing PM (UVPM) are in the table. Sampling period for ICP-MS analysis is marked bold (8:47:00-10:28:30)*

ID	Location	Duration	Start	Stop	Train frequency	PM_{10}	$PM_{2.5}$	PM_1	PNC	eBC	UVPM
		min.	h:mm:ss	h:mm:ss	no. of trains (trains/hour)	µg m^{-3}	µg m^{-3}	µg m^{-3}	pt cm^{-3}	ng m^{-3}	ng m^{-3}
1	Uni >> NS-U/S (aw)	18	7:59:55	8:17:45		7 ± 6	4 ± 3	4 ± 2	8551 ± 11656	682 ± 517	945 ± 512
2	**NS-U/S (s)**	5	8:17:46	8:22:30		9 ± 5	6 ± 1	5 ± 1	7064 ± 1218	95 ± 0	1138 ± 275
3	NS-U/S >> CS-U1 (r)	22	8:22:31	8:44:20		115 ± 58	57 ± 25	18 ± 6	5123 ± 1657	5248 ± 3506	4732 ± 2328
4	**CS-U1 (s)**	23	8:44:21	**9:07:20**	18 (47)	165 ± 46	67 ± 9	20 ± 2	10496 ± 2823	10355 ± 2015	6781 ± 1841
5	Elevators (iw)	4	**9:07:21**	**9:11:15**		180 ± 91	57 ± 20	16 ± 4	13520 ± 5973	5489 ± 3011	4889 ± 2348
6	**CS-U2 (s)**	19	**9:11:16**	**9:29:50**	16 (51)	243 ± 84	77 ± 13	20 ± 2	7709 ± 770	6035 ± 2303	5540 ± 1783
7	Elevators (iw)	6	**9:29:51**	**9:36:00**		163 ± 101	57 ± 28	17 ± 6	10947 ± 6473	6358 ± 3480	5380 ± 2594
8	**CS-R (s)**	48	**9:36:01**	**10:23:50**	~2	20 ± 24	10 ± 7	8 ± 3	4212 ± 2538	544 ± 749	626 ± 745
9	CS-U1 >> NS-U/S (r)	19	**10:23:51**	10:42:47		120 ± 48	53 ± 15	17 ± 4	6024 ± 1866	5095 ± 2308	4533 ± 1557
10	NS-U/S >> Uni (aw)	19	10:42:48	11:02:00		7 ± 9	3 ± 2	3 ± 2	17156 ± 81964	1189 ± 1247	1080 ± 969

Tab. S5: *Fourth scouting route (E) on 24. 11. 2021 segmented into units, where ">>" indicates movement from place to place and the abbreviations are the names of stations (university campus is Uni), which are explained in Table 1 in the article. In brackets, aw is ambient walk, s stationary, r ride. Average values and SD of particulate matter (PM_x), particle number concentration (PNC), equivalent black carbon (eBC) and UV absorbing PM (UVPM) are in the table. Sampling period for ICP-MS analysis is marked bold (9:31:21-10:22:39).*

ID	Location	Duration	Start	Stop	Train frequency	PM_{10}	$PM_{2.5}$	PM_1	PNC	eBC	UVPM
		min.	h:mm:ss	h:mm:ss	no. of trains (trains/hour)	µg m^{-3}	µg m^{-3}	µg m^{-3}	pt cm^{-3}	ng m^{-3}	ng m^{-3}
1	Uni >> NS-U/S (aw)	13	7:55:35	8:08:06		11 ± 20	4 ± 2	4 ± 1	22411 ± 82839	643 ± 305	928 ± 429
2	**NS-U/S (s)**	4	8:08:07	8:11:56	2 (~30)	14 ± 49	5 ± 3	4 ± 0	2154 ± 300	264 ± 81	813 ± 330
3	NS-U/S >> CS-U1 (r)	19	8:11:57	8:31:12		139 ± 78	58 ± 28	22 ± 8	4229 ± 1114	8372 ± 5356	5790 ± 3219
4	Elevators (iw)	3	**8:31:13**	**8:34:25**		191 ± 66	67 ± 17	23 ± 4	11775 ± 5901	12739 ± 2905	8689 ± 2096
5	**CS-R (s)**	31	**8:34:26**	**9:05:11**	~8	33 ± 24	12 ± 2	10 ± 1	10637 ± 4882	1111 ± 559	1626 ± 793
6	Elevators (iw)	3	**9:05:12**	**9:07:55**		104 ± 89	37 ± 29	14 ± 4	8107 ± 1849	2724 ± 2838	2301 ± 2404
7	**CS-S (s)**	20	**9:07:56**	**9:27:57**	16 (48)	236 ± 56	82 ± 9	21 ± 2	6205 ± 571	8446 ± 2753	6211 ± 1849
8	Elevators (iw)	9	**9:27:58**	**9:36:44**		131 ± 111	39 ± 30	12 ± 5	7666 ± 4751	4168 ± 2143	3473 ± 1519
9	**CS-U2 (s)**	2	**9:36:45**	**9:38:00**	3	228 ± 64	67 ± 7	16 ± 1	6570 ± 248	3982 ± 1050	3831 ± 757
10	**CS-U1 (s)**	26	**9:38:10**	**10:04:33**	13 (30)	196 ± 56	66 ± 10	20 ± 2	6646 ± 939	9941 ± 3313	6700 ± 1853
11	CS-U1 >> NS-U/S (r)	18	**10:04:34**	**10:22:22**		130 ± 47	53 ± 9	18 ± 3	4565 ± 582	7963 ± 3097	5444 ± 1549
12	NS-U/S >> Uni (aw)	12	10:22:23	10:34:46		7 ± 17	3 ± 1	3 ± 0.2	3635 ± 2258	1642 ± 1471	1628 ± 992

1.4 Repetition of the same subway route

The tables below are in the same style as in the previous chapter, here exactly the same route is repeated, however, some of the times spent at different locations vary due to train arrivals and departures.

Tab. S6: *First repetition of the same route (F1) on 7. 12. 2021 (7:27:50-10:14:00) segmented into units, where ">>" indicates movement from place to place and the abbreviations are the names of stations (university campus is Uni), which are explained in Table 1 in the article. In brackets, aw is ambient walk, s stationary, r ride. Average values and SD of particulate matter (PM_x), particle number concentration (PNC), equivalent black carbon (eBC) and UV absorbing PM (UVPM) are in the table. Sampling period for ICP-MS analysis is marked bold (7:54:45-9:53:10).*

ID	Location	Duration	Start	Stop	Train frequency	PM_{10}	$PM_{2.5}$	PM_1	PNC	eBC	UVPM
		min.	h:mm:ss	h:mm:ss	no. of trains (trains/hour)	µg m^{-3}	µg m^{-3}	µg m^{-3}	pt cm^{-3}	ng m^{-3}	ng m^{-3}
1	Uni >> NS-U/S (aw)	25	7:27:50	7:52:50		6 ± 11	1 ± 1	0.3 ± 0.1	5530 ± 3902	284 ± 392	389 ± 378
2	**NS-U/S (s)**	6	7:52:51	**7:58:50**	1	8 ± 10	1 ± 2	0.4 ± 0.4	5109 ± 1249	55 ± 230	270 ± 0
3	NS-U/S >> MC-U (r)	6	**7:58:51**	**8:04:30**		87 ± 39	34 ± 12	9 ± 3	4911 ± 436	632 ± 1615	2327 ± 973
4	**MC-U (s)**	6	**8:04:31**	**8:10:13**	4 (40)	89 ± 44	43 ± 19	13 ± 5	4670 ± 554	5098 ± 2102	4156 ± 1446
5	MC-U >> OB-U (r)	4	**8:10:14**	**8:13:50**		126 ± 36	63 ± 7	22 ± 2	5202 ± 308	6546 ± 771	5465 ± 711
6	**OB-U (s)**	14	**8:13:51**	**8:28:00**	5 (21)	211 ± 58	88 ± 16	22 ± 4	4984 ± 439	8436 ± 1688	6718 ± 1315
7	OB-U >> OD-U (r)	5	**8:28:01**	**8:32:40**		203 ± 52	94 ± 8	25 ± 1	4755 ± 788	9253 ± 1566	6436 ± 1464
8	**OD-U (s)**	10	**8:32:41**	**8:43:00**	4 (24)	188 ± 52	71 ± 9	20 ± 2	6779 ± 860	10675 ± 1566	6574 ± 1916
9	OD-U >> CS-U1 (r)	3	**8:43:01**	**8:46:20**		188 ± 53	79 ± 11	26 ± 4	6779 ± 478	10014 ± 3101	6961 ± 1619
10	**CS-U1 (s)**	12	**8:46:20**	**8:58:15**	9 (45)	197 ± 55	73 ± 12	19 ± 3	6482 ± 570	8629 ± 4105	5978 ± 1628
11	Elevators (iw)	19	**8:58:16**	**9:17:00**		30 ± 38	10 ± 13	4 ± 4	9758 ± 4870	1779 ± 2275	1545 ± 1576
12	**CS-S (s)**	10	**9:17:01**	**9:27:00**	7 (42)	33 ± 21	13 ± 4	4 ± 1	6532 ± 1439	1052 ± 1087	711 ± 837
13	CS-S >> NS-U/S (r)	26	**9:27:01**	**9:53:10**		39 ± 37	12 ± 6	4 ± 2	6597 ± 3318	1280 ± 702	1150 ± 689
14	NS-U/S >> Uni (aw)	21	9:53:11	10:14:00		6 ± 11	1 ± 1	0.4 ± 0.2	6475 ± 13906	187 ± 3067	126 ± 2963

Tab. S7: *Second repetition of the same route (F2) on 7. 12. 2021 (12:10:20-14:45:15) segmented into units, where ">>" indicates movement from place to place and the abbreviations are the names of stations (university campus is Uni), which are explained in Table 1 in the article. In brackets, aw is ambient walk, s stationary, r ride. Average values and SD of particulate matter (PM_x), particle number concentration (PNC), equivalent black carbon (eBC) and UV absorbing PM (UVPM) are in the table. Sampling period for ICP-MS analysis is marked bold (7:54:45-9:53:10).*

ID	Location	Duration	Start	Stop	Train frequency	PM_{10}	$PM_{2.5}$	PM_1	PNC	eBC	UVPM
		min.	h:mm:ss	h:mm:ss	no. of trains (trains/hour)	µg m^{-3}	µg m^{-3}	µg m^{-3}	pt cm^{-3}	ng m^{-3}	ng m^{-3}
1	Uni >> NS-U/S (aw)	18	12:10:20	12:28:38		4 ± 5	1 ± 0.6	0.4 ± 0.1	6865 ± 31489	32 ± 0	310 ± 148
2	**NS-U/S (s)**	10	**12:28:39**	**12:38:39**	2 (~40)	6 ± 7	2 ± 1	0.6 ± 0.3	3401 ± 765	32 ± 0	221 ± 111
3	NS-U/S >> MC-U (r)	11	**12:38:40**	**12:49:27**		46 ± 53	20 ± 10	5 ± 2	4219 ± 1123	558 ± 1009	1401 ± 729
4	**MC-U (s)**	10	**12:49:28**	**12:59:26**	3 (18)	26 ± 22	11 ± 6	3 ± 1	4309 ± 763	1488 ± 626	1316 ± 496
5	MC-U >> OB-U (r)	4	**12:59:27**	**13:02:59**		132 ± 52	60 ± 17	15 ± 5	3794 ± 368	4697 ± 2077	4075 ± 1511
6	**OB-U (s)**	10	**13:03:00**	**13:12:35**	5 (33)	118 ± 38	54 ± 10	14 ± 2	5166 ± 930	5283 ± 1185	4522 ± 882
7	OB-U >> OD-U (r)	5	**13:12:36**	**13:17:46**		118 ± 37	49 ± 6	15 ± 1	3780 ± 631	5607 ± 1428	4232 ± 756
8	**OD-U (s)**	15	**13:17:47**	**13:33:05**	5 (20)	113 ± 41	45 ± 11	13 ± 3	6041 ± 987	6786 ± 1800	5040 ± 1776
9	OD-U >> CS-U1 (r)	3	**13:33:06**	**13:35:37**		168 ± 50	78 ± 8	27 ± 1	5319 ± 357	10196 ± 1871	8717 ± 1238
10	**CS-U1 (s)**	13	**13:35:38**	**13:48:20**	6 (28)	122 ± 42	47 ± 10	13 ± 2	6976 ± 998	6770 ± 2293	5527 ± 1856
11	Elevators (iw)	8	**13:48:21**	**13:56:46**		28 ± 32	10 ± 9	3 ± 3	8535 ± 4535	2140 ± 1239	1578 ± 888
12	**CS-S (s)**	10	**13:56:47**	**14:07:04**	7 (42)	80 ± 34	25 ± 4	7 ± 1	5541 ± 583	3953 ± 1268	2745 ± 968
13	CS-S >> NS-U/S (r)	20	**14:07:05**	**14:27:27**		39 ± 32	15 ± 8	5 ± 3	6043 ± 2173	2494 ± 1529	3550 ± 2914
14	NS-U/S >> Uni (aw)	17	14:27:28	14:44:15		4 ± 5	2 ± 0.5	0.5 ± 0.1	8709 ± 19712	1272 ± 1013	984 ± 982

Tab. S8: *Third repetition of the same route (F3) on 7. 12. 2021 (16:10:05-18:25:50) segmented into units, where ">>" indicates movement from place to place and the abbreviations are the names of stations (university campus is Uni), which are explained in Table 1 in the article. In brackets, aw is ambient walk, s stationary, r ride. Average values and SD of particulate matter (PM_x), particle number concentration (PNC), equivalent black carbon (eBC) and UV absorbing PM (UVPM) are in the table. Sampling period for ICP-MS analysis is marked bold (16:32:40-18:10:00).*

ID	Location	Duration	Start	Stop	Train frequency	PM_{10}	$PM_{2.5}$	PM_1	PNC	eBC	UVPM
		min.			no. of trains (trains/hour)	µg m^{-3}	µg m^{-3}	µg m^{-3}	pt cm^{-3}	ng m^{-3}	ng m^{-3}
1	Uni >> NS-U/S (aw)	20	16:10:05	16:30:00		6 ± 7	2 ± 1	0.6 ± 0.2	24765 ± 29486	864 ± 886	1605 ± 1140
2	**NS-U/S (s)**	7	16:30:01	**16:37:10**	2 (17)	15 ± 13	3 ± 1	1 ± 1	24119 ± 6727	82 ± 0	1275 ± 903
3	NS-U/S >> MC-U (r)	7	**16:37:11**	**16:44:20**		63 ± 36	18 ± 7	7 ± 2	19411 ± 2232	714 ± 1466	2478 ± 533
4	**MC-U (s)**	5	**16:44:21**	**16:49:30**	3 (24)	53 ± 25	23 ± 5	7 ± 1	8073 ± 1063	3611 ± 1122	3256 ± 940
5	MC-U >> OB-U (r)	4	**16:49:31**	**16:53:20**		119 ± 45	46 ± 11	14 ± 3	8543 ± 717	6094 ± 1716	4870 ± 1045
6	**OB-U (s)**	10	**16:53:21**	**17:03:07**	5 (30)	199 ± 48	87 ± 7	25 ± 2	10105 ± 848	11090 ± 1928	7708 ± 1504
7	OB-U >> OD-U (r)	5	**17:03:08**	**17:08:30**		172 ± 47	72 ± 6	22 ± 1	7844 ± 598	10253 ± 1467	6028 ± 1796
8	**OD-U (s)**	10	**17:08:31**	**17:18:30**	5 (30)	175 ± 48	71 ± 7	22 ± 1	9301 ± 732	12194 ± 2383	6992 ± 1644
9	OD-U >> CS-U1 (r)	3	**17:18:31**	**17:21:45**		199 ± 52	75 ± 9	23 ± 2	7896 ± 602	7153 ± 2763	5850 ± 1605
10	**CS-U1 (s)**	12	**17:21:46**	**17:33:50**	12 (60)	212 ± 59	75 ± 9	21 ± 2	11313 ± 1144	8837 ± 2983	6530 ± 1586
11	Elevators (iw)	11	**17:33:51**	**17:44:50**		96 ± 62	30 ± 16	11 ± 4	14729 ± 6640	3758 ± 2528	3373 ± 1682
12	**CS-S (s)**	4	**17:44:51**	**17:48:50**	6 (90)	155 ± 53	48 ± 7	14 ± 1	9491 ± 597	5013 ± 2480	3875 ± 1172
13	CS-S >> NS-U/S (r)	20	**17:48:51**	**18:09:00**		47 ± 39	17 ± 12	7 ± 3	15647 ± 7250	3139 ± 1464	3065 ± 1119
14	NS-U/S >> Uni (aw)	17	**18:09:01**	18:25:50		9 ± 8	3 ± 1	2 ± 1	24923 ± 23754	2479 ± 1531	3342 ± 1667

1.5 Differences between the travelling in new and old trains

Tab. S9: *Difference between concentration of particulate matter (PM) in µg m^{-3} and particle number concentration (PNC) in pt cm^{-3} inside old (type B) and new (type C) train during the repetition of the same route between Neuperlach Süd NS-U/S and Hauptbahnhof Oben CS-U1, while the direction of 1 and 3 are from CS-U1 to NS-U/S and 2 in the opposite direction, 28. 8. 2022 between 20:15-21:50.*

Median	PM_1	$PM_{2.5}$	PM_{10}	PNC
1 New >	24.0	74.6	112.7	11120
2 New <	22.1	67.0	101.0	10884
3 Old >	25.9	81.7	127.8	12750

1.6 SEM-EDX analysis

Based on the mapping of 180 000 particles described in the Materials and methods of this paper (Section 3.5.3: Imaging and single particle elemental analysis using SEM-EDX), the particle size distribution is illustrated (Fig. S7).

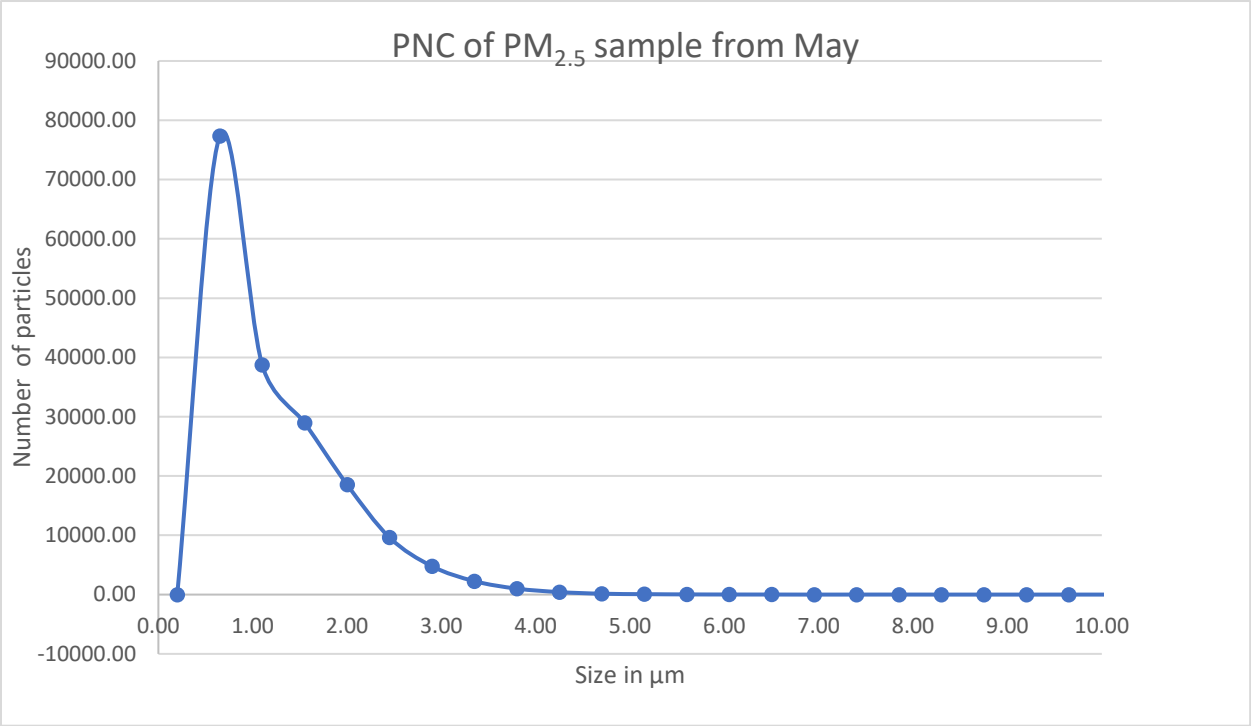

Fig. S7: *Particle size distribution based on the mapping of 180 000 particles by the EDX sensor, bin size 0.25*

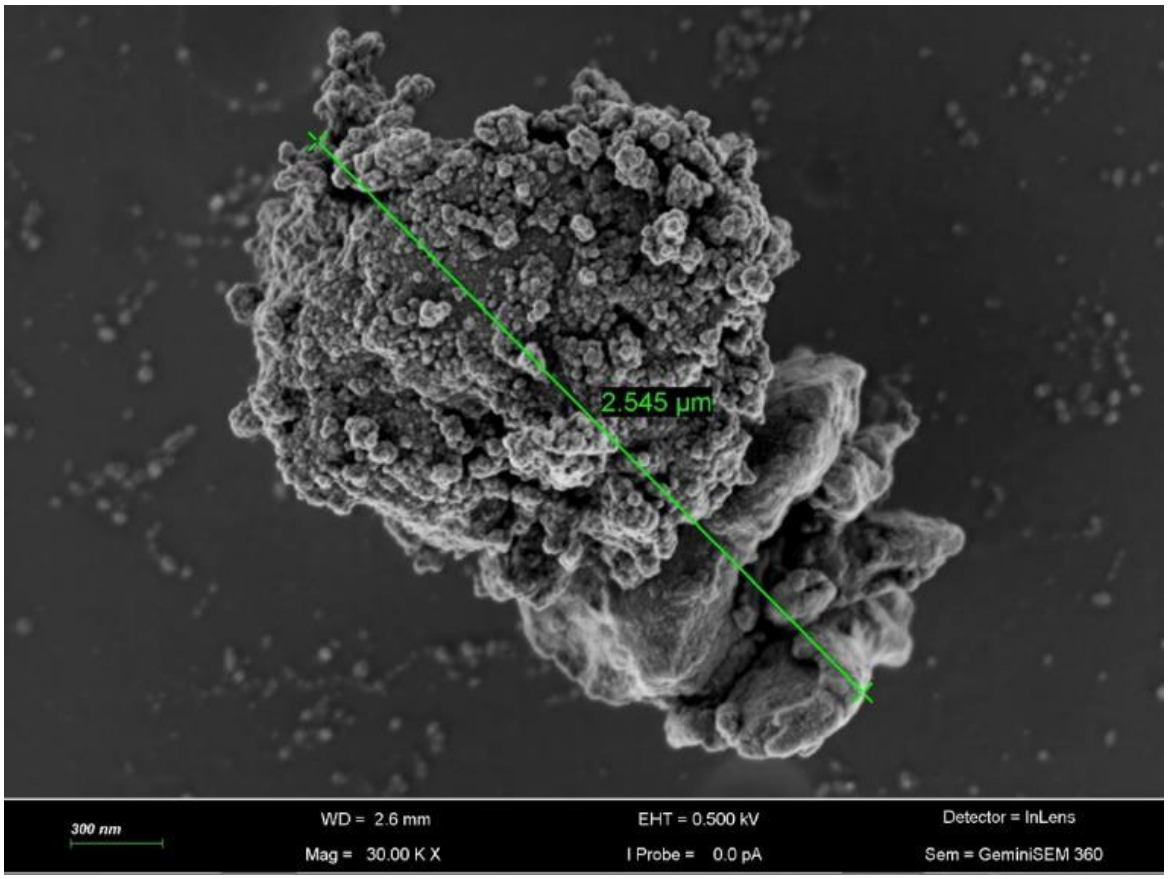

Fig. S8*: SEM micrograph of an iron oxide particle from the Munich subway*

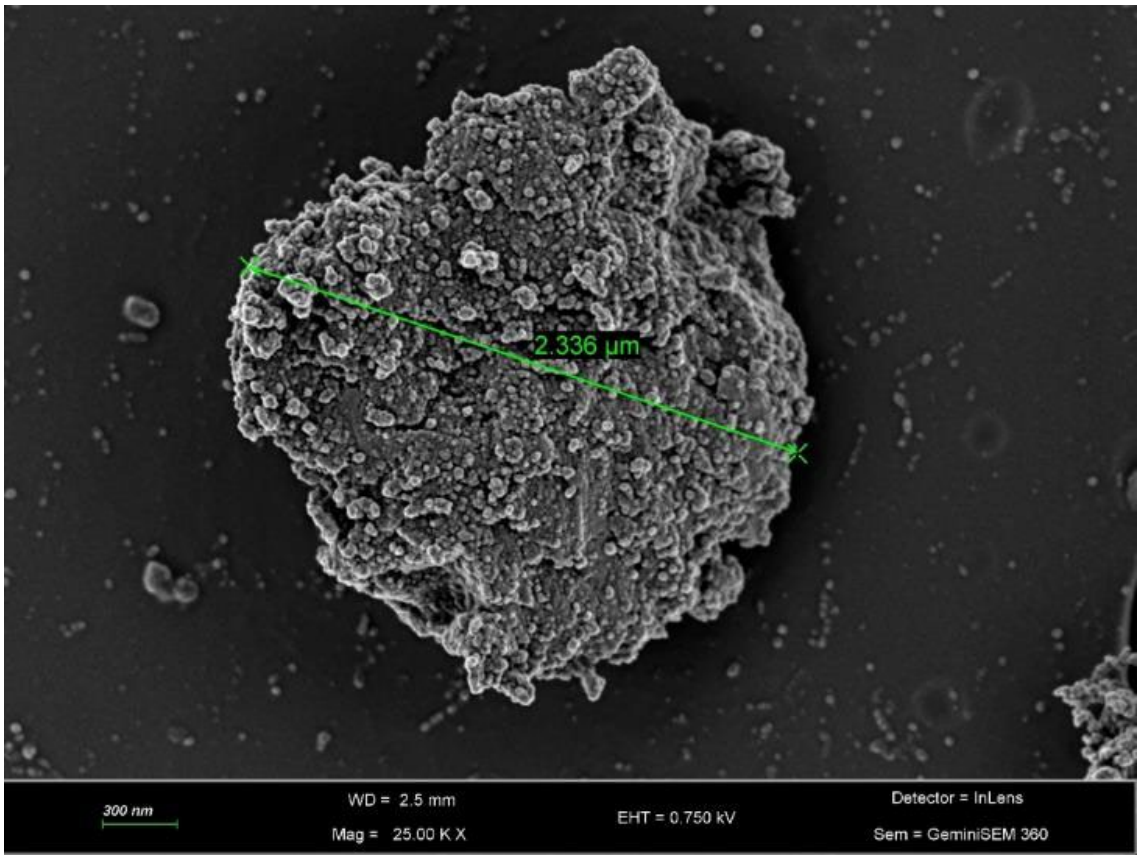

245

246 ***Fig. S9**: SEM micrograph of an iron oxide particle from the Munich subway*

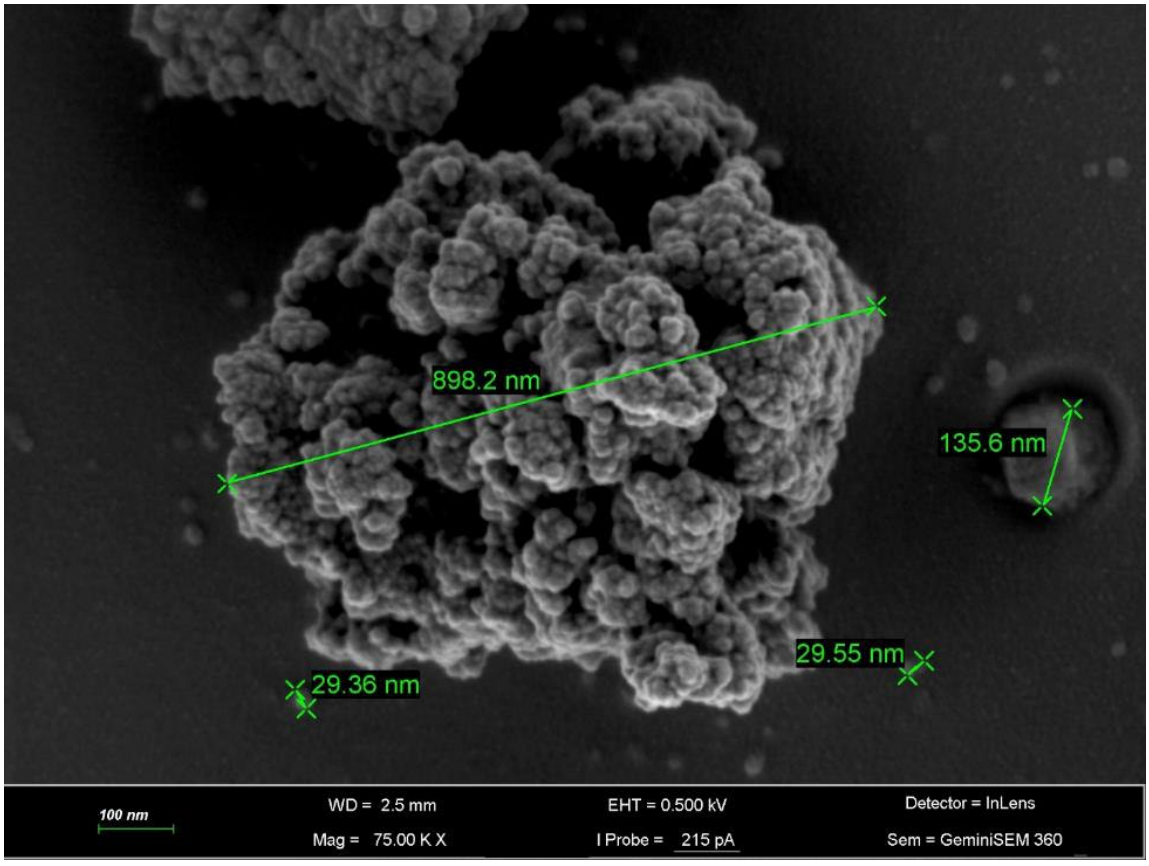

247

248 ***Fig. S10**: SEM micrograph of an iron oxide particle from the Munich subway*

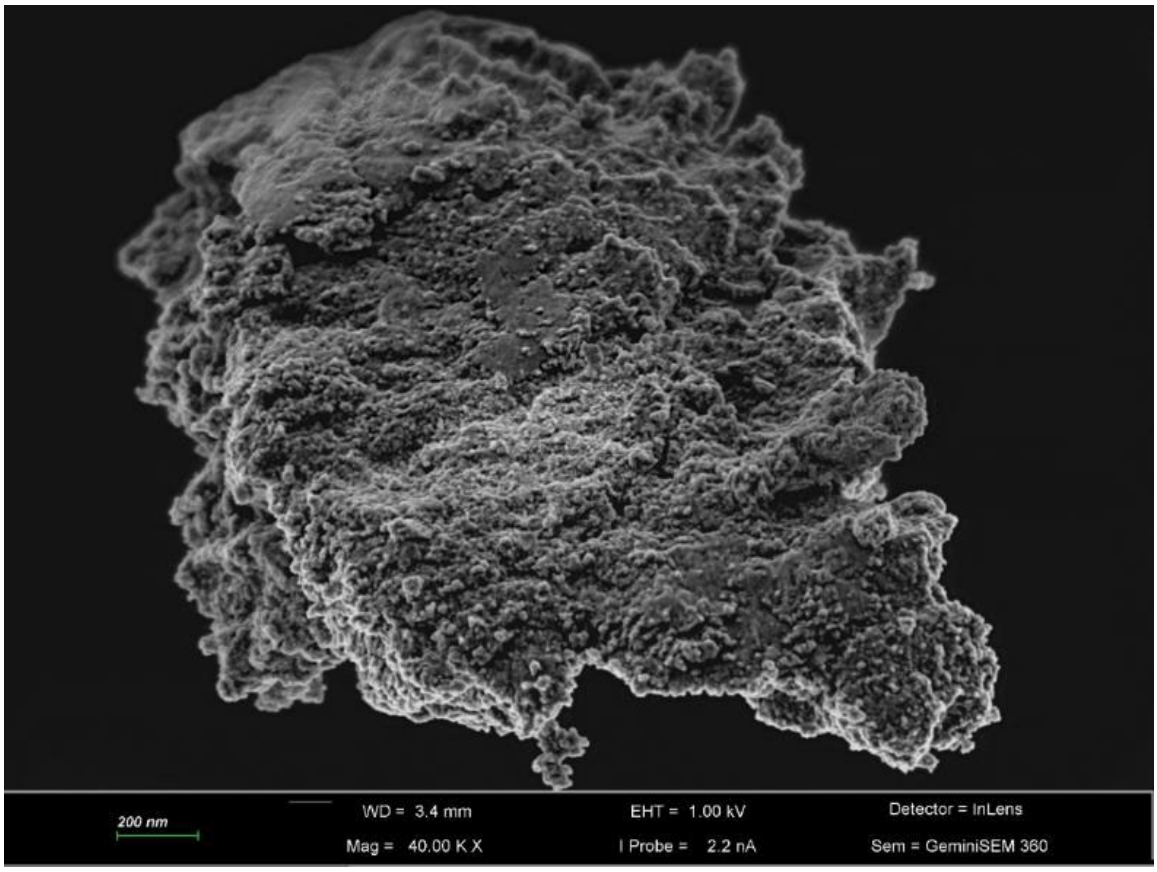

***Fig. S11**: SEM micrograph of an iron oxide particle from the Munich subway*

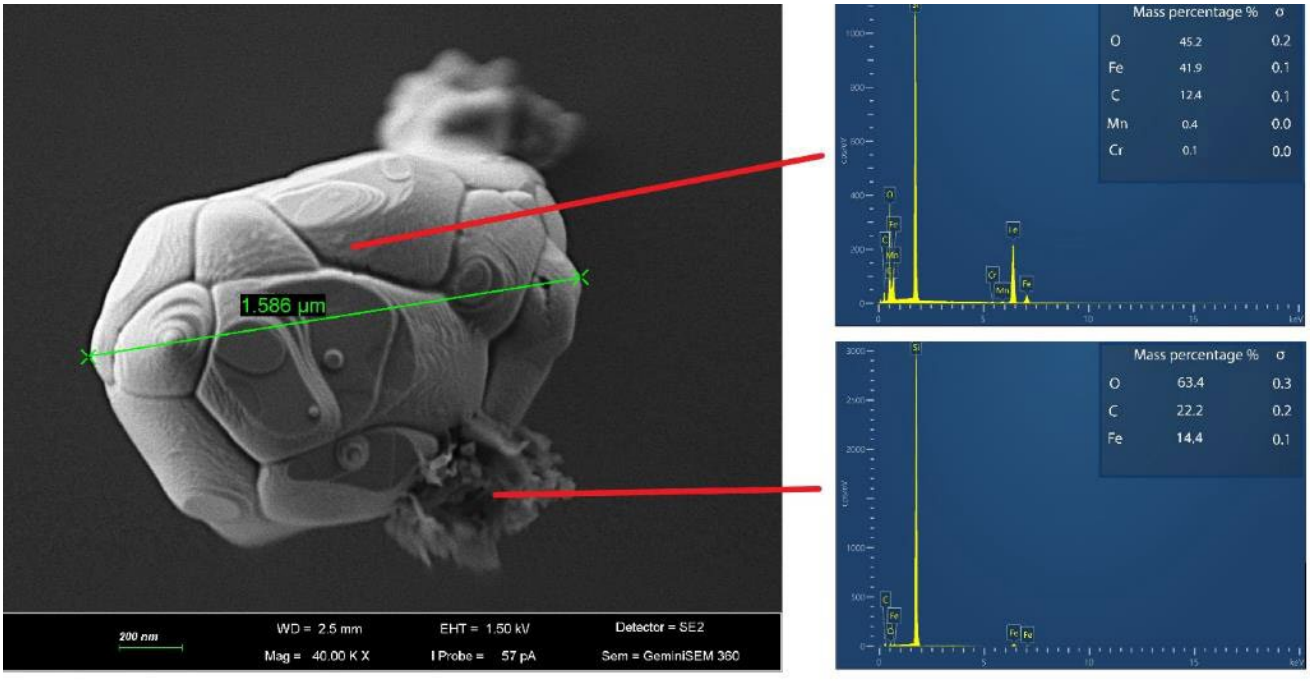

***Fig. S12:** SEM micrograph + EDX spectra of a layered iron oxide particle of unknown origin from the Munich subway*

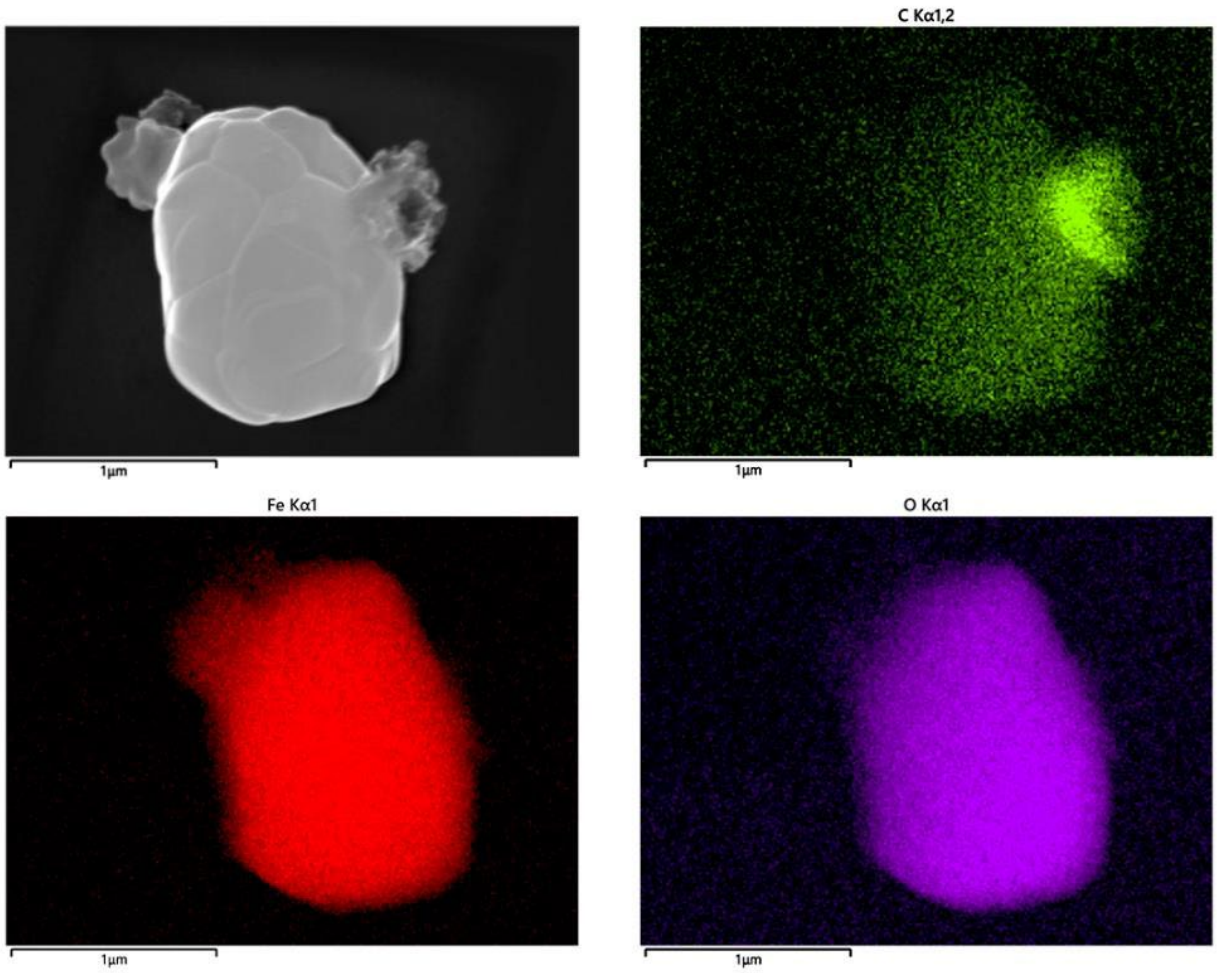

254

255 ***Fig. S13**: EDX mapping of a layered iron oxide particle of unknown origin from the Munich subway*

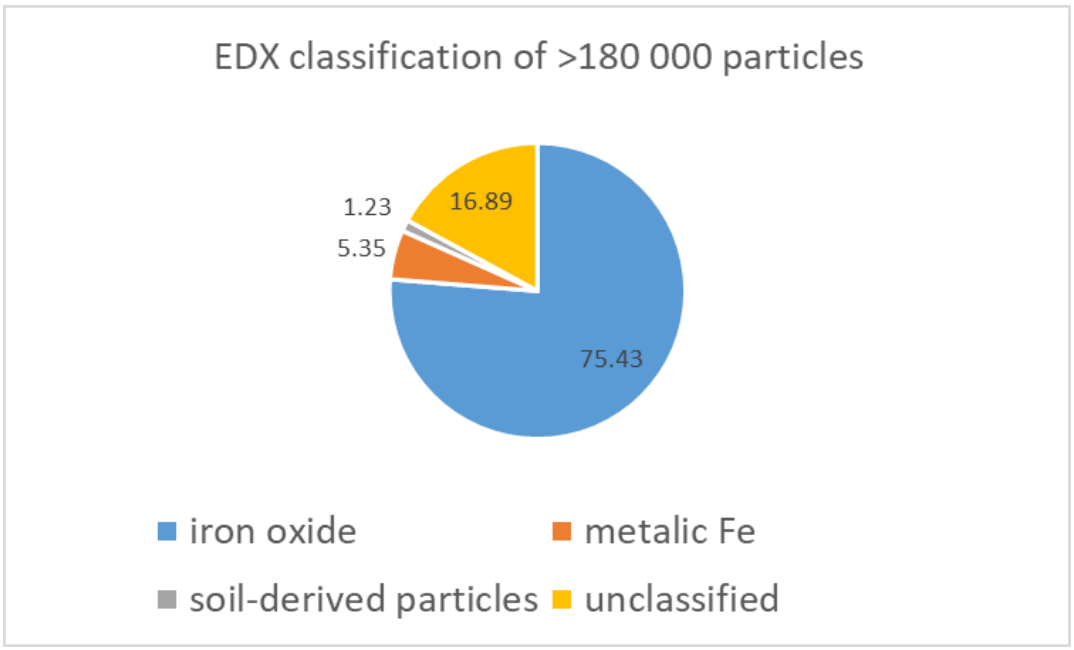

256

257 ***Fig. S14**: EDX classification of more than 180 000 particles, sampled at U-Bahn station CS-U1*
258 *platform on 28. 8. 2022 (14:06–20:06)*

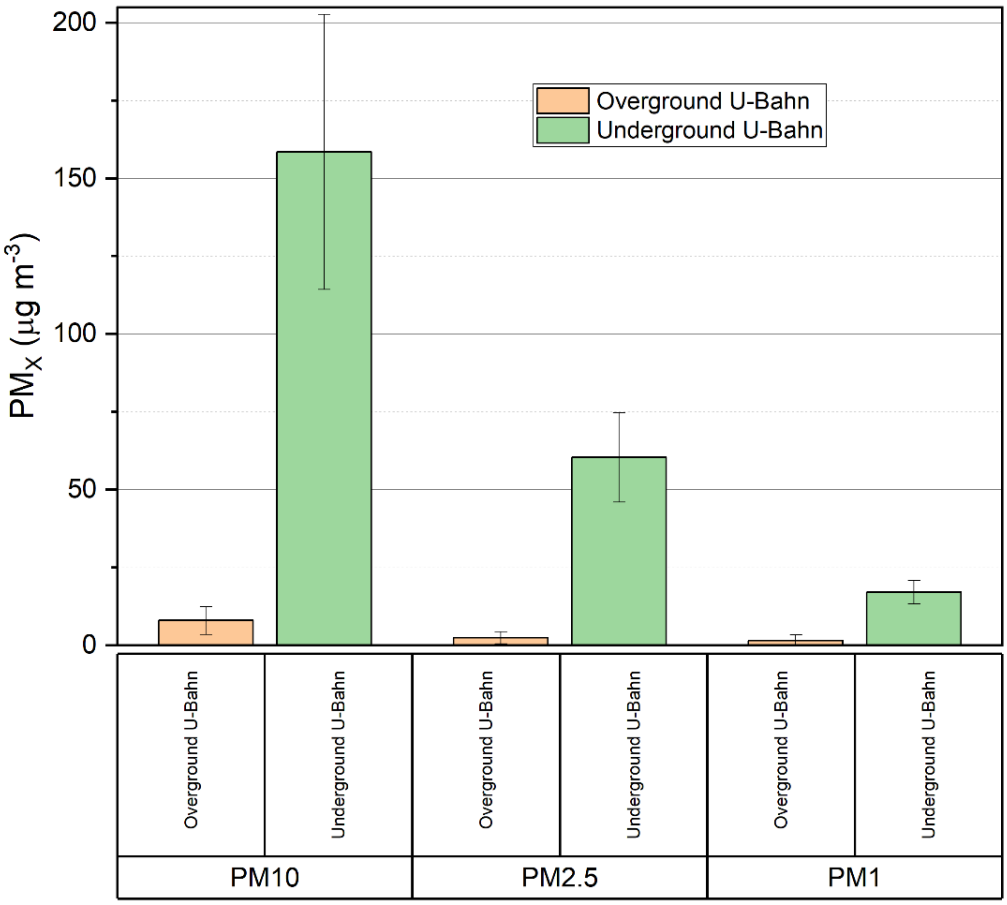

***Fig. S15**: Comparison of underground and overground stations: Underground stations: Michaelibad U5, Ostbahnhof U5, Odeonsplatz U4/U5, Hauptbahnhof U4/U5, Hauptbahnhof U1-U8, Innsbrucker ring U2/U5, Overground: Neuperlach Süd. Data for each station are available in the Table 1*

1.7. ICP-MS analysis

Standard calibration mix used for this study with the ICP-MS Agilent 8900:

- ICV-Standard calibration line: Agilent Technology Co., Part number: 5183-4682; Ca, Fe, K, Mg, Na, Sr, Ag, Al, As, Ba, Be, Cd, Co, Cr, Cu, Mn, Mo, Ni, Pb, Sb, Se, Th, TI, U, V, Zn
- Internal standard mix for ICP-MS systems: Agilent Technology Co., Part number: 5188-8525, 100 µg mL Bi, Ge, In, Li, Lu, Rh, Sc, Tb in 10% HNO_3)